NEAR-SURFACE STUDY OF STRUCTURE-PROPERTY RELATIONSHIPS IN ELECTROCHEMICALLY FABRICATED MULTI-COMPONENT CATALYSTS

A Dissertation
Presented to
The Academic Faculty

by

Robert E. Rettew

In Partial Fulfillment
of the Requirements for the Degree
Doctor of Philosophy in Materials Science and Engineering

Georgia Institute of Technology
December 2011

NEAR-SURFACE STUDY OF STRUCTURE-PROPERTY RELATIONSHIPS IN ELECTROCHEMICALLY FABRICATED MULTI-COMPONENT CATALYSTS

Approved by:

Dr. Faisal Alamgir, Advisor
Materials Science and Engineering
Georgia Institute of Technology

Dr. Preet Singh
Materials Science and Engineering
Georgia Institute of Technology

Dr. Brent Carter
Materials Science and Engineering
Georgia Institute of Technology

Dr. David Sholl
Chemical & Biomolecular Engineering
Georgia Institute of Technology

Dr. Larry Bottomley
Chemistry and Biochemistry
Georgia Institute of Technology

Date Approved: September 7, 2011

ACKNOWLEDGEMENTS

I wish to take this space to acknowledge, first and foremost, my loving wife Kelli who has been by my side throughout my graduate school process. I would also like to acknowledge my family, particularly my parents David and Robin and my brother Samuel who have been a loving support network throughout my education.

I would also like to acknowledge the professors and colleagues who have been influential during my time at Georgia Tech, specifically those of my dissertation committee. First among these is Dr. Faisal Alamgir, who I would like to thank for giving me the opportunity to participate on the ground floor of a new laboratory's startup. His guidance, support, and friendship have been invaluable. I also acknowledge Dr. Larry Bottomley and Dr. Preet Singh for help with electrochemistry questions and critical insights into important scientific questions. I acknowledge Prof. David Sholl for discussions related to theoretical and DFT questions, and Prof. Brent Carter for assistance with XPS-related questions. There are also several beamline staff from the National Synchrotron Light Source who I would like to thank for their assistance during synchrotron experiments, including: Dr. Bruce Ravel, Dr. Cherno Jaye, and Dr. Daniel Fischer. Finally, I would like to thank my friend Matthew Taylor for countless scientific discussions, as well as assistance with graphical software.

TABLE OF CONTENTS

LIST OF TABLES

LIST OF FIGURES

SUMMARY

This work outlines a series of developments and discoveries related to surface chemistry of controlled near-surface architectures. Through a combination of various cutting-edge X-ray spectroscopy techniques and innovative electrochemical fabrication techniques, valuable knowledge has been added to the fields of electrochemical fabrication, electrocatalysis, and fundamental surface chemistry.

Described here is a specific new development in the technique of surface limited redox replacement (SLRR). This work, along with an accompanying journal publication[1], reports the first-ever use of nickel as an intermediary for SLRR. In addition, this work identifies specific deviations from the nominal reaction stoichiometry for SLRR-grown films. This led to the proposal of a new reaction mechanism for the initial stages of the SLRR process, which will assist future fabrication attempts in this field.

This work also discovered fundamental changes in Pt overlayer systems as the thickness of the overlayer on a gold support is increased from less than a single atomic monolayer to multilayer thicknesses. It was found that Pt overlayers below a certain threshold thickness exhibited increased affinity for hydroxyl groups, along with an increased propensity for formation of oxide and chloride species. These films were also studied for methanol, carbon monoxide, and ethylene glycol electro-oxidation.

Finally, this work reports controlled surface architectures of Pt and Cu deposits on application-oriented TiO_2 nanotube arrays and Au-carbon supports. This work shows a correlation between Pt growth method, resulting atomic and electronic structure, and reactivity. In appendix A, a complementary vacuum-based study is reported in which monolayer-scale silver deposits on nickel single crystals are studied.

CHAPTER 1

INTRODUCTION

1.1 Motivation

There is a wide range of applications and devices that rely on surface-chemical interactions at an atomic or nano-scale. The potential for the surface of a material to influence ongoing reactions in its vicinity is of extreme importance to a variety of industries. When this effect causes a decrease in the temperature or energy required to drive a reaction, and the surface itself is not consumed as part of the reaction, the effect is said to be catalytic in nature. Thus a catalyst can be defined as a material that decreases the energy input required to progress the reaction of one material converting into another. Across the board, the world's current and future energy and chemical economies will rely heavily on the use of catalysts[2]. By exposing a reactant feed to a catalyst surface, a chemical conversion can be conducted with lower energy requirement than in the absence of the catalyst. Decreased energy requirements lead to decreased monetary costs associated with the process. Catalyst-driven reactions are used in a wide variety of applications, from chemical refining in the oil and pharmaceutical industries, to conversion processes necessary for the proper operation of advanced fuel cells and batteries.

The importance of surface chemistry is of course not limited to catalysis. Other types of interactions of a material with its environment, often in the form of surface reconstruction, corrosion or other processes in which the surface itself is a reactant, are important to any field that utilizes materials, whether as reaction vessels or structural members. All of these types of interactions, taken together, encompass the field of

surface chemistry. While these varied types of interactions have been of vital importance for decades, their significance is continuing to increase in recent years as more and more demands are made on our understanding of the fundamental science of surface chemistry.

Examples of new technology leading to this type of increased demand can be found in the advent of fuel cells and advanced battery systems, which require a complex interplay between a large variety of chemicals, including solid-phase cell components as well as gas-phase and liquid-phase fuels. In fuel cells, these solid-phase components are not restricted to mechanical members, but also include catalysts designed to promote both gas-phase and liquid-phase reactions. For energy storage, novel battery technologies require electrode surfaces at which important electrochemical reactions can proceed in an energetically favorable way. In addition to energetics, the kinetics of reaction rates must be considered in order to maximize power output. Even biofuels require cheap and efficient catalysts to allow the conversion of biomass-derived hydrocarbons into usable fuel. Finally, there is an increasing drive to understand the complex surface chemistry required to create and improve catalytic solutions to greenhouse gas emissions. Applications such as this, which aim to make traditional hydrocarbon energy sources more environmentally friendly, range from catalytic converters in cars to advanced techniques of carbon sequestration or other techniques.

Two important surface-chemical properties that influence the behavior of these systems are the chemical state and local atomic structure of the surface. Therefore, changes in the chemical identity, electronic structure, and atomic arrangement of the outer few layers of atoms in a catalyst material can have profound influences on the type and rate of reactions that proceed in a given system. This work provides a multifaceted

study of surface-chemical interactions for a series of representative catalyst surfaces, including Pt-Au and Ag-Ni monolayer-substrate systems, as well as high surface area Pt-TiO_2. By employing a suite of complementary electrochemical and X-ray techniques (using both in-house and synchrotron sources), a comprehensive understanding of the chemical state and structural properties of these systems is made possible.

1.2 Relation of Chemical State and Structure to Surface Properties

The first of these properties, chemical state, concerns itself primarily with the oxidation state and chemical bonds associated with a given material. At near-surface length scales (within a few nm of the surface) electronic perturbations are fundamentally linked to changes in surface chemistry, such that a consideration of chemical state must also consider changes in electron arrangement. In the case of metal catalysts, these changes can take the form of oxidation of the metal from the zero-valency to positive-valency states (often 2+ or 4+ for Pt). This oxidation is typically accompanied by the coordination of the metal atoms with anionic species such as oxygen or Cl atoms. These changes will in turn influence the interaction of the catalyst with the reactant feed. Changes in valency can be measured using X-ray photoelectron spectroscopy (XPS), a technique in which the sample is exposed to X-rays of a known energy and a spectrum of emitted photoelectrons can then be analyzed for specific photoemission peaks. It has also been shown that alloying of multiple metals leads to advantageous catalytic properties. For example, alloying of Pt with Pd has been shown to be effective for hydrogen oxidation [3-4], while Ru is well known to have a positive influence on the carbon monoxide poisoning resistance of Pt[5-8]. Alloying with non-precious metals has also been shown to increase noble metal durability. These types of catalysts are not limited to

applications for new energy, and have been shown to be applicable for water purifying applications[9] and chemicals conversions as well.

In addition to changes in the formal oxidation state of a material, nano-scale surfaces often exhibit subtle, weaker, electronic shifts arising from structure-induced perturbations in local electron distribution. This can lead to changes in the energy state of electrons in orbitals (in the case of molecules) or bands (in the case of metals or semiconductors). Often, the combination of two different metals in an alloy or a nanostructured arrangement will lead to a shift in the energy levels of electrons present in the material. This type of shift has a corresponding effect on the propensity of reactant feeds to accept or donate electrons to or from the catalyst. This work measures these effects by examining electron-transition-specific features of the X-ray absorption spectrum of a target element, using a unique technique called X-ray absorption near edge spectroscopy (XANES).

This final property, atomic structure, can be measured by a second X-ray absorption technique called extended X-ray absorption fine structure, or EXAFS. This technique gives information such as nearest neighbor distances and local structural order of a material by processing and transforming the absorption spectrum. In this way, the material itself is studied, and changes in its structure can be correlated with changes in reactivity. For example, specific crystalline facets of a given metal may show different levels of reactivity of selectivity[10], while it has also been shown that the presence of voids and disorder in a catalyst surface is of significant importance[11]. Specific geometries such as the core-shell architecture have also been studied.[12-22]

The type of reaction that proceeds can vary widely depending on the catalyst and its environment. These reactions can include processes such as hydrogenation, dehydrogenation, oxidation, epoxidation, or reduction. Reactants can range from gas molecules such as O_2 or CO, liquid-phase reactants including hydrocarbons such as methanol, ethylene glycol, or various alkenes, or even H_2O itself. An excellent example of the propensity for different metals to catalyze different reactions can be found in the comparison of Ag to Ni. Metals like Ni promote C-C bond splitting and dehydrogenation of ethylene, while Ag promotes the epoxidation of ethylene. Similarly, bimetallic systems (in which two metals are paired together in intimate contact at the surface) may feature the best of both individual materials. For example, the Ag/Ni(111) monolayer-modified surface exhibits excellent dehydrogenation and epoxidation activity due to oxygen at Ni sites, while the Ag modification removes the unwanted C-C bond breaking at Ni sites, creating a surface at which ethylene oxide (the desired product) is stable at higher temperatures than it otherwise would be.

The kinetics of chemical transformation, generally measured in terms of reaction rates, are also dependent on these properties. For example, the dominant crystal facet of a Pd metal particle will affect the selectivity and activity of hexane dehydrogenation. Knowledge of the different properties of specific facets allows chemists to isolate the properties of a single facet by selectively blocking undesired facets using methods such as polymer modification or sintering [23]. Thus there is a significant need for fundamental work such as UHV single crystal and theoretical studies to determine the catalytic properties associated with specific facets of various materials.

This type of intimate understanding of the workings of nanoscale mono- and multi-metallic catalysts is a major goal of much research. This research in particular focuses on the interaction of noble metals such as Pt and Ag with a variety of substrates, including Au, Ni, and TiO_2. These metal-support pairs were chosen due to their high applicability to a number of systems. Pt serves as a very important catalyst in a number of systems, particularly the oxygen reduction reaction in fuel cells. Ag can be exploited for its advantageous properties toward epoxidation reactions, while Ir has been shown to be an effective catalyst for hydrogen generation from chemicals such as hydrazine[24]. Ni, as mentioned earlier, serves as an important dehydrogenation catalyst, and TiO_2 is an appealing support for many nanoparticles due to its photoelectric properties as well as the stability afforded by oxidic supports in general[25-26]. This work shows that all of these metals, when grown as ultrathin films, exhibit changes in chemical identity, electronic structure, and atomic arrangement as a result of the influence of the metal or metal oxide support that they are paired with.

1.3 Applications of Catalysts in Industry

It is important to differentiate between the two main families of catalysts that exist in industrial use today. The first of these, heterogenous catalysts, encompasses solid-phase catalysts, often nanoparticles, supported on larger particles of a metal oxide or carbonaceous powder. These catalysts act as reaction sites for adsorbing and desorbing reactants and products, and are responsible for a variety of reactions that would otherwise not be energetically favorable. The second family of catalysts, homogeneous catalysts, is also responsible for a favorable manipulation of the energetics of desired reactions. In contrast to the first group, homogeneous catalysts are dissolved in the chemical reactant feed as part of the liquid phase. This means that homogeneous catalysts can provide higher mass-activities than heterogeneous catalysts as well as allowing reactions to occur that would be impossible for heterogeneous catalysts. On the other hand, homogeneous catalysts must be removed from the product stream after the reaction is complete, often by a complicated combination of chemical and mechanical filtering. This work restricts itself to the study of various metals used as heterogeneous catalysts.

By far the most common application for catalysis in everyday life is that of the catalytic converter system present in most modern automobiles. These systems contain elements including Pt, Pd, and Rh, and are primarily used to reduce the amounts of toxic carbon monoxide and nitrogen oxides that are produced from the partial combustion of hydrocarbon fuel[27]. These important reactions often require two types of catalysts to be present in series. First, a reduction catalyst must be used to convert the volatile nitrogen oxides to molecular nitrogen and oxygen. Then a second oxidation catalyst is used to oxidize the gaseous carbon monoxide to less-toxic carbon dioxide. Since these reactions

require a minimum temperature threshold in order to proceed, there is a great deal of interest in low-temperature carbon monoxide oxidation catalysts[28-30]. While automobile applications are the most relatable implementation of modern catalysis in our daily life, there are many other applications that are vital to the chemical and energy economies of our world today. These applications require various catalysts composed of different metals, including Ag, Pt, Ni, Ru, and many others.

Silver is currently the foremost heterogeneous ethylene epoxidation catalyst. Specifically, nanoparticles of silver immobilized on a metal oxide support (usually Al_2O_3) can be employed with satisfactory results. It has also been seen that modification of the Ag surface with other metals can improve the performance. If only chemical reactions for which an Ag electrocatalyst surface is suited are considered, it can be seen that these reactions are limited to only those reactions which occur at potentials for which the Ag surface is stable against oxidation or dissolution. Since Ag dissolves at a relatively low potential compared to Au or Pt electrocatalysts, this eliminates methanol, ethylene glycol, or carbon monoxide electro-oxidation as possible reactions that can be performed on the surface. Note that this limitation only applies for aqueous electrocatalysis, and that Ag is a useful gas-phase catalyst in many cases. The remaining options for electrocatalysis on Ag include reduction reactions such as organic halide reduction[31-34], alkyl iodide reduction[35], benzyl chloride reduction[36], or oxygen reduction[37-39]. There are also a few select electro-oxidation reactions that proceed at lower potentials than the oxidation potential of Ag, such as hydrazine[40-41], borohydride (useful for borohydride fuel cells) [42], or formaldehyde[43]. It has also been suggested that the oxides of Ag may exhibit some catalytic activity towards electro-oxidation of organic molecules[44].

Another important heterogeneous bimetallic catalyst in industrial applications is the Lindlar catalyst[10, 45]. This catalyst employs a Pd-Pb composite nanoparticle structure supported on calcium carbonate, and is used to selectively hydrogenate alkynes to alkenes without fully hydrogenating the molecule to an alkane. This catalyst employs the Pb additive to poison certain Pd reaction sites. Specifically, some crystal facets of Pd are responsible for the conversion of triple bonds to double bonds (the desired reaction) while others are responsible for the conversion of double bonds to single bonds. By exposing the Pd surface to a catalytically inactive material like Pb in such a way that the facets responsible for the double-to-single conversion are poisoned, a high selectivity of alkene hydrogenation can be obtained. Since Pb is highly toxic, other materials (such as adsorbed polymer groups) are currently being explored to take over the facet-blocking role[23]. Other applications for the original Lindlar catalyst system are also being investigated[46-47]. Apart from the Lindlar system, Pd is also used for hydrogen splitting, with Pd compounds and alloys providing useful hydrogen storage materials[48-52]. This is in part due to the high hydrogen permeability of Pd, which can Pb to breakdown and damage to the Pd structure if too much hydrogen is forced into the lattice [48] at sufficiently cathodic potentials.

Pt is another of the most important catalytic metals in heterogeneous catalysis today. It is used in a wide variety of applications, ranging from catalytic converters in automobiles to the oxygen reduction catalyst in hydrogen fuel cells[53-57]. Unfortunately, Pt is an extremely expensive material, which has led to increased efforts in Pt reclamation from used-up or spent catalysts via means such as acid treatment, Cl treatment, cyanide treatment, or complex ion-exchangers[58-63]. Ru is another important catalytic element. It

plays a role in both bimetallic heterogeneous catalysis as well as homogeneous catalysis. In the first case, it is present in the Pt-Ru alloy as a poison-mediating agent. By reducing the energy required to remove CO, which poisons the important oxygen reduction reaction, Ru acts as a valuable member of the Pt-Ru couple. As a homogeneous catalyst Ru complexes are more common than other Pt-group metals, and are often used to catalyze electron transfer steps in various hydrocarbon feeds[64-65].

Ni has been employed as a catalyst for breaking C-C bonds, particularly for ethane reforming. It has also been explored extensively as a catalyst for hydrogenation reactions of a variety of organics, including methyl acetoacetate[66], aromatic nitriles[67], and other aldehydes and alkenes[68-69]. It has been paired with Pt in bimetallic catalysts as well[70].

In addition to these traditional applications, there is a large body of work dedicated to employing surface chemistry techniques to develop materials targeted for photocatalysis. In these materials, a catalytic surface is paired with a photoelectric material, which utilizes incident photons to generate the free electrons required for the catalytic process to proceed. This process could be applied to a variety of different reactions, but the most promising (and most vigorously researched) reaction is the photo-assisted electrolysis of water to create hydrogen gas. One of the most promising materials for this application is TiO_2[71-73], which can be used for photocatalysis after doping[74] or after surface modification by other materials[75]. These surface modifications can either perform the relatively simple role of providing catalytically active sites for the reaction to proceed at, or they can influence the photoelectron generation process as well through plasmon resonance effects.

The above section has outlined in a very brief way several of the catalytically relevant metals to be investigated in this study. Applications for these elements in catalysis vastly exceed the scope of this work and thus only select applications have been examined. The important commonality between all of these various processes is the surface-intensive character of the specific chemical or electrochemical reaction that they catalyze. The differing electron arrangements and surface morphologies of the various elements and catalyst systems lead to varying activity for different reactions. Thus it is very difficult to force a relatively abundant element such as Cu or Ni to perform the catalytic role of a rare element such as Pt. While the catalyst surface by definition does not participate in the formal stoichiometry of a reaction, an industrial catalyst does in fact exhibit a finite lifetime due to deactivation processes and corrosion processes inherent in the process. In the next section, attempts to reduce the costs associated with production of catalyst materials, concerns related to materials durability, and scientific and engineering challenges arising from these important issues will be examined.

1.4 Cost Saving Techniques in Catalysis

1.4.1 Decreasing Noble Metal Loading

One important trend in the catalysis community pertains to the limited supply of valuable noble metals, which comprise a large portion of catalytically relevant systems. In particular, Pt conservation is of great interest. This interest arises from the relatively high costs associated with acquiring and refining these elements, and the extremely localized geographic regions in which these metals can be found. For example, Pt, the most sought-after of this group of metals, is primarily produced from ores mined in only two locations: South Africa and Russia[76]. Even the most Pt-rich ores, however, may only include 3 ppm of Pt, meaning the 1 metric ton of raw ore must be processed to obtain only 3 grams of pure Pt metal. Figures on the same order of magnitude apply for other Pt-group metals as well, including Ru, Pd, Rh, and Ir. In addition to limited supply, the demand for these elements continues to rise, with these elements playing important roles in chemicals synthesis, petrochemical refining, and (most notably) emissions control in the form of catalytic converters. Figure 1.1 shows the rising cost of Pt and Pd in USD, while figure 1.2 shows the world demand for Pt in 2010. It is clear that demand is currently exceeding supply, and with increasing requirements for Pt in fuel cell catalysts, this demand will likely continue to increase.

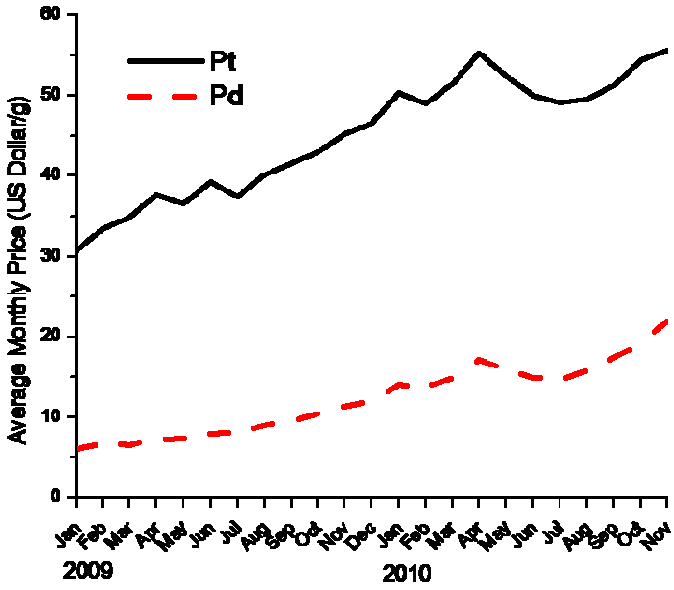

Fig 1.1: Average monthly price of a gram of Pt or Pd in USD. [77]

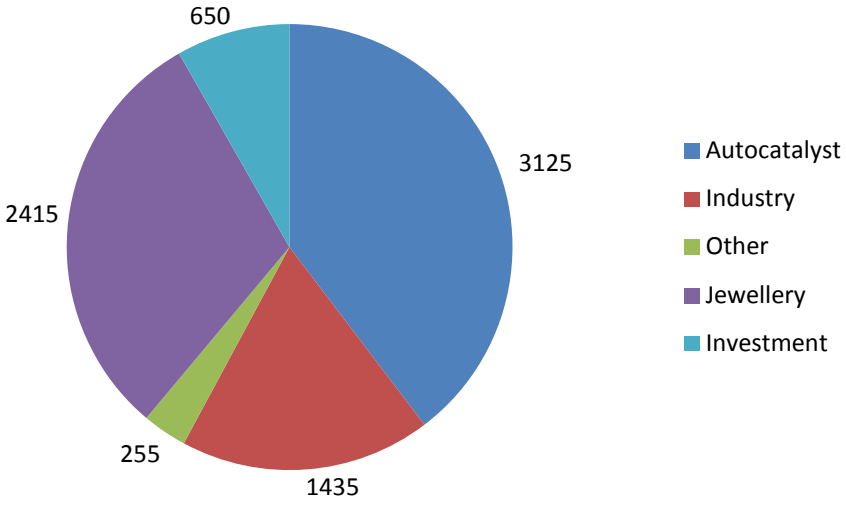

Figure 1.2: Total world demand for Pt (in 1000 oz) in 2010. Total demand = 7880 koz. Total supply = 6060koz. [77]

In order to mitigate the impact of these trends, many industries employ noble metal recycling programs, by which a customer purchases the catalyst from a catalyst development company and pays an additional deposit for the Pt content of the catalyst. After deactivation of the catalyst by usage in a reaction, the customer returns the used product to the catalyst developer, who recovers the noble metal for re-use and then returns the deposit to the customer. It is important to consider not only the metal-efficiency of the recycling program (i.e. what percentage of the valuable noble metal is recovered) but also the energy cost associated with the recovery, which determines whether or not the process is economical or not. This type of process is the subject of ongoing research to enable the most efficient recovery of noble metal possible, and is illustrative of the lengths to which industries currently go to lower consumption of precious noble metals.

In addition to recycling programs, development is currently underway for a variety of methods to reduce dependence on these metals. This can be accomplished either by decreased loading in traditional noble-metal catalyst systems or by replacing them with cheaper alternatives that function acceptably well. It has already been established that surface area is of prime importance in a catalyst system, since the rate at which reactants can interact with the catalyst material is limited by the amount of that material's surface available for interaction. The practice of noble metal scale-down, which involves using as little of a specific element as possible, has a broad range of consequences, including loss of durability and loss of catalytic activity. Durability loss can result both from size effects, whereby smaller clusters of atoms are less stable, as

well as from bimetallic or support effects, where the adhesion of the noble metal to its support suffers.

Many researchers have embraced the idea of a noble metal 'skin' encapsulating a more affordable metal structure, allowing the surface area to be preserved while cutting the cost of the entire structure. This type of architecture is referred to as 'core-shell', in that the core is composed of a more affordable filler material and the shell is the active catalytic skin. These approaches lack stability, due in part to morphological changes inducing exposure of the more easily corroded core, and also because such ultra-thin skins often exhibit properties significantly different from that of the bulk noble metal this structure is attempting to approximate. These scale-down effects, arising from materials properties changing at the nanoscale, are one of the main subjects of this study.

It is often difficult to separate, much less to quantify, the extent to which scale-down effects (as opposed to morphological rearrangement effects) are responsible for changes in the performance of core-shell systems compared to corresponding single-element systems. These scale-down effects may range from structural effects, by which the metal itself rearranges due to strain effects, to electronic effects, which encompass electron orbital shifts and band structure changes. In real applications, it is often seen that agglomeration of the catalyst surface occurs, during which the noble metal clusters into shapes with lower total surface area than the film morphology. This type of phenomenon has previously been observed during oxidation/reduction cycling of ultrathin films[78]. This indicates that the nanoscale 'skin' is thermodynamically unstable compared to the agglomerated nuclei. This agglomeration is often accompanied by dissolution, and both

steps can be treated as corrosion phenomena that occur faster for small deposits than for larger deposits.

Nevertheless, the economic incentive to decrease noble metal loadings is very strong. In a typical single-element 100nm diameter nanoparticle, for the simple approximation that only a few atomic layers below the surface play a role in the catalytic processes, the remaining core of the particle constitutes a >99% waste of material. That is to say, only the outer 10-atoms-deep 'skin' of any given particle is actually participating in the catalytic process, and the bulk of the particle is simply providing a physical support structure. In many applications, the cost of the catalyst is dominated by the materials cost of the valuable noble metals involved. While it is possible to decrease the amount of waste by decreasing particle size (which leads to higher surface area/volume ratios), this technique cannot eliminate the predominance of unutilized core atoms entirely.

Additionally, there are a plethora of benefits to be reaped by understanding the nanoscale multi-component interactions that arise when ultrathin 'skins' of one metal are grown around another metal. Many examples of this can be seen in the literature for so-called monolayer bimetallic surfaces (MBS), in which a monolayer of one metal is grown on the surface of a dissimilar metal. These studies have shown that the influence of an adlayer can dramatically alter the properties of the substrate, and, conversely, that the adlayer itself shows altered behavior due to the substrate it is grown on. Taking these studies a step further, multilayer bimetallic surfaces can be grown, in which the adlayer forms an ultrathin film, the thickness of which is measured in integers of atomic thickness.

This work evaluates these type of effects by using electrochemical and physical vapor deposition techniques to generate controlled-thickness structures at an atomic monolayer scale on a variety of substrates, including metallic substrates such as Au and Ni, as well as oxidic substrates such as TiO_2. The samples employed span a range of geometries, from monolithic single crystal surfaces to micron-size supports on carbon fiber paper to ordered nanotube arrays. The use of flat, and particularly monocrystalline, surfaces allows orientation-specific surface spectroscopy to be conducted more easily. By controlling the thickness of a wetted adlayer on a monolithic support, core-shell geometries can be approximated in a planar arrangement, where the core is approximated by the underlying substrate layers and the shell by the overlayer. By tracking a variety of effects for a range of overlayer thicknesses, this work establishes length scales for a range of effects.

1.4.2 Catalyst Durability

Durability is one of the primary concerns when using ultrathin nanofilms as catalyst materials. For this reason, many different substrates have been employed to support such nanofilms, based on the principle that the substrate-catalyst interaction will assist in stabilizing the morphology of the catalyst deposit. It has been shown that certain substrates, including polymer structures or TiO_2 nanofilms, can stabilize a catalyst against breakdown[79-80]. While it appears that the elemental and chemical identity of the support plays a significant role in stabilizing the catalyst deposit[81], the structure and scale of the deposit itself also influences the nanofilm's behavior and durability significantly. By deliberately choosing a substrate on which the catalyst deposit adheres but is not significantly stabilized, it is possible to discount the substrate-catalyst interaction and study the dependency of catalyst stability on other factors, such as growth method or morphology.

An electrochemical durability test, also known as an accelerated aging test (AAT) can be conducted by applying an electrochemical potential to the electrode surface and sweeping this potential between two extremes. In this type of polarization or cyclic voltammetry (CV) test the amount of reaction proceeding at a given potential is proportional to the current measured at that potential. It is necessary to choose an electrochemical system with a probe reaction that allows for differentiation of reactions on the catalyst from reactions on the support. This probe can take the form of a reactant molecule which oxidizes at different potentials on each component, or is inert towards one component compared to the other. This probe can either involve an adsorbing molecule (such as ethylene glycol, methanol, or H_2) or the probe reaction can be the

direct oxidation/reduction of the material itself. In cases where the oxidation state of the film or substrate is changed, it is important to consider how that change will affect the analysis. Since this type of test tracks component stability by monitoring total electrochemically active surface area, changes in surface area arising from film reconstruction during reversible oxidation/reduction cycling must be considered. By conducting this test in different pH regimes, the stability of the catalyst in different environments can be determined.

Other types of AAT protocols can also be employed by which the catalyst is tested under actual reaction or device conditions. These tests often employ a reaction-specific measurement, such as current (for electrochemical devices) or yield selectivity (for chemical reaction processes). Rather than providing specific information about morphological changes such as surface area loss or agglomeration, these tests focus on tracking performance loss over time. These types of tests might be performed in a diagnostic laboratory setup such as a small-scale flow reactor [82], or may employ true *in operando* conditions by measuring the output of a device or process in realistic operating conditions.

As a first approximation, nanoparticle or nanofilm corrosion can be treated as a combination of two degradation methods: coalescence and dissolution. In the first stage, the deposit agglomerates to a critical size, at which the deposits partially stabilize and degradation slows. This step has been reported to occur by one of three mechanisms: dissolution & precipitation, sintering, or Ostwald ripening[83]. These mechanisms can be distinguished from one another by quantitative analysis of particle size distributions in *ex-situ* microscopic studies[84]. These larger deposits then begin to dissolve over time. For

the specific case of Pt catalysts, this dissolution step is hypothesized to occur when the Pt deposit oxidizes, creating a more soluble oxide film that is then broken down by simple dissolution in the solvent. It is well known that bulk Pt will form a surface oxide, but this oxide is usually quite stable in comparision to other materials. It is possible that the oxide stability shows a dependency on film thickness or particle size, leading to an effect by which deposits or layers below a critical size threshold are more easily compromised than layers grown on bulk Pt[85]

In this work, catalyst durability is one of a series of important properties studied using a representative system of a gold substrate with Pt overlayer. The next two chapters will outline the full suite of properties to be studied, as well as previous work conducted in the literature that informs this study. Additionally, the techniques employed will be discussed, and the interrelationship between chemical identity, electronic structure, and atomic arrangement will be further explored.

CHAPTER 2

LITERATURE REVIEW

2.1 Traditional Catalyst Nanoparticles

Nanoparticles are ubiquitous in today's scientific news and are increasingly more commonplace in daily life and culture. However, the advent of nanoparticle technology is not new to the catalysis industry, which has been employing nano-scale architectures for years. In fact, catalysts are one of the earliest applications of nanoparticles in an industrial setting, with their use in catalytic processes preceding even the coining of the term nanotechnology. While the use of nanoparticle catalysts preceded the international drive to engineer controlled systems at the nano-scale, the advantages granted by these systems were already being put to good use as important members of a string of reactions necessary for the development of the chemicals required for the modern western lifestyle.

The history of catalysis itself can be traced as far back as the early invention of fermentation or the medieval desire for alchemy- that is, the spontaneous conversion of material into gold. It was not, however, until 1835 that the field of catalysis itself was recognized by Berzelius, who summarized the requirement that a catalyst accelerate a reaction without participating in it, and coined the term 'catalytic force[86]. While early studies of catalysts employed solid bulk catalysts such as Pt foil or niter, the field advanced rapidly towards more finely-divided catalysts [87]. After a period of initial investigation and advancement in the understanding of the chemistry of catalysis through the late 1800's, the turn of the 20th century heralded a new golden age for catalysis, due to increased demand for chemicals such as petroleum products, pharmaceuticals, and

polymers [88-89]. As technology progressed, empirical catalyst development led to many applications in which nanoparticles resulted as the forefront catalyst technology.

Catalyst nanoparticle fabrication can be performed in a variety of ways, including chemical, thermal, colloidal, templated, or electrochemical methods. All of these techniques share two primary goals: (1) the control of the composition/structure of single particles, and (2) the control of the size distribution of a batch of particles. While the specific composition and structure desired may change from one application to another, a very narrow distribution of particle sizes is generally desired for most applications. Depending on the type of structure and composition desired, different methods will lend themselves more readily to a successful fabrication process.

It is worthwhile to examine the various fabrication methods mentioned above briefly, in order to understand their advantages and disadvantages. All of the mentioned techniques utilize solutions of a dissolved form of the element of interest, and these dissolved species (usually positively charged cations) must be reduced to the zero-valent metallic state in a controlled way. Often it is possible to take advantage of chemical properties of the specific element in question such as solvation or affinity for specific molecules to facilitate particle size control. Chemical methods of achieving this reduction step are the most common, and involve the use of reducing agents or pH-changing additives to induce the transformation. This technique, while providing a simple avenue for nucleation of the zero-valent metal phase, does not on its own provide an easy route to the control of structure or size distribution. Thermal techniques manipulate the temperature of the solution to influence the thermodynamic behaviors such as agglomeration or coalescence, but is often insufficient to induce cation reduction on its

own. Colloidal fabrication methods use additives such as polymer molecules to restrict particle growth, ideally leading to a controlled size distribution, but these techniques leave behind polymer residues that must then be removed or risk interfering with the intended application. Templated particle synthesis utilizes similar polymer or organic molecules and grows the particles within nanoscale void spaces in a molecular template, which must subsequently be removed by chemical dissolution or thermal breakdown. These techniques are constantly being revised and improved, and innovation in nanoparticle synthesis abounds.

This study focuses on the final fabrication technique mentioned above, that of electrochemical methods for nanoscale catalyst formation. While the other methods discussed here provide relatively simple routes to well-controlled single-element particle catalysts, they are not well-suited to creating atomic monolayer-scale coatings. Electrochemistry is advantageous in this regard because it is inherently a surface-active technique, with electrode surfaces serving as the dominant reaction sites for a given process, whether etching or deposition. Since this work focuses on nanoscale film interactions, the most suitable technique for fabrication of such films has been an electrochemical fabrication technique known as surface limited redox replacement (SLRR).

2.2 SLRR and Nanofilm Studies

The development of techniques for atomic layer-by-layer growth of ultrathin films has been a long one. Techniques range from vacuum methods such as vapor deposition and e-beam deposition to gas-phase techniques such as atomic layer deposition (ALD) and liquid phase techniques, mostly based around electrochemical methods. The various techniques have their advantages and disadvantages. Vacuum methods in particular require precise calibration and expensive and intricate apparatus, while gas-phase methods require elevated temperature and are limited in the scope of metals they can grow by the existence of specific precursor molecules unique to each substrate. Electrochemical methods provide a route of ultrathin film fabrication that requires relatively little in terms of equipment and set-up. A simple electrochemical fabrication cell can consist of the substrate material, several electrodes of varying materials, and an electrolyte bath consisting of electrolyte and the appropriate dissolved metal. Because of the potentiostat's convenient ability to apply a controlled voltage (provided a reliable reference is used), the energy required to induce phase formation and transformation can be supplied directly to the system in question while isolating the reaction to a specific surface, namely, the interface between the electrode and electrolyte.

Because of these advantages, many researchers have attempted to replace traditional film fabrication methods with electrochemical ones. The majority of these attempts employ a technique called underpotential deposition (UPD)[90-93]. UPD relies on a phenomenon by which the solid phase of a dissolved material A is nucleated on a second material B. However, there is in many cases a difference in the activation energy required to nucleate a bit of A on a B-site and the energy required to nucleate an identical bit of A

on top of the resulting A-site. This leads to the situation where, if the energy applied to the system can be specified directly between these two thresholds, all exposed B-sites at the solid-electrolyte interface will be covered with nucleated bits of material A. This situation is called a monolayer, by which a layer of material A of single atomic thickness coats the original material B. This monolayer can grow no further than single atomic thickness, unless the energy supplied to the system increases past the threshold activation energy for which material A can grow upon itself. Fortunately, electrochemical systems are well-suited to this task, with potentiostats allowing application of voltages at precisely the required voltage to grow the so-called underpotential monolayer, but not any following multilayers.

The theory behind the existence and location of UPD regimes is still the subject of some debate[94]. Many models have been proposed to explain the UPD shift from the expected and experimentally verified bulk deposition potential. While the Nernst potential can be easily predicted for a given system (its shifts on the absolute electrochemical potential scale can be accounted for based on electrolyte concentration and temperature), no definitive model for the location of a UPD peak has been accepted. Many bimetallic systems show no evidence of UPD behavior, while others may evidence multiple UPD peaks or even feature peaks that cannot be individually analyzed due to their coincidence with an inherent electrochemical feature of the system, such as oxidation or reduction of the electrolyte solvent on the substrate. For example, the first UPD peak of silver on gold is difficult to discern due to its location. This peak, responsible for the first ~0.3 ML of Ag deposition, occurs near 0.9V (relative to Ag/AgCl), placing it squarely within a larger Au reduction peak. It is necessary to either

avoid oxidizing gold or manipulate the electrolyte solution via pH buffering to eliminate the reduction peak or resolve it from the UPD peak, respectively. This type of complication, along with a lack of definite theory to accurately predict the location of UPD peaks, makes discerning their existence and location difficult.

The first attempts to grow multi-layer ultrathin films with single atomic-layer degrees of control came in the form of electrochemical atomic layer deposition, or EC-ALD. This technique, pioneered by Stickney[95], exploited a ternary system of materials, by which a monolayer of A could be grown on B, followed by a second UPD reaction where a following monolayer of material C could be grown on top of the already existing monolayer of A. Then, the third monolayer (of A) could be grown on top of the deposit of C, resulting in an alternating A-C-A-C multilayer grown on top of the solid B substrate.

It was not until later that the combination of UPD techniques with galvanic replacement allowed the growth of pure metal films with high degree of thickness control at the atomic scale. This technique, called surface limited redox replacement (SLRR), uses the same approach of first growing a monolayer of A on a substrate B, but then goes further to remove the A-monolayer, the act of which causes a deposit of a third material, C, to deposit on the surface[93]. This process can then be repeated, resulting in films of pure C grown on top of the B substrate. Initial attempts at SLRR used Pb and Cu as so-called 'sacrificial' 'A' materials, due to the ease of which single UPD monolayers can be formed from simple electrodeposition baths of these metals. This thesis employs these techniques, focusing primarily on the use of Cu 'sacrificial' layers, but also explores the use of a new material, Ni, as the sacrificial layer [1]. Newer sacrificial layers have the

advantage of lower redox equilibrium potentials, making them more difficult to grow stably, but more potent when used as the driving force for the replacement reaction.

This driving force can be calculated as the difference between the redox potentials of any two metals coexisting in the same system. In this specific case, the redox potential of the 'sacrificial' metal defines the potential at which that layer will dissolve. The redox potential of the metal salt to be deposited, often Pt^{4+} or another cationic noble metal ion dissolved in solution, defines the potential at which that metal will cathodically deposit, or reduce, onto the surface of the substrate. When two metals with different redox potentials are placed in the same system with electrical and ionic conductivity, the metal with the more positive redox potential will be reduced and form a solid-phase deposit, while the metal with the lower redox potential will oxidize and dissolve into solution. Furthermore, the magnitude of the driving force responsible for this replacement reaction is given by the difference between the two component redox potentials. Various redox potentials for a range of applicable metals are provided in Table 2.1. It can be seen that the new metal explored in this work (Ni) has a lower redox potential than Cu or Pb.

Table 2.1: Selected standard reduction potentials relevant to SLRR[96].

Reaction	Equilibrium Potential (V)
$Au^{+} + e^{-} \leftrightarrow Au$	1.692
$Pt^{2+} + 2e^{-} \leftrightarrow Pt$	1.18
$Pd^{2+} + 2e^{-} \leftrightarrow Pd$	0.951
$Ag^{+} + e^{-} \leftrightarrow Ag$	0.7996
$Rh^{3+} + 3e^{-} \leftrightarrow Rh$	0.758
$Ru^{2+} + 2e^{-} \leftrightarrow Ru$	0.455
$Cu^{2+} + 2e^{-} \leftrightarrow Cu$	0.3419
$Ru^{3+} + 3e^{-} \leftrightarrow Ru$	0.2487
$2H^{+} + 2e^{-} \leftrightarrow H_2$	0.00
$Pb^{2+} + 2e^{-} \leftrightarrow Pb$	-0.13
$Ni^{2+} + 2e^{-} \leftrightarrow Ni$	-0.257
$Co^{2+} + 2e^{-} \leftrightarrow Co$	-0.28
$Cr^{3+} + 3e^{-} \leftrightarrow Cr$	-0.7
$Zn^{2+} + 2e^{-} \leftrightarrow Zn$	-0.7618
$Cr^{2+} + 2e^{-} \leftrightarrow Cr$	-0.913
$Ti^{2+} + 2e^{-} \leftrightarrow Ti$	-1.6
$Al^{3+} + 3e^{-} \leftrightarrow Al$	-1.662
$Ce^{3+} + 3e^{-} \leftrightarrow Ce$	-2.336
$Li^{+} + e^{-} \leftrightarrow Li$	-3.04

The key to SLRR involves two metal salt baths, the first of which is used to deposit the 'sacrificial' layer, and the second of which is used as a replacement bath for the 'sacrificial' layer to dissolve and the desired layer to form. This leads to two possible experimental setups: one type of setup where the electrode is moved from the first bath to the second iteratively, and a second type in which the electrode remains stationary and the different bath compositions are flowed past the electrode surface, in a so-called 'flow-cell' arrangement. These flow-cells utilize a series of automated pumps which alternately flow the two metal salt baths and a rinsing bath to avoid cross-contamination of the reactions. A flow-cell apparatus is advantageous for large-scale SLRR growth, allowing automated film growth using 50 or more iterations of layer deposition and replacement. On the other hand, by moving the electrode between two different baths, greater control of the bath composition at any given point in time can be achieved, since there is no dilution of the salt mixtures with rinsing solution. The major disadvantage of electrode-switching arrangements manifests itself in the labor-intensive manual operation, which limits the number of layers which can be grown, despite the greater precision afforded.

A significant advantage for SLRR techniques was discovered by Weaver et al.[97] This work examined the morphology of the multilayer deposit grown by replacement of Cu, which dissolves as Cu^{2+}, by Pt^{4+} cations in solution. It was found that significant improvements in film epitaxy and wetting could be achieved by performing a 1:1 place exchange, as opposed to a 1:2 place exchange. This was accomplished by matching the valency of the replacing cation with the valency of the dissolving film (i.e. using Pt^{2+} cations instead of Pt^{4+} cations to replace Cu UPD layers). Furthermore, it will be shown in this work that the coverage and morphology of the sacrificial layer plays an important

role on the final chemical state and reactivity of the ultrathin film ultimately grown. Furthermore, this work explores the possibility that the metal grown by SLRR is not fully reduced, an effect suggested by previous work which indicated non-traditional stoichiometry in specific cases of SLRR growth[98].

2.3 Nanoporous Surfaces

In addition to allowing monolayer-scale electrodeposition on massive, flat, surfaces, SLRR can also be conducted an roughened surfaces such as nanoporous surfaces. Nanoporous surfaces provide interesting opportunities for electroplating and catalysis reactions, since they offer an extremely high electrochemical surface area per unit mass or nominal electrode size. Two types of nanoporous surfaces are considered here as representative of the multitude of various metal and metal-oxide porous electrodes examined in the literature: nanoporous gold (NPG), and highly ordered titania nanotubes (TNTs). Both of these surfaces provide high surface area with which to interact with electrochemical and chemical reactants, but the two surfaces are significantly different in their chemical and structural composition. Nanoporous gold can be generated by dealloying processes through the electrochemical dissolution of Ag from a disk of Ag-Au alloy. As the Ag is selectively dissolved, it leaves behind voids in the remaining Au matrix, which are rearranged within the Au structure, creating nanoscale porosity and increasing the surface area significantly. While the dealloying process is often performed electrochemically, it can also be conducted chemically (that is, with no applied potential or current flow) in nitric acid[99]. These structures exhibit interesting and advantageous properties for a variety of reactions[100]. This process can also be applied to other metals, including Cu, Ag, or alloys such as PtRu or AuPt[101-103].

These structures can also be generated by etching or templating processes. Etching is performed via the large-scale anodic oxidation of a Au surface followed by reductive etching of the resulting thick oxide film, leaving behind a porous metal surface. Similarly, TNTs can be created by the oxidation of a piece of titanium foil and

subsequent or simultaneous electrochemical dissolution of the oxide film. In both cases, a structure with porosity on the nanoscale is left behind. Templating processes involve a nanoscaled templating material, with the material in question being grown into the pores or voids of the template. This template can either be a contiguous barrier material, or a composite of multiple smaller objects such as polymer spheres[104].

NPG exhibits disordered pore structures, while the porous oxide film of a TNT sample becomes an ordered array of vertically oriented hollow tubes. NPG leaves behind a predominantly zero-valent metal material, while TNT samples are oxides of the form TiO_2, and can be heat-treated to alter the crystallinity of the TiO_2 phase. NPG has the advantage of lending itself readily to monolayer growth methods such as SLRR, due to the advantageous UPD processes exhibited on gold surfaces. On the other hand, TNT samples allow us to probe the interesting electronic and structural effects arising from the pairing of a metal with a metal oxide. NPG samples have already been shown to possess attractive properties for gas-phase catalytic reactions[105]. This arises from their high surface area, which enhances the already desirable attributes of gold by increasing the rate at which reactions can proceed on the surface. These reactions are rate-limited by the surface area since they are catalyzed by metal-reactant surface interactions.

Similarly, metal-reactant surface interactions govern the electrocatalytic properties of TNT arrays. These arrays, which are often used for photocatalytic or photoelectrochemical applications such as water splitting, combine advantageous photoelectric properties of the semiconductor TiO_2 with high surface area. This high surface area creates as many metal oxide-reactant interaction sites as possible, where the

reactant (in the case of water splitting) is water molecules, which permeate the TNT structure. The product in this case is hydrogen or oxygen gas.

One interesting side effect of the nanoporous-type samples is that the porous structures act as diffusion sinks, slowing the diffusion of ionic species through their pores and causing features in voltammograms to appear broader and more washed out. To combat this effect, voltammetry on nanoporous surfaces was collected at much slower sweep rates, to allow the system to reach diffusional equilibrium more easily during the sweep. Despite the added complications, nanoporous surfaces are still an important part of this work as they provide more applicable, economically feasible substrates for reactions than massive, flat, gold discs, which are better suited to fundamental studies aimed at understanding properties.

2.4 Bimetallic Catalysts

Many catalyst systems benefit from the utilization of a multi-component metallic phase. These bimetallic catalyst systems are currently being explored for applications in a number of catalytic reactions, and are also in use in a variety of industrial applications. Across the field, nanostructured bimetallic systems are proving more catalytically active than their monometallic or heterogenous bimetallic counterparts. These catalysts can be classified into three categories: (1) alloys, (2) mixed-phase segregated, and (3) core-shell. True alloy nanoparticle catalyst structures rely on solid solutions of the constituent metals. These structures benefit from changes in electronic and surface structure arising from their multimetallic composition. However, they are difficult to produce and maintain due to the tendency for the metals employed to segregate into small domains rich in either of the two elements. This effect arises during the elevated temperature or extreme chemical conditions in which catalysts are often employed, and leads to the second and most common type of catalysts: mixed-phase. It is also important to consider the difference between lateral phase segregation (where both phases are exposed to the surface) and vertical phase segregation (where one phase encapsulates the other).

Mixed-phase catalysts are the most common type of bimetallic nanoparticle, especially after repeated usage in a reaction (which can tend to cause phase separation in alloys or breakdown of the precise architecture in core-shell particles). This type of particle exhibits unique phase boundary sites where the adsorbing molecule interacts with both phases simultaneously. These catalysts may exhibit increased activity at boundary sites orders of magnitude greater than non-boundary sites, such that the engineering target is to increase the surface area of boundaries as much as possible. In other cases, the

non-boundary sites of the different phases will each be active for two different sequential reaction steps, and the boundary sites may be neglected due to their relatively low surface area relative to the single-phase sites.

Pt-Ru catalyst structures provide some of the strongest evidence of a bimetallic catalyst interaction. Inoue et al. show structurally-dependent variations in the O_2 reduction capability of Pt-modified Ru catalyst surfaces[106]. Higher CO tolerances than bulk Pt have also been achieved via similar Pt-Ru structures[107]. The H_2/CO oxidation capability of Pt-Ru and Pt-Au nanoparticles has also been studied, with positive results[108].

Au-Pd has also been shown to be a catalyst system that benefits from its bimetallic nature. This system's application to alcohol/carbonyl evolution is reported by Wang et al.[109]. The catalytic activity of Au and Pd has been correlated with the bimetallic structure and the degree of Au-Pd segregation. Samples with less segregation and closer to monolayer coverage of Pd on Au show higher catalytic activity. The bimetallic catalytic effect has also been studied in H_2O_2 evolution by Edwards et al., reporting increased catalytic activity for the bimetallic system compared to monometallic systems[110].

Pt-Au has been suggested as a candidate for a methanol-resistant fuel cell cathode material[111]. The advantages of a bimetallic catalyst material are not limited to noble metals. Nickel-alumina is a current candidate for use in the decomposition of methane feedstocks[112]. These bimetallic systems represent only a few of the elemental pairs currently being explored and serve only as a starting point for element choice for this project.

2.5 Ultra-high Vacuum Studies

In order to facilitate a fundamental understanding of catalyst and surface properties, many previous studies have been conducted in which single crystals of catalytically relevant metals have been employed. An entire field of vacuum-based surface science has grown around the study of these fundamental properties in controlled environments. Techniques typically employed by these studies include XPS, STM, or mass spectrometry. Typically these tests focus on the addition of small amounts of chemical reactants to a very well-controlled surface. The study of the surface chemistry, the atomic morphology, and the chemical products generated by such an experiment allows for the determination of catalytic materials properties with a degree of precision not possible in ambient or reactor environments. A study of this type has been conducted by the author and included in this work in Appendix A.

UHV studies of single-crystal-based bimetallic systems have recently been conducted using X-ray photoelectron spectroscopy (XPS) and density functional theory (DFT). Combined with temperature-programmed desorption (TPD) studies, shifts in the binding energy of adsorbed gases have been correlated with shifts in the energy location of the d-band[113]. Experimental work contributing to these studies has been conducted primarily on precisely prepared single crystal specimens[114]. Preparation steps include polishing to sub-micron levels followed by annealing in controlled atmosphere.

Deposition methods including physical vapor deposition (PVD) and chemical vapor deposition (CVD) have been employed to coat the single crystals with the chosen metal monolayer. Due to the surface sensitivity of XPS and TPD, a significant part of these studies has been devoted to the characterization of bimetallic growth modes.

Knowledge of island formation vs. layer-by-layer growth is significant, because these studies concern themselves with electronic properties induced by the atomic-level morphology of the surface.

Recent studies can be divided into four categories: (1) the study of electronic properties via XPS, (2) the study of catalytic surface adsorption via TPD, (3) surface morphology verification via STM, and (4) correlation with theory via DFT. In addition to providing compositional information regarding the surface of a bimetallic structure, XPS can provide information regarding the location of the d-band peak for a given metal. By measuring the shift in this peak with respect to its equivalent in bulk single metals, some electronic effects of the bimetallic structure has been observed. TPD of selected probe gases adsorbed onto bimetallic surfaces relates directly to catalytic properties. By measuring the temperature at which an adsorbed gas desorbs from the surface of a bimetallic system and making comparisons to single metals, catalytic surface properties can be correlated to bimetallic structures. STM is an ideal tool for confirming these structures, and can be conducted in vacuum or *in-situ* within electrochemical cells. DFT, an ab initio technique based on quantum principles, has been used to predict the density of states and the previously mentioned d-band shift.

These studies generally have not, however, been conducted on more realistic systems, including polycrystalline substrates or surfaces fabricated outside of a vacuum chamber. XPS provides limited information compared to XANES, while DFT is a non-experimental technique. This leaves considerable room for studies that directly probe electron occupancies and implement samples fabricated in ambient conditions. Studies such as these that use UHV techniques to examine electrochemically prepared samples

are often referred to as UHV-EC studies. One of the primary advantages of a UHV-EC study is that identical samples can be tested using UHV methods in addition to electrochemical reactions outside of vacuum.

2.6 Important Reactions

2.6.1 Oxidation of Alcohols

Of the electrochemical reactions that may be employed as probe reactions, electro-oxidation of alcohols such as ethylene glycol, methanol, or ethanol on Pt and Pt-based materials provides an interesting set of experimental challenges[115-118]. While typical cyclic voltammetry techniques rely on the so-called 'reversible' reactions, which exhibit forward (oxidative) peak currents on the positive-going voltage sweep and backward (reductive) peak currents on the negative-going voltage sweep[119], electro-oxidation of the particular chemicals is accompanied by a range of side-reactions and by-products which compromise the reduction process. This results in a double-peak structure, in which two oxidation peaks occur during the sweep, one during the forward sweep and a second during the reverse sweep. This type of behavior is typically seen in systems that exhibit EC (Electrochemical-Chemical) reaction pathways, by which the reaction product of the positive-going sweep is consumed by a side reaction, preventing the reverse reaction from occurring during the negative-going sweep[120-121].

The situation with these two alcohols is somewhat more complicated than a simple EC reaction[122]. In addition to some of the reaction products being consumed in a following chemical reaction, other reaction products selectively adsorb to the surface, blocking reaction sites in a method known as poisoning. However, as the negative-going voltage sweep progresses, these poisons are removed from the surface, allowing the

original oxidation reaction to resume. This effect is what causes the second oxidation peak to occur at a more negative potential than the first. In some cases, depending on the solution conditions and the boundaries of the voltammetric sweep program, the peak occurring on the reverse sweep may actually be large than the original forward-going peak.

Finally, the initial electro-oxidation processes themselves are not simple one-step oxidation reactions with a specific reaction potential. Rather, the reaction can proceed across multiple pathways depending on the potential currently applied to the electrode surface. That is to say, the reaction can begin by making a certain set of oxidation products at the start of the oxidation peak, and by the end of the peak, a different set of products are being generated (since the voltage as changed during the course of the sweep).

This work takes advantage of one of these difficulties, specifically the problem of adsorbed species limiting the reaction. By tracking the voltage at which these species are removed from the surface (during the negative-going sweep) and the amount of species removed, valuable information about the surface, the species themselves, and the all-important surface-adsorbate interaction can be discerned.

Another way in which this work takes advantage of specific properties of alcohol oxidation reactions is by employing specific properties of ethylene glycol electro-oxidation to track surface properties. Ethylene glycol is an interesting molecule in that it electro-oxidizes at a different potential on gold sites than on Pt sites. This effect has been seen in alloy materials before, but has not been employed to measure surface coverages until now. Essentially, the electro-oxidation profile of ethylene glycol on a mixed Au-Pt

surface will evidence two peaks during the forward-going sweep, the lower voltage of which corresponds to Pt, and the higher voltage of which corresponds to gold. The difference in potential of these two peaks can be considered as ΔE. This ΔE shows a strong dependence on pH, thus, the most effective employment of EG as a surface coverage probe is performed at high pH values, in order to achieve the maximum separation between the Au-site and Pt-site reaction peaks. Thus it is possible to perform site-specific reaction probes using electro-oxidation tests in an aqueous environment[123].

2.6.2 Methanol Electro-oxidation:

One of the most applicable tests for an electrocatalyst is the methanol electro-oxidation reaction[122]. This reaction is currently of great interest due to its applicability to direct methanol fuel cells (DMFC)[124-125]. A DMFC relies on a methanol fuel stock rather than a hydrogen fuel stock, generating power by its catalytic ability to split (oxidize) methanol. By performing this reaction, which involves an electrode in acidic solution containing methanol, potential is swept across the potential at which methanol oxidizes, producing a typical positive-current peak in the voltammogram. However, if the reverse sweep is then performed, a second peak in the positive current regime is again seen. This is unusual since the norm for negative-going sweeps is to have peaks in the negative current direction. That is to say, positive-going sweeps are responsible for oxidizing (positive current) reactions, and negative-going sweeps are responsible for reducing (negative current) reactions[121]. The reason that the reverse reaction is not seen for methanol electro-oxidation is not entirely clear, but could be due in part to poisoning effects as well as following chemical reactions that consume the products of the original

electro-oxidation reaction (thus preventing these products from being used in a reverse electro-reduction reaction).

This type of cycling can be repeated again and again, and by tracking the maximum current seen in these peaks over the course of up to 500 cycles, the rate of catalyst de-activation or degradation can be measured as a function of cycle number.

In addition to potentiodynamic methods, catalysts for the methanol reaction can also be tested by potentiostatic methods. In this type of test, the electrode containing the catalyst material is biased to a specific potential (or series of potentials if the test is to be repeated). Then, the current arising from the reaction proceeding at this potential is measured as a function of time. This current inevitably drops, and the rate of decrease is indicative of the robustness and poison resistance of the electrocatalyst itself. This type of test has the advantage of allowing long-term testing in a more realistic environment, since real devices will not be cycled across a range of voltages, but rather be operated at a specific voltage for a relatively long period of time. However, during potentiostatic testing, the electrode is never brought to more negative potentials for a so-called 'cleaning' step, by which poisons are removed. This can make it difficult to deconvolve poisoning effects from structural breakdown effects, which are occurring simultaneously during the potentiostatic test.

The primary catalyst used in DMFC systems is Pt. This is due to Pt's high electrocatalytic activity. One of the primary difficulties with a Pt catalyst is its tendency to be poisoned by the above mentioned byproducts and intermediaries arising from the methanol electro-oxidation process. Most problematic of these intermediaries is CO, which forms a strong bond to the Pt surface and, by bonding to the surface, blocks

reactions sites, essentially decreasing the amount of Pt available to the fuel cell for the methanol splitting reaction. The electro-oxidation of methanol proceeds by a variety of different mechanisms, leading to the creation of CO, CO_2, or a wide variety of intermediaries depending on the potential at which the reaction is allowed to proceed. Thus it is of great importance that the production or the deleterious effects of CO be mitigated by catalyst surface properties. This leads us to a study of electro-oxidation of CO itself.

2.6.3 Carbon Monoxide Electro-oxidation

Electro-oxidation of carbon monoxide is an important reaction for many reasons. Carbon monoxide is one of the primary poisons responsible for performance loss in direct methanol fuel cells (DMFCs). This poisoning causes dramatic current loss over the performance lifetime of the fuel cell. As such, the ability of a fuel cell catalyst to resist poisoning is one of the most important parameters to consider when choosing or designing a catalyst system. The ease of carbon monoxide electro-oxidation (which can be related to the voltage required) can be directly related to the ease of poisoning removal and poisoning resistance.

A second reason that carbon monoxide electro-oxidation is being investigated pertains to the study of fundamental metal-adsorbate interactions on an atomic and electronic level. As a directional molecule, carbon monoxide exhibits interesting behavior when adsorbed onto the surface of a metal. The $2\pi^*$ orbital, which is an unfilled antibonding orbital in the gaseous phase, becomes hybridized with metal d-band states when the molecule is adsorbed to a surface, creating the partially filled $2\pi^{\sim}$ state. This model, which relies on backdonation of electrons from the σ states and the metal d-band, is generally referred to as the Blyholder model[126]. This model has been continually explored and refined.[127-129] The resultant molecular states associated with covalent CO-metal bonding can then be studied by techniques such as adsorbate XANES. Previous such studies have explored the Pt backdonation effect, and found that changes in the surface architecture and composition have a strong influence on the amount of backdonation and the strength of the Pt-CO bond[130]. The specific π^* resonance at 287.8eV in the C K-edge spectrum can be treated as corresponding primarily to

photoexcitation of the C1s->2π* transition.[130-131] Thus, the intensity of this resonance can be treated as a measure of the occupancy of the 2π* (or π~) orbital, with increased intensity corresponding to decreased occupancy.

When this metal-adsorbate bond is influenced by a secondary metallic species, as in the case of alloys (specifically PtRu or PtAu alloys), there are two distinct possibilities when searching for a physical cause. The first of these, referred to as a bifunctional effect, applies to systems where both metal components of the alloy are present on the surface and each interact with the adsorbate[132] . The second effect, referred to as a ligand or electronic effect, refers to changes in one metal's electronic band structure due to influence from the other metal. This influence can arise as a function of strain-mismatch or simply from electron transfer. This type of effect has been shown for the PtRu system and others as well.[113, 133] A specific subset of this case arises when one of the two metal species is segregated to the surface of the sample, leading to adsorbtion events occurring preferentially at one metal compared to the other. This arrangement has been the subject of much DFT and STM study[134].

This metal-molecule bond, when formed electrochemically, takes on multiple configurations depending on the voltage at which the adsorption process has taken place. Lower voltages cause stronger bonding, corresponding to a rearrangement of the CO molecules on the surface. The evidence of these different bonding types can be seen as shifts in the location of the CO electro-oxidation peak in cyclic voltammetry.[135] These bonds have also been explored spectroscopically by previous researchers[136-138]. In particular, much work has focused on how the adsorption process influence the intermolecular C-O bond, with much study focusing on infrared and vibrational analysis

[139]. Furthermore, simple simulations have been conducted to predict the affinity of CO bonding to metal surfaces. [140]

Another interesting feature of CO adsorption, specific to the CO-Pt system, is the importance of applied voltage during introduction of CO into the electrode-electrolyte system. If Pt is allowed to rest at open circuit potentials in solution while the CO is added to the electrolyte, the subsequent CO oxidation-stripping peak will occur at a higher voltage, corresponding to stronger CO-Pt bonds. If, on the other hand, Pt is held at a negative voltage corresponding to processes such as H_2 and CO adsorption during the bubbling process, this peak will occur at a lower voltage, indicative of weaker CO-Pt bonds. While conclusive evidence of the cause of this effect has not yet been published, it is possible that the interaction of solution-phase CO with adsorbed H_2 or OH^- may play a role in this process.

In addition to showing a strong dependence on the adsorption potential, CO electro-oxidation shows a major dependence on the presence of bulk carbon monoxide dissolved in the solution phase of the electrolyte. Specifically, the presence of bulk CO increases the peak oxidation voltage by as much as 300mV, making the reaction more difficult. It has been suggested by Markovic et al that this shift is due to the bulk CO inhibiting the adsorption of OH^- groups on the electrode surface.[135] It is widely accepted that these OH^- groups are necessary for the electro-oxidation of CO to proceed, and it is also known that surface CO prevents the adsorption of OH^-. It has also been shown that, for pre-adsorbed CO in the absence of bulk CO, the adsorption coverage plays a role in the oxidation voltage. Presumably the free area not covered by CO will be available for OH^- nucleation, which promotes the oxidation reaction.

2.6.4 Orbital Theory

One important aspect of this work revolves around XANES study of the molecular electron orbitals that are created when two atoms covalently bond with one another. In these cases, some of the atomic electron orbitals of each atom (for now only diatomic molecules are considered) become hybridized. While these types of interactions have been explored thoroughly in other works[141-142], a brief summary of the important properties is pertinent here as well. What this means is that specific orbitals from each atom will combine, often forming a pair of energy states associated with the diatomic molecule. Generally, one of these energy states will occupy a lower energy than the individual atomic orbitals that are responsible for the creation of the molecular orbital. This molecular orbital will be referred to as a 'bonding' orbital, and electron occupancy in this orbital will contribute to strengthening the intramolecular bond. The second energy state formed during the hybridization process is often referred to as an 'antibonding' or 'virtual' orbital, since it usually unpopulated (or populated very little). This occurs since it is at a higher energy level than the original atomic electron orbitals involved in the hybridization process. In a simple approximation, one can think of the energy state of the entire molecule, and realize that the highest energy state occurs when the 'antibonding' orbitals are occupied. Thus, it makes sense that the electrons will move to one of the two available lower-energy configurations available to them; the first of which involves breaking the covalent bond and returning to individual atoms, and the second of which (at a lower energy) involves occupying the hybridized 'bonding' orbital.

This type of analysis becomes more complicated as multiple molecules are considered, and becomes extremely complicated when even one molecule adsorbed on the surface of a bulk material is considered. For the case in which the adsorbate is

chemisorbed (adsorption with an accompanying chemical bond), it is necessary to consider secondary hybridization of the molecule's already once-hybridized molecular orbitals with the atomic orbitals (or band structure) of the material. In many cases, specifically in the case of carbon monoxide, the metal-molecule bond involves back-donation of electrons from the metal to unoccupied anti-bonding orbitals of the molecule. In this type of arrangement, which is often referred to as the Blyholder model, strengthening of the metal-adsorbate bond can lead to weakening of the intramolecular bond. One can easily see how the population of antibonding orbitals via backdonation from the metal substrate can lead to a phenomenon known as "dissociative adsorption," in which the adsorbing molecule breaks apart due to this weakening of the intramolecular bonds by interaction with the surface. This kind of material-adsorbate bonding is not always a simple covalent interaction. For example, much theoretical work has focused on the d-band energy and occupancy for adsorbates on transition metals. These studies have found that the d-band of the metal support has a much more profound effect on the degree and type of substrate-adsorbate electron transfer than the valence shell does.

2.6.5 Hydrogen Evolution from Water Splitting

A final relevant electrochemical reaction studied in this work involves the generation of hydrogen and oxygen gas from water molecules by the employment of a photoelectron generated from the interaction of light with an active electrode surface. This process is referred to as water splitting, electrolysis, or photo-assisted water splitting. This requires a surface with both photovoltaic properties (to generate the required electron-hole pairs) as well as suitable electrocatalytic properties (to catalyze the

water splitting reaction at suitable low voltages). Doped titania films have been the target of much study in the subject[143-146].

This study also outlines results from a study of photoelectrochemical water splitting using the TNT substrates mentioned earlier. This builds on previous work using TNT's with various modifications for the same type of reaction[25-26]. TNT samples have been in use for water splitting applications for some time. By modifying the photoactive TNT substrate with Pt and copper in a method identical to that used in the Pt-TNT system for methanol electro-oxidation, it is possible to test the influence of cationic Pt nuclei, which act as electron "sinks" for the generated photoelectrons. The Pt-TiO_2 system has been studied in the past, but not on ordered nanotube arrays[146]. By exposing the sample to filtered light from a xenon lamp and collecting cyclic voltammetry data in aqueous solution, the activity of the Pt modification toward different reactions can be determined. The simplest of these is for the oxidation of water to oxygen, which proceeds at voltages near 1.0V (depending on pH) and would be shifted negatively for a positive influence from Pt. Alternatively, increases in rate of reaction would appear as increased current in the oxidation voltage range.

Another important parameter is the photocurrent generated at voltage ranges in which no reaction proceeds. This current is related directly to the efficiency of the tubes as a photovoltaic device. It is important to consider the crystallinity of the tubes themselves when measuring this current generated. While TiO_2 does not exhibit significant changes in photactivity from one crystalline state to another, the measured efficiency drops significantly for amorphous samples compared to annealed samples with a crystalline structure. This is due to the increased prevalence of defects which act as

recombination sites for the photogenerated electron-hole pair. After annealing and the formation of a more regular crystal lattice, these defects are minimized and efficiency increases.

CHAPTER 3

METHODS

3.1 Electrochemical Methods

3.1.1 Potentiostats and Reference Electrodes

Potentiostats are some of the most important devices in electrochemical work. These devices allow for the precise specification or measurement of current and potential in an electrochemical system. The typical potentiostat employs two pairs of electrical leads, for a total of 4 leads. One of these pairs is responsible for voltage measurements, while the other pair is responsible for driving a current through the electrochemical system. Most potentiostats can be operated in two modes for bulk electrolysis, controlled-potential or controlled-current. When operated in controlled-current mode, the second pair drives a controlled current while the first pair is used to simply measure a potential drop. When operated in controlled potential mode (potentiostatic or potentiodynamic), the system uses the measurement from the voltage probe pair as input to a feedback loop. This feedback loop is used to determine whether more or less current needs to be supplied to the current supply pair of leads, allowing the device to either maintain a constant potential setpoint, or conduct dynamic potential programs such as sweeps, cycles, or waveforms[147].

The simplest application for a potentiostat is a 2-electrode cell. In this type of cell, one lead from each pair is attached to each of the system electrodes. This setup has the advantage of simplicity, and is representative of the type of arrangement typically used in batteries. The disadvantage of a 2-electrode arrangement for analytical chemistry is that the potential measured by the potentiostat is actually the potential *difference* between the two electrodes. This is not a problem in and of itself, and only poses a difficulty when it

is desired to isolate one of the two electrodes for study. That is, as long as only two electrodes are used, and current is flowing between them, the absolute potential of *both* electrodes will be changing simultaneously, making it difficult or impossible to isolate one of the electrodes for specific study. In order to achieve this goal, a third electrode must be introduced to the system. Then, the electrode of interest will be attached to one lead each of both the current supply loop and the voltage probe loop, while the remaining two electrodes will each be attached to one of the remaining leads. Thus, our current applied (or measured) runs between two electrodes, and the voltage the system measures is determined across two electrodes, with the two loops sharing one electrode in common. This common electrode is called the working electrode (WE), and is the electrode of interest in any electrochemical study. The second electrode in the current supply loop is called the counter electrode (CE) or auxiliary electrode (AE). The final electrode, against which the potential of the WE is measured, is called the reference electrode (RE). By this three-electrode method, a current can be flowed through an electrochemical system, and all changes in potential drop measured can be attributed to the WE, since the RE has no current flowing through it. Finally, provided that the RE maintains a constant and known potential of its own, the potential *drop* between WE and RE can be converted to an absolute potential on an arbitrary energy scale.

Thus, it is easy to see why the RE is the lynchpin of reliable electrochemical measurements. A suitable RE must possess the following qualities: (1) it must be robust and not contaminate the test solution, (2) it must exhibit a known potential (3) it must be exhibit a stable potential over time. The first of these qualities simply means that the electrode must be able to withstand significant use, and that none of its chemical

components may be incompatible with the experiment being performed. Often, the Ag/AgCl electrode is employed due to the chloride film that it employs, which is insoluble, making a very durable electrode and stable potential. However, the Cl^- ions associated with the Ag/AgCl equilibrium reaction are often unacceptable contaminants (even at the low levels associated with traditional frits and barriers), thus the Ag/AgCl electrode cannot be employed. Similarly, the Pt/H_2 electrode, which exhibits a potential arbitrarily defined by the community as 0.0V and is often referred to as the standard hydrogen electrode (SHE) or normal hydrogen electrode (NHE), satisfies the second required quality of a known potential, but relies on bubbling hydrogen gas and thus is rarely used due to convenience and safety issues. Finally, the third quality, stability, is required for any long-term or high precision measurement. An excellent example of a workable reference electrode that exhibits poor stability is a simple type of reference electrode that is easily employed in battery testing or electroplating. By simply using a piece of metal that has corresponding cations in solution (Li for Li^+-containing battery electrolytes, Cu for Cu^{2+} electroplating baths), an equilibrium potential can be established. However, as the concentration of the potential-determining ions changes (during the course of battery operation or electroplating) this potential will change, since it relies on the active species. In many cases this type of reference electrode is sufficient, even though the potential it exhibits may not be stable under all conditions. A good example of a case when a simple wire is acceptable occurs during electroplating when the amount of ionic species being removed is negligible compared to the concentration in the system originally. In these cases, it is still important to ensure that the conditions in the cell do not change unexpectedly, leading to instability in the RE potential.

This leads to the topic of ionically conducting barriers to solution flow. In order to employ a reference electrode that does not share the same solution as the rest of the electrochemical cell, some sort of barrier must be employed. Generally, this barrier must allow ionic transport (to complete the circuit between the RE and the WE) but minimize bulk solution flow via convection or diffusion effects. One of the most popular materials for this application is a type of porous glass frit made of materials such as Vycor. However, Vycor and other glass frits are unstable in high pH environments, and alternate materials must be found. Often porous plastic frits such as PET can be employed. These frits function well enough, but are vulnerable to pore closure effects when heated. This effect can pose a problem since RE assembly typically employs heat-shrink tubing to create a watertight seal between the frit and the electrode body. If this heating step is not performed precisely, the plastic frit can melt slightly, closing the pores and eliminating ionic conductivity, resulting in a nonfunctional RE. Another possible option for frit selection is the use of a ceramic frit. A piece of molecular sieve or similar porous ceramic can be used in place of Vycor when required. All three of these types of frits have been employed in this work, with the majority of experiments being conducted using Vycor and the other frits only being used when required based on the solution chemistry employed.

Additionally, it is often important to consider drops in potential across these frits, resulting from the *junction potential* due to dissimilar solutions on each side of the frit. Since the two solutions on each side of the frit (which can be treated as a membrane of finite thickness) exhibit differing concentrations of charge-carrying ions, and since the diffusion through the frit occurs slowly, a buildup of charge on each side of the frit can

occur. This buildup of charge leads to a potential drop, which can cause inaccuracies in measurement.

Another type of potential drop that can be problematic for electrochemical measurements is a drop due to solution resistivity. This can be avoided simply by adding sufficient buffer electrolyte to the solution, in the form of a buffer salt or an anionic species to allow for charge transport through the solution. Additionally, a Luggin capillary can also be used to provide a shorter path from the RE to the WE. Care must be taken, however, to ensure that the Luggin capillary does not become blocked by a gas bubble (which would destroy all conductivity between RE and WE) or contaminated by concentration gradients of solvent/solute (which could lead to undesired potential drops). In fact, the entire cell must be examined for the presence of bubbles which would destroy this ionically conductive path through the electrolyte.

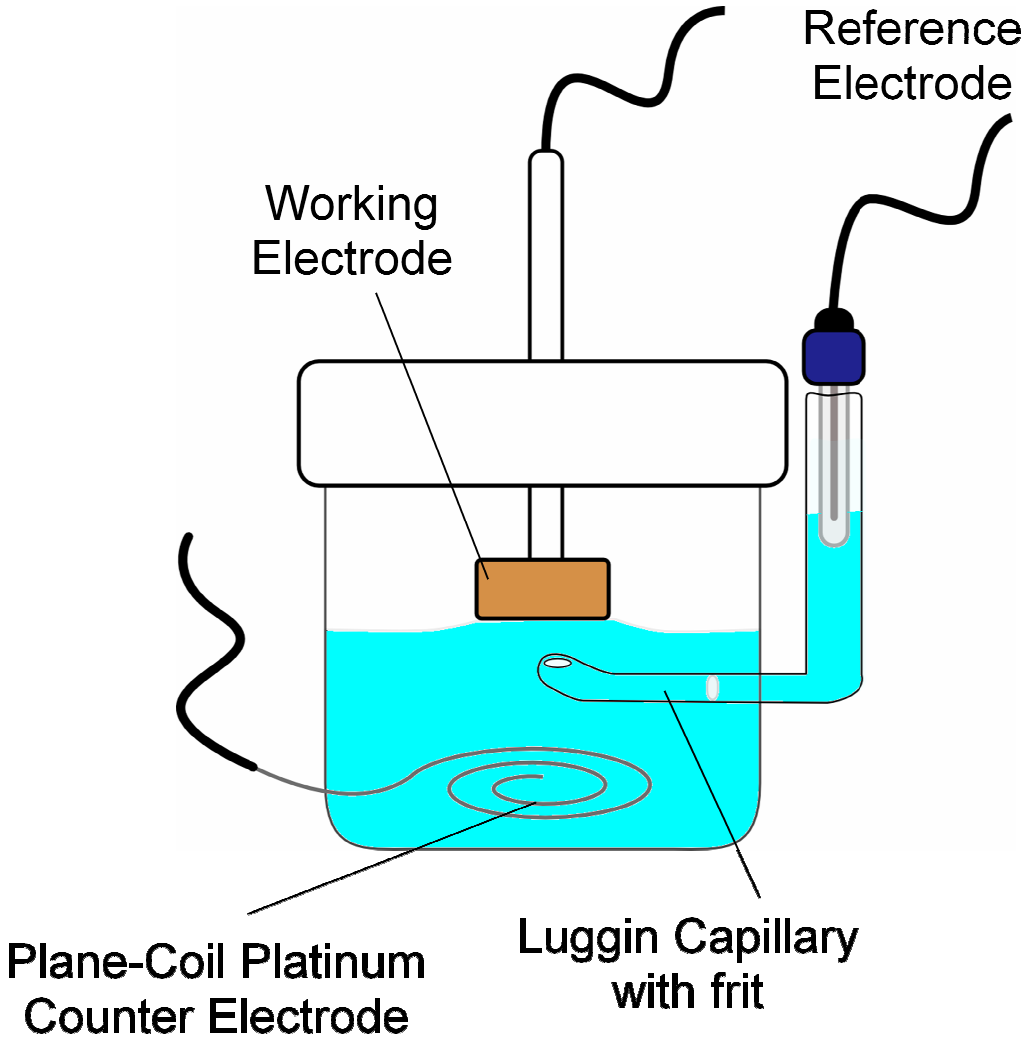

Scheme 3.1. Illustration of electrochemical cell geometry employed.

3.1.2 Electrolytic Deposition

Galvanic or electrolytic growth, the most common form electrodeposition, is a type of electrolysis that occurs when an external electrical potential is applied to an electrode surface in an electrochemical system containing dissolved ionic species of a metal. Provided that this external potential is of the appropriate magnitude, the solvated ionic species will undergo an electron-transfer reaction and form a solid-phase nucleus on the electrode surface. In the most common case, electrodeposition is conducted cathodically, meaning that the electrode surface is supplied with an excess of electrons, which react with positively charged ionic species, or cations, leading to a reduction reaction to convert these cations to their solid, zero-valent metal state on the surface. The other alternative, anodic electrodeposition, is conducted by applying a positive potential to the electrode surface and driving an oxidation reaction. Anodic deposition is often used to electrodeposit oxide layers rather than reduced metallic layers.

The morphology of an electrodeposited sample is dependent on a wide range of factors. Nucleation and growth kinetics play a major role in this process, but unlike traditional phase-change kinetics, the growth rate is also influenced by the current flowing through the electrochemical system. This has the advantage of providing the experimenter with an extra variable to be manipulated or measured. Since the reaction is assumed to consume or produce electrons, the electrochemical current is directly proportional to the reaction rate. As in other nucleation and growth phenomena, changes in the growth rate will lead directly to changes in growth morphology. For example, higher currents will lead to faster growth rates and cause the area near the electrode surface to become depleted of the cationic species necessary to create and grow solid-

phase nuclei. As a result, the reaction will become diffusion-limited, meaning that particle growth can only proceed when a cation diffuses to the surface, either by electric-field-assisted migration or by Fickian diffusion.

This type of diffusion-limited growth is analogous to diffusion-limited thermal oxidation, in which the reaction is rate-limited by the arrival rate of oxygen or solute atoms reaching the reaction front. In the electrochemical case, the impinging cations will invariably reduce preferentially at the outermost surface of the already-existing nuclei, causing these nuclei to grow faster at the most extreme protrusion. This eventually leads to the growth of dendrite structures characterized by long, needle-like spires. This is often problematic as one of the main goals of electroplating is fully wetted homogenous film growth. Examples of this type of electroplating are shown in the CV curves plotted for Ni and Cu being grown and removed from polycrystalline Au in Figure 3.2. Note the onset of growth (in the negative direction) and dissolution (in the positive direction) occurs at different potentials for each metal.

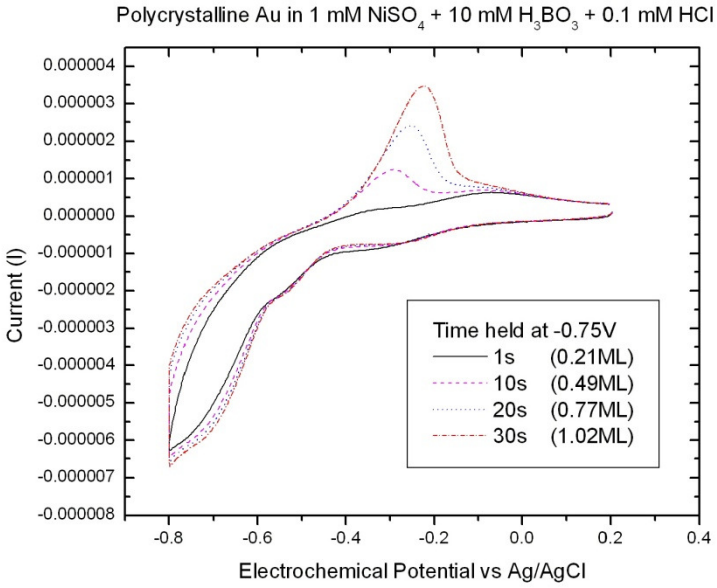

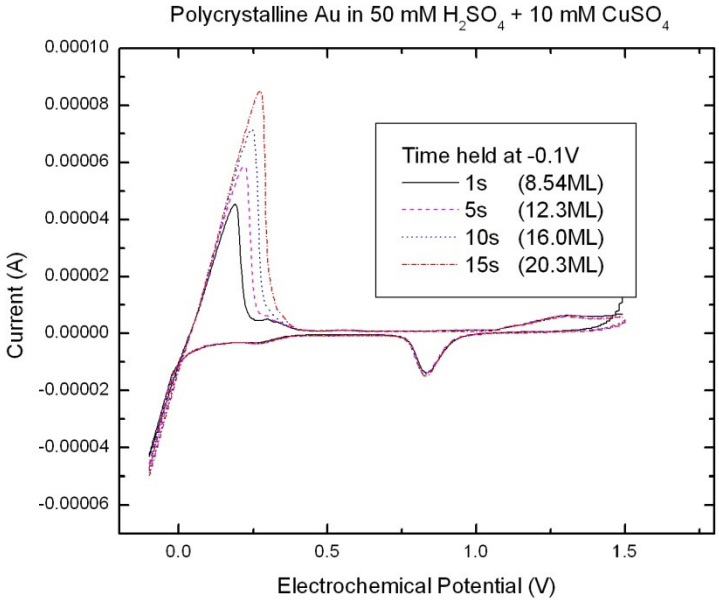

Figure 3.2 Electrolytic growth and anodic stripping of (a) Ni and (b) Cu on polycrystalline Au.

To combat the problems of diffusion-limited growth, the first and simplest solution is to slow the growth rate by decreasing the applied current. However, this does not always address the entire issue, and it is sometimes necessary to use a square-wave signal, amounting to a type of pulse deposition, by which cations are permitted to diffuse to the electrode surface in between deposition pulses. This avoids the diffusion-limiting case entirely, increasing the likelihood of a smooth deposit. A third type of solution relies on slowing the charge-transfer kinetics to a point at which diffusion can keep up. This solution relies on the addition of complexing agents which entangle themselves with the dissolved cations, slowing the kinetics of the reduction reaction which is responsible for solid-phase growth.

The first proposed solution, slowing the galvanic growth rate by current decrease, poses a variety of problems. The theoretical advantage of this approach is that slower growth rates deplete the near-electrode area of the electrolyte less rapidly, allowing more diffusion to occur from the bulk of the electrolyte. However, in order to maintain the current at a given value, growth must be conducted in what is called galvanostatic mode, by which the potential must be increased over time to combat the depletion of the electrolyte, which will occur eventually. This means that current-controlled growth may not be suitable for systems where the reaction pathway is determined by the exact voltage the deposition is being conducted at. Additionally, if the voltage applied to sustain a given current reaches a high enough limit, breakdown of the electrolyte material can occur, causing volatile gas to be generated and slowing the film growth rate even further.

The second solution, involving the use of pulsed voltammetry techniques, combats the problem of large nuclei and dendrites very well by essentially pausing the

growth cycle for a short period of time to allow diffusion of the active ionic species from the bulk of the electrolyte back into the depleted zone. This technique avoids the problems of a galvanostatic approach in that the voltage is always precisely controlled by the experimenter. However, films grown by pulsed-current methods may evidence smaller grain size and a more porous structure. This occurs as a direct result of the voltage step process. Each time the growth process is resumed after the pause, new nuclei are formed (as opposed to continuing growth of existing nuclei). Thus, a compromise between large-scale growth of only a few nuclei and generation of many tiny nuclei must be met, usually by adjusting the waveform parameters. However, sometimes this balance cannot be achieved and the problem must be resolved by the addition of chemical additives to the bath.

These additives comprise the third technique suggested to combat dendrite formation in electroplating. Complexing additives generally play the same role as pulse-plating techniques, in that they attempt to slow down the reaction enough to allow diffusion (assuming the growth reaction is diffusion-limited) to catch up. Since undesired dendrite morphologies are primarily a result of diffusion-limited growth, additives that cause the reaction to proceed in a kinetically limited mode are desirable. Additive chemicals are not always limited to slowing reactions, however. In some cases a complexing molecule such may be added to the electroplating bath to alter the growth of metal in a specific feature, such as a pit or crevice. In some cases, it may be possible to tune the additive chemistry such that the additive prevents growth in a specific region of the feature in question, such as the bottom of a pit that the electroplater does not want to fill in with material. On the other hand, additives can also be used to slow the reaction at

the surface of the pit, allowing preferential growth in the pit to occur, in case it is desirable to fill in all such features.

A fourth solution is also available. If none of the previous techniques are employed, it is possible to simply accept that the reaction will be mass transfer-limited, but influence the mass transfer in such a way that Fickian diffusion is not the only factor affecting the arrival of cationic species to the surface. This technique involves agitation of the bath solution to induce convection of charged species to the surface. As mentioned earlier, electrodes operating under diffusion-controlled reaction conditions create a depletion zone near the electrode surface. In unstirred systems, this depletion zone is constantly growing and causes ever-decreasing current flow (when the electrode is operated in potentiostatic mode). By agitating the electrode or solution such that reactive species are brought in contact with the surface at a much higher rate, it is possible to stabilize this depletion zone in time. Furthermore, increasing the degree of electrode-solution agitation, as is performed at rotating disc electrodes, can decrease the size of this depletion zone, further reducing the influence of diffusion terms in the reaction.

Because of these reasons, galvanic electroplating recipes are often specific to a given electrolyte-substrate system. Attempts to simplify and improve the electroplating process have been made, resulting in techniques such as electroless deposition and layer-by-layer growth methods such as surface limited redox replacement (SLRR) or electrochemical atomic layer deposition (EC-ALD). All of these techniques rely on an alternative electron source to provide the charge transfer needed to reduce cationic species to metallic species. In the case of electroless deposition, a reducing agent such as a chemical additive or hydrogen gas is often employed. In these systems, the reducing

agent is a component that easily oxidizes, donating the electrons generated in this process to the metal cations to be plated. In the case of SLRR and EC-ALD, a precursor layer of a sacrificial metal is employed. This precursor functions as a reducing agent, but has the advantage of being confined to the surface of the sample in a known quantity. Selection of this sacrificial metal or reducing agent is of great importance. Since, in both techniques, no external voltage is applied, the driving force for the reduction reaction arises from the difference in reduction potential of the sacrificial layer (or reducing agent) and the reduction potential of the material being deposited. In order for the plating process to proceed, this difference must be a negative value. Thus, metallic Cu oxidizing to solution-phase Cu^{2+} (formal reduction potential 0.34V) is able to act as the reducing agent for Au (formal reduction potential 1.5V) but not for Ni (formal reduction potential -.26V). It is important to remember that the thermodynamic requirement that this difference be negative is not the only requirement present, though. This difference must also be large enough to overcome any kinetic barriers to the process, and results in most systems requiring a certain minimum threshold difference without which the reaction will not proceed.

3.1.3 Underpotential Deposition

Underpotential deposition is similar to bulk electrochemical deposition in that they both share the same source of electrons used for the anodic reduction of metal cations onto a working electrode substrate. In contrast to electroless deposition and galvanic replacement, which employ reducing electrolytes and sacrificial secondary metals, respectively, electrodeposition and it subsidiary, UPD, employ an external EMF to supply the requisite electrons for their plating reactions. Underpotential deposition is referred to as such because it occurs at a potential lower than the Nernst potential for the system in question. That is to say, that for some systems there exists a potential at which it is thermodynamically favorable for metal A to deposit, to a certain extent, onto exposed surfaces of metal B but it is not favorable for metal A to continue to deposit on top of itself. This leads to the case where all exposed B sites will be coated with adsorbed A of single-atom thickness. Examples of this phenomenon can be seen for various metals, including Sn, Ru, Cu, and Pb[148-153].

This is, of course, a generalization of the theory of UPD, and a system's UPD properties will vary with solution ph and choice of bimetallic system, as well as with the presence of ions such as sulfates and chlorides in the depositing electrolyte solution[94]. The most important characteristic of underpotential deposition is that it is a voltage-limited process. Regardless of *how much* material may be deposited by a given UPD feature, the extent of electrodeposition in a UPD regime is not diffusion-limited or solution-limited, but rather it is capped at a maximum dependent on the absolute electrochemical potential of the working electrode substrate. This puts UPD in the

interesting position of being a self-limiting electrochemical technique, the growth modes of which can be studied via in-situ scanning tunneling microscopy (STM) techniques.

The theory behind the existence of UPD regimes is still the subject of some debate[94]. Many models have been proposed to explain the UPD "shift" from the expected and experimentally verified Nernst bulk deposition potential. While the Nernst potential can be easily predicted for a given system (its shifts on the absolute electrochemical potential scale can even be accounted for based on to electrolyte concentration and temperature), no definitive model for the location of a UPD "peak" has been accepted. It has been shown, however, that the existence of a UPD feature (and the degree of monolayer coverage associated with that feature) depends on the difference between the work function of the substrate and the metal being electrodeposited.

Many bimetallic systems show no evidence of UPD behavior, while others may evidence multiple UPD "peaks" or even feature peaks that cannot be individually analyzed due to their coincidence with an inherent electrochemical feature of the system, such as oxidation or reduction. For example, the first UPD peak of silver on gold is difficult to discern due to its location. This peak, responsible for the first ~0.3 ML of Ag deposition, occurs near .9V (relative to Ag/AgCl), placing it squarely within a wider, larger, Au reduction peak. It is necessary to either avoid oxidizing gold or manipulate the electrolyte solution via "pH buffering" to eliminate the reduction peak or resolve it from the UPD peak, respectively. This type of complication, along with a lack of definite theory to accurately predict the location of UPD peaks, makes discerning their existence and location difficult.

Once identified and located, however, a given UPD feature can be characterized relatively easily through the use of cyclic voltammetry (CV) and scanning probe techniques such as STM. CV is performed through the use of a potentiostat in a three-electrode arrangement, controlling the electrochemical potential of the working electrode relative to an equilibrium reference electrode in electrolytic contact with the working solution. By sweeping or "cycling" the voltage between two vertices and allowing the cell to draw as much current as necessary at a given voltage, a current/potential plot can be made, producing "peaks" that can correspond to oxidation and reduction of the substrate, or plating and stripping of ions in solution. Integration of these peaks gives the total charge density associated with a given peak. Correlation of these peaks with electrochemical processes gives information pertinent to the extent of the process performed. This type of "coulomb counting" method, combined with direct in-situ STM examination of a sample surface, provides an accurate picture of any given UPD process. Previously studied UPD processes have exhibited epitaxial growth up to two atomic monolayers thick.

It is also worth noting here that the morphology and chemical properties of a UPD layer appear to be related to the method of UPD layer growth and not merely the emersion potential of a UPD-coated electrode. That is, a UPD film grown potentiostatically at a specific voltage will behave differently than a UPD film grown by bulk deposition and stripping at the same voltage.

Along the same lines, it is important to realize that UPD adlayers, although typically grown as actual layers on top of the substrate system, do not always remain on the surface. A particularly notable example of this phenomenon occurs for the UPD of Li

on Au, during which some Li atoms actually intercalate into the bulk Au structure itself, forming an alloy structure[154]. This phenomenon is not unexpected in electrochemical studies, as a multitude of vacuum studies have already indicated, for a variety of systems, that this type of subsurface 'adlayer' growth may occur under specific conditions[155-156]. Thus it is informative to consider representative pairings of metals in which there is little to no miscibility of the two components in order to isolate effects arising from this surface alloying phenomenon from the variety of other phenomena co-existing on the surface.

3.1.4 Galvanic Replacement

One of the primary weaknesses of UPD techniques is their specificity to particular metal/metal systems. This limits the applicability of UPD for use as a universal layer-by-layer growth method to specific systems in which the depositing metal exhibits a UPD feature on the underlying metal. Furthermore, UPD cannot be repeated on top of itself, limiting its application as a fabrication technique to films of single atomic monolayer thickness. The early approach that successfully used UPD to grow thicker films in a layer-by-layer fashion employed alternating layers of UPD repeated iteratively[95]. In this method, a deposit of alternating layers could be grown, provided that the first layer exhibited UPD properties on the second layer, and vice versa. This approach still exhibited the critical weakness that it could not be used to grow films of a pure element in a layer-by-layer fashion.

This weakness can be overcome via the creative application of a galvanic corrosion process, in which a metal in solution reduces onto the surface of a less noble substrate, oxidizing a surface atom of the substrate to obtain the electron necessary. This

corrosion process will proceed until one of three conditions is met: (A) the nobler metal plates to a thick enough layer that no porosity remains for the oxidation of the substrate, (B) the noble metal in solution is completely depleted, or (C) the less noble substrate is completely corroded. Condition A is only satisfied at extremely high deposition thicknesses (micron scale) and is irrelevant to this project. Condition B could be satisfied via precise calculation of metal in solution, however these calculations are difficult and require extreme exactness. Condition C is well-suited to this procedure. Through combination with UPD, the amount of 'less-noble substrate' can be controlled to within 1-2 atomic monolayers. That is, the UPD-grown layer behaves as a sacrifical anode for the cathodic reduction of the metal to be grown. Thus, the metal deposited by UPD processes is commonly referred to as a 'sacrifical layer'. By repeated iterations of UPD growth and redox replacement of the sacrificial layer, an ultrathin film of thickness ranging between submonolayer coverages to hundreds of nanometers can be grown. This film can be grown with degrees of precision at an atomic monolayer scale. This technique has been referred to by a multitude of acronyms, including electrochemical atomic layer deposition (EC-ALD), electrochemical atomic layer epitaxy (EC-ALE), monolayer restricted galvanic displacement (MRGD), as well as surface limited or sacrificial layer redox replacement (SLRR). It is worth mentioning that underpotential growth methods have also been employed in nontraditional electrolytes, specifically non-aqueous electrolytes.[157] These techniques offer an interesting range of materials growth techniques, opening up the possibility of studying monolayer growth of metals such as Ce and Li, which normally exhibit no stability in water-containing media. These techniques are still in the process of being studied and are not yet completely understood or

characterized. Furthermore, nonaqueous UPD has (to this author's knowledge) never been used to create sacrificial layers for SLRR.

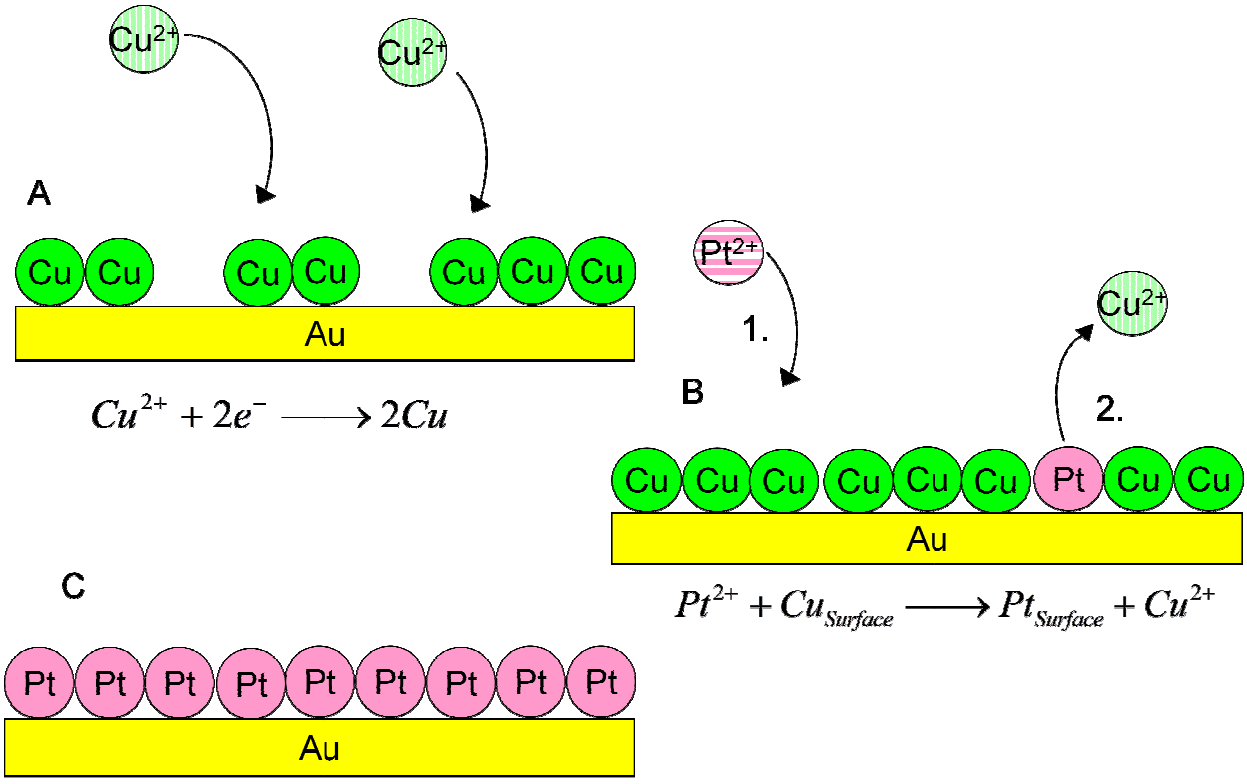

Scheme 3.3 Example of nominal reactions used in galvanic replacement process.

3.1.5 Cyclic Voltammetry

In the previous sections, several different types of voltammetric techniques have been referred to. These techniques include constant-current (galvanostatic) and constant-potential (potentiostatic) measurements as well as dynamic methods such as potential sweeps and cycles. These latter techniques, which are referred to by a variety of names including linear sweep voltammetry, stripping voltammetry, or cyclic voltammetry, use a moving potential setpoint or waveform to cycle the potential at a specified rate[119, 121]. As the voltage setpoint is ramped, the potentiostat must continually flow a small trickle of current to achieve the desired potential at the specified rate. For cases where no electrochemical reaction (defined as a chemical reaction in which electrons are present as either a reactant or a product) is proceeding, this current is referred to as a charging current and can be thought of in terms of a parallel plate capacitor, which requires incremental increases in charge to accommodate incremental increases in potential. Thus regions for current-voltage plots of a potential sweep, potential windows devoid of electrochemical reactivity exhibit slopes of zero. If a voltage is reached at which a reaction can proceed, the charge buildup accumulated on the surface changes, and the potentiostat must increase the magnitude of current flow to accommodate the reaction but maintain the set-point sweep rate. Thus cyclic voltammograms are typically seen with positive currents corresponding to oxidation reactions and negative currents corresponding to reduction reactions.

In cyclic voltammetric studies, the terms “reversible,” “irreversible,” and “quasi-reversible” take on unique meaning. In contrast to the standard usage, an electrochemically reversible reaction is not just any reaction that can be reversed to yield

the original reactants once again. Rather, the definition of electrochemical reversibility restricts itself to reactions in which the forward and reverse reaction both occur quickly. Fundamentally, this condition may be described as a reaction with a large exchange current density. In CV, this condition restricts the definition of reversibility to reactions which exhibit a specific relationship (in terms of currents and potentials) between the forward reaction and the reverse reaction. Specifically, in order for an electrochemical reaction passing *n* electrons to be electrochemically reversible, the voltage spacing between the forward peak potential and reverse peak potential must be 59 mV[121]. It is important to remember that current is proportional to the amount of reaction occurring, so the ratio of the forward peak current to the reverse peak current is expected to approach unity for reversible reactions.

Reactions that would traditionally be considered reversible, but which exhibit electrochemical behavior other than this (typically with larger potential spacings between forward and reverse features), are referred to as quasi-reversible to indicate that there is some kinetic barrier to the reverse reaction causing deviation. These reactions will also be characterized by forward:reverse peak current ratios greater than unity. Irreversibility describes systems in which the reverse reaction is impossible.

The question of voltage spacing between the forward and reverse peaks can also be used to understand whether a process is surface-confined or not. Surface-confined reactions will not exhibit a voltage difference between the forward and reverse peaks of a reaction. This leads to the distinctive case where the forward peak and reverse peak occur directly on top of one another in the traditional CV plot. This allows for the relatively

easy identification of charge-transfer adsorption processes (such as UPD), or processes that involve immobilized adsorbed reactants or products on the electrode surface.

Typical sweep rates range from 2 mV/s at the absolute slowest (corresponding to the minimum speed at which noise from equipment, thermal convection, and environmental vibration can reasonably be neglected) to 100 mV/s or more. In general, slower sweep rates allow for better resolved peak structures, although faster sweeps allow a potential range to be scanned through while minimizing the total amount of reaction driven. It is important to remember that currents at peak maxima will increase with increasing sweep rates, as will the charging current. This phenomenon can be thought of intuitively as the potentiostat being forced to flow more charge over a shorter period in order to maintain the higher sweep rate. However, the charging current and the peak current (for a reversible reaction) will not scale at the same rate, leading to changes in signal/noise ratio (where the charging current is the noise) as a function of sweep rate. Conducting tests at a series of sweep rates allows us to determine rate constants for any time-dependent coupled chemical reaction. If potential is swept faster than the time-dependent step can keep up with, a feature will be eliminated from the voltammogram.

One important aspect of cyclic voltammetry lies in the ability to quantitatively characterize surface reactions. If a given reaction is known to be surface-restricted (such as adsorption reactions which only proceed to the limit at which the surface is covered), electrode surface area can be inferred from the total amount of charge passed. Inversely, if electrode surface area is already known, percent surface coverage can be calculated. These techniques are very useful for determining catalytic surface area or partial adlayer coverage (such as in the case of surface oxide formation on Pt-Au hybrid electrodes).

In most cases, particularly for the Pt-H_2SO_4 and Au- H_2SO_4 oxidation systems, the limits of the potential sweep are of particular importance. This is because the surface oxidation features do not occur as simple one-step processes with a single distinct peak, but rather occur as the superposition of multiple peaks, leading to a plateau-type voltammogram across which multiple oxide species might be spontaneously present. Depending on the potential of sweep reversal, the resulting reduction peaks will correspond to the state of the oxidized/oxidizing electrode surface at the moment of sweep reversal. In this manner it is possible to see potential shifts as large as 200mV for the reduction of Pt surface oxides, depending on the maximum oxidation potential (which determines the presence of PtOH versus PtO_2 or PtOOH oxide species). Since each of these species reduces at a different potential, it is possible to obtain multiple reduction peaks during one reductive sweep for the same surface (as is often seen for Au oxidation/reduction cycling).

3.2 X-ray Photoelectron Spectroscopy

3.2.1 Technique Overview

X-ray photoelectron spectroscopy (XPS) is one of the primary techniques employed in this work, due to its ability to pinpoint elements and valencies as well as its high degree of surface sensitivity[158]. This technique involves the exposure of a sample surface to X-rays of a narrow band of energies. This is achieved by the use of specific X-ray emission lines (such as Al or Cu K_α), and the implementation of techniques to "monochromatize" the resulting emission to achieve higher energy resolution. These X-rays excite electrons from the bulk of the material, creating photoelectrons, or electrons freed from their original atomic states by interaction with incident photons. However, the majority of these photoelectrons interact with other nearby atoms in the sample, being re-absorbed into the material or losing energy over relatively short length scales. It is only the photoelectrons that are freed from atoms extremely close to the surface of the sample (which is in contact with the vacuum of the system) that manage to escape the sample with no energy loss and move through vacuum towards the detector.

It is important to note that a broad range of photoelectrons, escaping from many different types of atoms, and from many different atomic states within those atoms, will be excited simultaneously. These photoelectrons are distinguishable from one another by virtue of their different kinetic energies. These varied kinetic energies are what allows the detector to discriminate between different elements, and different valencies of those elements, in the near-surface regime of the sample. By passing the emitted photoelectrons through a curved detector with an electric field, the higher energy photoelectrons impact the detector at a different location than the lower energy electrons. Through precise

measurement of the location of these impacts, the broad range of escaping photoelectrons are binned and sorted to create a spectrum. This spectrum can then be converted from kinetic energy space to binding energy space according to equation 3.1:

$$B.E. = \hbar\nu - K.E. - WF \qquad \text{(Eq. 3.1)}$$

Where B.E is the binding energy, $\hbar\nu$ denotes the incident photon energy, K.E. denotes the kinetic energy of the photoemitted electron, and WF denotes the work function associated with removing an electron from the surface. These features in binding energy can then be associated not only with specific elements, but with specific electron orbitals within each element. Thus it is possible to study the photoemission spectrum of a specific electron energy level for a specific element, such as the C 1s or the Pt 4f emission. Values for these binding energies for pure elements are well known, and various shifts about the expected value can be associated with an assortment of compounds or chemical bonds.

Elements will exhibit shifts in the photoelectron binding energy of specific electron orbitals due to the participation of those orbitals in covalent bonding, or the influence of this bonding on the degree of 'shielding' that these orbitals receive. For example, the shifts in binding energy of the Oxygen 1s emission line are well known for molecular oxygen compared with atomic oxygen, O^{2-} species in an oxide, or O^{1-} species in a hydroxide or a defect oxide. One of the more common methods of conducting this type of analysis is by "fingerprinting" a known reference compound and looking for photoemission peaks at the same binding energy in the sample of interest. When such reference compounds are not available, either due to expense or experimental difficulty (often some reference compounds are volatile and decompose before accurate XPS

spectra can be taken), other identification techniques such as comparison to literature references or calculated spectra must be undertaken.

It is important to realize that formal charge is not the only contributing factor to shifting XPS spectra. For example, Pt^{4+} salts with different coordinating anions (H_2PtCl_6, PtO_2) will exhibit minor shifts in the Pt 4f binding energy relative to each other[159]. These shifts arise from the differing electron interactions between salts, which are dependent on the strength and number of cation-anion bonds. These shifts can also arise from deviations in atomic charge on the Pt atom itself. Despite Pt having a *formal, stoichiometric* charge of 4+ in both of these compounds, the actual charge may be somewhat different (if non-integer charges arising from changes in the electron distribution function are considered). This type of difference can be referred to either as a ligand effect, which emphasizes the influence of the neighboring atom's electric field, or as a chemical shift, which emphasizes that the bonding is the primary factor. In actuality the chemical shift encompasses both the ligand effect and the valency effect.

Thus, it is instructive to remember that the larger shifts caused by changes in the formal valency of the atom are also subject to relatively smaller shifts arising from local electron configuration effects. This means that the spectroscopist using XPS to determine valence state must consider a window of various binding energies that may be associated with a specific valency. This is usually not a problem as the shifts arising from formal valency change are usually quite larger than the shifts associated with electron configuration changes.

3.2.2 Complications of XPS

It is instructive to consider here the presence of Auger electron peaks, which are ubiquitous in XPS data. These peaks arise from the emission of Auger electrons, which are excited during the relaxation of electrons within the atom. This means that specific Auger electrons are always emitted at a characteristic kinetic energy, regardless of the excitation energy used. This can be problematic if the Auger emission occurs at the same kinetic energy as the photoelectrons being studied for XPS. In most cases when XPS data are being collected, Auger peaks are ignored. In cases where it is possible to use more than one incident photon energy, such as synchrotron XPS or dual-source lab XPS, it is possible to positively identify the Auger peaks as they will be the peaks that appear to shift (when plotted on a B.E. axis) as a result of the changing incident photon energy.

A second complication that can arise during XPS analysis is due to charging of the sample surface[160]. For poorly conducting samples, the continued ionization of the surface atoms by removal of photoelectrons cannot be compensated by conduction of electrons from the bulk of the sample. Thus the binding energy measured in XPS will shift due to interaction of the emitted electrons with the surface-confined electric field arising from the accumulated charge. One way to minimize this difficulty is through the use of alternative charge neutralization methods such as an electron flood gun. These guns operate across a range of energies, typically between 0 and 500eV, and are employed to counteract the surface charging effect mentioned above. While the flood gun succeeds in neutralizing the charge-induced shifts in the XPS spectra, often it will induce shifts of its own which must still be accounted for in the data analysis stage.

A third difficulty that arises when conducting XPS of electrochemically grown samples is due to changes in the sample during transport to the XPS vacuum chamber. This is primarily due to the amount of unwanted contaminants the sample is exposed to en route from the electrochemical apparatus to the vacuum chamber, and even in the electrochemical cell itself. Even though most aqueous electrochemistry is conducted in solutions purged with inert gas, it is impossible eliminate OH^- groups from the solution and surface. Additionally, carbonaceous species which may be electrically inert in the electrochemical cell (meaning they do not contribute significantly to net measured current) can easily adsorb onto the surface after the growth process. Finally, oxygen adsorption and carbonaceous species in atmosphere can adsorb to the sample surface during the transfer step, resulting, at best, in sample contamination and, at worst, in oxidation of the sample surface. Certain of these concerns apply to varying degrees depending on the sample surface. For example, Pt films are extremely sensitive to carbon contamination due to the strong Pt-C affinity, but are not particularly vulnerable to oxidation reactions. On the other hand, a sample with an electrochemically grown layer of adsorbed CO is less sensitive to carbonaceous adsorption (because the CO molecules are blocking many surface sites that would otherwise be available to carbonaceous species) but is extremely vulnerable to oxidation of the CO film by atmospheric oxygen.

Some spectroscopy methods are more vulnerable to these types of contaminations than others. For example, XANES of adsorbate species is extremely sensitive, as the adsorbate competes with contaminant molecules for surface sites on the sample. On the other side of the spectrum, EXAFS analysis primarily focuses on atomic structure measurement within the sample, and surface effects are less important. This is not to say

that EXAFS samples are entirely immune from these considerations, as air-sensitive samples will always require special consideration no matter what technique is performed. In the middle of the spectrum of contamination-sensitive techniques, XPS is moderately sensitive to these issues because the signal detected is generally emitted from a sampling depth of a few nanometers, so the spectrum will contain information about the sample even though it is preferentially probing the contaminant.

3.2.3 XPS In This Work

Both films and adsorbates can be studied by an XPS technique referred to as temperature-programmed XPS, or TP-XPS. This technique, which is similar in concept to that of temperature programmed desorption (TPD), involves the collection of a series of XPS spectra over a range of temperatures, across which the surface composition may change. This type of analysis is well suited to study of surface adsorbates leaving the surface upon heating, since they are not a structural part of the ultra-thin metal film, and are merely lightly bound to the surface by physi- or chemi-sorption processes. Furthermore, these adsorbate species may undergo chemical changes before desorption (as in the example of hydrocarbons which tend to dehydrogenate before leaving the surface). These changes can be identified, tracked, and quantified using XPS fingerprinting based on analysis of the photoelectron spectra. Thus, when used to quantify absorbate interactions, TP-XPS provides an excellent complement to a mass spectrometer system. The TP-XPS is used to study species on the surface, while the mass spectrometer detects the species that have left the surface. On the other hand, a system equipped with TP-XPS capability can be used to conduct similar experiments as a mass spectrometer-equipped system, as the species leaving the sample surface can often be

deduced from the TP-XPS spectra. TP-XPS is not limited to adsorbate characterization, however, and can also be used to track changes in the chemical state of a film itself as a function of temperature.

Furthermore, two types of physical XPS apparatus have been utilized in this work. The first, and most common, of these, is a fixed-energy laboratory XPS, which uses a X-ray source to create a constant supply of monochromatic X-rays. The second uses a synchrotron as the X-ray source. The synchrotron provides a high-intensity light source over a continuous energy range, which can then be filtered to select a specific energy by a device called a monochromator. This device lends the synchrotron one of its greatest strengths, the tunability of the incident photons' energies. By manipulating the incident energy of X-rays used, the XPS data collected can be made even more surface sensitive than the average laboratory source. Conversely, the tunability of synchrotron light also allows XPS to be used in a non-destructive depth profiling manner. By increasing the incident X-ray energy, the sampling depth is increased, allowing a greater depth of the sample to be studied. This can be advantageous in cases where a coating or film is covering the sample.

3.2.4 XPS Data Processing

Analysis of XPS data is conducted by a process called peak-fitting, which often utilizes software algorithms to quantify the amount of different species. The integrated area of a peak in an XPS spectrum is related to the amount of material emitting photoelectrons at that peak's binding energy. For elements that exist in multiple valencies or oxidation states, this process allows the experimenter to estimate the proportion of that element that is in each state. Furthermore, quantitative analysis of peak-area ratios for

multiple elements can allow the experimenter to calculate film thickness based on elastic or inelastic scattering theory and the attenuation of the underlying layer.

Peak-fitting analysis must often be performed under strict constraints. These constraints can arise as the result of a variety of physical phenomena. The first and foremost of the constraints to be considered is the actual peak shape itself. Whether to use a Gaussian waveform or modulate the waveform with the addition of some amount of asymmetry is an important consideration. Additionally, the width of the peaks (often treated as the full-width at half-maximum, or FWHM) is an important parameter. In cases where XPS analysis of multiple chemical states is being performed, it is often necessary to consult theoretical values for peak waveforms and widths, or to collect accurate reference data for each of the target chemical states being examined. Additionally, when performing XPS fitting, relationships between individual peaks must be considered. These relationships can take the form of shifts in the binding energy domain in cases when one peak is known to be at a specific binding energy relative to another. They can also take the form of area ratios, for cases in which one peak is known to exhibit a specific amount of photoemission compared to another. Oftentimes a given material will exhibit a pair of peaks, called a 'doublet', resulting from spin-orbit coupling[161]. This coupling arises from the difference in angular momentum component between two electrons at the same energy level. Since each of these split energy levels has a different binding energy associated with it, two peaks will appear in XPS. Each of these two peaks will then be related to the other in terms of a binding energy shift and in terms of the relative peak area (which is given by the occupancy of the two energy levels associated with the spin-orbit coupling).

3.2.5 Depth Profiling using XPS

Since XPS provides such a high level of surface sensitivity, it is possible to use it to conduct depth-profiled data collection if paired with a method for removing controlled increments of material from the sample surface. Thus it is common that an XPS system will be paired with an ion ablation gun or sputter gun that is capable of removing the outermost atomic layers of the sample surface. By collecting XPS spectra between intervals of sputtering, it is possible obtain a set of XPS spectra corresponding to increasing etch times. It is important to calibrate the etch rate of the sputter or ion gun, however, if an actual length scale is to be assigned to the XPS depth profiles that are collected in this manner. This type of calibration can be performed by independently measuring the depth of the etch pit created by the sputter gun itself, or by sputtering through a film of known thickness and using the XPS to watch for the elemental signature of the underlying support.

Another variant of depth-profile XPS analysis involves the use of a synchrotron X-ray generator as the source of incident photons for the XPS experiment. Tunable source energy XPS (TSE-XPS) uses the broad-spectrum light of the synchrotron in combination with a tunable monochromator to conduct XPS of a sample at a series of different incident X-ray energies. Since higher energies lead to greater sampling depths, this practice allows experimenters to conduct non-destructive testing with a variation in sampling depth from experiment to experiment as the energy is changed. Thus it is possible to non-invasively probe the composition and chemical state of the sample at a range of near-surface depths. However, it is more difficult to perform a length scale calibration on TSE-XPS depth profiles than it is to perform on the etched samples.

3.2.6 Surface Core-Level Shifts

Not all shifts in XPS spectra can be attributed solely to changes induced by oxidation state changes, bimetallic effects, or size effects. There is another type of structural effect that is well understood, that of the surface core-level binding energy shift [162]. The core level shift arises both from geometric coordination effects and from final state effects. It encompasses deviations in the photoelectron binding energy of near-surface atoms in a material as compared to the atoms in the bulk. It is possible to observe this effect by lowering the incident X-ray energy to the point where the XPS technique becomes significantly more surface sensitive. For most laboratory sources, this shift can be neglected as its contribution to the signal is very small. These changes result from lower atomic coordination among the surface atoms, and lead to lower binding energies for the outermost layers of atoms when compared with the bulk of the sample. In the case of ultrathin nanofilms, the entire film may exhibit this type of shift, which is typically less than 1eV in magnitude. This type of shift has been shown to correlate with the interaction of a metal's d-band and the reactivity of adsorbed CO on the metal surface[134].

For bimetallic systems, the core-level shift is more complicated. In addition to geometric and final state effects, the system will be influenced by both initial and final state effects arising from the interaction of the surface film with the substrate material in a so-called vertical electron transfer. In the case where the film itself is not homogeneous, it is possible that further deviation arising from lateral transfer will occur. This effect appears when a specific component of the film is influenced by neighboring dissimilar components, such as the case where an adlayer film is composed partially of a metallic species and partially of an oxide species. This effect has also been referred to as a dipole effect. Although this terminology has been primarily used for adsorbed organic

molecules, it is appropriate here as it describes the influence of adsorbed species on other adsorbates.

3.3 Scanning Electron Microscopy and EDS

The high surface area samples employed, including carbon fiber paper, and titania nanotube arrays, were all characterized before and after surface modifications using scanning electron microscopy (SEM) and accompanying energy dispersive spectroscopy (EDS). Since SEM relies on the use of an electron gun to generate its images along with large amounts of X-rays as by-products, it makes sense to pair SEM techniques with EDS techniques which can take advantage of the X-rays produced. By allowing simultaneous characterization of the morphology of the structure, as well as compositional analysis of the features in the structure, a better understanding of the arrangement of the bimetallic or metal-oxide architecture can be gained. In this study specifically, EDS was used to identify local regions of Pt concentration on Pt-TiO_2 surfaces. Additionally, EDS was used to identify gold nuclei on carbon fiber paper.

Unfortunately, EDS analysis is not very surface sensitive, nor is it sensitive to changes in chemical identity (valency). This means that the spectra created by EDS analysis sample extremely large depths compared to the single- and multi-atomic layer films that this work has focused on growing on flat substrates. Additionally, the EDS spectra only indicate the presence of an element, and do not have access to information regarding the interactions of that element with the support onto which it is grown. For this reason, SEM and EDS have not been successfully applied to polycrystalline or monocrystalline metallic surfaces, remaining restricted to the nanoporous surfaces of NPG and TNT samples. At the same time, EDS is able to simple confirm the presence of an element in a given region, whether an ultrathin film or unresolvably small particles. In this manner, EDS (in combination with SEM images) has been used to verify increased

dispersion of Pt films on TiO_2 substrates, in addition to characterization of the Pt nuclei which coexist with the films. Additionally, SEM was used to quantify the size and morphology of Au and Pt deposits on carbon fiber paper samples.

Two SEM machines were used in the characterization of these sampled. For high-resolution images, a Zeiss Ultra60 field-emission SEM was used. For insulating samples that exhibited large amounts of charging it was advantageous to use a Hitachi variable pressure (VP)-SEM which is capable of obtaining images at elevated pressures compared to typical SEMs. Although this technique is typically used to allow the imaging of biological samples without rupturing the fragile liquid-containing cells in the tissue, it is also a useful tool for charge neutralization in cases where gold-coating is not an option. This allows images of these insulating films to be taken without the detrimental effects of charging, and without the necessity to contaminate the film with gold-coating. Unfortunately, the increased charge neutralization ability of the VP-SEM leads to reduced image quality at higher magnifications.

In addition to advantages over the VP-SEM arising due to the variable pressure capability, the Zeiss SEM obtained better image resolution due to its use of a field-emission source (rather than a tungsten filament source) and the ability to use an in-lens detector rather than the traditional secondary electron detectors used in the VP-SEM. Furthermore, better vacuum pressures could be obtained in the Zeiss SEM system due to its use of a load-lock entry chamber. The VP-SEM apparatus simply opened the entire imaging chamber to atmosphere whenever a sample was exchanged, leading to increased adsorption of volatile organic molecules from atmosphere and, in turn, increased chamber pressure and decreased image quality.

3.4 X-ray Absorption Spectroscopy

3.4.1 XAS

X-ray absorption spectroscopy, or XAS, is a technique that enables element-specific analysis of targeted electron transitions. Since each transition occurs at a specific energy, this technique requires a tunable synchrotron X-ray source[163]. In XAS, the incident photon energy is rastered, by use of a single crystal monochromator, from below an absorption edge to above an absorption edge (an edge is the energy above which a specific electron transition is excited). By measuring the amount of X-rays absorbed at a series of points above the edge, the amount of electron transitions available in that material at a given energy is discerned. The density of these transitions can depend on the number of initial states (usually core electrons) as well as final states, which are usually the dominant factor. This information can then be processed and analyzed to deduce atomic structure, electron behavior, or both. These transitions are also influenced by scattering and absorption of secondary photons off of near-neighbor scatterers in the material being studied.

By measuring one of a variety of the resulting emitted (or transmitted) signals, which are proportional in intensity to the number of absorption events, a spectrum can be collected for a range of incident energies. This results in an experimental data set that probes the various transitions that can be excited in a material across a range of excitation energies. Since a given transition will not be excited until the requisite incident energy is reached, this allows for selective probing of specific transitions. The spectrum can then be manipulated in a variety of ways, including binning for a specific energy window of fluoresced photons by using a detector similar to that used for X-ray fluorescence. This,

along with the ability to tune the incident energy to a specific transition, gives XAS a component of element-specificity on the data-collection side of the experiment in addition to the specificity achieved through the stimulation side of the experiment.

XAS experiments are either conducted in transmission mode (where transmitted photons are measured), electron yield mode (where excited electrons are measured, either by means of a drain current or by an electron detector) or fluorescence mode (where fluorescing photons are collected and measured). In transmission mode, the absorption spectrum is calculated from a measurement of the total amount of photons detected on the opposite side of the sample from the X-ray source. Thus, by measuring the magnitude of the transmitted signal and normalizing to the amount of incident signal originally present, it is possible to calculate the absorption that occurred as a result of interactions between the X-rays and the sample. In fluorescence mode, the X-ray detector is generally placed at an angle to the side of the sample and incident photon beam, and measures the magnitude of the signal arising from secondary excitations (whether electrons or photons). The angle between the incident beam and the detector should ideally by 90 degrees to minimize interference from Compton scattering. Based on the assumption that the secondary excitation events (fluorescence and photoemission) are proportional to the total amount of X-ray absorption, it is possible to calculate the absorption spectrum in this way as well.

One of the main advantages of conducting XAS testing in non-transmission mode is the ability to selectively probe a subset of the secondary signal. For fluorescence experiments, this can be done through the use of an energy-discriminating photon detector such as the Si drift detector (SDD), which is commonly used for energy

dispersive analysis in SEM systems. This allows the experimenter to essentially perform an initial background subtraction during the data collection phase, and in some cases permits the exclusion of fluorescence from interfering elements.

For photoelectron measurements conducted in a vacuum, a commonly employed technique is the partial electron yield (PEY) detector[164]. Comprised of a standard photomultiplier tube paired with a screening grid that can be independently biased to a selected potential, the PEY detector can selectively reject photoelectrons below a specified kinetic energy threshold. This allows the experimenter, in specific cases, to eliminate a large portion of unwanted signal and preferentially measure a subset of the photoemission spectrum.

For transmission-mode experiments, it is important to prepare the sample after consideration of the X-ray absorption properties of the material at the specific incident energy for which the experiment will be conducted. In particular, there are two competing factors which influence the thickness of the sample to be assembled for the transmission-mode experiment. The first of these imposes a limit on the thickness of the sample arising from the total absorption of the material. That is, the sample should not be more the 4-5 absorption lengths thick, otherwise nearly all of the incident photons will be absorbed and the experiment is futile. The origins of this rule of thumb can be seen in the Beer-Lambert law:

$$I = I_o e^{-\alpha/\mu} \quad \text{(Eq. 3.2)}$$

Where I_o is original intensity, I is transmitted intensity, μ denotes the absorption length, and α denotes the path length. Thus it is easy to see that for each absorbtion length of sample that the beam must pass through, the signal is attenuated by a factor of e^{-1}. At the

same time, a second criterion must be considered, which requires that a minimum amount of the component to be studied (the absorber) be present in the sample. This criterion can lead to increases in the amount of sample employed to ensure that enough of the component in question is present to provide a measurable absorption signal.

3.4.2 Extended X-ray Absorption Fine Structure

Extended X-ray absorption fine structure (EXAFS) refers to a specific method of analyzing the X-ray absorption spectrum. In order to glean atomic structure information from the XAS spectrum, an extended 'tail' of energies above the absorption edge is collected. This 'tail' is then analyzed for fine structure elements, or oscillations that are induced by electron waves arising in the crystalline structure of the material. This analysis is typically conducted by means of a Fourier transformation, which must be preceded by a series of normalization steps.

By convention, most EXAFS processing begins by normalizing the edge-step of the pre- and post-edge backgrounds to one. This normalization accounts for changes in the actual amount of material present in the sample, since the magnitude of the edge-step is proportional to the amount of absorption occurring (which is in turn proportional to the amount of material present). After normalization, a background line (called a spline) is then fit to the post-edge wave. By subtracting this background from the experimentally measured spectrum, the structure-induced oscillations in absorption as a function of incident energy can be isolated. These oscillations can then be converted to k-space (with units of $Å^{-1}$) and Fourier transformed to real space (with units of Å). This leads to a new technique known as extended X-ray absorption fine structure (EXAFS). Through this

type of analysis, information such as crystallinity and nearest-neighbor distance can be derived from the original spectrum.

The EXAFS equation is given as follows:

$$\chi(k) = \sum_{shells} \frac{n_X \cdot S_0^2 \cdot f_X(k) \cdot e^{-2k^2\sigma^2}}{k \cdot r^2} \sin(2kr + \alpha(k)) \qquad \text{(Eq. 3.3)}$$

With the total absorption (χ) as a function of shell population (n_x), amplitude reduction factor (S_o), backscattering amplitude function (f_X), Debye-Waller term, interatomic distance (r), and phase shift (α).[163, 165]

Since the Fourier transform of the X-ray absorption spectrum is performed on the data in k-space rather than in energy-space, it is often worthwhile to perform a process called k-weighting during the course of data collection. A single spectrum is collected by measuring absorption data at a series of discrete points in the incident energy domain, with a dwell (or integration) time at each point on the order of seconds. The process of k-weighting can be applied during experimental execution to both the step size and the integration time used in spectrum collection. This allows for fewer data points (corresponding to larger step sizes) to be collected at higher k-values, but for more time to be spent collecting data at each point (since the collection time is a linear function of k). Since the magnitude of the features of interest decreases with increasing k, these methods are of particular utility. During data analysis, k-weighting can be used to amplify the magnitude of features at high k values relative to features closer to the absorption edge.

EXAFS data can also be fitted with calculated distribution functions based on a model crystal structure. These model structures rely on the specification of a single unit cell and extrapolate a spectrum from this input. By calculating several hypothetical models and performing goodness-of-fit checks between the experimental and the model-derived spectra, an accurate fit to the data can be found.

3.4.3 X-ray Absorption Near Edge Structure

In the other extreme, there is a wealth of information-rich fine structure close to the absorption edge itself. The study of this region is knows X-ray absorption near edge structure, or XANES[166]. Often this technique is also referred to as near-edge X-ray absorption fine structure, or NEXAFS, although this work will use XANES for consistency of terminology. XANES is the term used for this technique when studying relatively low-energy absorption edges (such as carbon or oxygen), while a second term X-ray absorption near edges spectroscopy (XANES) is used to apply to essentially the same type of analysis when conducted on higher energy absorption edges (such as Pt or Pd L3 edges). Features in the XANES region are not typically treated with the same type of mathematical transforms as EXAFS data[165], but rather can be treated similarly to XPS data, where peak areas are analyzed directly. The difference in this case is that XANES peaks all correspond to specific electron transitions to unoccupied crystalline or molecular states, such as the e_g or t_{2g} orbitals in semiconductors, or the $2\pi^*$ orbital in carbon monoxide.

Carbon monoxide provides an excellent example of a subset of XANES measurements which focuses on the study of molecules stuck on the surface of a sample. Either by exposing a sample to vapor-phase levels of a chemical compound or reactant molecule, or by pre-depositing a layer of the compound before introduction into the XANES chamber, the sample surface can be coated with an adsorbed layer of a target compound. In this way, only the compound (called the adsorbate) is analyzed when conducting XANES measurements. This has the advantage of letting the experimenter

target only the surface of the sample, as that is the only location at which the adsorbate will be present.

A second important advantage of synchrotron XANES arises from the polarization of the synchrotron-generated photon beam. Since the polarized beam preferentially excites electron orbitals in a specific orientation on the sample surface, XANES can be employed to determine the orientation of adsorbed molecules at a well-defined single-crystal sample surface[167-168]. This technique proves difficult with electrochemically or polycrystalline samples and is not employed in this work.

Both of the previously mentioned techniques for adsorbing the layer of interest to the sample surface will be examined and compared in this study. The first technique, which involves creating electrochemically fabricated samples that are as clean as possible, is very difficult and will be shown to produce less desirable data in the form of lower signal/noise ratios and more contaminant signal. The second technique takes advantage of electrochemical cleaning during the adsorption step, occurring when the adsorbate displaces contaminants that would otherwise be on the surface.

All forms of XAS benefit from a wide selection of possible detectors to be employed. For XAS performed in a vacuum (including XANES), experimenters have the option of measuring absorption by tracking the electron yield emitted from a sample, or by tracking the photon signal emitted through excitation-fluorescence mechanisms. Even more options exist for XAS or EXAFS conducted in atmosphere, with types of detectors ranging from PIPS detectors, multi-element fluorescence detectors, or transmission detectors (in the form of ionization chambers).

One type of XANES detector employed in this current work is known as a partial electron yield (PEY) detector, which essentially means that electrons (both Auger and photoelectrons) generated by the incident photon beam are measured, but that only a fraction of the total electron signal is measured[164]. This fraction is determined by a voltage bias applied to a grid in front of the detector electronics, which functions as a rejection filter for electrons with a kinetic energy below a specific threshold. By increasing this threshold, greater surface sensitivity and element specificity can be achieved. However, if this threshold is increased to a value too close to the energy of the absorption features to be studied, a large part of the electron signal that is important to the spectrum will be excluded from the data, resulting in the appearance of strange features such as oddly shape peaks or negative step-edges.

3.4.4 XAS Data Processing

When conducting XAS data reduction, it is important to know which of these types of detectors and experiment geometries were used in the data collection process. The most obvious time when this knowledge is necessary comes when the initial calculation of absorption is performed. For example, the calculation of absorption from a transmission experiment involves the logarithm of the inverse ratio of experimentally measured signals when compared to the ratio required for a fluorescence experiment. It is also necessary when interpreting non-transmission data to know if the absorption signal was measured from an electron yield detector or X-ray fluorescence detector, as the two signals probe different depths of the sample. This is important not only for accurate data processing, but (perhaps more significantly) for accurate data interpretation.

This type of data processing follows a specific and complicated procedure. The first step in this procedure it to fit the spectrum with a pre-edge and a post-edge background curve, which is used to normalize and flatten the data. By normalizing all spectra from a given sample set such that the magnitude of the difference between the pre-edge and post-edge backgrounds is unity, it is possible to account for changes in the amount of the element in question across the sample set. This allows individual features to be compared with one another across multiple samples, even if the two samples were composed of different amounts of the element under investigation. If XANES analysis is being performed, then this normalization may be the first and final step of the XAS-specific data processing sequence. After this point individual features can be compared and fitted via traditional curve-fitting methods, allowing qualitative and quantitative conclusions to be drawn.

The type of conclusions that can be drawn from this type of analysis depend strongly on the type of material being studied. The simplest analysis that can be performed is an analysis of the white line intensity of an absorption edge. This intensity, which is taken as the amplitude of the first oscillation closest to the absorption edge, is related to the occupancy of the d-band in metals and metal oxides, and as such grows more intense for oxidized materials than for corresponding metallic forms of the same element[169].

If EXAFS analysis is being conducted, the data must be processed more even after normalization of the spectra. The next step in preparing the data for a fourier transform is to fit the normalized spectrum with a background function for the post-edge region and subtract that background from the data. This leaves behind only the

fluctuations arising from the interaction of the electron wave with the atomic structure of the material. These fluctuations, or 'wiggles,' are easily converted from energy (eV) space to k-space ($Å^{-1}$). From there, a window for the forward fourier transform must be chosen, and the transform can be taken, resulting in a plot in real space (Å). Oftentimes this process will be performed iteratively, with minor corrections to the background function being made in each iteration in order to eliminate artifacts in real space that appear at physically unreasonable length scales (such as interatomic bond lengths of less than 1Å). Finally, the resulting real space curve can be fitted with a combination of multiple theoretically derived radial distribution functions and conclusions regarding the identity of the species responsible for each peak may be drawn. This entire process is generally performed using a data processing suite such as ATHENA[170].

This use of theoretically derived spectra in real space is performed by constructing a series of candidate structures that may be present in the sample and then calculating, usually by an algorithm such as FEFF, the expected spectrum for that ideal atomic arrangement[170]. Then the expected theoretical spectra can be compared with the experimental spectra, and the most suitable structure can be chosen. In cases where multiple species may be simultaneously present, a combination of calculated spectra may be used to fit the experimental data. After this step, a goodness-of-fit χ^2 test can be conducted to quantify the accuracy of the data treatment process employed.

One important addition to the suite of post-processing steps performed on XAS data in this work is the use of a dead-time correction algorithm[171]. When collecting data using a Si drift detector, it is important to consider the possibility of two photon events being counted as a single artificial photon event of energy equal to the sum of the two

real events' energies. This type of error is made possible by the way in which a SDD converts particle energy from total charge imparted to the detector during a specific time window. Thus if the event rate is high enough, it becomes more likely that two discrete events will occur during one sampling window and the sum of their respective charges will be interpreted as corresponding to a single event. This phenomenon is known as dead time, and must be corrected for if it occurs in excess. This is possible after the experiment, provided the raw number of total events is recorded during data collection. This is achieved by measuring the total number of events before any post-processing by the detector electronics, then comparing that figure to the total number of events output from the electronics.

3.5 Sample Preparation

3.5.1 Sample Treatment and Polishing

Polycrystalline gold samples were manufactured by sectioning of a 6mm diameter gold rod (99.9% purity, Goodfellow). Before sectioning, the gold rod was set in polymethylmethacrylate (PMMA) disk to add rigidity to the samples while being sectioned. Then, the samples were polished using a series of grinding disks and alumina polishing powder of sequentially smaller grit, terminating in 0.05um, or Masterprep, suspension. Standard Buehler polishing cloths of medium nap were used. This polishing process presented a series of problems, primarily arising from the embedment of alumina particles into the gold surface. This embedment evidenced itself both in optical and electron microscopy, as well as in XPS measurements. In microscopy, the embedded particles could be seen as scratch-dot patterns, with the embedment forming a dot or crater at the end of a scratch in the sample surface. In XPS, characteristic photoemission peaks of elemental aluminum and Al_2O_3 were seen, which overlapped with some Pt XPS features, causing problems in the XPS analysis. This issue was solved by altering the final polishing solution to include trace amounts of hydrogen peroxide (added to the polishing solution on the polishing cloth itself) to prevent embedment[172] and by ultrasonicating the samples in isopropyl alcohol solution after polishing to remove any particles that were embedded despite the altered polishing process. This approach is successful in creating alumina-free surfaces, and relies on the so-called attack-polish effect, by which H_2O_2 attacks the gold surface to help remove larger embedded particles and prevent the smallest particles from the smallest polishing step from embedding.

Additionally, polishing was either conducted by hand with extremely low vertical force, or automatically to prevent embedment. After polishing and ultrasonic cleaning, samples were often annealed by use of propane flame and either air-cooling or nitrogen-cooling. The annealing process involved heating the sample to orange-yellow heat and maintaining the heated flame such that this temperature was preserved for ten to thirty seconds. This process allowed the surface of the gold sample to be reconstructed to increase the proportion of Au(111) facets exhibited on the surface. This is achieved at higher temperatures by increasing the average surface mobility of Au atoms, allowing them to arrange to form the (most favored) Au(111) facet. This effect can be seen during Cu UPD of samples with and without annealing stages, with the annealed samples showing more distinct UPD features.

Single crystal gold samples were treated similarly to polycrystalline gold samples. The single crystal samples were cut and polished originally by the manufacturer, but after electrochemical use, these samples were re-polished by hand using only 0.05um Masterprep suspensions. Subsequent ultrasonic cleaning and annealing steps were identical to those for the polycrystalline samples.

For Pt foil and wire electrodes, cleaning was performed by flame-annealing in a propane flame and CV in acidic solution (1M H_2SO_4). The importance of flame-annealing a Pt electrode can be readily seen in the facet-dependent voltammetry studies avaialable from the literature[173-175]. Since annealing changes the predominant facet on the electrode surface by increasing atomic mobility at higher temperatures[176], one can easily see how the reactivity and surface chemistry of an electrode can be changed by annealing steps.

3.5.2 Sample Preparation for X-ray Spectroscopy

Sample preparation for X-ray absorption spectroscopy requires a specific methodology, and this study uses traditional methods for preparing such samples. For reference samples, which mostly consisted of powder samples, the powders were first ground to the smallest grain size practically achievable by mortar and pestle. This fine powder was then distributed evenly over the adhesive surface of X-ray transmissive kapton tape. Larger particles were removed from the surface by simply shaking them free. This tape was then folded over on itself multiple times to increase the total cross-section until approximately one absorption length was achieved. Care was taken to ensure that the powder film was in all points pinhole-free, although one advantage of the multiple-fold approach to sample fabrication is that any inhomogeneities in one patch of the film would be averaged out by comparable inhomogeneities in the other layers. The majority of powder references were collected in transmission mode. For air-sensitive powders, the kapton pouches created in this manner were made and doubly sealed in an inert atmosphere glovebox, and the sealed pouches were stored and transported in inert atmosphere until used for spectroscopy, at which point they were studied in air (but still sealed).

Non-powder samples did not require any special sample preparation for non-vacuum XAS analysis. For ultrathin film samples grown on flat surfaces, the samples were generally studied in glancing-incidence fluorescence-mode geometries in order to maximize the flux of photons through the film. This was achieved by laying the sample nearly flat and allowing the incident beam to splay itself out onto the sample surface. For samples on porous surfaces such as the titania nanotube arrays, the carbon fiber paper samples, and the nanoporous gold samples, the geometries employed varied according to

specimen geometry. For the titania and nanoporous gold samples, the samples were too small to permit significant tilting of the sample without the incident beam leaving the sample surface. In most cases, low-angle incidence geometries were not required of the high-surface-area samples due to increased amounts of Pt present. This allowed for low-noise experiments to be conducted in a timely fashion without resorting to glancing geometries.

3.5.3 Sample Preparation for Adsorbate XANES

Samples that were studied by adsorbate XANES were fabricated at Georgia Tech by the usual methods and transported to the synchrotron in enclosed containers. For the final preparation stages and adsorption step, the samples were prepared on-site at the synchrotron facility in inert atmosphere glovebags after three cycles of filling and purging with nitrogen. Samples were then sealed in nitrogen-filled containers and transported to the X-ray absorption UHV chamber. During transfer from the container to the UHV chamber, the samples briefly (<5 sec) passed through atmospheric conditions before being placed in the nitrogen-backfilled UHV chamber. The total time between leaving the nitrogen-filled container and beginning pumpdown to vacuum conditions was less than 30 seconds, the majority of which was inside the vacuum chamber load lock, which was continuously being purged with nitrogen.

3.5.4 Vapor Deposition of Metal Films for Substrates

In addition to the use of bulk metal substrates, it was also useful to grow monolithic metal films on glass slides for use in certain spectroscopic and electrochemical experiments. Since the bulk metal substrates were usually in the form of disks with a relatively small surface area (6mm-10mm diameter), it was difficult to

perform X-ray absorption spectroscopy on them. For normal XAS analysis, sample size is not a significant issue, but with ultrathin films on the order of several angstroms thickness, collection times must increase to unfeasible lengths unless a larger sample area can be probed by the incident beam. The use of coated slides solved this problem as the slides were able to provide larger exposed surface areas of approximately 2cm x 4cm, across which the incident beam could be incident at an oblique angle.

For the initial set of such samples, slides were created by sputtering in a bell jar after chemical etching of the slides in hydrofluoric acid. Additionally, a sputter-grown adhesion layer of tungsten was employed between the glass and the gold film to ensure that the gold did not flake off during use. Trace amounts of tantalum and gallium were detected by X-ray fluorescence in the sample films. These trace amounts were due to the tantalum weigh boat employed for evaporation. Trace amounts of gallium were due to the fact that the sputter-coating system employed was also used for gallium evaporation from time to time. Because of this contamination, the bell jar method was eliminated and another replaced with a large-scale CVC DC Sputterer in a cleanroom environment. This allowed for larger batches of samples to be grown and also permitted a more homogenous distribution of samples to be made due to the rotostrate capability of the system, which rotated the different slides continuously throughout the growth process.

These slides were also employed as electrode surfaces for the flow-cell electrochemistry arrangement. The flow cell consisted of a two-piece plastic block with an o-ring seal and space for reference and counter electrodes. The plated slide itself forms one wall of the electrochemical cell and is the working electrode. Additionally, the cell features inlet and outlet nozzles which are used to exchange the electrolyte solution

employed. The important feature of the flow-cell geometry is the ability to maintain a specified potential on the electrode surface during the transfer from one electrolyte bath to another. This is in contrast to moving the electrode between two physical cells, which involves exposure to atmosphere as well as loss of potential control. Without the use of vapor-deposited metal films on larger monolithic substrates, this type of electrochemical setup would not be possible.

3.5.5 Carbon Fiber Paper Substrates

Carbon fiber paper electrodes were also employed for a variety of materials growth systems. Carbon fiber is an attractive material in that the carbon-metal interaction can stabilize nanoscale metal deposits and provide an efficient, conductive support for many reactions. Additionally, carbon fiber paper provides a higher electrochemically active surface area per mass, and per nominal electrode area, than solid metal electrodes such as massive disks or foils. This greatly increased the ease with which X-ray absorption analysis of monolayer coatings could be conducted, as the monolayer (which may conformally coat the porous paper surface) is given more X-ray cross section, since the X-rays penetrate the surface of the paper multiple times. A negative aspect of CFP usage is that overlayer thickness calculation using XPS techniques (as applied earlier in the case of Ni-mediated Pt monolayer growth) is rendered nearly impossible, as the thickness calculation for XPS is based on a flat substrate with a flat overlayer. This is required in order for the elastic scattering attenuation theory on which the thickness calculation is based to hold.

One further advantage of carbon fiber paper electrodes is that they can easily be sectioned into smaller pieces. This makes it experimentally simple to eliminate variance across multiple sample preparations, as pieces of the same sample can be used for electrochemical analysis, spectroscopic analysis, and any other form of testing required. For certain tests in which it is difficult to retrieve the sample after characterization, such as spectroscopic analysis in which the sample must be mounted using an adhesive or tape, it is convenient to simply cut a small corner of the paper off for spectroscopy and continue using the remainder for other tests.

Carbon fiber paper used was purchased from the Fuel Cell Store and was sold as a component of a membrane electrode assembly. The initial choice to use carbon fiber arose from its stability in aqueous solutions at the pH's employed, as well as its lack of significant electrochemical reactions across the voltage regimes considered. As a durable, low-cost, high surface area material that did not add significant complications to the experiments, either from a spectroscopic or chemical viewpoint, it was a prime candidate.

Complications can arise with the use of carbon fiber paper, however. Specifically, the carbon fiber paper can be rendered non-conductive if a thick enough deposit of an insulating material (such as ceria) is grown on it. This results in significant charging of the sample as evidenced by shifts in the XPS binding energy (this type of problem is not exlusive to carbon fiber paper and also appears on Au substrates). Additionally, larger samples of carbon fiber paper (more than 1 sq. inch) begin to show a high degree of inhomogeneity across the sample surface in terms of the amount of material electrodeposited. This problem could possibly be resolved through different cell and electrode geometries, but as these factors were fixed for the experiments described here, the CFP electrodes employed were limited in size to less than 1 sq. inch.

Noble metal electrodeposition on the CFP supports was conducted by potentiostatic growth. This method was used to grow Au, Pt, and Ag films on the CFP support. These films were then used as substrates for modification by other metals and subsequent analysis of the bimetallic interactions that arose. In the majority of cases, the first metal deposited was grown in a large quantity, and the second was grown in a relatively small quantity, so that the influence of the CFP substrate on the bimetallic system could be effectively neglected. In order to get a baseline for the metal growth on

CFP, it was necessary to compare the electrodeposited metal film with the much smaller deposit that would arise from spontaneous deposition without electron flow. It was found that a small amount of Pt or other noble metals would adsorb on the CFP surface without reducing. This was seen in XPS in the form of a small salt residue on the CFP after dipping in a solution at open circuit. In the case of Au electrodeposition on the CFP surface, a fully reduced metallic deposit was formed. In the case of Pt depositions of 10 minutes length, a significant portion of the film remained on the surface as a cationic species.

CHAPTER 4

IMPROVEMENTS TO THE SLRR TECHNIQUE

4.1 The Necessity of Less Noble Sacrificial Layers

Monolayer galvanic replacement, also called surface-limited redox replacement (SLRR), involves the electrodeposition of single sacrificial atomic monolayers and their replacement by a second element via redox galvanic replacement. The replacement reaction is thus limited by the amount of sacrificial material predeposited. This technique has received interest as a method of large scale layer-by-layer growth of metals under the name electrochemical atomic layer deposition (EC-ALD) [92-93, 177]. Previous techniques have employed the use of intermediaries such as Cu and Pb due to their advantageous underpotential deposition (UPD) characteristics. [91, 178-181] This method has also been shown to be a feasible method for creation of core-shell catalyst nanoparticles. [90, 182] This section outlines improvements made to the traditional SLRR methodology, specifically the use of Ni as an intermediary for redox replacement, which was recently published by the author as the first reported use of this technique for growing Pt monolayer films[1]. Because SLRR is limited by the nobility of the sacrificial metal, the use of Ni instead of Cu or Pb opens new possibilities for this technique. The use of Ni instead of Pb as an intermediary also promises more environmentally friendly applications for the method.

Redox replacement shows particular promise as a synthesis method for monolayer bimetallic systems, (MBS) which are of particular interest to catalytic systems. [114] Defined as a metal substrate upon which an atomic monolayer of a foreign admetal has been deposited, an MBS offers the unique opportunity to probe electronic effects that arise as a result of the configuration of two metals. MBS structures make excellent model

catalysts, allowing surface science techniques that are unsuitable for use on catalyst nanoparticles, such as low energy electron diffraction/microscopy (LEED/LEEM) and surface XANES, to be employed. The MBS configuration can be considered representative of core-shell geometries in that a full coverage surface species (shell) of minimal thickness is in intimate contact with a substrate (core) while isolating the substrate from any possible feedstock reactants. This type of bimetallic geometry has recently been explored in catalysis for several applications, including oxygen reduction, methanol oxidation, acetylene hydrogenation, and formic acid electrooxidation [183-186].

Electrochemical deposition techniques allow one to actively control the growth of deposited metals through the manipulation of experimental parameters.[187] In particular, deposition speed and growth mode (2D vs. 3D) can be manipulated via the tuning of solution composition and deposition voltage. The amount of electrodeposited metal can be measured by charge integration and controlled with submonolayer-scale precision by varying deposition times. By combining well-controlled electrodeposited layers with galvanic replacement, a corrosion method in which a more noble metal oxidizes and replaces an adsorbed baser metal, spontaneous monolayer replacement can be used to achieve well-defined MBS structures.

Spontaneous monolayer replacement is accomplished by the initial deposition of a precisely controlled sacrificial layer, which is then exposed to a more noble metal in solution. The more noble metal galvanically replaces the sacrificial layer via redox reactions, resulting in a bimetallic system in which one layer sits atop a bulk substrate, often retaining the epitaxy of the sacrificial layer (Fig. 4.1). The driving force for the replacement reaction is given by ΔE, the difference in standard reduction potentials of the

two metals. It is possible for metals that are only slightly more noble than the sacrificial layer to fail to replace it if ΔE is not large enough. A good example of this is Ru, which can replace Pb but not Cu, even though it is more noble than both. The requirement that the replacing layer be sufficiently more noble than the sacrificial pretreatment layer provides a constraint on the possible bimetallic systems that can be synthesized with this method. Previous implementations of this method have been limited to sacrificial metals such as Cu and Pb due to their advantageous underpotential deposition properties. The current work is the first implementation of well controlled 2D growth mode overpotential deposition to fabricate the sacrificial layer.

In all cases when performing SLRR growth methods it is imperative to first characterize the monolayer growth properties of the metal to be used as a sacrificial layer. In traditional SLRR cases where a UPD adlayer is used as the sacrificial metal, this entails tuning the electroplating bath composition in order to enable the UPD growth to occur at a significantly different potential than the bulk growth. This requires an iterative approach whereby cyclic voltammetry is used to determine the UPD properties of a variety of bath chemistries before choosing one chemistry and a specific voltage for the growth to be conducted at.

In cases where the sacrificial metal used does not rely on UPD properties, this characterization step is slightly different. In these cases, it is necessary to tune the sacrificial layer electroplating bath such that the film growth rate is very slow. This is necessary if monolayer- to bilayer levels of precision are to be achieved when growing the sacrificial layer. This measurement is typically performed by integrating the charge passed during anodic stripping of the sacrificial film for a series of different growth

potentials and times. If the valency of the cationic species being electrodeposited is known, this total charge can then be converted to a monolayer-equivalent charge.

In both cases the morphology of the deposit is also important. In cases of UPD there is often a body of literature available to describe the growth mode and surface reconstruction of the adlayer at various potentials[149]. In cases of slow-growth overpotential deposition, there is usually less work available in the literature since this field is, in general, less interesting as it is a less cutting-edge technique. Nevertheless, works of this sort have been published and make valuable resources[187].

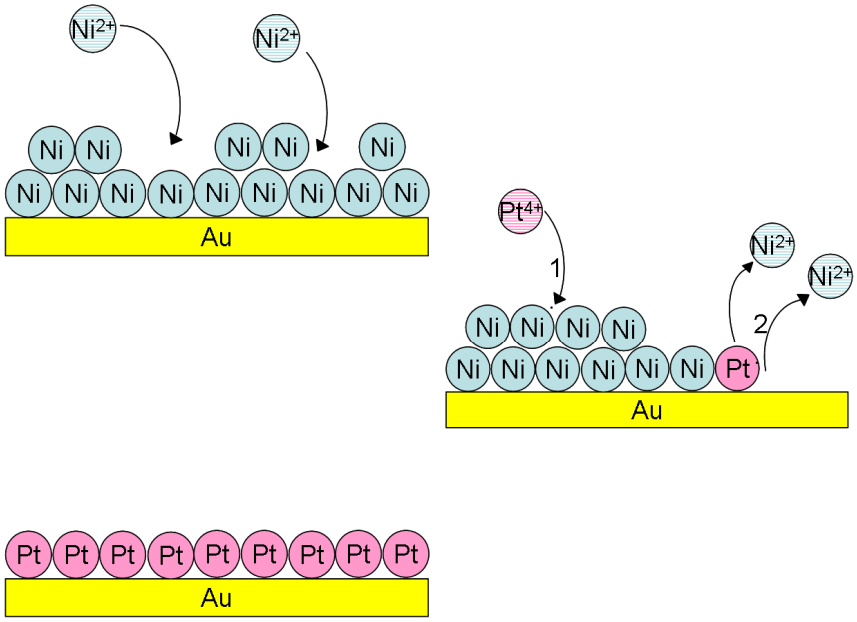

Figure 4.1: Schema depicting (A) the potentiostatic growth of a Ni bilayer, (B) The nominal 1:2 replacement by Pt by Ni, (C) The complete Pt monolayer.

By broadening the scope of galvanic replacement techniques to include more base sacrificial layers such as Ni, we can increase the selection of possible replacing elements available for use with this technique. Possible replacing candidates that fall between Cu and Ni on the potential series, and thus may replace Ni but not Cu, include Mo, Sn, and Pb. These candidates bear further investigation into whether or not the driving force for their replacement reactions is large enough. Additionally, the feasibility of Ni as an alternative for Pb intermediaries is a desirable avenue for the growing field of film fabrication via monolayer replacement, as Pb is highly toxic.

It has previously been shown by Wang et al that Pt replacement on bulk Ni substrates proceeds via a monolayer growth mode [188]. A study by Morin et al has also shown using scanning tunneling microscopy (STM) that 2D layer-by-layer Ni growth can be accomplished via the use of a modified Watts electrolyte.[187] By pairing this modified Watts electrolyte deposition with replacement methods previously used to fabricate Pt/Au electrodes via Cu replacement, [189] we have studied the first layer-by-layer multilayer growth of Pt on Au via Ni monolayer replacement. While such a method does not employ surface-limited techniques such as underpotential deposition to create the sacrificial layer, the deposition of the final layer is still limited by the amount of sacrificial pre-deposit on the surface and the exchange ratio that governs the replacement reaction.

4.2 Theory and Practice of Ni Deposition

Any electrochemical reaction must necessarily have an equilibrium reaction potential. This potential is often referred to as the redox potential or standard potential. In practice, the equilibrium potential is modified by concentrations of reactant and product by the Nernst equation:

$$E_{Eq} = E_0 - \frac{RT}{nF} ln \frac{a_{Red}}{a_{Ox}} \qquad \text{(Eq. 4.1)}$$

Where E is the observed equilibrium potential, E_o is the standard equilibrium potential, R is the universal gas constant, T is the temperature (K), n is the number of electrons exchanged per reaction, F is Faraday's constant, a_{Red} and a_{Ox} are activities of reduced and oxidized forms of the species in question, respectively.

Since negative perturbations from the equilibrium potential lead to reduction reactions, and positive perturbations lead to oxidation reactions, overpotential cathodic electroplating methods rely on the application of a potential more negative than this equilibrium potential. Thus the overpotential, η, is defined by the following relation:

$$\eta = E_{applied} - E_{Eq} \quad \text{(Eq. 4.2)}$$

Finally, for the replacement reaction to proceed, the difference between equilibrium reduction potentials for the replacing metal and for the sacrificial metal, ΔE, must be positive:

$$\Delta E = E_{Eq}^{Pt} - E_{Eq}^{Ni} \qquad \text{(Eq. 4.3)}$$

Electrodeposition and galvanic replacement reactions were conducted at room temperature in a glass cell in a hanging meniscus arrangement. Solutions were deaerated by bubbling with ultra high purity dry nitrogen or argon before all chemical processes. Water was deionized in a Barnstead NanoPure system (18.2MΩ). Chemicals used were obtained from Sigma-Aldrich and Alfa Aesar. Electrodes were sectioned from a 99.95% purity polycrystalline Au rod obtained from Goodfellow and polished using Buehler Masterprep alumina suspensions to 0.05 um before being annealed in a propane flame. The Pt foil electrode (99.99% purity, Alfa Aesar) was cleaned in 1M H_2SO_4 and flame-annealed before use. Reference electrodes were homemade Ag/AgCl electrodes. Auxiliary electrodes were Pt wire. X-ray photoelectron spectroscopy (XPS) was conducted in an SSX-100 system using Al Kα radiation (1486.6 eV), and cyclic voltammetry (CV) data was collected on a Solartron 1287 potentiostat, with which all deposition processes were controlled.

Cyclic voltammetric characterization of electrodes was performed in 50 mM H_2SO_4. Layer-by-layer Ni deposition was performed using a Watts electrolyte modified for layer-by-layer growth (1 mM $NiSO_4$ + 10 mM H_3BO_3 + 0.1mM HCl) as outlined by Morin et al. [187] Pt replacement was conducted in 1 mM H_2PtCl_6. The exact Ni deposition protocol, including deposition parameters such as potential and time, was determined by performing sweep voltammetry Ni deposition/stripping cycles and integrating the Ni stripping current. It was found that 60 seconds of Ni deposition at -0.9V vs. Ag/AgCl resulted in slightly less than 2 atomic monolayer (ML) charge-equivalent of Ni on the Au surface (Fig. 4.2). Charge-stripping experiments performed on Pt-modified gold indicate that, for this protocol, nearly equal amounts of Ni are deposited on the Pt-modified surface as on the clean gold surface. Stripping currents for identical voltage treatments revealed that, on

average, 7% more Ni was deposited on a Pt-modified Au surface than on a clean Au surface. A 2 ML charge-equivalent deposit was used rather than 1 ML due to the fact that H_2PtCl_6 provides Pt^{4+} ions while Ni is replaced and removed from the surface as Ni^{2+} according to the following reaction:

$$Pt^{4+} + 2Ni_{Surface} \longrightarrow Pt_{Surface} + 2Ni^{2+} \qquad \text{(Eq. 4.4)}$$

Additionally, the required precision for a 2ML Ni deposit can be achieved more easily than for a 1ML Ni deposit. This is due to the speed at which the electrodeposit forms, with the first monolayer forming much more quickly than the second, resulting in a wider window in which to terminate the Ni growth for the 2ML deposit than for the 1ML deposit. Due to charge balance, a nominal Pt:Ni exchange ratio of 1:2 occurs during the Pt replacement step. Thus 2 ML of sacrificial Ni is required to result in approximately 1 ML charge-equivalent (ML-EQ) of Pt.

Samples were transferred from the Ni deposition cell to the Pt replacement cell in open air. The transfer was made in less than 10 seconds with a protective wetting of de-aerated Ni Watts solution still present on the sample surface. After emersion from the final Pt bath, samples were rinsed briefly in deionized water and dried in air. Samples were transferred in capped containers from the electrochemical station to the XPS apparatus, and were analyzed without further treatment in the vacuum chamber.

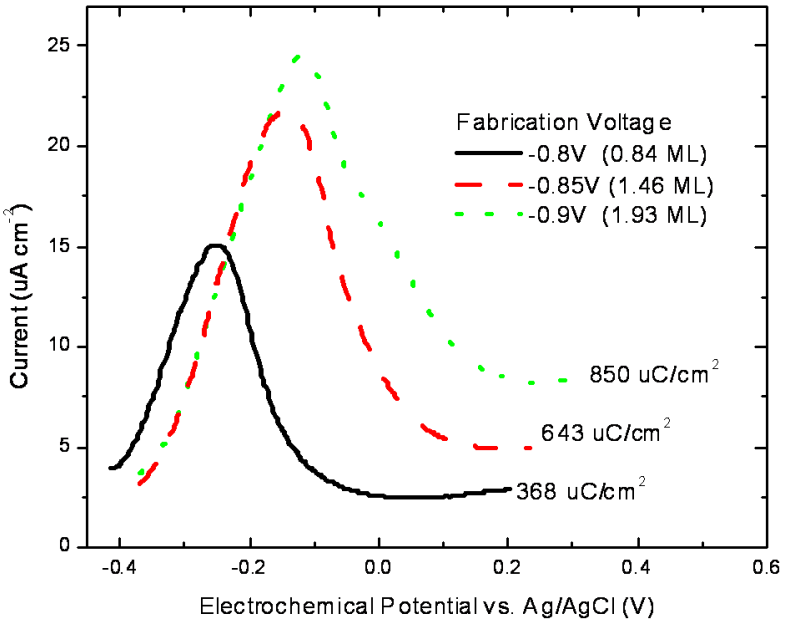

Fig. 4.2: Ni stripping current peaks on polycrystalline Au for three different 60s potentiostatic pretreatment voltages. Listed next to each curve is the total integrated stripping charge for each. Monolayer (ML) charge-equivalents for each voltage are shown in the legend. All stripping was performed immediately after deposition in the same electrolyte.

4.3 Replacement of Ni Adlayers by Pt

XPS and CV analysis were performed before and after single- and multi-layer deposition processes. XPS analysis was performed by comparing the 4f doublets of Pt (74.4 eVand 71.1 eV) and Au (87.7 eV and 84 eV). Surface coverage can be inferred by the ratio of these peak areas after correcting for XPS sensitivity factors. It is worth mentioning here that the Pt spectra for both the 1ML-EQ and 2ML-EQ cases show some peaks that exhibit significant shifts to higher binding energy. These shifts arise from changes in the valency of the Pt film for thicknesses less than 2ML, and have been seen for Pt SLRR growth via Cu sacrificial layers as well. Trace amounts of O and C are also present on the surface. When approximated quantitatively using peak-area analysis, these elements are found to comprise 10 and 15 atomic percent, respectively, in the region sampled by XPS.

Control samples were used to verify that electroless Pt deposition was occurring by replacement of Ni and not by spontaneous deposition on the Au surface itself (Fig. 4.3). Spectra were collected after only Ni deposition, after only exposure to Pt solution, and after a Ni pretreatment followed by Pt exposure. Some Pt XPS signal is apparent without Ni pretreatment; this is indicative of limited spontaneous Pt deposition on the Au surface. The Pt signal resulting from this spontaneous deposition is insignificant compared to that resulting from the replacement reaction and allows us to attribute virtually all increases in Pt XPS signal to the replacement of Ni. It is readily apparent that the Ni 2p peak at 66 eV in Fig. 4.3 disappears after immersion in Pt solution. This suggests that for single repetitions of Pt-replacing-Ni, the residual Ni is negligible and the replacement of Ni by Pt is nearly complete.

It is also worth mentioning that a small component of the Pt evident in XPS analysis is present at a binding energy of 78eV. This peak is indicative of the presence of a small amount of oxidized Pt, either coordinated with Cl or oxygen ligand atoms. We see this peak's presence in Figures 4.3 as well as in Figures 4.4 and 4.6 for single iterations of Ni replacement. It can be seen that this species is then eliminated with further iterations of the growth process. It will be shown in this work that the formation of Pt adlayers with small amounts of oxide/chloride content is deleterious to performance for a range of applications, and the specific mechanism of this species' formation will be explored in depth. For further investigation of this phenomenon, the reader is referred to chapter 5.

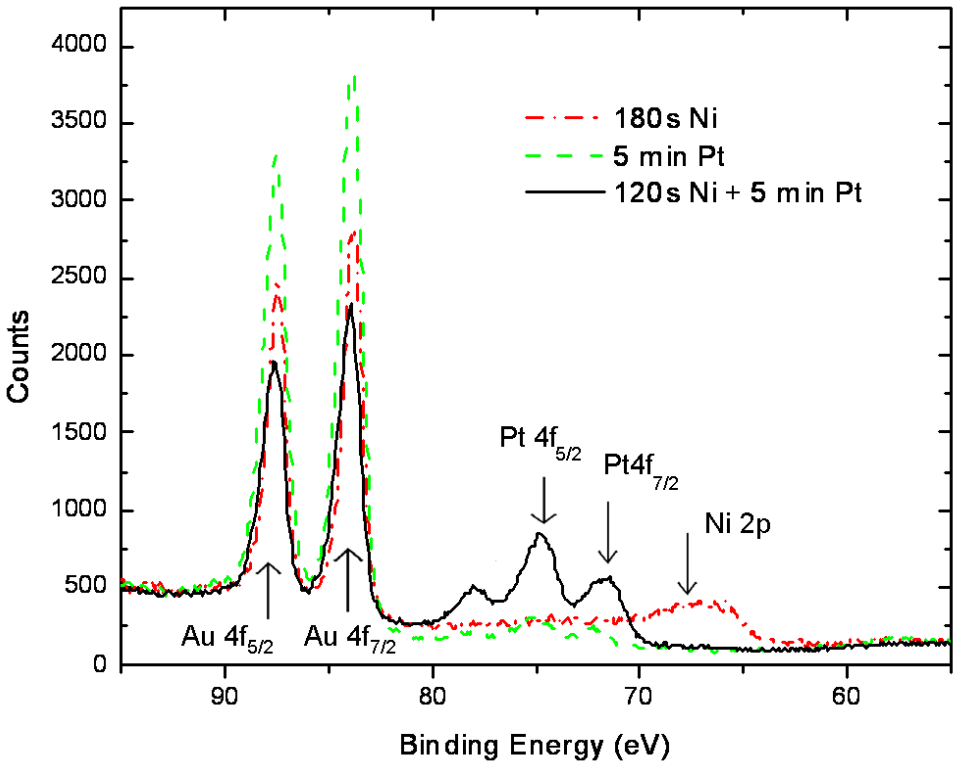

Fig. 4.3: XPS of polycrystalline Au control samples. Ni potentiostatically deposited at -0.9V vs Ag/AgCl for 180s (180s Ni), Pt allowed to deposit at open circuit potential for 5 minutes (5 min Pt), Ni potentiostatically deposited at -0.9V vs Ag/AgCl for 120s followed by 5 minutes Pt exposure (120s Ni + 5 min Pt)

Two methods have been employed to increase the amount of Pt deposited in this study. The first method increases the amount of Pt deposited by increasing the amount of Ni pretreatment, while the second uses repeated replacements of small amounts of Ni. The first is accomplished by increasing the length of time the potentiostatic Ni deposition is performed. Since the amount of Pt deposited is proportional to the amount of Ni present according to Eq. 4.4, increases in pretreatment time should yield increased Pt deposition. XPS spectra resulting from this technique are shown in Fig. 4.4, where a singly replaced 120s Ni pretreatment is compared with two repetitions of Pt replacing 60s Ni pretreatments. The two-iteration method clearly results in more Pt deposited on the surface, although comparable amounts of Ni should have been replaced in both cases. This discrepancy could be caused by increased Pt island formation (corresponding to decreased wetting of the surface) when replacing large amounts of Ni at a time.

The iterative technique employed is similar to that used by Viyannalage et al. to create multilayers of Cu on Au. [181] This technique achieves controlled multilayer thicknesses by repeating the previously described single-layer replacement, one on top of another. After the first replacement reaction, the sacrificial layer is deposited a second time on top of the replacing metal, then immersed in the replacement bath again. This is repeated until the desired number of layers is deposited.

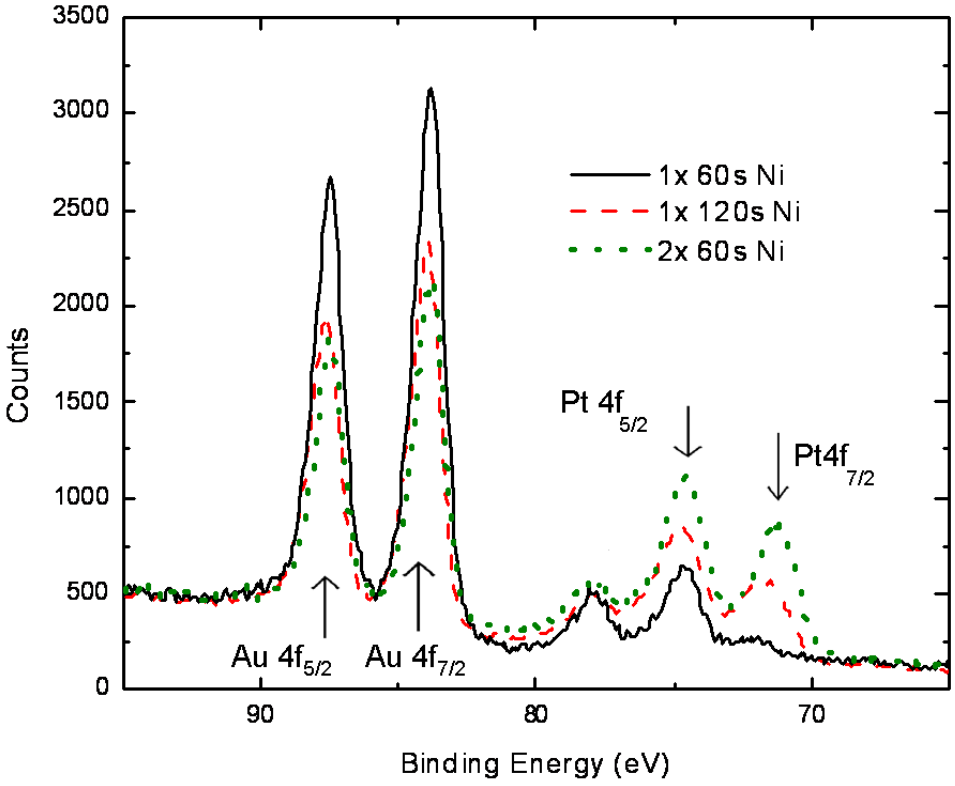

Fig. 4.4: XPS of Pt/Au samples resulting from increasing Ni pretreatments followed by Pt exposure.1 iteration 60s Ni deposition followed by 5 minutes Pt (Solid). 1 iteration 120s Ni deposition followed by 5 minutes Pt (Dash). 2 iterations 60s Ni deposition followed by 60s Pt. (Dotted)

4.3.1 Multilayer Deposition via Repetition of Ni Replacement

Our method repeats the 60s (2 ML charge-equivalent) Ni deposition followed by 60s Pt replacement to create the multilayers. As mentioned previously, XPS indicates minimal residual Ni after a 60s Pt exposure. Even after 8 replacement repetitions, XPS indicates (based on sensitivity-calibrated estimates using Surface Physics software) less than 1 atomic percent of residual Ni in the resultant film. This, combined with charge-integration calibration of the Ni deposition and the replacement charge balance from Eq. 4.4, indicates that each iteration of the replacement process should yield ~1 ML of Pt of the surface. This procedure has been characterized in Figs. 4.2 and 4.3. CV and XPS data were collected for samples fabricated by 1-8 iterations of the replacement process and are presented in Figures 4.5 and 4.6, respectively.

CV was performed as shown in Fig. 4.5 on samples fabricated by increasing iterations of the deposition protocol. CV was initiated at open circuit potential and swept negatively to -0.2V then samples were cleaned by sweeping to 1.3V. The data presented here thus begin at 1.3V, after the cleaning cycle corresponding to one oxidation of the surface. After 1 iteration of the deposition process, we see a marked decrease in the Au reduction peak at 0.9V and the appearance of a Pt peak at 0.39V. This feature at 0.39V has been previously correlated with reduction of Pt sites by Van Brussel et al. [189] Increases in this feature are proportional to the surface area of Pt deposits on the surface of the sample. This indicates significant surface coverage of Pt, blocking Au oxidation/reduction sites. At 3 and 5 repetitions, the Au reduction peak has almost completely disappeared and Pt reduction dominates the profile. The shift in the Pt reduction peak from 0.39V at 1 iteration to 0.43V at 5 iterations is consistent with previous studies on core-shell Au/Pt

nanoparticles [182] and on Pt-modified nanoporous gold [190]. This shift to higher voltages may be indicative of a bimetallic electronic interaction by which oxygen is more easily removed from Pt in intimate contact with Au than from Pt in a bulk phase, such as a foil as depicted in Fig. 4.5 as well. For 3 and 5 iterations “hydrogen waves” between 0V and -0.2V characteristic of Pt are also evident.

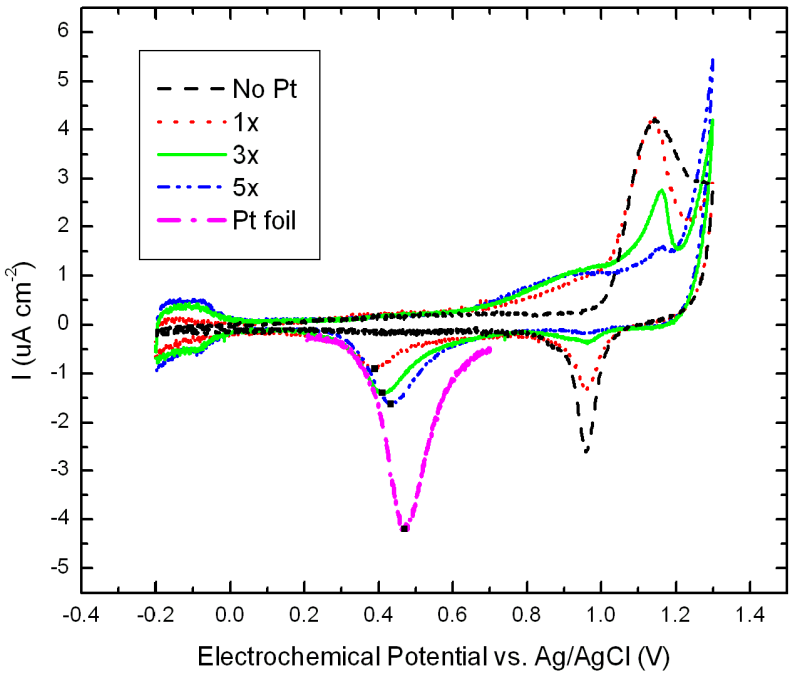

Fig. 4.5: CV of Pt/Au samples with increasing iterations of 60 second Ni potentiostatic deposition followed by 60 second Pt replacement. CV was conducted in 50 mM H_2SO_4. Scans have been normalized to surface area with the exception of the foil, which is shown truncated in increased scale for reference. Minima corresponding to Pt reduction are marked as an aid to the eye.

XPS spectra were collected for the same set of samples. In Fig. 4.6 we see, for increasing numbers of iterations, a significant increase in Pt peak area accompanied with a corresponding decrease in Au peak area. This attenuation of the gold peaks fits a simple model for layer-by-layer growth based on attenuation lengths of photoelectrons in Pt. By comparing the peak intensity of Au 4f photoemission lines with Pt 4f lines, the thickness of the Pt overlayer in nm can be calculated according to Eq. 4.5 as derived by Cumpson and Seah [191]:

$$d = \lambda_{AL} \cos(\theta) \ln(1 + I_A / I_B) \qquad \text{(Eq. 4.5)}$$

Where λ_{AL} is the elastic-scattering-compensated attenuation length, θ is the photoemission angle from normal, and I_A and I_B are the sensitivity-corrected XPS peak areas for the overlayer and substrate, respectively. Sensitivity factors used were tabulated by Wagner et al [192]. Our calculations were performed assuming λ_{AL} for Pt 4f photoelectrons traveling through a Pt matrix. The binding energies of Au 4f and Pt 4f emissions are close enough to each other to allow this approximation to be made. For approximations neglecting absorption by carbon contamination, our results match this type of model to within the limits of reasonable accuracy for the calculation of photoelectron attenuation length. These results have been plotted in Fig. 4.7 along with theoretical thicknesses for multilayers of Pt in face-centered cubic (FCC) crystalline structures. The measured thicknesses match relatively closely with the expected thicknesses. Deviation is attributed to carbon contamination which increases the absorption of Au photoelectron signal, making the Pt overlayer appear thicker than it actually is.

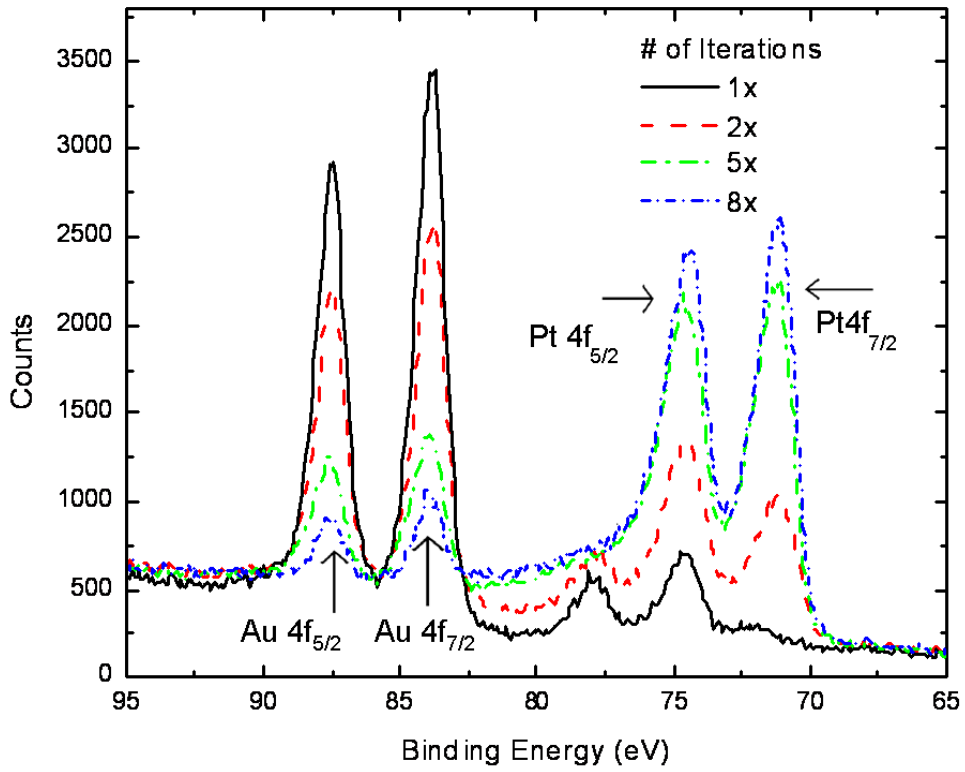

Fig. 4.6: XPS spectra of Pt/Au samples with increasing numbers of Pt/Ni replacement iterations. One iteration comprises a 60 second potentiostatic Ni pretreatment followed by 60 second Pt exposure, with the exception of 1x, which used a 5 minute Pt exposure.

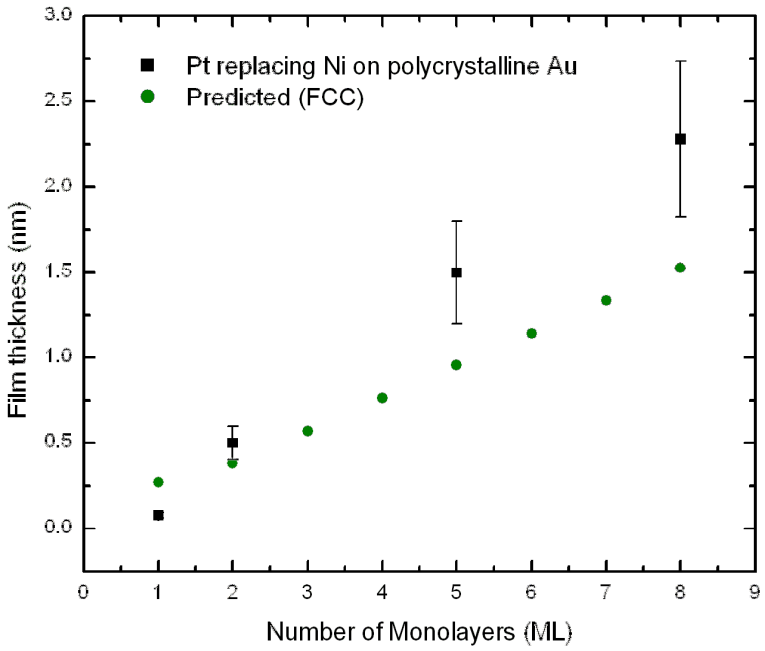

Fig. 4.7: Estimated thickness of deposited Pt film calculated from XPS peak area ratios as outlined above, compared with expected film thickness calculated for close packed layer growth.

4.4 Impact of Ni SLRR

It has been shown that layer-by-layer growth of Pt on Au via redox replacement can be achieved through the galvanic replacement of overpotentially deposited sacrificial Ni bilayers. It is evident from analysis of the XPS data that repeated cycles of Pt monolayer replacement is effective for approximate layer-by-layer Pt deposition. It has also been shown that XPS spectra of the resultant Pt overlayer systems are consistent with established attenuation models used for calculating film thickness.

This constitutes two important improvements for layer-by-layer redox replacement techniques. First, it has been shown that UPD techniques are not required for layer-by-layer redox replacement to be successful. Films grown by replacing well-controlled overpotential 2D-growth systems exhibit comparable structures to those created by UPD sacrificial layers. Second, the use of Ni as intermediary layers increases the number of viable finishing metals that can be deposited using this technique.

CHAPTER 5

PLATINUM OVERLAYERS ON GOLD

5.1 Study of Near-Surface PtAu Chemistry

The study of near-surface electronic and atomic structure is of direct applicability to a variety of devices. This section presents a comprehensive study of the near-surface electronic and atomic structure and outlines the dependency of electrochemical reactivity on these properties. By iteratively growing atomic monolayers and multilayers using an electrochemical technique and studying these films using X-ray spectroscopy and electrochemical methods, the fundamental interactions that govern oxidation state and electron transfer at small length scales near the surface of a Pt-Au bimetallic electrode have been explored. It has been shown that submonolayer coverages of Pt on Au exhibit deviated electronic structure, reactivity, and stability compared to films in excess of two monolayers in thickness. It has also been shown that the surface limited redox replacement technique is subject to a substrate-induced effect which causes the formation of cationic Pt surface complexes. Thus, this section will explore two fundamental properties of the Pt-Au overlayer-substrate system: (1) the substrate-induced formation of partially oxidized overlayers and (2) the effect of electron transfer from the substrate to the metallic component of the overlayer.

Near-surface electron transfer is one of the fundamental properties in bimetallic systems that governs the performance of a wide variety of materials, particularly those used in catalytic applications. Pt in particular is of great interest due to its excellent properties as a catalyst for a wide range of reactions. Previous studies of Pt as a component in a wide range of bimetallic systems, whether alloy or adlayer systems, have

found that these desirable properties may be altered by the presence of a neighboring metal at the nano or atomic scale.[193] The knowledge of these exact changes is important, both to minimize possible negative effects arising from decreased Pt loading as well as to understand possible beneficial behaviors arising from the contact of two dissimilar metals on an atomic scale. This work characterizes both the electronic and atomic structure of ultrathin Pt films on Au supports, and then examines how changes in these properties influence the film's interactions with adsorbed OH^-, ethylene glycol, and carbon monoxide. Scheme 5.1 indicates the changing behavior of the Pt/Au surface observed in this work, with increasing thickness leading to decreased film oxide content as well as enhanced durability and reactivity after a threshold film thickness is achieved.

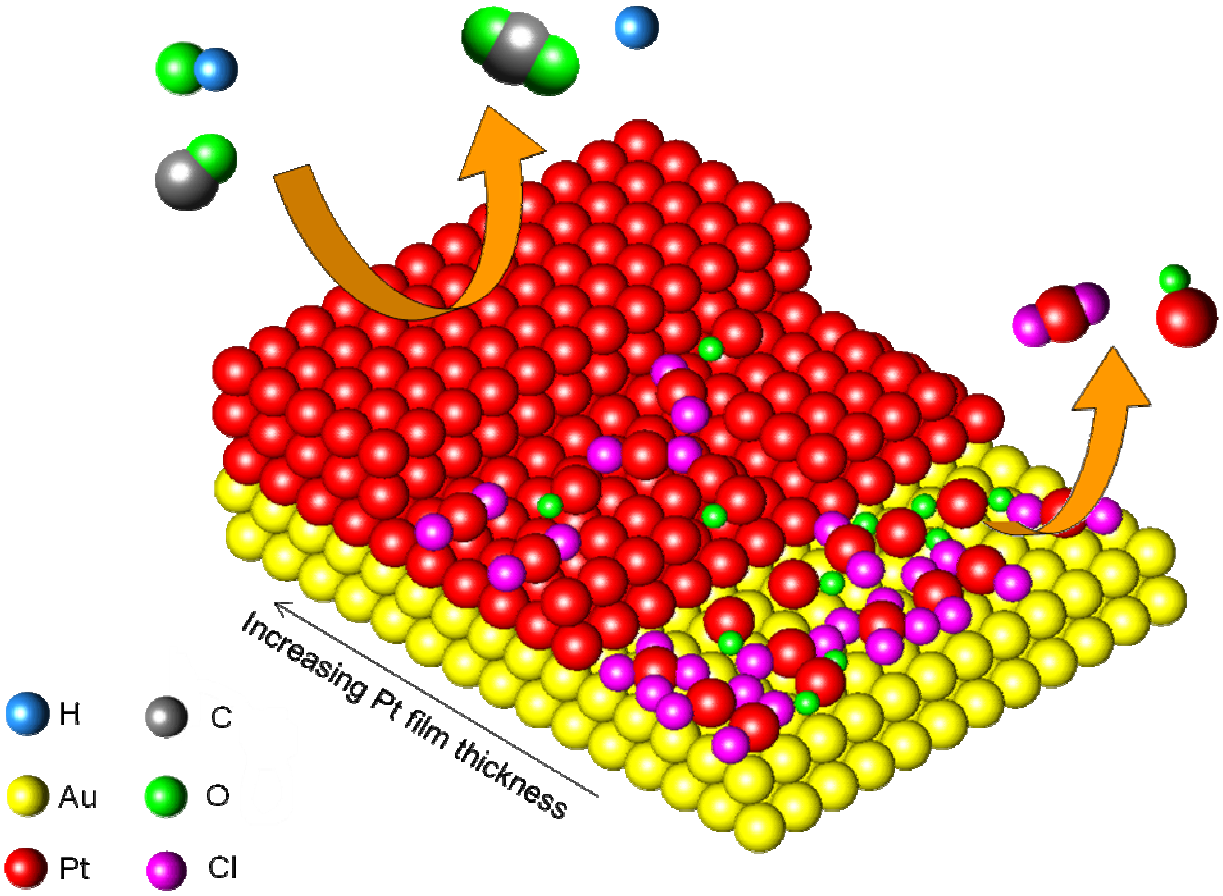

Scheme 5.1: Pt-Au surface for three different thicknesses of Pt, indicating the prevalence of cation-anion complexes for thinner Pt deposits. Reaction arrows (orange) indicate CO electro-oxidation (left) and film dissolution (right).

Two major effects have been reported to influence the surface chemistry of bimetallic systems. The first of these, the bifunctional effect, refers to effects arising from the co-existence of multiple surface reactions occurring at neighboring sites, where reactant molecules may interact with two different components sequentially. The second effect, the ligand effect, describes modification of the electronic structure of the reaction site by nearby atoms which do not play a direct role in the surface reaction. In alloy structures, both of these effects are present, and it is difficult to distinguish between the two. However, by correlating the reactivity of electrode surfaces with the electronic and atomic structure of fully wetted ultrathin overlayers of a variety of thicknesses, the influence of this ligand effect over extremely short distances can be examined. Recent work has focused on the treatment of substrate-overlayer electrochemical systems by theoretical methods [194-195]. This study uses surface limited redox replacement (SLRR) to create Pt-Au adlayer-substrate samples for the electrochemical and spectroscopic observation of the ligand and bifunctional effects at submonolayer-to-multilayer scales.

The two electrochemical equations that are traditionally used to describe the growth of films via SLRR are given in equations 5.1 and 5.2. In equation 5.1, traditional electrodeposition by specifying a growth potential (or sweeping the potential) is performed, with the caveat that the reaction is limited by thermodynamic considerations which create a voltage regime in which a single monolayer or submonolayer is created. This technique is termed underpotential deposition (UPD). In equation 5.2, the precursor layer is exposed to a more noble metal in solution. In this step, the more noble metal is reduced onto the surface in the zero-valent state, with the electrons for this reduction being provided by the oxidation and dissolution of the precursor layer.

$$Cu^{2+} + 2e^{-} \rightarrow Cu \qquad \text{(Eq. 5.1)}$$

$$2Cu + Pt^{4+} \rightarrow Pt + 2Cu^{2+} \qquad \text{(Eq. 5.2)}$$

In this way the amount of noble metal grown is restricted by the (sub-)monolayer of precursor on the surface and by the ratio of the charge on the precursor cation to the charge of the noble metal cation. The procedure can then be repeated iteratively to grow multilayers of the noble metal. This study will show that the above reaction pathway is not accurate to describe the Pt-Cu exchange reaction for very small iteration numbers, with Pt forming cationic species on the surface in these instances. In fact, a recent electrochemical STM study by Brankovic et. al. has found that the Pt-Cu replacement reaction does not always behave according to this model, reporting that it is in some cases possible for the Cu sacrificial layer to dissolve as Cu^{1+} anions rather than Cu^{2+} anions [98]. Thus it is clear that the exact reaction mechanism for the SLRR process is not yet fully understood. This study will examine the changing oxidation state of the SLRR-deposited films as a function of thickness, and also show that the traditional reaction pathway becomes more accurate as the iteration number is increased.

In addition to its use as a fabrication technique for novel catalyst structures, SLRR provides the unique opportunity to probe transitions occurring in materials properties as films are grown from sub-monolayer and monolayer coverages to multi-layer coverages. By characterizing these films at various growth intervals, we can target the transition from thin-film behavior, which is influenced by size and substrate effects, to bulk-metal behavior, which is characteristic of larger deposits. This is a fundamental transition that affects a wide range of surface- or interface-intensive material properties, from chemical sensing to photoelectricity to catalysis. Whether the influence of the subsurface structure

is helpful or detrimental, fundamental knowledge of the tunneling length of sub-surface electrons to the surface atoms is critical. For example, in designed core-shell systems, the resistance of the shell atoms against corrosion will depend on the type of chemical bonding manifest at the surface and the transitions in these chemical bonds from the surface of the material into the bulk. It has been shown that Au/Pt surfaces can have favorable results for the oxygen reduction reaction[196] as well as increased reactivity towards CO oxidation as a result of gold-induced d-band shifts[197]. PtAu alloys have been studied for ethylene glycol oxidation[123, 198] and methanol oxidation[199], which are important reactions for direct alcohol fuel cells[118]. While ethylene glycol is not widely in use as a fuel cell fuel, it is currently under investigation for this application[116-117, 200-201].

Furthermore, an understanding of the oxidation state of the near-surface atoms of functional systems is important as well. Evidence of substrate-induced benefits arising from oxidation state changes is widespread, as several supported catalyst systems enjoy increased performance and durability due to an oxidic character lent to them by their supports[202-203]. Specifically, partially oxidized Pt has been reported to have a high activity towards gas-phase carbon monoxide oxidation [204-205]. The stability of such surface-induced Pt oxides has also been shown to depend strongly on the nature of the substrate on which the Pt is grown[206]. While these effects have been widely reported, it is still difficult to quantify the morphological length scales associated with these bimetallic and substrate-induced effects.

The present study takes advantage of the SLRR fabrication process to study these effects in ultrathin films with a high degree of precision in film thickness at an atomic level. We combine measurements of electrochemical behavior (specifically, shifts in

voltages required to perform characteristic electrochemical reactions) with photoelectron and X-ray absorption spectroscopic studies intended to detect oxidation state changes, atomic structure, and shifts in binding energy associated with changes in surface electronic structure. The present work is based on X-ray photoelectron spectroscopy (XPS), X-ray absorption spectroscopy (XAS) and cyclic voltammetry (CV) data collected for ultrathin Pt layers (from submonolayer to multiple monolayers thick) grown on polycrystalline Au substrates. In addition to CV in blank acidic media, electro-oxidation of ethylene glycol and carbon monoxide was also performed. The layers studied were fabricated by Cu UPD precursor layers galvanically replaced by Pt^{4+} cations.

The data collected indicate two types of deviations from the expected metallic overlayer growth mode. The first deviation occurs for submonolayer growth coverages, and involves the formation of cationic Pt species, while the second deviation is apparent for multilayer growth and appears as a binding energy shift resulting from changes in the electronic structure of the Pt overlayer as a function of distance from the Au substrate. For submonolayer coverages of SLRR-grown Pt, the Pt^{4+} cation is not completely reduced to the zero-valent state but is rather immobilized on the surface in an intermediary complex which still contains the cationic Pt ions. For repeated iterations of the deposition process, this intermediary is then reduced to the zero-valent state during plating of the next precursor layer. The second deviation we identify is trends in the magnitude of the surface core-level-shift (SCS) in the $4f_{7/2}$ photoelectron binding energy of the zero-valent Pt species. We attribute the presence of this shift to the influence of the gold substrate underlayer and trends in the electrochemical behavior of the film,

including electrochemical hydroxide removal from the surface, alcohol oxidation, and carbon monoxide oxidation.

5.2 Theory and Practice of Cu UPD Replacement

Samples were fabricated by plating of controlled sub-monolayer Cu precursor deposits in one cell, followed by emersion of the sample from the Cu bath and immersion in a 1 mM H_2PtCl_6 replacement bath for 10 minutes at open circuit. Coverage of Pt deposits was controlled by use of Cu UPD and manipulation of the emersion potential. Cu UPD is a well-studied process and is known to proceed in two waves, with the first wave depositing 2/3 of a monolayer and the second wave completing the full monolayer coverage[207]. By emersing samples from the Cu bath at a potential between these two deposition waves, we were able to limit the Cu deposit to ~0.6ML per iteration. Due to the 2:1 Pt:Cu replacement ratio, it is possible to determine the Pt loading of a given sample in terms of monolayer-equivalent (ML-EQ) charge, with one iteration of the growth cycle corresponding to 0.3ML-EQ of Pt.

Just as the growth of Ni layers in the previous chapter relied on an applied overpotential, η, for cathodic electrodeposition, the Cu UPD growth here can be described by the underpotential shift, Φ, which is a function of surface Cu coverage in monolayers, Θ. This shift is given as the difference in potential at which bulk Cu is removed from the surface and the potential at which a given percentage of Cu UPD coverage is removed[94].

$$\Phi(\Theta) = E_{Eq}^{Cu} - E_{strip}^{UPD}(\Theta) \qquad \text{(Eq. 5.3)}$$

Where E_{Eq} denotes, as before, the equilibrium potential for Cu in the given experimental conditions, and E_{strip} denotes the potential at which a given portion of the UPD monolayer is removed from the surface during anodic stripping. This phenomenon can be seen in

Fig. 5.1, where Cu UPD occurs in two waves, one corresponding to $\Theta = -.67$ and another corresponding to $\Theta = 0.33$.

Multiple iterations of Pt replacing 0.67ML of UPD-grown Cu were conducted. A typical cyclic voltammetry curve for Cu UPD on Au is shown in Figure 5.1. By removing the electrode from the Cu^{2+}-containing solution during the positive-going sweep at ~250mV vs Ag/AgCl, we strip off all bulk Cu and 1/3 of the Cu UPD monolayer, leaving the surface with only 0.67ML of Cu[208]. The transition from the Cu^{2+}-containing cell to the Pt^{4+}-containing cell was performed in air with a thin film of Cu^{2+} solution still present on the surface. Samples were not rinsed during the transfer from the Cu^{2+} cell to the Pt^{4+} cell to minimize the opportunity for the Cu UPD layer to oxidize en route, but were rinsed in DI water during the reverse transition to minimize drag-in from the Pt solution to the Cu solution. After fabrication, XPS and CV of Au samples with 1 iteration (0.3ML-EQ) through 6 iterations (2ML-EQ) of Pt on the surface were conducted. XAS was conducted for 1ML-EQ and 2ML-EQ films of Pt on Au.

Au samples were either Au-coated glass slides or polycrystalline Au discs polished to 50nm using Buehler alumina suspensions mixed with H_2O_2, then immediately cleaned ultrasonically in DI water and isopropyl alcohol. Solutions were de-aerated using dry nitrogen for a minimum of 10 minutes before being used. The precursor solution was 10mM $CuSO_4$ + 50mM H_2SO_4. The Pt replacement bath used was 1mM H_2PtCl_6 in DI water (18.2MΩ). Voltammetry was conducted using a Pine WaveNow potentiostat and a Solartron 1287 potentiostat with homemade Ag/AgCl reference electrodes calibrated to a commercially available reference. All samples were rinsed in deaerated 1M H_2SO_4 and dried in nitrogen after fabrication. Gasses used were of 99.99% purity (N_2) or 99.9%

purity (CO) and were obtained from Airgas and Sigma Aldrich. XPS data was collected using a high resolution Thermo K-Alpha spectrometer. EXAFS and XANES data was collected at beamlines X23A2 and X18B at the National Synchrotron Light Source, Brookhaven National Laboratory. XAS analysis was performed using Athena, and XPS fitting was performed using XPSPeak software.

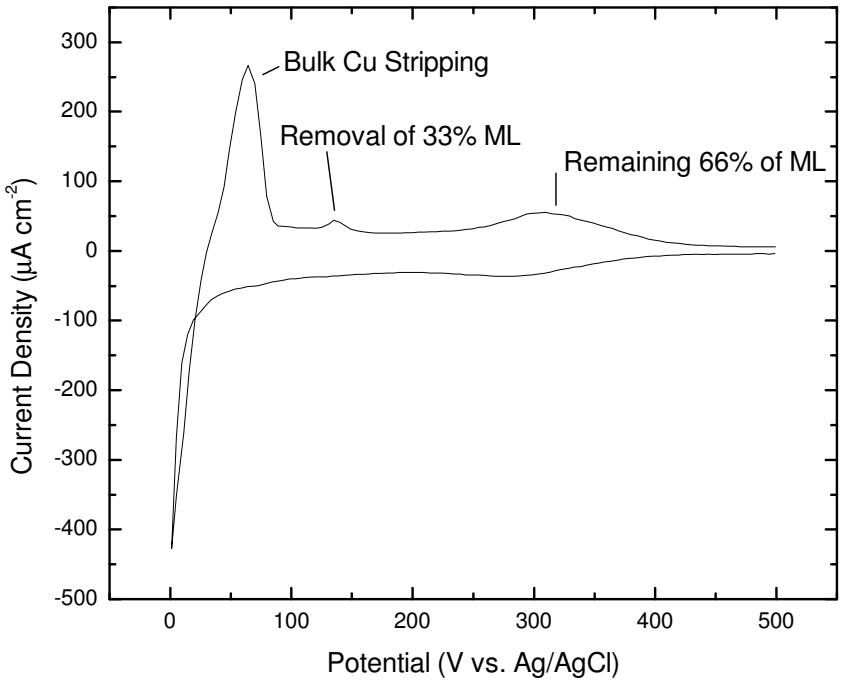

Figure 5.1: Cu UPD on Au polycrystalline electrode. Markers indicate stripping of bulk Cu deposit, followed by stripping of the UPD layer in two waves. Pt SLRR was performed by replacing partial Cu UPD layers grown by terminating the CV between the two UPD stripping waves.

5.3 Film Characterization

Two significant phenomena were observed during film characterization by X-ray techniques. The first is the presence of cationic surface Pt for small iteration numbers of the SLRR process, evidenced in both XPS and XAS, while the second arises from trends in the SCS of the photoemission binding energy of reduced (zero-valent) Pt observed in XPS. In this first section we address the evidence for the existence of the cationic species as seen in the XPS and XAS data. In the second section, we address the SCS trends seen in XPS, which arise as a result of substrate-film electronic interactions.

5.3.1 Evidence for Cationic Pt Intermediaries:

Figure 5.2 contains the XPS spectra of several different coverages of Pt grown on Au using the SLRR method. Two reference curves provide spectra for Pt^{4+} (PtO_2, H_2PtCl_6) and one reference curve for metallic or zero-valent Pt. Based on these reference spectra and previous work (see Table 5.1) we determined the coexistence of various oxidation states of Pt in the SLRR-grown film. The known position of metallic, or zero-valent, Pt (71eV and 74.3eV) is indicated by vertical lines coincident with peaks for Pt reference foil. For the spontaneously grown curve, multiple features are apparent at various binding energies, indicating the simultaneous presence of Pt^{4+}, Pt^{2+}, and minimal metallic (zero-valent) Pt. It is apparent that the overall quantity of Pt on the Au surface increases with increasing iterations. For the 0.3ML-EQ curve, we see the same features present in similar proportions between the different valencies. After the growth of the second SLRR deposit (0.6ML-EQ), all three species are still present but the Pt^{2+} and metallic species have become more predominant. After the third deposition, we see the elimination of the Pt^{4+} species and the Pt^{2+} species is present as only a shoulder on the

metallic peaks. After six iterations, there is a very small amount of Pt^{2+} present as a non-resolvable shoulder and the majority of signal arises from the reduced Pt.

The iterative accumulation of Pt on the Au surface can be better visualized in Figure 5.2b, which shows XPS difference spectra for the same set of samples (excluding references). Difference spectra were calculated by subtracting the spectrum for a given monolayer-equivalent from the spectrum for the following coverage. The '0.3ML-EQ-spont' curve indicates that Pt growth between 0.3ML-EQ and the spontaneous reference occurs in the metallic (70.8eV and 74.1eV) as well as cationic (72.2 and 75.6, 74.0 and 77.1) regimes. The '0.6ML-EQ-0.3ML-EQ' curve indicates mostly growth in the metallic regime, with small increases in cationic species. The '1ML-EQ-0.6ML-EQ' curve indicates removal of cationic species (negative portions of the curve) and an increase in metallic content. Finally, the '2ML-EQ-1ML-EQ' curve indicates that the overall addition of the fourth through sixth iterations is primarily metallic.

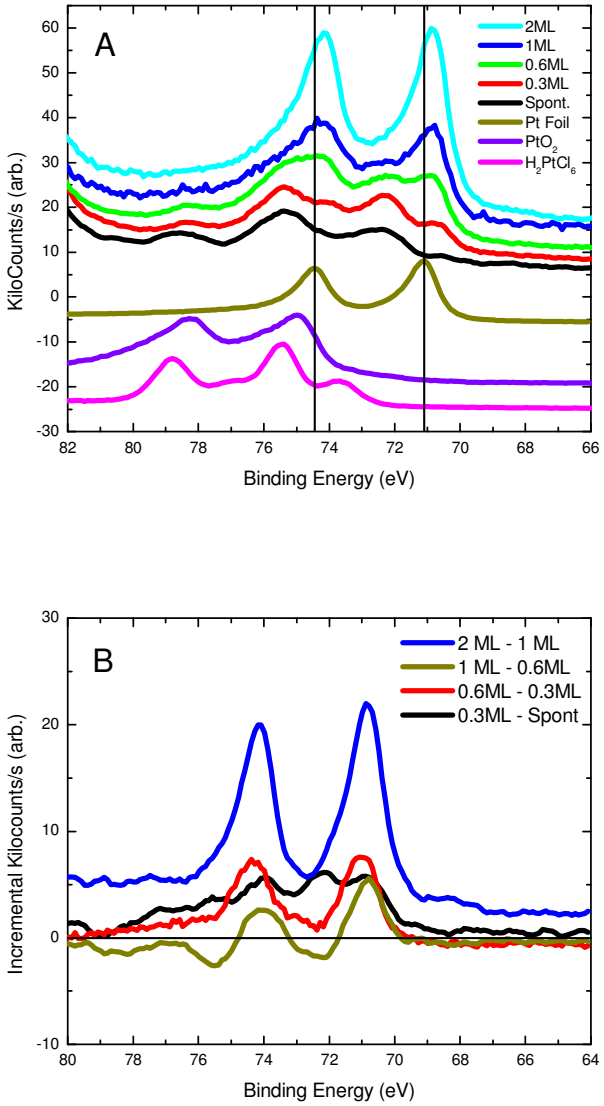

Figure 5.2: (a) Pt 4f XPS spectra of reference materials and series of SLRR-grown samples on Au substrates. Vertical lines correspond to the location of bulk Pt foil reference. (b) Pt4f XPS difference spectra for SLRR-grown Pt on Au substrates. The legend indicates how the difference calculation was performed, with each curve indicating incremental increase in Pt with following iterations.

Table 5.1: Pt photoemission binding energies for each sample/reference.

	Metallic		Pt^{2+}		Pt^{4+}	
	$4f_{7/2}$	$4f_{5/2}$	$4f_{7/2}$	$4f_{5/2}$	$4f_{7/2}$	$4f_{5/2}$
H_2PtCl_6 (IV)	N/A	N/A	73.6	77.0	75.4	78.8
PtO_2 (IV)	N/A	N/A	N/A	N/A	74.9	78.2
Spontaneous	70.47	unresolved	72.3	75.4	75.4	78.5
0.3ML-EQ SLRR	70.65	74	72.3	75.3	75.3	78.3
0.6ML-EQ SLRR	70.81	74.2	72.3	75.4	75.4	78.3
1 ML-EQ SLRR	70.78	74.2	72.3	75.4	75.4	78.3
2 ML-EQ SLRR	70.85	74.2	72.3	75.4	N/A	N/A
Pt foil (bulk)	71.1	74.4	N/A	N/A	N/A	N/A

One possibility that was considered when determining a possible reaction pathway that might result in the observed intermediary was that the Pt^{4+} and Pt^{2+} species were arising on the surface only from spontaneous adsorption on exposed gold sites and not from exchange with the precursor Cu. Pt^{4+} has been previously shown not to fully reduce in some previous studies[209-210]. At first this theory was enticing because the formation of these two cationic species is suppressed with increasing Pt coverage and decreasing Au surface area. This hypothesis was disproven by comparing XPS difference spectra (Figure 5.2b) with known coverage values determined electrochemically (Figure 5.5) and determining that the amount of cationic species grown did not decrease proportionally to the electrochemically active Au surface area. We calculated difference spectra by subtracting Pt4f spectra for a given SLRR iteration from the spectrum for the subsequent iteration (i.e. subtracting the 0.3ML-EQ spectrum from the 0.6ML-EQ spectrum) to determine the exact contribution of the subsequent growth step to the Pt species present on the surface. In this manner the curves in Figure 5.2b can be viewed as the incremental addition to the Pt species present caused by each iteration of the deposition cycle.

When analyzing Figure 5.2b, it is important to remember that reduction of the cationic intermediaries during the Cu precursor deposition is inherent to the SLRR process. In this way it is possible for both the first and second iterations to create Pt^{4+} species and still show relatively little signal in the difference spectrum (because the Pt^{4+} created in the *first* iteration was eliminated during the *second* iteration's precursor growth, then replaced during the Pt-Cu exchange). This process is illustrated in equations 5.4-5.6, where L is an unidentified complexing anion such as O^{2-} or Cl^{-}. Residual traces

of both oxygen and Cl have been detected in XPS (not shown) and we do not attempt to identify the exact Pt complex formed on the surface.

$$Cu_{so\ln}^{2+} + 2e^- \rightarrow Cu_{ads} \qquad \text{(Eq. 5.4)}$$

$$2Pt_{so\ln}^{4+} + 4Cu_{ads} + 3xL^{y-} \rightarrow 2x(L^{y-})Pt_{ads}^{4+} + x(L^{y-})Pt_{ads}^{2+} + 4Cu_{so\ln}^{2+} \qquad \text{(Eq. 5.5)}$$

(2nd Iteration): $Cu_{so\ln}^{2+} + Pt_{ads}^{4+} + Pt_{ads}^{2+} + 8e^- \rightarrow 2Pt_{ads} + Cu_{ads}$ (Eq. 5.6)

By examining the 0.3ML-EQ and 0.6ML-EQ curves in Figure 5.1b, we see that for the first two growth iterations, cationic as well as metallic Pt is being added to the surface. This means that the cationic growth is not restricted to Au sites but is actually promoted by the presence of the initial Pt deposit. After the third iteration, we see the elimination (negative portions of the curve) of most of the cationic features at 75.4eV and 78.3eV corresponding to Pt^{4+} as well as further growth in the metallic regime (70.8eV and 74eV). No change is observed in the Pt^{2+} region, which indicates that for the third iteration of growth, Pt^{2+} ions are still being created (since the previously grown Pt^{2+} species were reduced during the third iteration's precursor growth). The final curve in Fig. 5.2b indicates the difference spectrum between 6 iterations and 3 iterations. It is readily obvious that primarily metallic Pt is being added to the surface, although a small shoulder indicates that some Pt^{2+} may still be formed. When considering that the majority of Pt signal is metallic, it is still important to note that the zero-valent Pt grown in these cases is shifted negatively from the foil reference. These shifts are all measured from the actual XPS spectra (Fig. 5.2a) and not from the difference spectra, which may be distorted due to overlapping cationic peaks. These negative shifts arise from SCS-induced deviation from bulk behavior and will be addressed in the following section.

Figure 5.3a provides a direct comparison of XPS spectra for 0.3ML-EQ of Pt growth, both as-grown (I) and after potentiostatic reduction at 0V vs Ag/AgCl in 1M sulfuric acid (II). The application of a reducing voltage, in addition to lowering the formal oxidation state of the Pt ad-atoms, also removes anionic species such as Cl^- and O^{2-} from the surface and has the potential to rearrange the Pt atoms remaining on the surface. CV of Pt-Au samples after the reduction step was comparable to that of the as-grown Pt-Au samples. This suggests that the reduction step at 0V is not responsible for any serious degree of rearrangement of the surface adataoms.

Also shown here are fitted spectra representative of the fitting process employed. Figure 5.3b tracks the peak binding energy of the primary metallic Pt feature, the $4f_{7/2}$ emission, for the series of samples shown in Figure 5.2a. Despite the prevalence of cationic Pt for the spontaneous deposit and the lower iteration numbers of SLRR fabrication, a small amount of metallic Pt is present in all samples and allows the measurement of the $4f_{7/2}$ binding energy. Just as we tracked the presence of cationic Pt species based on positive binding energy shifts, we are able to track the presence of metallic Pt species exhibiting SCS effects by the negative binding energy shift of the metallic peak relative to its bulk position. For the spontaneous deposit, the zero-valent Pt photoemission deviates from that of bulk Pt by -0.65eV. With increasing SLRR iterations, we see a clear trend with this deviation decreasing as the zero-valent photoemission feature shifts towards the binding energy characteristic of bulk Pt. Additionally, we see that the growth of one SLRR cycle onto a bulk Pt sample shifts the binding energy of the zero-valent component of the photoemission negatively.

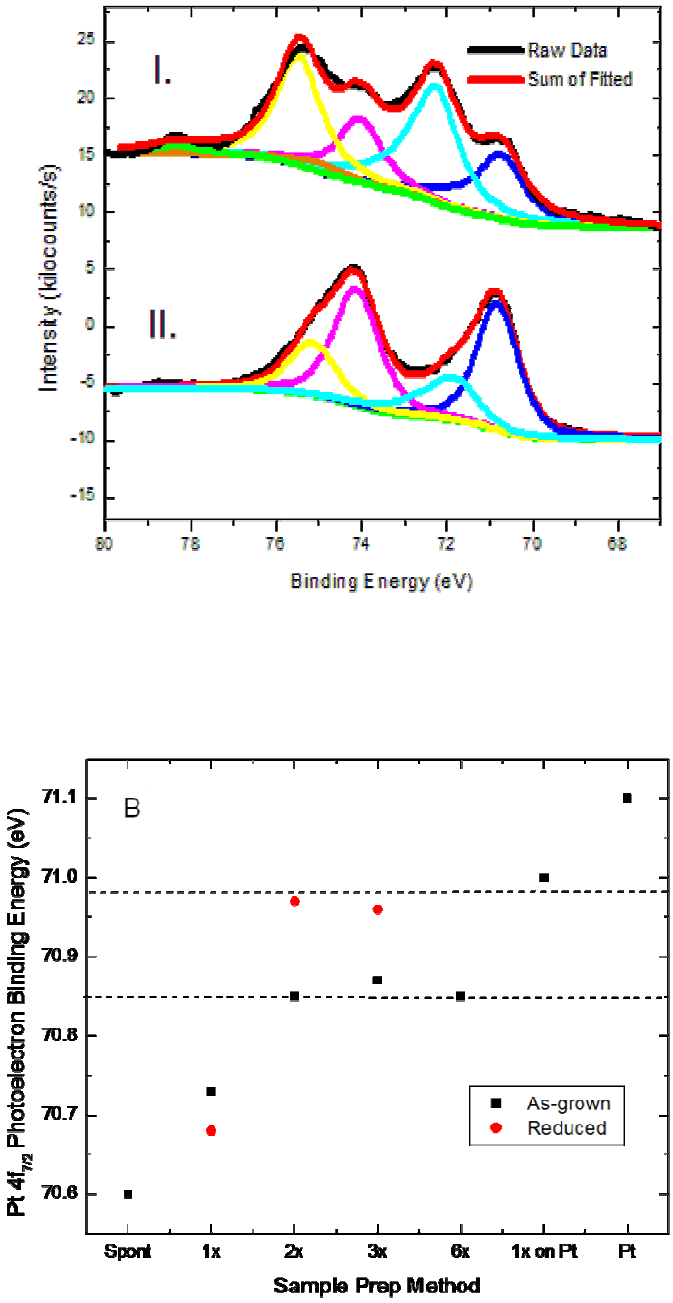

Figure 5.3: (a) Example fitted spectrum for one iteration of Pt grown on Au before (I) and after (II) electrochemical reduction. (b) $Pt4f_{7/2}$ binding energy for SLRR samples as grown and reduced on Au and Pt, compared with references for spontaneous growth on Au and untreated Pt foil.

Further evidence for the presence of cationic Pt species can be seen in the XAS analysis (Figure 5.4), which confirms the XPS result indicating the presence of cationic Pt for small iteration numbers of the SLRR process. Figure 5.4a presents the Pt L3-edge EXAFS spectra of the reference materials H_2PtCl_6, K_2PtCl_4, PtO_2, and Pt foil. Figure 5.4b plots the same type of data for 1 ML-EQ and 2 ML-EQ of SLRR growth. All data are plotted in real space after being Fourier transformed in ATHENA. Two curves are provided for each of the monolayer samples, representing the as-grown state and the same sample after electrochemical reduction at 0.0V in H_2SO_4. Note that the Fourier transforms here are not phase-shift corrected since this type of correction would require an assumption of the identity of the first scatterer. For both the 1ML-EQ and 2ML-EQ samples, significant deviation in first-neighbor location peaks compared to metal foil are seen. This type of shift has in the past been assigned as Pt-anion bonds by other researchers[211-212]. In this case the shift may arise from a combination Pt-O bonds or Pt-Cl bonds. Pt-O bonds have been previously reported at 2.0Å, with Pt-Cl bonds reported at 2.2Å and Pt-Pt bonds at 2.77Å. It is important to remember that our EXAFS spectra reported here are not phase-shift corrected, which explains why the reference spectra shown here deviate from that seen in literature. As a simple analysis, it is enough to accept the shifts observed here in the location of the first EXAFS peak as evidence for cationic surface Pt. However, since the same processing parameters were used here for both the reference samples and the SLRR samples, we are able to make a direct fingerprinting comparison between both sets of data and attempt to identify the type of Pt structures being created on the SLRR-grown surfaces.

Figure 5.4c shows the same Pt L3-edge spectra in the XANES region for the same set of SLRR and reference samples. We can clearly see the differing intensities of the white lines corresponding to different film growth and treatments, with the 1ML-EQ as-grown sample exhibiting the most intense white line. The rest of the SLRR-grown samples are similar in white line intensity to the Pt foil, but a trend is seen from most intense to least intense white line: 1ML-EQ, 1ML-EQ (reduced), 2ML-EQ, 2ML-EQ (reduced). As expected, the PtO_2 and H_2PtCl_6 reference exhibit more intense white lines, only being exceeded in intensity by the as-grown 1ML-EQ sample. Since the white-line intensity is related to d-band occupancy, this data will be examined in the next section on substrate-film electron transfer.

By utilizing the dashed vertical lines in Figures 5.4A and 5.4B, we have simple markers for the location of first neighbor shells for Pt-O, Pt-Cl, and metallic Pt-Pt bonds. It is clear from qualitative examination that the as-prepared 1ML-EQ SLRR sample exhibits a shorter first neighbor distance than any of these lines. This indicates the possibility of a compressed defect-type oxide on the surface with both Cl and O present. This is supported by the presence of Cl and O in the XPS spectra. Meanwhile, the as-prepared 2ML-EQ sample exhibits a first-neighbor distance close to that of Pt-Cl bonding, although the peak itself is broad enough not to preclude any Pt-O bonding from also being present. After the electrochemical reduction step, it is apparent that the 2ML-EQ Pt deposit has converted to FCC Pt similar to that in the bulk foil, while the first peak of the 1ML-EQ deposit still shows a significant shift to lower interatomic distances, indicating the presence of residual oxides. The increase in resonance intensity when going from the 2ML-EQ as-prepared sample to the 2ML-EQ reduced sample indicates a

significant increase in ordering of the deposit. On the other hand, it is apparent that the reduced 1ML-EQ deposit is still dominated by the residual oxide feature, indicating that no such ordering of the metallic phase has occurred.

Even though XPS has indicated that the 1ML-EQ and 2ML-EQ deposits are dominated by zero-valent Pt, these oxide-type signals in the EXAFS data are not unexpected. XPS has also indicated that trace amounts of Pt oxides are present for all thicknesses of deposit up to 2ML-EQ, with 1ML-EQ showing the presence of 2+ and 4+ oxides, while the 2ML-EQ deposit evidences only 2+ oxide. The dominance of the oxide signal in the Fourier transformed EXAFS data, despite its presence in relatively lesser amounts compared to the metallic signal in XPS, can be explained by the existence of a high degree of order in the oxide phase, while the metal phase exhibits a large degree of disorder. This disorder is then removed (along with some of the oxide itself) during the electrochemical reduction step, causing the Pt-Pt bonds of the metallic phase to begin to dominate the Fourier transformed EXAFS spectrum. The fact that the 1ML-EQ deposit could not be converted fully to a metallic-type atomic structure while the 2ML-EQ deposit was able to indicates a fundamental difference in the type of Pt growth occurring in the two regimes. We suggest that the inability to convert the 1ML-EQ deposit to bulk-type structure is due to a combination of substrate-induced effects and lattice distortion arising from the extremely thin nature of the deposit.

5.3.2 Evidence for Substrate-Induced Electron Transfer

The trend in zero-valent Pt $4f_{7/2}$ binding energy location mentioned earlier (and seen in Figure 5.3b) manifests as a shift in peak location to more negative binding energies. This negative shift in the metallic $Pt4f_{7/2}$ is largest for small iteration numbers (-0.65eV), but even for larger iteration numbers of the SLRR fabrication process, at which point all cationic Pt has been removed, there is still a deviation of -0.2eV from bulk-type photoemission spectra. In addition to the cationic features at higher binding energies as seen earlier, the zero-valent features are shifted negatively from that of bulk Pt, similar to a Pt-Au alloy. However, we conclude that this surface is not forming a surface Pt-Au alloy because the Au 4f photoemission (not shown) does not shift or broaden, as would be expected for an alloy. It has long been known that metals such as Au and Pt exhibit surface core-level shifts (SCS) on the order of 0.3eV to 0.5eV for the near-surface atoms, due to variation in coordination number compared to the bulk structure [162, 213-214]. It has also been shown that trends in the SCS of a material can be correlated with trends in the d-band center[134]. For bulk structures and traditional non-synchrotron X-ray sources, the influence of this feature is minimal as it is convoluted with the bulk photoemission spectrum. For our SLRR-fabricated samples, however, the Pt detected is exclusively in the near-surface regime and thus exhibits a minimum SCS of -0.2eV at 6 and 3 iterations of the growth process. For 1 iteration and spontaneous growth, this shift increases to -0.65eV. This trend in the SCS indicates that the sub-monolayer structure of the Pt ultrathin layer also plays a role in the photoemission binding energy. An example of this type of fitting is given in Figure 5.2a. The unfitted spectral features can be seen in Figure 5.2a, but are more easily analyzed when viewed as trends in Figure 5.3b.

In order to discern the extent to which the Au substrate is active in this process, we also performed one iteration of SLRR growth on a Pt substrate. It was found that this shifted the emission line negatively as well, but not to the extent seen on the Au substrate. This indicates that the anionic shift is a result of two separate effects working together, one dependent on the Au substrate, and one dependent on the arrangement of the deposit itself. For the single iteration growth on Au, both of these effects are present. For the single iteration performed on bulk Pt, only the effect induced by structural distortion of the deposit itself is present. If we attribute all of the changes in binding energy for layers grown on a gold substrate to changes in the SCS, we can conclude that the submonolayer deposit exhibits the largest d-band variation and that this deviation decreases as the layers increase in coverage and thickness. Unfortunately, this neglects the distortion- and structure-induced effects inherent in this method of film growth and does not correlate well with the Norskov d-band model for Pt monolayers on Au surfaces, which suggest that the 1 ML-EQ deposit should exhibit the largest d-band deviation (and corresponding SCS deviation)[197]. Thus we conclude that the structural effects and d-band/SCS effects both play comparable roles in the determination of photoemission binding energy for these films. Unfortunately, further deconvolution of the two effects is difficult to conduct based only on XPS data, so we must examine the XANES spectra, which provide another avenue towards understanding the metal d-band.

The analysis of the white-line intensity at ~4eV in the XANES spectra (Fig. 5.4b) allows us to qualitatively examine the occupancy of the Pt d-band directly. It is known that the intensity of the Pt L3-edge white line (after normalization to the total amount of Pt present) scales with increasing vacancies in the Pt d-band [56]. Thus, we would expect

oxides or cationic Pt species to exhibit more intense L3-edge white lines. This is exactly what we observe in the current XANES spectra, with a large decrease in d-band vacancy upon the initial reduction of the 1ML-EQ deposit. However, it is important to remember that the XPS data for the as-grown 1ML-EQ deposit indicated relatively little cationic species present, with only small shoulders for Pt^{2+} and an anionic shift in the location of the Pt^0 photoemission. We see further reductions in d-band vacancy with further monolayer growth, trending towards characteristic spectra for Pt foil. Although the extremely intense white line is only exhibited for the as-grown 1ML-EQ deposit, the as-grown 2ML-EQ and both reduced samples still exhibit increased d-band vacancies relative to the Pt foil. This is to be expected, as predicted by the previous work of Norskov, in which the Pt d-band is susceptible to both strain effects and ligand effects.[113, 134] In fact, the unique d-band properties of the first monolayer of Pt on Au have been predicted as well. Thus these results agree with the findings of Pedersen et al, which predicted that the first monolayer of Pt on Au would exhibit a distorted d-band compared to the second and following monolayers[195]. However, the degree of d-band distortion is significantly reduced after electrochemical reduction. This observation, combined with the EXAFS analysis that indicates restructuring of the film during the reduction step, indicates that the SLRR process creates a unique surface arrangement of Pt that induces unique electronic properties.

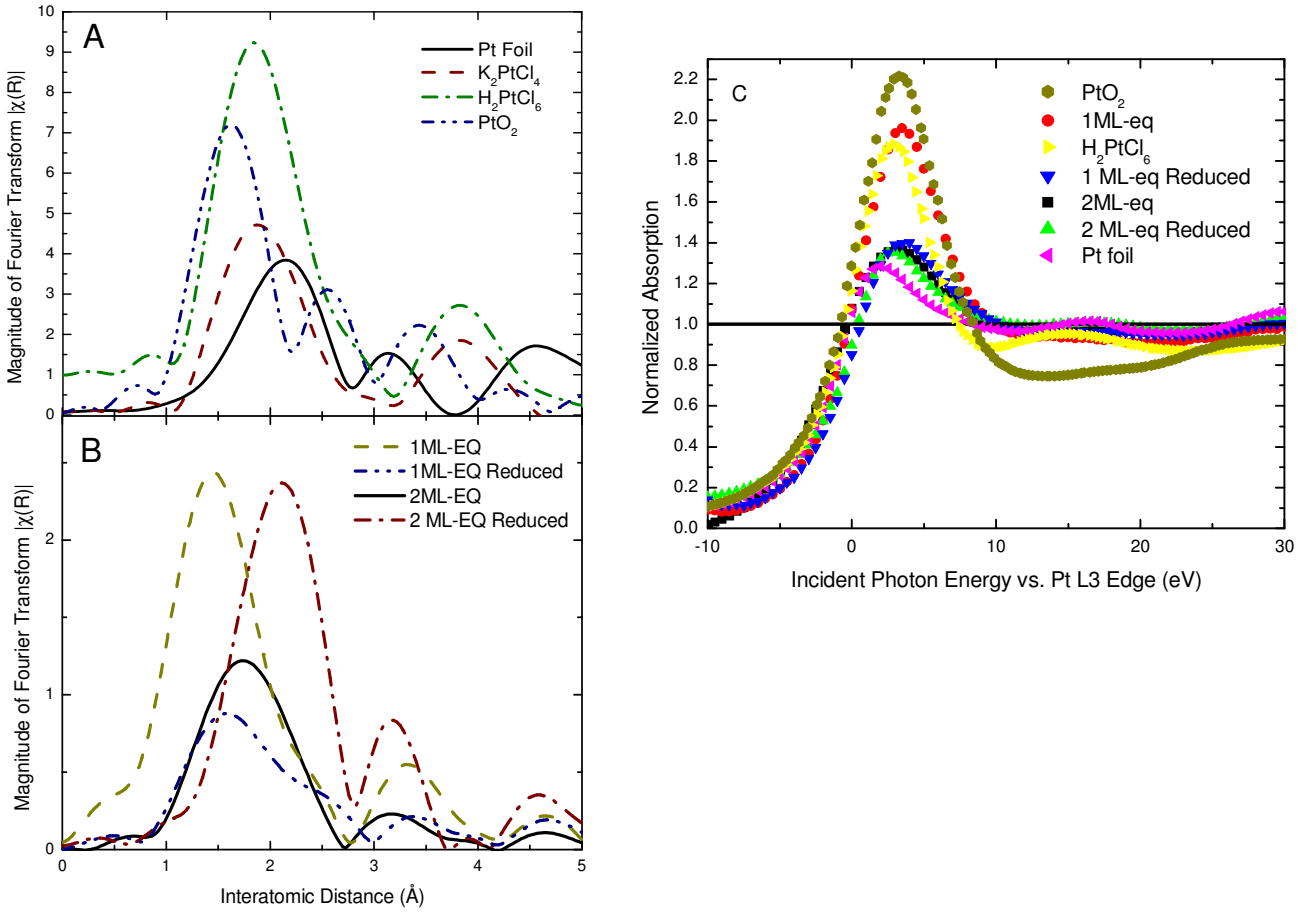

Figure 5.4: (a) Normalized Fourier transformed X-ray absorption data in real space.

(b) XANES spectra for the SLRR and reference samples

In summary, the various X-ray spectroscopic techniques employed above have allowed a series of conclusions to be reached regarding the Pt SLRR film on a Au surface. It has been shown that the SLRR process, for very small iteration numbers, creates a distorted cationic surface complex that contains both Pt-O and Pt-Cl bonding. Furthermore, the fully reduced metallic Pt that forms in these structures displays disordered atomic structure as well unique electronic properties, showing significant shifts in its d-band center (as inferred from the SCS) and occupancy (from the XANES white-line intensity). These two effects suggest that the thinnest (submonolayer) Pt deposits on Au show an increased propensity to oxidize by complexing with either oxygen or chlorine, and also that the remaining Pt atoms which are formally zero-valent exhibit deviated electronic structure due to both vertical electron exchange with the substrate as well as lateral electron transfer with neighboring oxidized Pt.

5.4 Film Reactivity & Durability

In this second section, the interaction of the Pt films with various liquid phase reactants (CV in H_2SO_4 with and without CO and ethylene glycol) is addressed.

5.4.1 OH^- Affinity

Cyclic voltammetry performed in 1M H_2SO_4 is shown in Figure 5.5. Voltammetry was initiated at open circuit potential and scanned negatively to 0V before cycling began. In addition to the simple determination of Pt surface coverage (which can be determined by examining decreases in the Au oxide reduction peak at 1.0V), the CV in Figure 5.5 further support for the revised SLRR process suggested in the previous section. An initial reductive sweep is presented for the 1ML-EQ case, indicating reduction of surface-confined cationic Pt intermediaries at 0.24V (Arrow 1). These surface oxide species are likely the same as the Pt^{2+} and Pt^{4+} cationic intermediaries detected in XPS and XAS. This reduction step occurs once initially and is not repeated during further oxidation cycling. The following oxidation/reduction cycles for the remaining samples (0.3ML-EQ through 3ML-EQ) allow us to analyze the electrochemical behavior of the ultra-thin Pt layers after this initial reduction of these intermediaries.

Most interestingly, Figure 5.5 illustrates an effect that we have previously reported[1] but now explore in more detail, the shift of the oxide/hydroxide reduction feature to more negative voltages for ultrathin Pt deposits iterations. It has been previously shown that reductive voltage sweeps of a bulk Pt electrode after oxidation to 1.5V result in shifted reduction peaks compared to oxidation treatments at lower voltages. The reduction peak after 1.5V oxidation corresponds to OH^- desorption from the surface.[215-217] We demonstrate this feature here for bulk Pt as well as varying coverages

of Pt SLRR on a Au surface. For the 1 iteration case, we see a -160mV deviation in the applied voltage required to strip adsorbed OH^- from the surface compared to bulk Pt. Since overpotentials are measured in the negative direction for reduction processes, this means that an additional 160mV must be applied to the Pt(0.3ML-EQ)/Au electrode compared to the bulk Pt electrode in order to remove the adsorbate (in this case OH^-). Interestingly, for the 1ML-EQ and greater cases, this deviation decreases, although we still see some overpotential required when compared to bulk Pt, with the 1ML-E and 2ML-EQ cases exhibiting a 50mV shift from the peak location for bulk Pt.

The presence of this shift indicates that for up to 6 iterations of the growth cycle, OH^- is more difficult to remove from the SLRR surface than from a similarly treated bulk Pt surface. Furthermore, the submonolayer 0.3ML-EQ deposit showed evidence of a Pt specied with an even greater Pt-OH^- bond strength. These two desorption potentials can be thought of as corresponding to distinct Pt surface species: one species that is thinly coated as a submonolayer across the surface and requires added potential to strip OH^-, and a second species that has agglomerated to a sufficient thickness that it behaves more similarly to bulk Pt. Even at this point, however, a small additional voltage required to remove OH^- is still present. Of these two species, it is likely that the species that displays a greater affinity for surface OH^- is the same species which displays negative binding energy shifts in XPS and structural deviation from metallic in XAS, even after electrochemical reduction. It will be shown in the following sections that these two different species exhibit further deviations from bulk Pt in their performance in durability and CO electro-oxidation testing, largely as a result of their affinity for OH^- groups.

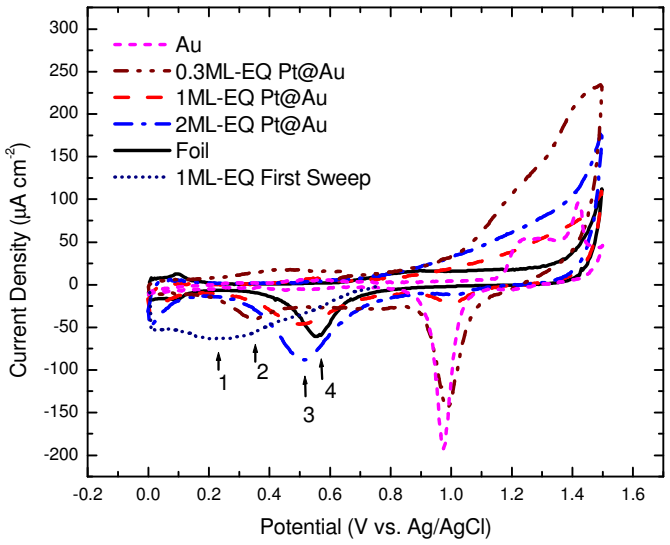

Figure 5.5: Cyclic voltammetry in 1M H_2SO_4 of Au, Pt, and samples with between 0.3ML-EQ and 2ML-EQ of Pt. Also included is a representative initial reductive sweep, starting at open circuit potential, to illustrate transient reduction of intermediary cationic Pt species (Arrow 1). Reduction of oxidic species at Au sites occurs near 1.0V and can be seen to decrease with increasing Pt coverage. Reduction of Pt oxides at submonolayer (0.3ML-EQ) Pt sites (Arrow 2) occurs at 0.35V and shifts positively to 0.52V for thicker deposits (Arrow 3). Reduction of hydroxides from bulk-type Pt occurs for Pt wire at 0.56V (Arrow 4).

5.4.2 Durability During Electro-oxidation of Ethylene Glycol

It is also instructive to consider the effect that the deviations in electronic and structural properties of the Pt film have on the durability of the Pt film. Since the films have already been shown to have an increased affinity for OH^- adsorbates on the surface, a strong base environment of 1M NaOH solution was chosen to explore this relationship in more detail. Ethylene glycol oxidation is an excellent probe reaction for determining Au/Pt surface coverage due to the large voltage shift between oxidation at Pt sites and at Au sites. In contrast, methanol oxidation only proceeds in the voltage regimes examined on Pt sites. For Figure 5.6a, we see a large (390mV) difference in reaction voltage for Pt sites (-0.18V), and Au sites (0.21V). We see in Figure 5.6a that the initial curve shows a majority of reaction occurring on Pt sites, while the reaction on Au sites increases slowly with further oxidation cycling, indicating that Au sites are becoming re-exposed and available for adsorbate electro-oxidation reactions.

To facilitate the processing of the CV data, a custom script was written in Python programming language that is able to identify the maximum current exhibited by the system in a specific voltage range. The histograms of peak current vs. cycle number were obtained using this program. Figure 5.6b plots the peak currents for several samples as a function of repeated ethylene glycol oxidation cycling. It has been proposed that the loss of Pt surface area in reactions such as this occurs by agglomeration and removal of Pt from the surface. The curves plotted in Figure 5.6b seem to indicate two modes of Pt loss from the 0.3ML-EQ deposit, one type which is relatively easily removed (the steep-sloped section of the curves), and a second type which is more difficult to remove (the shallow-sloped section). In contrast to this, the 1ML-EQ and 2ML-EQ deposits show

flatter curves, with 1ML-EQ exhibiting three slightly different modes, while the 2ML-EQ exhibits only one mode. We correlate the more easily removed Pt with unstable Pt grown on the surface. This Pt species was seen in XPS as highly deviated from metallic (-0.65eV) and in oxidation/reduction cycles as a species with increased affinity for OH^- groups. The high rate of surface area loss for such small deposits can either be explained by agglomeration of the initial deposit into thicker isolated islands, or by simple removal of the Pt that deviates from bulk properties. It is also apparent that the small amount of bulk Pt present in the 1ML-EQ sample, and in greater quantities in the 2ML-EQ sample, corrodes more slowly and is thus more robust.

This conclusion is consistent with the results reported in Figure 5.5, in which the 0.3ML-EQ sample showed a greater affinity for adsorbed hydroxide groups than the 1ML-EQ or 2ML-EQ samples. Since the 0.3ML-EQ deposit exhibits a greater affinity than thicker deposits for Pt-OH bonding, it is natural to conclude that under oxidizing reaction conditions the 0.3ML-EQ sample may exhibit an increased rate of corrosion, during which Pt-Au bonds are broken in favor of soluble Pt-OH complexes. Rather than showing distinct regions of different slopes, the data indicate simpler Pt removal mechanisms by which the submonolayer and single monolayer deposits are less robust than the 2 monolayer deposit. We suggest that it is an increase in bulk-type Pt with increasing iteration numbers that accounts for this trend to a more robust Pt deposit with increased growth iterations. This claim is supported by the other trends noted in this paper with increasing deposit thickness: the trend in XPS binding energy towards bulk and the trend in XAS data towards bulk-type atomic structure.

Another interesting aspect of the ethylene glycol electro-oxidation experiments occurs during the reverse (negative-going) sweep of the cyclic voltammogram (Fig. 5.6c). In CV of a typical reversible reaction, this would correspond only to reduction reactions, but as we have already discussed, for methanol and ethylene glycol electro-oxidation, the reverse sweep exhibits further oxidation features characterized by positive currents. In this case, the anomalous 're-oxidation' feature shows a constant potential shift from the forward oxidation feature for both pure Au and pure Pt. It is interesting that the reverse sweep for the Pt-Au monolayer-substrate system shows three distinct re-oxidation features instead of the expected two. Initially, only one feature corresponding to Pt is present, which decreases over time as a second unidentified feature appears. As cycling progresses, this second feature decreases as well, giving way to the appearance of a third feature corresponding in potential to that expected of the Au-site re-oxidation. We already know from the histograms of the forward-going sweeps that the Pt surface area is decreasing monotonically with cycle number. This new observation in the negative-going sweep suggests that new reaction sites are being created and then annihilated during the course of Pt surface area loss. This is consistent with the hypothesis of agglomeration (which creates new sites for reactions on the negative-going sweep) followed by dissolution (which annihilates both original and new sites).

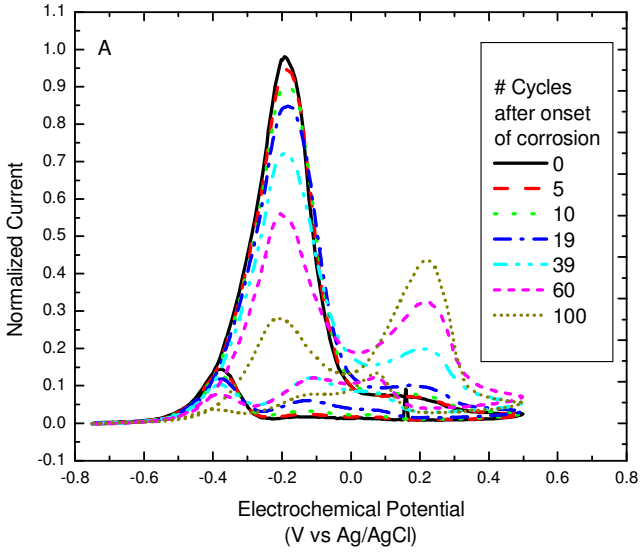

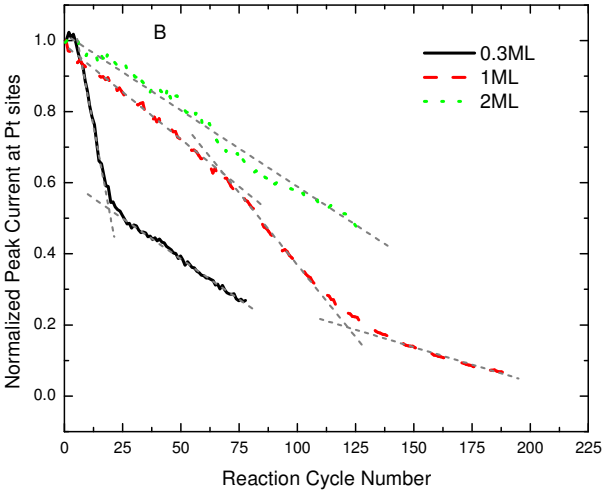

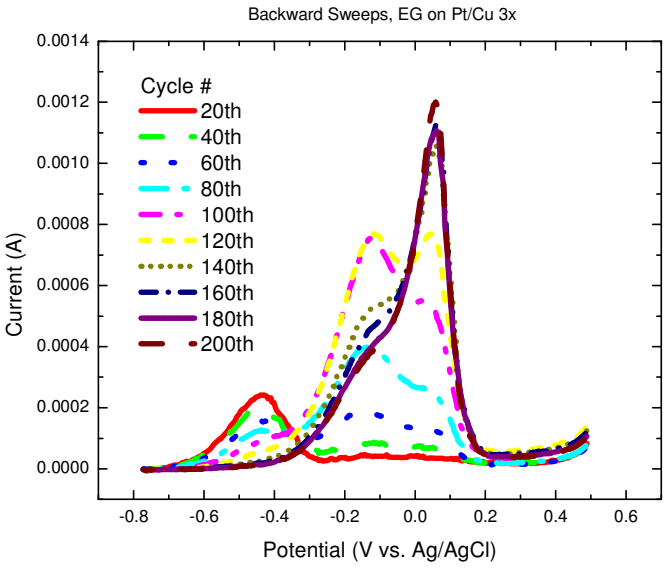

Figure 5.6: (A) Voltammetry of 1ML-EQ Pt@Au electrode for multiple reaction cycles in 0.1M Ethylene Glycol + 1M NaOH. Oxidation of EG occurs on Pt sites at -0.18V and on Au sites at 0.21V. (B) Normalized peak current for oxidation at Pt sites (-0.2V) as a function of cycle number. Dashed lines have been added as a guide to the eye. (C) CV of only the negative-going sweeps from figure (a).

5.4.3 Film Interaction with Electroadsorbed CO

The final tests performed on the Pt-Au surfaces involved electrochemical adsorption of CO molecules on the surface from solution phase. Figure 5.7 shows the electro-oxidation of carbon monoxide (CO) in CO-saturated 1M H_2SO_4 solution on a flame-annealed Pt wire electrode, compared with SLRR-fabricated electrodes of submonolayer through 4 ML-EQ thickness. We see that the thicker overlayers of SLRR-fabricate Pt exhibit CO electro-oxidation at a much lower potential (.8V for 4ML-EQ) than the bulk Pt electrode (1.1V). We also notice that the submonolayer deposit behaves most similarly to bulk Pt, with the deviation from bulk increasing with film thickness. It is important to note that no potential was applied to the Pt electrode during CO bubbling; rather, the electrodes were introduced to the solution after CO saturation.

The adsorbed layers were tested by anodic stripping voltammetry (ASV) in CO-saturated solution. The Pt-CO electrooxidation reaction exhibits a unique property of dependence on the electrode potential during introduction of CO into the system, usually by bubbling. Specifically, the subsequent ASV of a CO adlayer exhibits CO oxidation features which shift negatively in potential with increasingly negative adsorption potential before and during CO introduction. This potential, referred to as the admission potential, or the potential at which the electrode is biased during CO admission, is responsible for potential shifts as large as 0.2V. In addition to the admission potential, the electro-oxidation features exhibited in the ASV step are strongly dependent on the presence or absence of bulk CO in the solution phase. Solution phase CO has the ability to inhibit OH^- adsorption on the Pt surface. It has been known for some time that electro-oxidation of CO requires the presence of surface-adsorbed OH^- species[140], and it has also been shown that solution-phase CO will readsorb onto the Pt surface after initial

oxidation, preventing further OH^- groups from reaching the surface. This phenomenon inhibits the electro-oxidation reaction by blocking OH^- adsorption, which occurs by dissociative adsorption of H_2O, shifting the so-called 'ignition' voltage at which oxidation begins by as much as 0.3V [135, 140].

In order to form a mechanistic understanding of the observed increase in CO electro-oxidation activity, it is important to consider previous work that has been conducted for the Pt-Au system, in particular in relation to carbon monoxide adsorption and removal. Pedersen et. al. have already shown using vacuum-based TPD and STM of CO adsorbed on Pt monolayers at Au(111) surface that the first monolayer of Pt is (a) disordered and (b) has stronger Pt-CO bonds than bulk Pt[197]. In fact, the disordered state of the first monolayer has been confirmed here by the EXAFS analysis presented earlier. The Pedersen study has also shown that CO-Pt bonds for the second monolayer are similar to that of bulk Pt. The changes in bond strength have been explained by Pedersen in terms of shifts in the Pt d-band center, a theory which has been proposed earlier by Norskov et. al and studied in some depth[134]. In summary, the bulk of theoretical and experimental vacuum-based studies of CO adsorption on the Pt-Au monolayer bimetallic surface indicate that CO will bond more strongly to, and be harder to remove from, a Pt monolayer on Au than a Pt bilayer or bulk Pt.

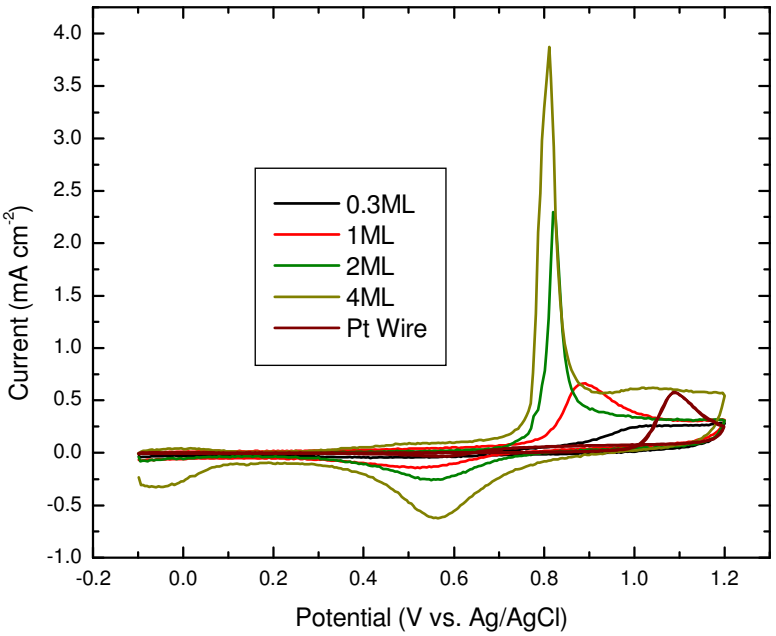

Figure 5.7: First-cycle CV of carbon monoxide electro-oxidation on multiple electrodes in CO-saturated 1M H_2SO_4 solution after adsorption of CO at -0.1V.

However, the data presented in Fig. 5.7 are not collected in a vacuum environment in the absence of oxygen-containing species. Thus, it is important to consider the influence of other species, most notably OH^- species, on the surface-adsorbate interaction. It is important to recall that electro-oxidation of CO species on Pt relies on the nucleation of OH^- sites, which then enable a lower voltage oxidation reaction of the CO. On this note it is instructive to consider theoretical studies of OH^- interactions with Pt monolayers from the literature. DFT calculations of potentials of zero charge for adsorbed OH^- on bulk Pt indicate that it is feasible for some OH^- to be adsorbed onto the surface at the open-circuit CO admission potentials used in the current work[218]. Additionally, further theoretical work by Niekar and Mavrikakis addressed OH^- adsorption on the Pt-Au(111) monolayer system, and indicated that OH^- can be expected to bind more strongly to the first monolayer of Pt grown on a Au substrate than to bulk Pt[219]. These two studies lead us to expect that an ultrathin Pt layer grown on Au will exhibit increased Pt-OH^- bond strength compared to a bulk Pt electrode.

Recent electrochemical studies of preadsorbed CO on SLRR-grown layers of Pt exclusively employed reducing CO admission potentials in the region of H^+ adsorption [220]. These tests indicated that SLRR films of 4ML-EQ thickness or less exhibit stronger CO-Pt bonding (higher CO electro-oxidation potentials) than bulk Pt when both are treated with this type of pre-dosing voltage treatment. Our tests, which bubbled CO prior to electrode immersion rather than applying an admission potential, show similar results, in that the 1ML and 2ML deposits exhibit higher CO electro-oxidation potentials than the 4ML deposit. Thus we confirm the previous finding that monolayer and submonolayer Pt SLRR deposits show greater Pt-CO bond strengths than thicker SLRR-grown layers.

Where our results differ from those previously reported is that in all cases our SLRR-fabricated films showed *lower* CO electro-oxidation potentials than the bulk Pt electrode. When analyzing this important difference it is important to remember that the current study did not apply an admission potential during CO bubbling. Essentially, the SLRR-fabricated films studied here showed electrochemical behavior characteristic of the employment of an admission potential during CO bubbling, even though none was applied.

This phenomenon can be explained by an examination of the chemistry behind why the application of a reducing admission potential causes a decrease CO electro-oxidation potentials. As we have noted earlier, adsorbed OH^- species are required for the CO oxidation reaction to proceed. When an admission potential is applied to the Pt electrode such that H^+ UPD occurs prior to bubbling CO, the CO adlayer is prevented from forming completely, rather forcing the Pt-solution interface to comprise itself of a composite H^+/CO arrangement. These adsorbed H^+ species essentially 'reserve' space on the surface for dissociative water adsorption once the oxidative sweep is begun, making room for OH^- groups to contribute to low-potential CO electro-oxidation. If there had been no pre-admission potential applied, the adsorbed CO layer would be more complete and CO electro-oxidation could not proceed until a suitably high potential was reached for OH^- to adsorb through it.

In contrast, the SLRR Pt film, which has been shown in this work to be composed of a disordered zero-valent Pt species *with an increased affinity for OH^- groups*, enables this lower-potential electro-oxidation reaction to occur without any pre-admission potential applied. This occurs due to the disordered Pt film's increased affinity

for OH^- groups, as experimentally observed here in Fig. 5.5 and predicted in the literature. Thus it is important to realize that there are two competing effects at work when determining the CO electro-oxidation potential: the affinity for OH^- groups, but also the strength of the Pt-CO bond in the first place. Even though the Pt layers studied here show an increased Pt-CO bond strength for thinner deposits (as seen before in the literature), the ability to nucleate an adsorbed OH^- species through the CO adlayer leads to lower potentials required for electro-oxidation.

5.4.4 X-ray Absorption of Electroadsorbed Carbon Monoxide

In addition to electrochemical characterization of the adsorbed CO layer, adsorbate XANES of the C K-edge was conducted in vacuum for carbon monoxide electrochemically adsorbed on Pt mono- and multi-layer architectures grown on polycrystalline Au supports (Fig. 5.8). By first electro-adsorbing carbon monoxide from a saturated sulfuric acid solution, then transporting the sample to the XANES chamber as outlined in section 3.5.3, it was possible to perform *ex-situ* analysis of the electroadsorbed CO adlayer in an arrangement analogous to the electrochemical CO oxidation experiment presented in Fig. 5.7. In Fig 5.8, we track changes in the resonant intensity of the carbon monoxide $2\pi^*$ orbital at 287.8eV as a function of Pt overlayer thickness. There is also an artifact in all three spectra at 285eV. This artifact is generated by the electrically biased rejection grid which is employed to enable the partial electron yield measurement performed, and is amplified by the normalization inherent to the XANES data processing, which normalizes the orbital resonances to the total amount of carbon monoxide present on the surface.

The $2\pi^*$ orbital is key in the bonding of a CO molecule to the surface of a metallic substrate, and the intensity of this XANES feature is proportional to the number of electron transitions occurring at this specific energy. The number of transitions is related to the number of electrons present in the initial state as well as the number of vacancies in the final state. in the corresponding molecular orbital. Thus, if we assume that the number of electrons in the initial core state is constant with increasing Pt layer thickness, we can attribute all increases in XANES resonance intensity at 287.8eV to decreased occupancy of the C-O $2\pi^*$ orbital. Under these assumptions, it is apparent that

thinner layers of Pt lead to decreased occupancy of the $2\pi^*$ orbital, and that the 3ML-EQ Pt-Au sample exhibits the highest occupancy of the sample set examined. This suggests higher levels of electron backdonation from Pt to the C-O antibonding orbital for thicker Pt SLRR deposits, and is consistent with the electrochemical result which indicated enhanced CO electro-oxidation capability for thicker layers. Thus the electrochemical performance shown in Fig. 5.7 may not be entirely attributable to enhanced OH^- adsorption phenomena, but may be the result of a combination of surface adsorption effects in addition to surface electron transfer effects as revealed by XANES.

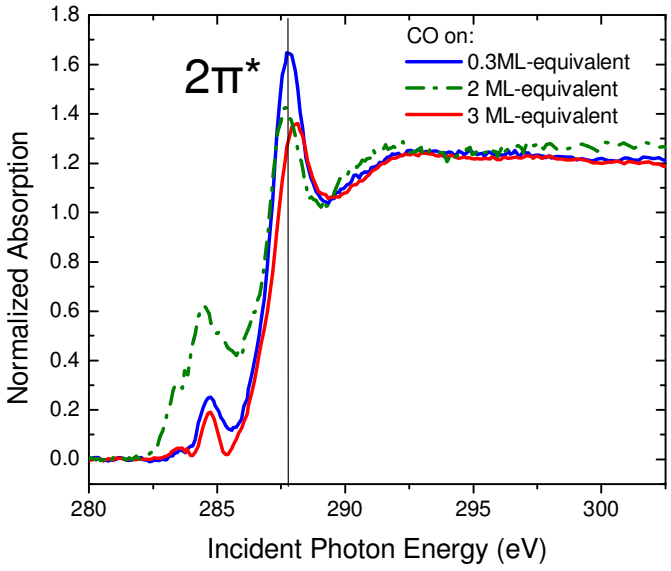

Figure 5.8: XANES spectra collected for carbon monoxide electroadsorbed onto Pt-Au monolayer-scale samples. The vertical marker indicates the location of CO 2π* electron orbital.

5.5 Pt Monolayers on Au-Modified Carbon Fiber

5.5.1 Growth of Au Deposits

In addition to the study of SLRR-grown Pt deposits on monolithic Au supports, ultrathin Pt deposits on Au-modified carbon fiber paper (CFP) were also conducted. These were performed on two different Au morphologies, one of which was grown by potentiostatic deposition (PSD) and resulted in large urchin-like structures, while the other was grown by potential square-wave deposition (PSWD) and led to nanoscale particles on the surface in addition some larger structures. Modification of the CFP electrodes with Au nuclei of varying sizes was conducted by electrodeposition using 30 minutes of either PSD at 0V or PSWD alternating between 0V and 0.6V. The voltage waveforms and current-time transients for the initial time period of both deposition methods can be seen in Figure 5.9a and 5.9b respectively. It can be seen for the PSD curve that the electrodeposition current drops off markedly in a short period of time. It is worth noting in the PSWD curve that the electrodeposition current is renewed with each current pulse, indicating that the desired effect of replenishing the depletion zone around the electrode was achieved.

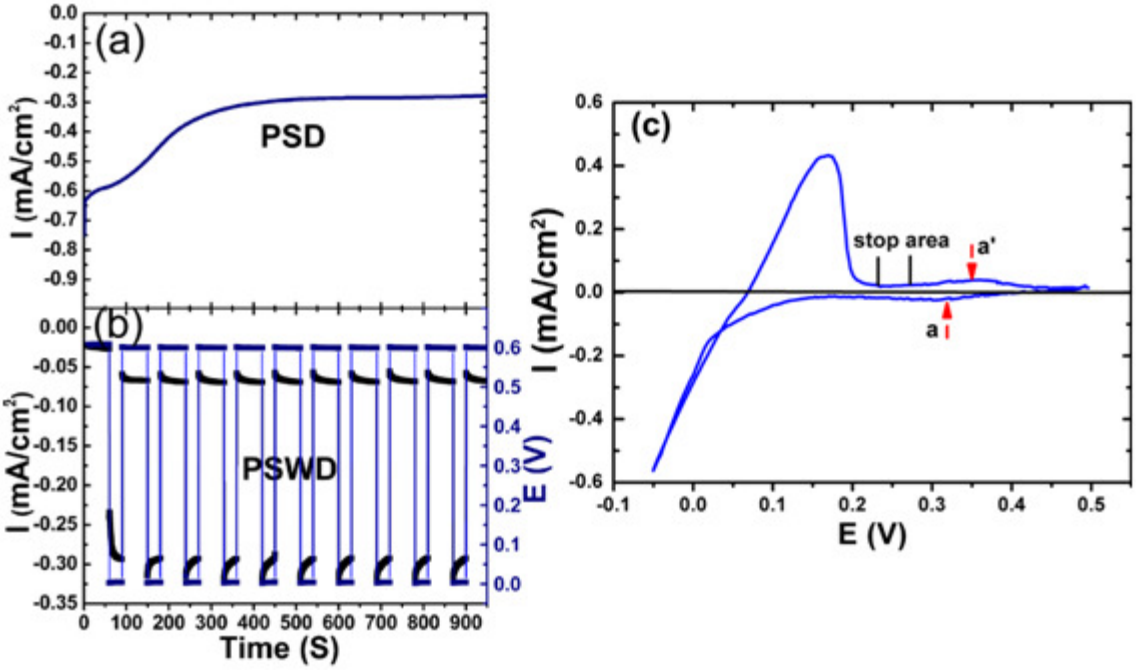

Figure 5.9: Voltage-time and Current-time transients for fabrication of Au-CFP electrodes by (a) PSD and (b) PSWD methods. Typical Cu UPD voltammetry (c) employed for SLRR modification of Au-CFP with Pt.

5.5.2 Modification of Gold-Carbon with Platinum

After preparation of the Au-CFP electrodes, the resulting Au surfaces were modified by iterative growth of sub-monolayer coverages of Pt grown via SLRR of Cu UPD films. This modification is illustrated in Scheme 5.2. The Cu UPD process was conducted by sweep voltammetry in which a bulk deposit of Cu was grown, then stripped, leaving behind only the UPD partial monolayer. A representative voltammogram of the Cu UPD process is shown in Figure 5.9c, by which the bulk deposition and stripping process can be seen. By stopping the voltage sweep at a potential between the bulk removal and the UPD removal features in the positive-going sweep, the surface coverage of the Cu UPD layer on Au was specified to 0.67ML. This value is obtained from previous STM studies for Cu UPD on pure Au electrodes.[150] The bulk-stripping method has the advantage of providing a cohesive UPD deposit as well as ensuring that no overpotentially deposited Cu remains on the CFP surface. The Cu UPD on Au/CFPs was performed in 50 mM H_2SO_4 containing 10 mM $CuSO_4$. Pt replacement was conducted in deaerated 1 mM H_2PtCl_6 for a minimum of 5 min.

As a result of the SLRR process, Pt is nominally deposited on the Au surface in a 1:2 Pt:Cu ratio. This ratio arises from the ratio of the valencies of the solvated species (Pt^{4+} and Cu^{2+}). As a result, each iteration of Pt replacing 2/3ML Cu nominally yields 1/3ML-equivalent (ML-EQ) of Pt. Thus one replacement iteration is denoted 0.3ML-EQ, while 3 growth iterations would be denoted 1ML-EQ. As before, it was found that this nominal stoichiometry was not entirely accurate, thus these ML-EQ values are called into question by the XAS and XPS results presented here and in section 5.4.

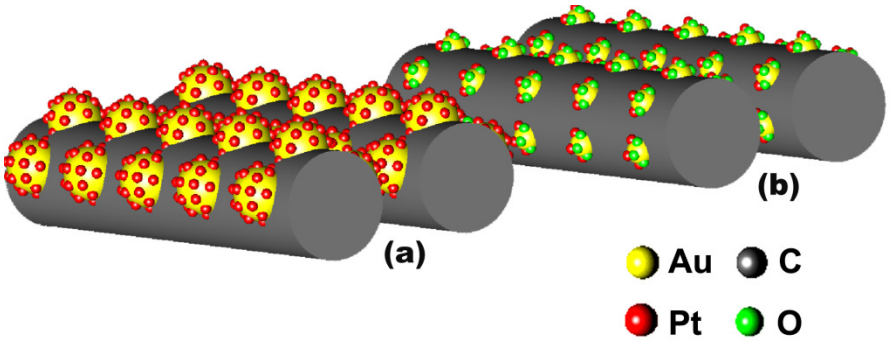

Scheme 5.2: Representative schema demonstrating (a) metallic Pt growth on carbon paper containing large Au structures and (b) oxidic Pt growth on carbon paper with smaller Au structures.

5.5.3 Characterization

The morphologies of the Au-CFP and Pt-Au-CFP nanostructures were characterized by scanning electron microscopy (SEM). It was found that there is no appreciable difference detectable in SEM imaging between the Au-CFP and Pt-Au-CFP electrodes. This is to be expected due to the extremely small scale of the Pt deposition being conducted. Thus only the images of Au-CFP prior to Pt deposition are shown in Figure 5.10. For PSD at 0V, the Au deposit takes on the morphology of nanoneedles aggregated into large urchin-like clusters with an average diameter of several microns (Figure 5.10a).

It was found that for the PSWD-grown Au (Figure 5.10b), there are two types of Au nanostructures coexisting on the CFP surface. First, the urchin-like structures noted earlier are once again present, this time smaller in size. In addition to these larger structures, we see the addition of highly dispersed Au nanoparticles with sizes in the tens nanometers as a result of the PSWD treatment. These particles are seen to coat the remainder of the exposed CFP. This morphological difference between the two growth modes is to be expected based on a simple model for diffusion-limited nucleation and growth. Here we make the reasonable assumption of diffusion-limited growth (that is, the rate-limiting step for $Au^{3+} \rightarrow Au$ is the arrival of solution-phase Au^{3+} at the CFP surface). During the PSD growth step, a depletion zone of Au^{3+} in the solution is formed after initial Au nuclei formation. Once this zone is formed, the arrival of further Au^{3+} ions to the Au-CFP surface will occur primarily at the nucleated Au nanoneedles, since they protrude into the depletion zone further than the (locally flat) CFP surface. This leads to large needle-like structures extending from initial Au nucleation sites, which also leads to increased electric fields near the surface sites. On the other hand, if we perform a pulsed

deposition such as that used for the PSWD samples, we allow this depletion zone to repopulate with solution-phase Au^{3+} during the pulse relaxation, such that new nuclei formation, rather than existing nuclei growth, is the primary reaction during the subsequent voltage pulse.

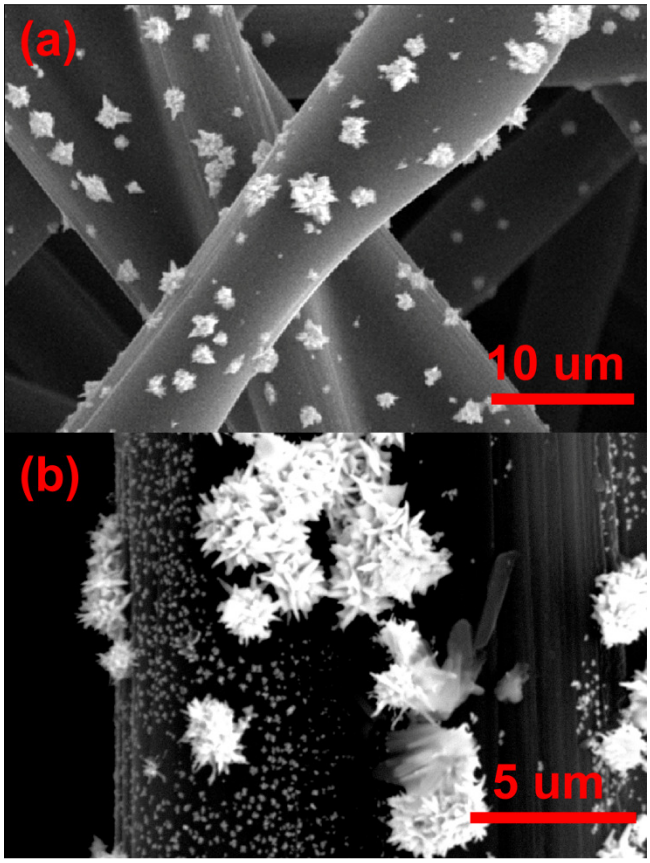

Figure 5.10: SEM images of the Au-CFP electrodes: (a) PSD at 0V for 30 min, (b) PSWD for 30 min.

In addition to morphological characterization using SEM, the surface coverage of Pt on the Au deposits was examined by CV in acidic media and comparison of the relative currents associated with Au or Pt surface oxide reduction. Figure 5.11 shows CV curves for Au-CFP with and without varying coverages of Pt. The CV presented here were recorded in 0.5M H_2SO_4 at 20mV/s. By examining the decrease in the Au reduction feature at 1.0V with increased deposition iterations, we can track the amount of Au surface area lost due to masking by Pt deposits. Similarly, increases in Pt surface area can be tracked by studying the Pt oxide reduction feature near 0.47V, or the hydrogen adsorption/desorption curves in the 0V region of the voltammograms. It can clearly be seen that, with increasing amounts of Pt, the Pt surface area increases at the expense of the Au surface area, indicating that Pt deposition at Au sites is dominant. This method of tracking Pt coverage on Au has been employed successfully in the literature as well as earlier in this section form Au substrates.[12, 221]

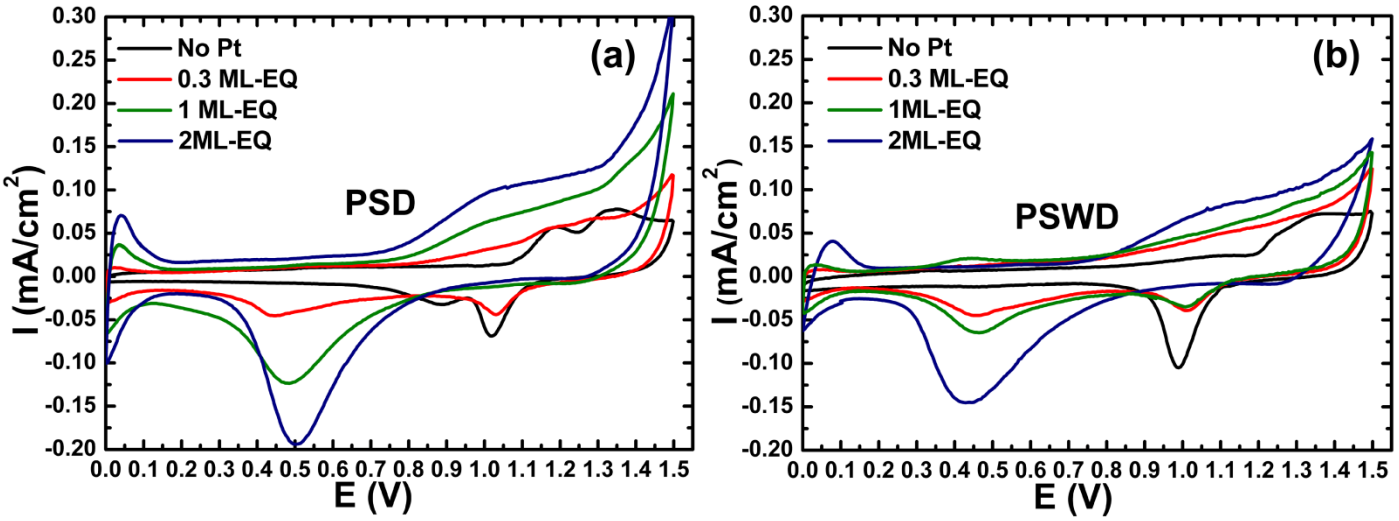

Figure 5.11: Cyclic Voltammograms (CVs) of Pt-Au-CFP electrodes in 0.5 M H_2SO_4 solution with a potential scan speed of 20mV/s.

Table 5.2: Binding Energy (BE) and relative intensities for Pt 4f photoemissions.

Pt Species	Binding Energy (eV)		Peak Area Percentage					
			PSD			PSWD		
	$4f_{7/2}$	$4f_{5/2}$	0.3ML-EQ	1ML-EQ	2ML-EQ	0.3ML-EQ	1ML-EQ	2ML-EQ
Pt^0	71.19	74.49	10.2	65.7	65.1	9.8	55	48.7
Pt^{2+}	72.46	75.76	14.5	34.3	34.9	15.3	15.6	17.9
Pt^{4+}	74.67	77.97	75.3	0	0	74.9	29.4	33.4

XPS analysis was employed to determine the oxidation state of the Pt. The Pt 4f photoemission region for Pt catalysts grown by SLRR on PSD and PSWD Au-CFP is presented in Figures 5.12a-5.12c and the results after peak fitting are summarized in Table 5.2. A representative plot of the peak-fitting performed is shown in Figure 5.12d, and a comparison of the Pt4f:Au4f ratio (Au4f spectra not shown) is plotted in Figure 5.12e as a means to track the total Pt content. The Pt4f photoemission exhibits a spin-orbit-split doublet, with two peaks ($4f_{7/2, 5/2}$) exhibiting a known spacing of 3.3eV. In this case, three pairs of peaks were observed in the Pt 4f region. This indicated the presence of three types of Pt in differing oxidation states. Each pair of peaks has a similar full-width at half-maximum (FWHM) and a separation of 3.3eV as expected. The peaks located at 71.19 and 74.49 eV are undoubtedly due to Pt^0, which is found to be the predominant species in most Pt catalysts. [222] The features located at 72.46 and 75.76 eV are due to Pt^{2+}, and the last pair at 74.67 and 77.97 eV originate from Pt^{4+} species. [223,6] The percentage of Pt^0, Pt^{2+} and Pt^{4+} for Pt on Au-CFP grown by PSD and by PSWD are summarized in Table 5.2. While the oxidation states for the PSD and PSWD samples are virtually identical for 0.3ML-EQ of Pt on Au, the Pt^{4+} state disappeared completely after 1ML-EQ of Pt deposition for the PSD-grown Au-CFP supports. In comparison, some Pt^{4+} species remained present in the film for all iteration numbers of Pt on PSWD-grown Au-CFP.

Even though the percentages of Pt^{4+} decrease along with the Pt thickness for both sets of samples, the rate of this decrease is much lower for the PSWD series than for the PSD series. Although the optimum ratio of these three states is unclear, it is clear from the literature that the existence of Pt oxides in catalysis plays a significant role in

performance.[1, 7] Thus it is of critical importance that the influence of support particle size be considered when growing ultrathin noble metal deposits for application. Based on the evidence for cationic Pt formation, we present here an alternate reaction pathway:

$$Pt^{4+} + 2Cu + L^{-} \rightarrow xPt + y[Pt^{2+}(2/\delta)L^{-\delta}] + (1-x-y)[Pt^{4+}(4/\delta)L^{-\delta}] + (2-y)Cu^{2+} \quad \text{(Eq. 5.7)}$$

Eq. 5.7 indicates the coexistence Pt^{0}, Pt^{4+}, and Pt^{2+} species on the surface, coordinated with an as-yet unidentified anionic ligand $L^{-\delta}$. We will see in later sections that the use of EXAFS analysis allows us to tentatively identify this complexing ligand species based on interatomic bond lengths measured for the cationic Pt.

A possible explanation of the Pt oxidation state change, whereby this effect was caused by partial oxidation of the Au particles grown by the PSWD method, was disproved by XPS analysis of the Au 4f photoemission (not shown), which indicated that the Au deposits were metallic. This leaves two alternative effects that could be responsible for this phenomenon, the existence of a size-dependent effect in the Pt-Cu replacement reaction, and/or the influence of Au-CFP boundary sites on the Pt^{4+} reduction reaction. The fact that the 0.3ML-EQ deposits are virtually identical for both series of samples seems to suggest that the size effect is more likely, as the difference in size would only become an issue once near-full coverage of Pt on Au was reached.

In addition to quantifying the portion of Pt present by valence state, it was possible to quantify the overall amount of Pt present on the surface relative to the Au support. By analyzing the peak area ratios of the Pt_{4f} and Au_{4f} photoemissions, a relative quantification of the Pt deposit can be achieved. These peak area ratios are shown as a function of Pt coverage in Figure 5.12e. For both groups of catalysts, the relative

intensity of Pt compared to Au increases along with increasing replacement iterations, as expected.

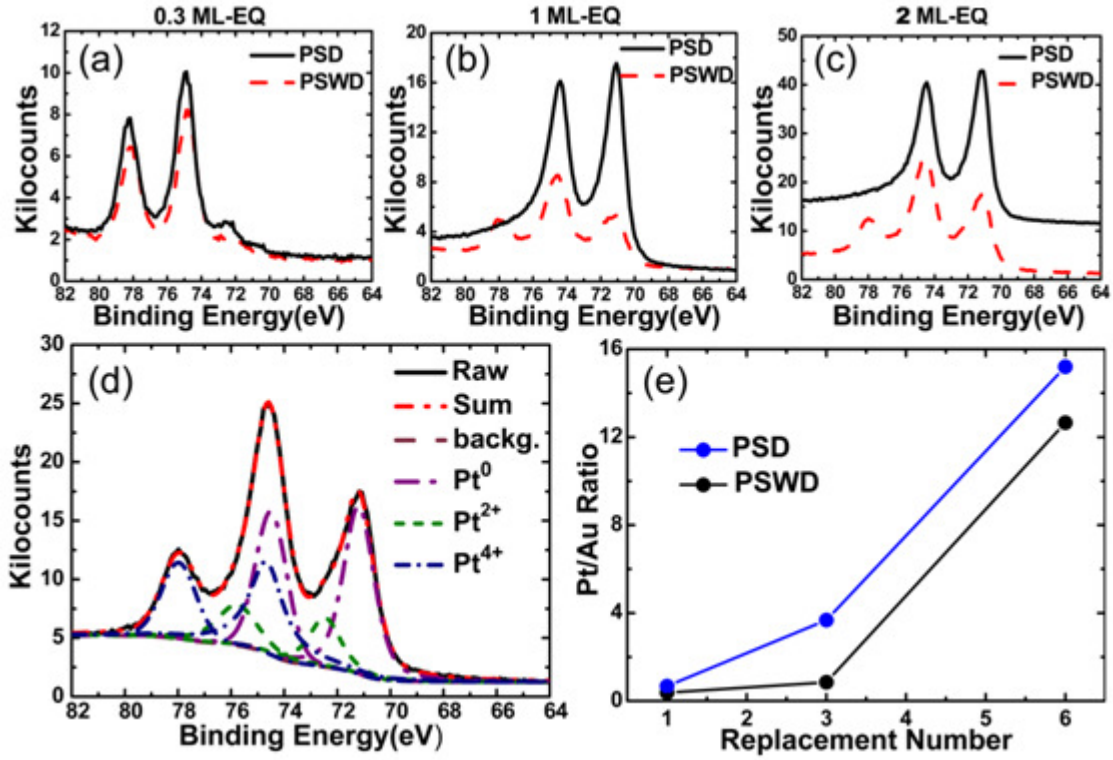

Figure 5.12: Pt4f XPS for Pt-SLRR on Au-CFP grown by PSD and PSWD. (a) 0.3ML-EQ, (b) 1ML-EQ, (c) 2ML-EQ. (d) Representative peak-fitting of the PSWD 2ML-EQ curve. (e) Plot of the Pt/Au peak ratios resulting from peak-fitting of Pt and Au 4f features.

In order to better understand the phenomenon of cationic Pt formation, EXAFS and XANES studies of the Pt-Au-CFP electrodes were conducted to investigate the local atomic structure and d-band occupancy of the Pt film, respectively. Figure 5.13 presents the EXAFS data for both the PSD and PSWD series of samples along with reference data, while Figure 5.14 presents the XANES data.

In Figure 5.13, we see the r-space spectra, which are proportional to the radial distribution function around an average Pt atom. The EXAFS data allow us to analyze the immediate atomic vicinity of the Pt atoms within the Pt film. By comparison of the location of the first peak with the reference spectra, we can begin to identify the type of bonding present around the average Pt atom. It is clear from examination of the reference spectra that Pt-Pt metallic bonding exhibits a peak near 2.2Å, while the Pt-Cl and Pt-O bonds show significantly shorter bond lengths (1.9Å and 1.7Å, respectively). It is important to note that backscattering phase shifts have not been corrected for in this analysis in either the sample spectra or the reference spectra. This allows for meaningful comparison between the reference and sample, although exact determination of bond length is not achieved. It is clear that the 0.3ML-EQ curves for both sets of samples in Figure 5.13 exhibits bond lengths characteristic of Pt-O, with a first coordination shell at 1.7Å lining up nearly exactly with the reference spectra for PtO_2. We see a small shift in the location of the first coordination shell for 0.3ML-EQ on PSD compared with 0.3ML-EQ on PSWD, which suggests that the Pt-O surface lattice exhibits some small amount of strain-induced distortion.

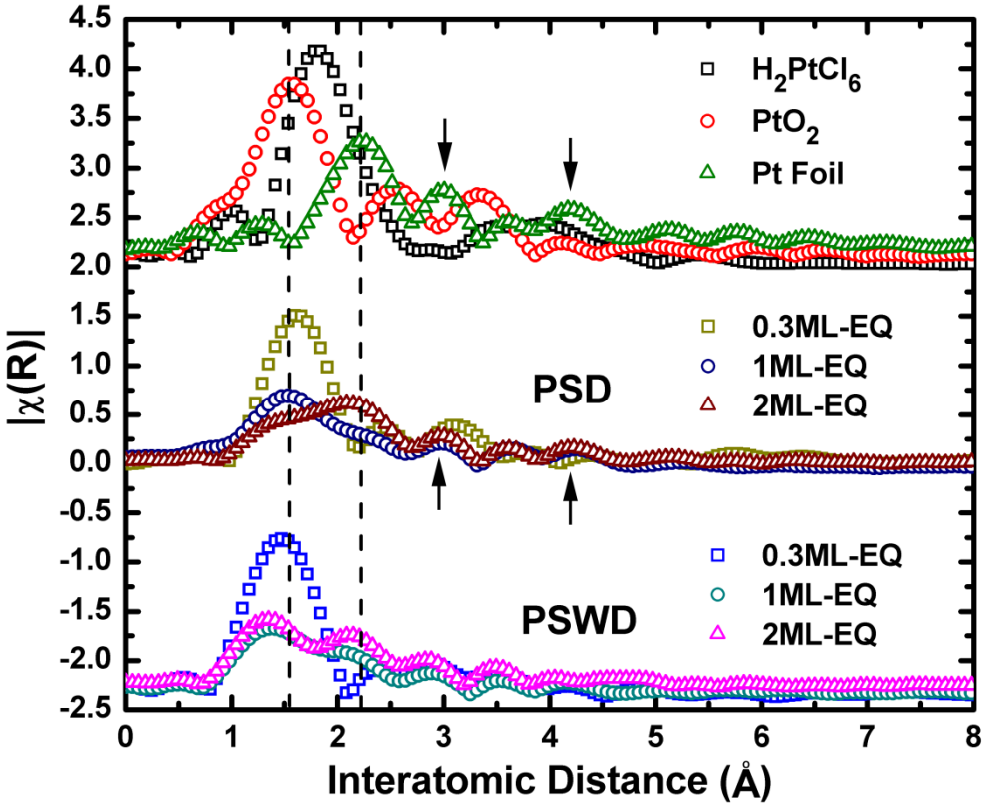

Figure 5.13: EXAFS spectra for reference compounds, PSD, and PSWD samples. Vertical lines mark the location of first-neighbors for reference PtO_2 and PtCl, and arrows mark the location of common features between the metal foil reference and the metallic components of the Pt films.

When examining the 1ML-EQ and 2ML-EQ films in Figure 5.13, we see that each film exhibits two coexisting components of the first neighbor shell, one located at 1.7Å and one located at 2.2Å. This holds true for both the PSD and PSWD series of curves, and indicates a mixed oxide-metallic structure, with the addition of metallic species upon increased deposition iterations appearing as increased intensity at 2.2Å. It is worth noting that by the time 2ML-EQ of Pt on PSD-grown Au-CFP has been reached, the metallic Pt-Pt contribution at 2.2Å is noticeably larger than the Pt-O at 1.7Å. In contrast to this, the Pt-Pt contribution for the same 2ML-EQ PSWD sample is significantly weaker than its corresponding Pt-O contribution. This confirms the finding in XPS that indicated that the PSWD samples had increased oxide content compared to the PSD samples. Furthermore, we are able to tentatively identify the complexing ligand for the cationic Pt surface oxides as oxygen based on these bond lengths. Thus it is possible to revise the nominal reaction mechanism:

$$3Pt^{4+}_{(aq)} + 3Cu_{(ads)} + 3O^{2-}_{(aq)} \rightarrow Pt_{(ads)} + PtO_2(IV)_{(ads)} + PtO(II)_{(ads)} + 3Cu^{2+}_{(aq)} \quad \text{(Eq. 5.8)}$$

Note that equation 5.8 still indicates the presence of Pt of all three valencies observed in XPS, and that the ratio of the two species is difficult to determine using EXAFS data. One final point to address in the EXAFS data analysis is the question of why the metal/oxide ratio appears higher in XPS than in EXAFS. This discrepancy results from the ordering dependence of the r-space EXAFS data. While XPS is only sensitive to the chemical bonding and the raw amounts of a given Pt species, EXAFS features will become more intense as a given phase increases in local ordering. Since we observe higher ratios of cationic species to metallic species in EXAFS than we do in

XPS, we can conclude that the cationic/oxidic phases formed by the Pt SLRR process are more ordered than the metallic phases.

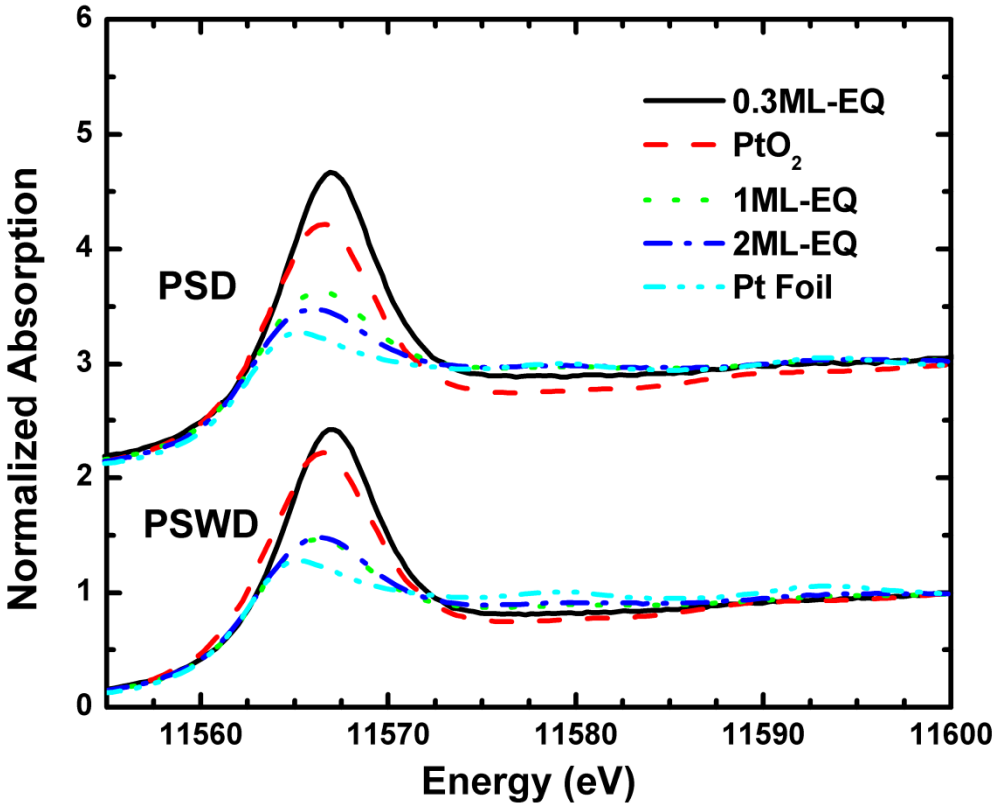

Figure 5.14: XANES spectra for the SLRR-fabricated samples and reference compounds. Reference spectra are shown for both PSD and PSWD series.

In the XANES spectra in Figure 5.14, we see a series of plots for reference spectra and Pt SLRR on PSD and PSWD samples. By tracking the intensity of the white line absorption, which is proportional to the density of unoccupied d-band states in the material, we find another marker for the oxidic character of the Pt film. Since oxides tend to display more intense white line resonances (because of the d-state holes), we expect the thinner Pt deposits to exhibit large peaks in R than the thicker Pt deposits. This trend is found to hold true exactly for the PSD series of samples, with each successive increase in Pt deposit thickness leading to a further decrease in XANES white-line intensity. However, if we examine the PSWD series of samples, we see that while the 1ML-EQ sample shows a weaker white-line intensity than the 0.3ML-EQ sample (indicative of reduced cationic content), the 2ML-EQ sample is virtually identical to the 1ML-EQ sample. This observation serves as a third independent confirmation of the result initially found in XPS: that the PSWD series of samples exhibits a marked increase in cationic Pt content compared to the PSD series of samples, particularly for Pt deposits of 2ML-EQ.

A second important observation of the XANES spectra is found by comparison of the PSD 0.3ML-EQ curve with the PSWD 0.3ML-EQ curve. Compared to the PtO_2 reference, which is the same in both sets of spectra, the PSD 0.3ML-EQ sample exhibits a more intense white line than the PSWD sample of similar coverage. This difference suggests that some degree of electron donation from the PSWD Au substrate is leading to decreased d-band vacancies in the Pt film. This is congruent with the smaller deposits arising from the PSWD fabrication process, which should exhibit a higher degree of Au-Pt interaction due to their higher Au surface/volume ratios compared to the PSD deposits.

5.5.4 Reactivity and Durability for Methanol Electro-oxidation

In order to test the electrocatalytic activity of the Pt-Au-CFP electrodes for MOR, samples were cycled from 0V-1.0V up to 300 times in 0.5M CH_3OH + 0.5M H_2SO_4. This data is presented in Figure 5.15, with plots 5.15a and 5.15c showing maximum peak currents for different SLRR treatments of the PSD and PSWD-grown Au-CFP electrodes, respectively. Plots 7b and 7d show the decay in methanol oxidation current over multiple cycles, in both cases for 2ML-EQ of Pt on PSD and PSWD samples, respectively. This type of multi-cycle oxidation test allows for relatively simple characterization of catalyst deactivation processes arising from poisoning or Pt dissolution. By tracking the peak oxidation current for any given cycle, a measure of the remaining electrochemically active Pt surface area can be obtained. Since Au does not appreciably catalyze the MOR compared to Pt, the entire oxidation current (and corresponding decreases in that current) can be ascribed to Pt sites. At the same time, since the MOR does not provide a method for testing for re-exposure of Au sites, it is difficult to determine whether the decreases in Pt oxidation current presented here arise from poisoning, agglomeration, or corrosion effects. Even though this determination cannot be performed exactly, we suggest that the majority of Pt current loss is due to Pt agglomeration and removal effects, since the surface poisons created during methanol electro-oxidation should be desorbed during the low-potential segment of each oxidation cycle.

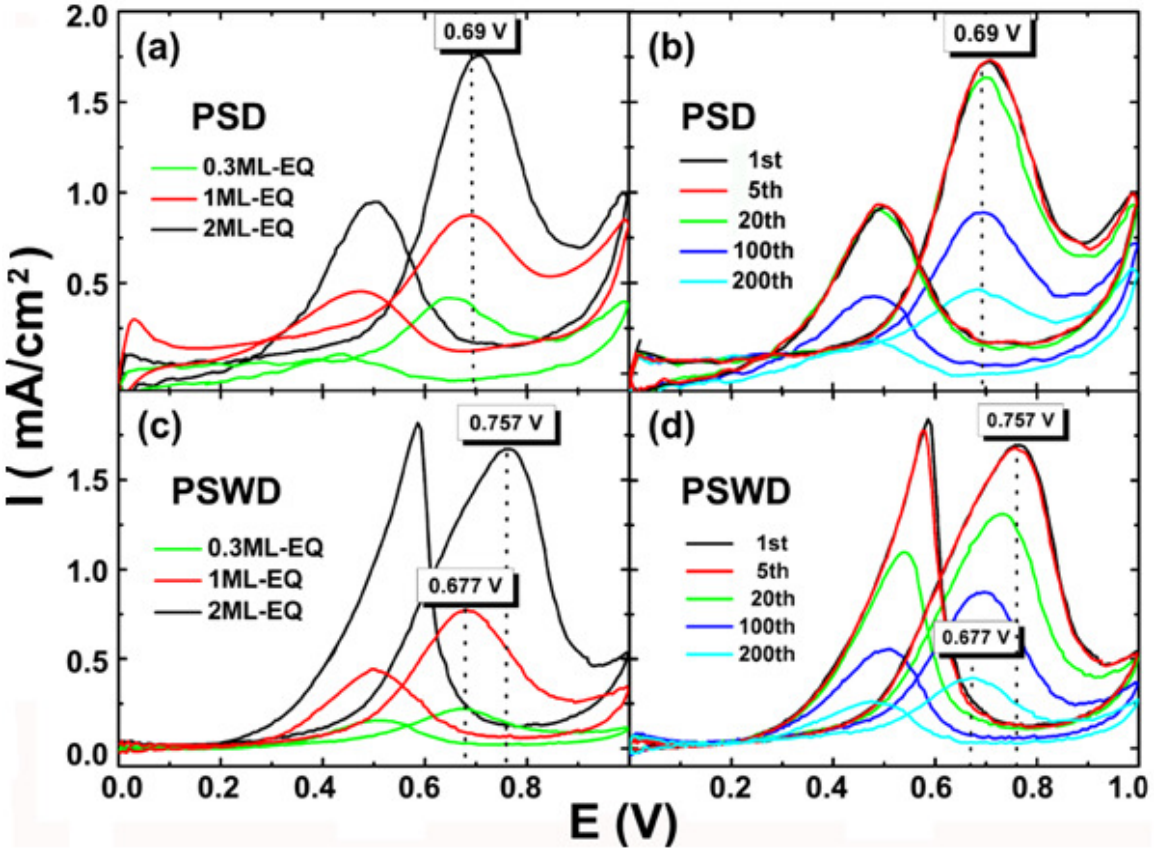

Figure 5.15: CV in 0.5M H_2SO_4 + 0.5M CH_3OH at 50mV/s for Pt SLRR grown on Au-CFP electrodes. (a) First cycle voltammetry for PSD samples (b) durability over multiple cycles for 2ML-EQ Pt on PSD-grown Au-CFP. (c) First cycle voltammetry for PSWD samples and (d) durability over multiple cycles for 2ML-EQ Pt on PSWD-grown Au-CFP.

All Pt-Au-CFP electrodes exhibited some degree of cleaning phase at the beginning of MOR cycling, during which the peak currents increased until reaching a maximum before decreasing once again. These cleaning stages are omitted from the plots here, with the initial cycle being ascribed to the maximum oxidation current observed. Increases in methanol oxidation currents are apparent from 0.3ML-EQ coverage to 2ML-EQ coverage in both groups of catalysts. The peak currents of the 1ML-EQ (3 iterations) and 2ML-EQ (6 iterations) catalysts are 3 and 6 times as high as the 0.3ML-EQ (1 iteration) catalyst, respectively. This indicates that the thicker deposits (which exhibited more metallic-type behavior in XPS and XAS) are in all cases more active for the MOR than the thinner deposits. While some portion of the effect may be attributable to increases in total Pt surface area, the oxidation state of the Pt film also make a definite contribution to the activity towards the MOR. This contribution can be seen by comparing maximum currents exhibited in Figure 5.15a with those in Figure 5.15c. It is apparent from direct comparison that the PSD-grown Au support leads to higher MOR currents than the PSWD-grown support. In the absence of any concerns regarding cationic Pt, one would expect the nanostructured architecture arising from PSWD growth to exhibit larger surface area than the micron-scale architecture arising from PSD growth. Thus we can attribute the decrease in activity shown by the PSWD samples to the increased cationicity already observed in XPS and XAS.

Further evidence for the detrimental effect of cationic Pt on the MOR is apparent in Figures 5.15c and 5.15d, in which a positive potential shift for the peak current of the MOR at early cycles of 2ML-EQ Pt can be seen. This type of shift is only seen for PSWD samples and not for PSD samples, indicating that the decreased size of the Au support

particles (and the corresponding increase in cationic Pt) is correlated with this positive shift. It has already been shown that lower reaction potentials for the MOR are indicative of a more active Pt catalyst. Thus it is clear that the positive shift in peak potential arises from a detrimental accumulation of cationic Pt, leading to deactivation of the catalyst surface. It is important to remember from the quantitative XPS analysis that, even though the proportion of cationic Pt remains roughly equal between 1ML-EQ and 2ML-EQ of Pt on the PSWD samples, the overall Pt content is increasing, leading to large quantities of cationic Pt in the 2ML-EQ film relative to the 1ML-EQ or 0.3ML-EQ films. In Figure 5.15d, we see that as the Pt loses active surface area, this positive shift is eventually eliminated, with the MOR curve after 20 reaction cycles having shifted to a potential more characteristic of the other Pt electrode surfaces.

In addition to the potential of maximum current and the total electro-oxidation peak current itself, the long-term stability of an ultrathin Pt film is a very important property for this type of fuel cell electrocatalyst. Even though voltammograms for all coverages of Pt on Au-CFP were collected, it is not practical to attempt to plot all of the voltammograms, so only the long-term stability results of 2ML-EQ Pt on PSD and PSWD Au-CFP are presented in Figures 5.15b and 5.15d. We see here clearly that the peak current obtained from the forward CV scans gradually decreases along with the successive CV scans. We can see clearly that for the 2ML-EQ PSWD sample in Figure 5.15d after 200 CV scans, the peak current density is 1.2 $mA \cdot cm^{-2}$, which is 40% of the value of the peak current density at first cycle (3.0 $mA \cdot cm^{-2}$). The decrease of the peak current density could result either from Pt degradation by agglomeration/corrosion processes or from the poisoning of the catalyst by the intermediates (such as (CO)

adsorption) of methanol oxidation. [221, 224] It is also worth noting that the peak current for the PSWD catalyst (Figure 5.15d) decays significantly more quickly than for the PSD catalyst (Figure 5.15b) in the first 20 cycles. This increased rate of decay corresponds with a return to lower MOR electro-oxidation potentials, and suggests that the cationic Pt is quickly attacked and compromised during the initial cycles of MOR reaction.

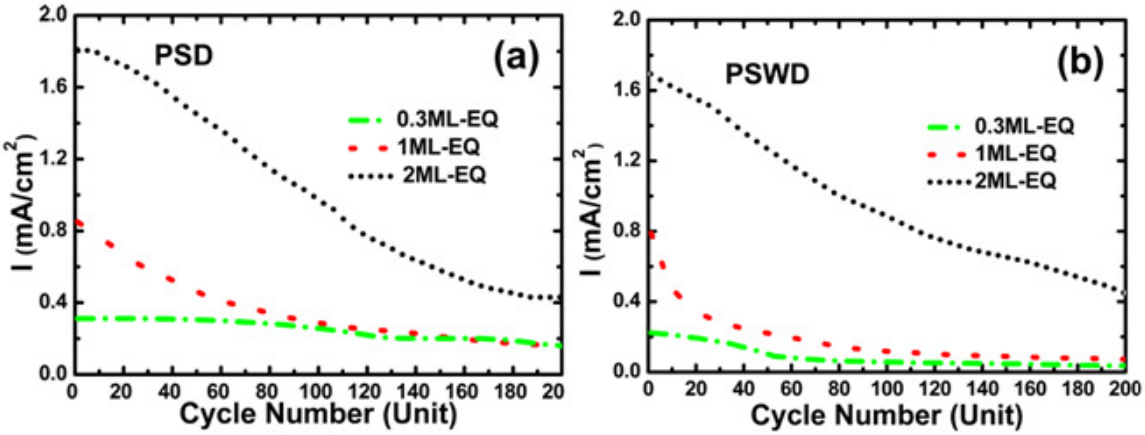

Figure 5.16: Peak current histogram for the methanol electro-oxidation reaction on all 6 Pt-Au-CFP electrode surfaces studied.

The MOR peak current histogram as a function of cycle number for the remaining coverages studied (0.3ML-EQ through 2ML-EQ on both PSD and PSWD) is plotted in Figure 5.16. From this data we can clearly see that after about 100 cycles, there is almost no remaining electro-oxidation current for 0.3ML-EQ and 1ML-EQ on both PSD and PSWD, which indicates that the Pt deposit has been mostly deactivated through either dissolution or poisoning. Additionally, the peak currents decay faster during the first 20 cycles for PSWD deposits than for the PSD deposits. It is possible that we witness easier deactivation of the PSWD sample due to the higher degree cationicity of the Pt deposit as proven in the above text. It is also possible that the smaller particles size of the Au substrate induced faster coalescence of the Au particles themselves, leading to decreased Pt surface area.[225]

Thus it can be concluded that the propensity to form cationic Pt as shown via XPS and XAS analysis is detrimental to the performance of the Pt/Au-CFP electrodes for monolayer and submonolayer coverages, leading to decreased activity and durability. However, for 2 ML-EQ, both the PSD and PSWD morphologies exhibit comparable MOR durability histograms, indicating that for Pt deposits of a minimum 2ML-EQ thickness, these detrimental effects can be eliminated. In summary, we have identified a low-loading thickness limit of 2ML-EQ, below which the Pt film exhibits decreased activity and durability due specifically to chemical and structural changes arising from the morphology of the Au support. Factors such as increased defect concentration or non-equilibrium structure of the PSWD-grown Au support may be responsible for the changes in Pt behavior observed. These possibilities are supported by the XAS data which indicates that the monolayer-scale Pt does not effectively arrange itself in FCC structure

on PSWD deposits. It is also supported by XPS data which indicates that partial oxidation of the smaller Au deposits is not the cause of these effects. Above the 2 ML-EQ limit, the Pt film may still behave differently than a bulk Pt structure, but the morphology of the Au support loses much of its influence on the Pt film behavior. These findings are of particular importance for the subset of the fuel-cell catalyst community that is focused on core-shell or layered structures, indicating that morphology-related support effects may lead to pronounced detrimental effects if a minimum amount of Pt is not achieved.

5.6 Impact of Pt Monolayer Findings

It has been shown by XPS analysis, XAS spectroscopy, and cyclic voltammetry, that in specific cases it is possible for surface limited redox replacement to yield a layer of immobilized cation-anion complexes instead of the desired zero-valent metal. We have also shown, for both monolithic Au substrates as well as carbon-supported nanoscale Au supports, that for the Pt-Au system this effect terminates after several multilayer thicknesses of deposit on the surface have been completed. This means that for the specific case in which very thick deposits of Pt are grown on Au, the presence of this intermediary does not pose a significant problem. However, for other systems, such as the case in which alternating layers of different elements are grown, there is a possibility that ionic complexes may be grown in cases where metals are expected and desired. We have proposed a possible reaction mechanism that accounts for this observed behavior. We suggest that future implementations of redox replacement for fabrication consider the possibility of unwanted complexes altering the desired fabrication chemistry.

In addition, we have identified the presence of a disordered zero-valent Pt species present at coverages less than 2 monolayers on Au, with lower photoelectron binding energy, a greater affinity for OH^- groups, less durability under reaction cycling, and increased d-band vacancies than bulk Pt. This species of Pt occurs as a result of ligand-effect electron transfer with the underlying Au substrate. We have demonstrated a correlation between thickness of ultrathin Pt films at Au electrodes and three important properties of ultrathin Pt films: (1) Pt photoelectron binding energy, (2) electrochemical affinity for oxide/hydroxide adsorbates and (3) durability of the deposit under reaction conditions. Finally, we have shown that the above described properties of ultra-thin Pt

films play an important role in the electrocatalysis of the CO oxidation reaction, and proposed a mechanism by which the properties of ultrathin Pt films can be exploited to achieve lower CO electro-oxidation potentials.

Finally, the Pt-Au-CFP surfaces were tested for performance and durability under oxidation cycling in the methanol-acid system. It was found that the Pt deposits grown on larger Au supports exhibited markedly improved durability during the first 20 electro-oxidation cycles, and slight improvements in activity compared to the nanoparticle Au supports. This leads to the conclusion that the cationic Pt species induced by the smaller-scale Au supports is less active towards the methanol electro-oxidation reaction as well as less durable than metallic-type Pt species shown to grow on larger-scale Au supports. Finally, it has been shown that an equivalent of two monolayers is the low-loading limit of Pt on Au below which the Pt film decreases in activity and durability very rapidly due to presence of cationic Pt in that dimensional domain.

CHAPTER 6

PLATINUM ON TITANIUM DIOXIDE NANOTUBES

6.1 Modification of Titania for Catalysis and Photocatalysis

This section presents the influence of the growth scheme of Pt films on the resulting atomic and electronic structure of Pt species and the consequent activity for methanol electro-oxidation in Pt/TiO_2 nanotube hybrid electrodes. X-ray photoelectron spectroscopy (XPS) and X-ray absorption spectroscopy (XAS) measurements were performed to relate the observed electrocatalytic activity to the oxidation state and the atomic structure of the deposited Pt species. The atomic structure as well as the oxidation state of the deposited Pt was found to depend on the pre-treatment of the TiO_2 nanotube surfaces with electrodeposited Cu. Pt growth through Cu replacement increases Pt dispersion, and a separation of surface Pt atoms beyond a threshold distance from the TiO_2 substrate renders them metallic, rather than cationic. The increased dispersion and the metallic character of Pt results in strongly enhanced electrocatalytic activity towards methanol oxidation. This work points to a general phenomenon whereby the growth scheme and the substrate-to-surface-Pt distance dictates the chemical state of the surface Pt atoms, and thereby, the performance of Pt-based surface-intensive devices. Parts of this section have been recently published by the author[226].

It is widely recognized that the development of fuel cells that directly utilize renewable liquid fuels will require the design and optimization of new catalytic materials as well as new protocols that involve the modification of the currently used materials.[227] One critical component in these systems is the catalyst-supporting material. Titanium

dioxide is an attractive material as a support for metallic electrocatalysts due to the strong nature of the metal-support interaction.[228] Traditional fabrication processing routes of TiO_2 nanoarchitectures include the thermal oxidation of titanium metal at very high temperatures, template assembly and colloidal methods.[144] However, high temperature processes usually limit control over the fine interfacial features of TiO_2 films which significantly affect their properties.[229] Templated and colloidal synthesis routes require subsequent careful assembly onto conductive substrates as needed for device integration. Further, the resultant nanomaterials are prone to aggregation when the templates are etched away.[144] It is only through recent development of metal oxide etching processes that highly ordered TiO_2 nano-tubular structures (TNT) were produced directly on Ti foil, resulting in a structure that has all of the morphological benefits of traditional TNT while also enjoying the advantages of vertically oriented nanotubes with tunable height and diameter.[25-26, 230-233] Furthermore, this synthesis concept retains a metal back foil as an efficient electrical contact, which is very useful for electrocatalysis.

As the Pt/TiO_2 system is stable over a wide range of pH values,[234] work has been conducted studying traditionally grown Pt-modified TiO_2 for applications including the methanol electro-oxidation reaction, among others.[235-236] Of particular interest is the work by Lida et al. indicating that the $Pt\text{-}TiO_2$ support interaction can be employed to weaken the Pt-CO poisoning interaction.[237] However, it is still a challenge to achieve a high degree of dispersion of Pt over TiO_2 surfaces as well as increasing the catalyst load.

As with the design of an efficient catalytic system, rational design of beneficial metal-support interactions requires fundamental knowledge of the structure and the chemical nature of the grown metal films on the support. Therefore, this study is aimed at

exploring galvanic replacement of a Cu precursor to improve the dispersion and loading of Pt on TiO_2 nanotube surfaces as well as exploring the fundamental structure-property relationships of Pt-TiO_2 hybrid surfaces. The application of these materials is then demonstrated for methanol electro-oxidation. Specifically, we investigate transitions in the local atomic and electronic structure of ultrathin Pt films as a function of the method and the extent of film growth. We further investigate the relationship between the atomic and electronic structure of Pt to the activity of the resulting Pt-TiO_2 towards methanol oxidation. We believe this work to be very important for both electrocatalytic and photocatalytic applications and hope that this study will open a new vista to explore more metal-TiO_2 combinations for a diversity of various applications.

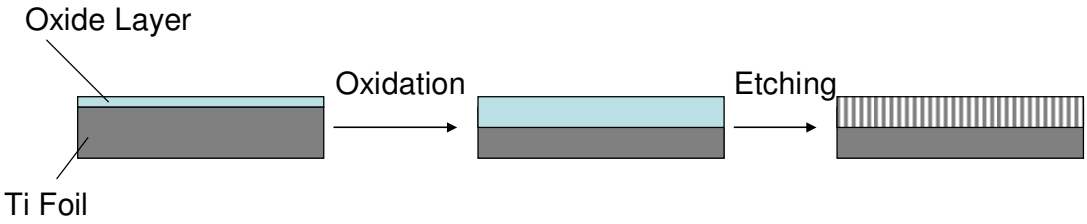

Scheme 6.1: Illustration of three-step formation of TNT array structure. In this specific case, the oxidation and etch steps were performed simultaneously in 0.2M NH_4F, 0.1M H_3PO_4 20V.

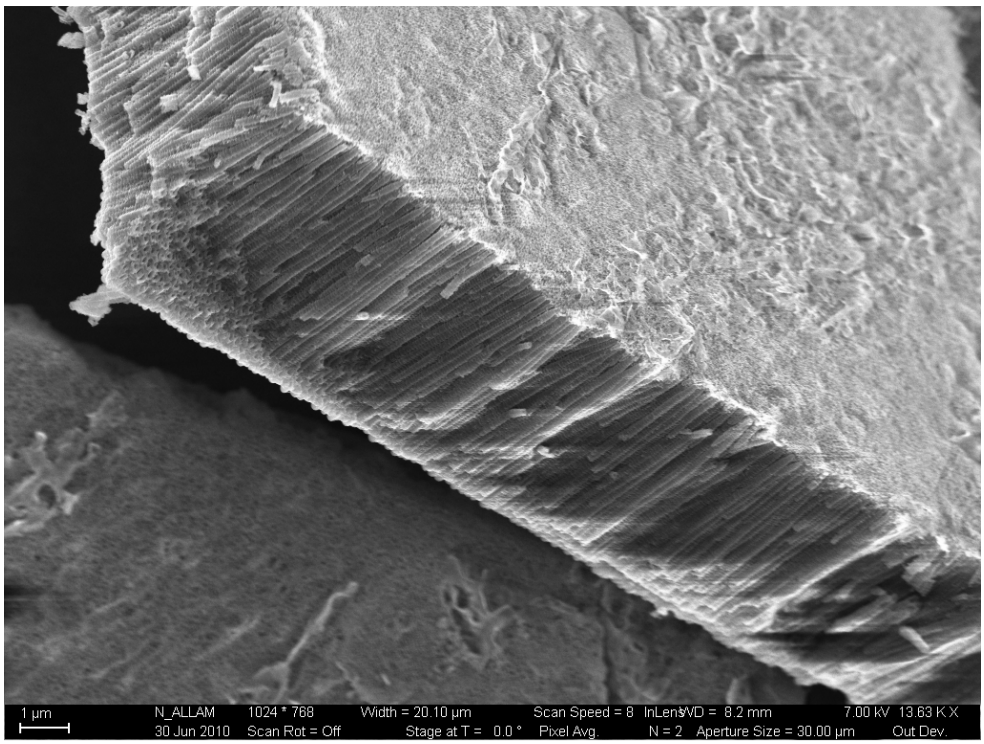

Fig. 6.1: Scanning electron microscope profile view of TNT array as grown by the oxidation/etch process. Note that the surface roughness of the top of the tubes is negligible compare to the overall tube length, and that all tubes are parallel to one another.

6.2 Details of Anodization and Modification

Prior to anodization, titanium foil samples were ultrasonically cleaned with acetone followed by a deionized (D.I.) water rinse. The anodization was performed in a two-electrode electrochemical cell with titanium foil as the working electrode and Pt foil as the counter electrode at room temperature (approximately 22°C) at 20V for 7h in an aqueous electrolyte containing 0.2M NH_4F, 0.1M H_3PO_4. An Agilent E3612A-CFG001 DC power supply was used for potentiostatic anodization. This procedure is illustrated in Scheme 6.1, and an SEM image of the resulting vertically oriented array of nanotubes can be seen in Figure 6.1. Afterwards, the samples were rinsed thoroughly with deionized water and isopropyl alcohol and then dried under nitrogen. Samples were not annealed, resulting in amorphous TNT structures. Pt deposits were formed by dipping in 1mM H_2PtCl_6 at open circuit for ten minutes with and without Cu precursor film. The Cu precursor, when present, was potentiostatically grown at -0.5V vs. Ag/AgCl from a 10 mM $CuSO_4$ + 50 mM H_2SO_4 solution for either 1 minute or for 5 minutes. This protocol is illustrated in Scheme 6.2.

The fabricated electrodes were examined using a Zeiss SEM Ultra60 field emission scanning electron microscope (FESEM). X-ray photoelectron spectroscopy (XPS) experiments were performed on the TiO_2 films using a Thermo Scientific K-alpha XPS system where the binding energy of all samples were calibrated to that of a Au reference sample. Pt L_3-edge EXAFS measurements were conducted at beamline X23A2 at the National Synchrotron Light Source (NSLS), Brookhaven National Laboratory. Measurements were made in glancing incidence fluorescence mode. The k-space data was truncated by a standard Hanning function before Fourier transforming to real space.

The electrodes were electrochemically characterized by cyclic voltammetry (CV) using a Pine WaveNow potentiostat in a three-electrode electrochemical cell with Pt wire as a counter electrode and a Ag/AgCl reference electrode. CV experiments were performed in 1M H_2SO_4 solution with 1M CH_3OH at a scan rate of 50 mV/s. Current densities are plotted as a function of Ti foil surface area before TNT growth.

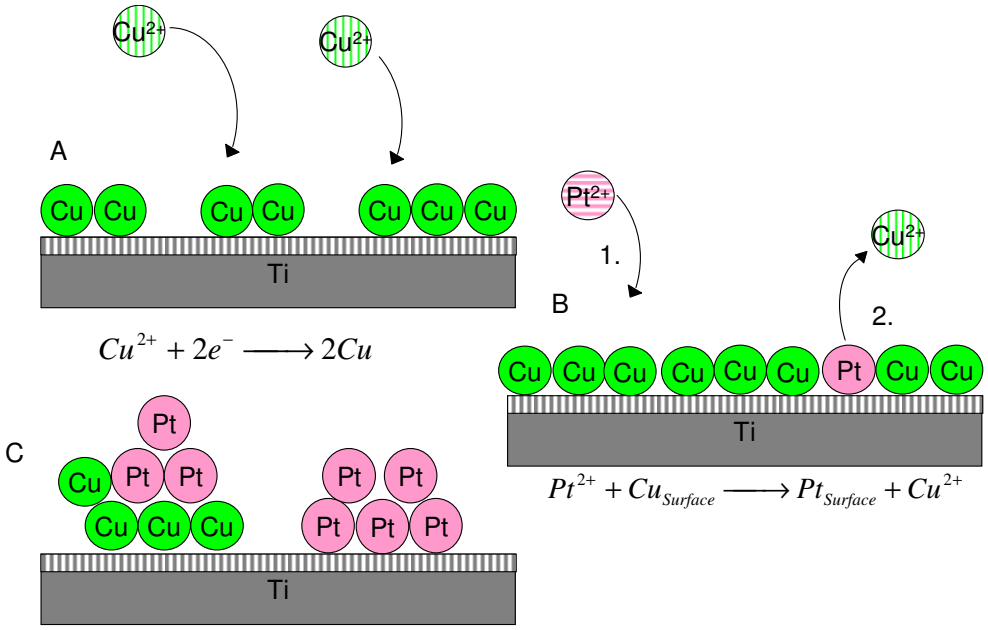

Scheme 6.2: Illustration showing Cu electrodeposition and replacement protocol on TNT surfaces. Note that some Cu deposit remains on the surface, and that a degree of clustering and nuclei formation is present for both Cu and Pt.

6.3 Sample Characterization

Samples were fabricated by exposing the TNT electrode to Pt^{4+} solutions with and without the presence of Cu precursors on the surface. The redox reaction of Pt^{4+} with Cu^{0} allowed Pt to grow in a highly dispersed manner on the surface at the expense of the Cu, which partially dissolved. This method resulted in morphologies with highly dispersed Pt co-existing with Cu/Pt. Scheme 6.3 portrays these microstructures in representative form, with Cu (blue) and Pt (red) deposits. The scheme illustrates the dispersion of small Pt nuclei that results from spontaneous Pt growth without Cu precursor. The increased dispersion which arises as a result of Cu-mediated growth is shown as a continuous red film coexisting with on-top Pt and Cu nuclei. 2D profile views of the scheme are provided to clarify that residual Cu is present both as an underlying film and as on-top nuclei. Cu-mediated growth is preferable to the direct galvanic growth of Pt, which would result in larger Pt nuclei. This type of redox replacement has been performed in the past for noble metals replacing Cu[93, 238], Ni[1, 239], and other metals on various substrates.

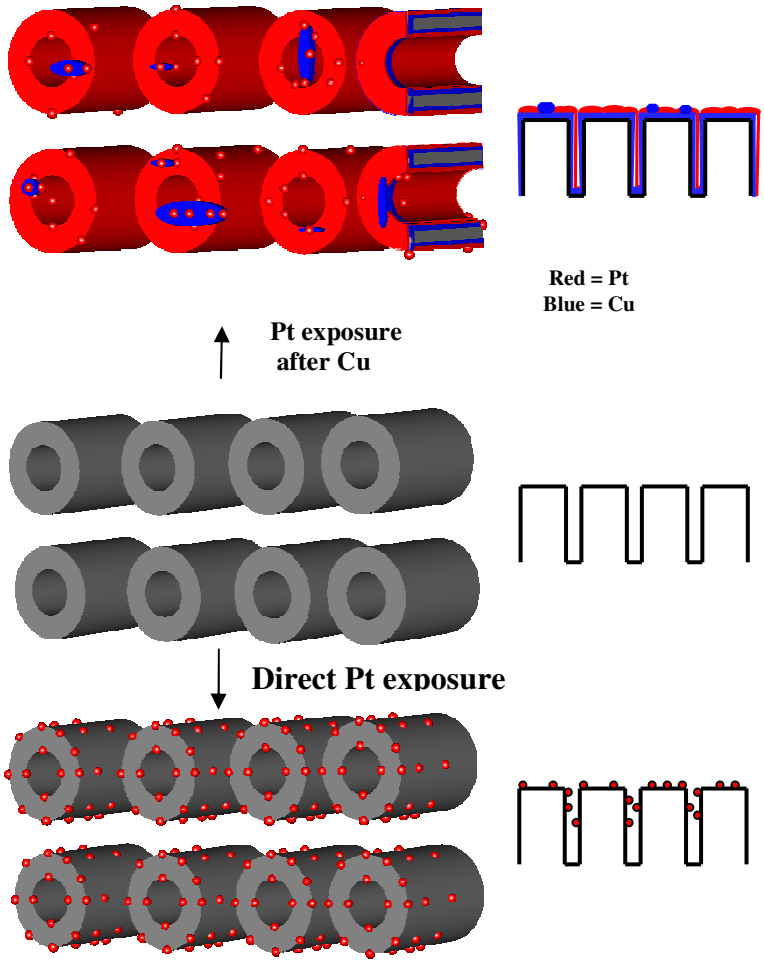

Scheme 6.3: Cartoon showing 3D and profile representations of TNTs with spontaneous Pt growth and Cu-mediated Pt growth. Note that Pt deposits (red) are grown on both Cu (blue) and TiO_2 sites in the Cu-mediated case.

Fig. 6.2 shows FESEM top-view images of the fabricated electrodes. Fig. 6.2A shows the as-grown TNT where highly ordered hexagonal close packed cells can be seen. Figure 6.2B shows the nanotubes after a 10 minute immersion in the Pt solution (1mM H_2PtCl_6) without any Cu precursor. Note the light-colored deposits nucleating around the rims of the tubes. Cu deposition for 1 minute followed by the same 10 minute immersion in Pt solution (Fig. 6.2C) resulted in coarsening of the tube walls due to thicker intra-tubular deposits as well as some supra-tubular nuclei 100-200nm in size. Increasing the Cu deposition to 5 minutes, followed once again by 10 minute Pt solution immersion, (Fig. 6.2D) appears to coarsen the TNT tubes further and increase the size of the supra-tubular deposits. Localized energy dispersive X-ray spectroscopy (EDS) analysis of the Pt-TiO_2 sample grown via 1 minute Cu precursor indicated that the supra-tubular nuclei contained both Pt and Cu in a 2:1 atomic ratio, on average, while the intra-tubular deposits showed a ratio of 5:1. For the 5 minute Cu growth, EDS indicated approximate Pt:Cu ratios of 4:1 on the nuclei and 1:1 on the tube sites.

To further investigate the surface composition and chemical state of the fabricated electrodes, XPS analyses were performed. Fig. 6.3 shows the Pt 4f XPS spectra for the different Pt-modified TNT electrodes. Lines at 71.1eV and 74.4eV indicate the location of Pt foil reference peaks. The spectra for the spontaneously grown Pt and the Pt after a 1 minute Cu treatment are positively shifted from that for the 5 minute Cu treated electrode, indicating that Pt exists in a cationic state. Specifically, the presence of a peak pair at 72.8eV, 76.2eV corresponds to $4f_{7/2}$ and $4f_{5/2}$ photoemission from Pt^{2+} species, while pairs in the ranges of 75.1eV-76.1eV and 78.4eV-79.5eV correspond to respective pairs from the Pt^{4+} species. The sample modified with electrodeposited Cu for 1 minute

has a higher proportion of Pt^{2+} compared to the spontaneously grown sample. However, the sample modified with a 5 minute Cu deposition does not show significant signs of cationic species, exhibiting only one pair of peaks (71.1eV, 74.4eV) indicative of metallic character. It is apparent that the chemical identity of Pt varies with growth treatment. However, XPS does not provide the atomic structure within the Pt deposits. Therefore, in order to characterize structure of the deposits, X-ray absorption measurements were performed.

Figure 6.4 depicts the magnitude of the real-space modified atomic radial distribution function, $|\chi(r)|$, of collected Pt L3-edge EXAFS data for 3 treatments of Pt on TiO_2 tubes, and a Pt reference. The inset provides the corresponding $\chi(k)$ functions. By examining the location of the lowest-coordination peak in real space, it can be seen that spontaneously grown Pt is nonmetallic in nature, with its first coordination shell located at 1.8Å (phase corrections not corrected for). Deposits grown via Cu precursors exhibit a first coordination shell characteristic of the metal reference, located at 2.4Å.

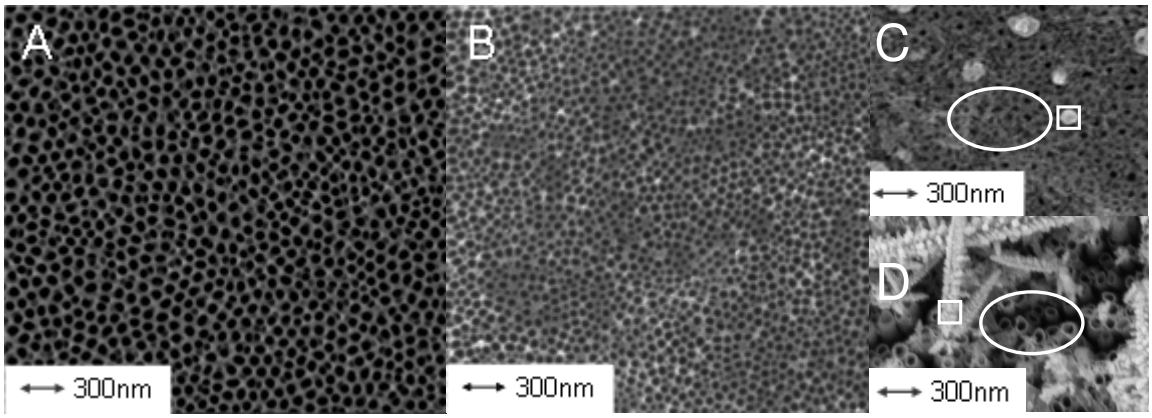

Figure 6.2: FESEM top view image of the TiO_2 electrode, (A) as prepared, (B) after 10 minute Pt exposure, (C) 1 minute Cu growth replaced by 10 minute H_2PtCl_6 exposure, and (D) after 5 minute Cu growth exposed to 10 minute H_2PtCl_6. EDS spectra were taken on tubular and supra-Cu regions as represented by the ovals and squares, respectively.

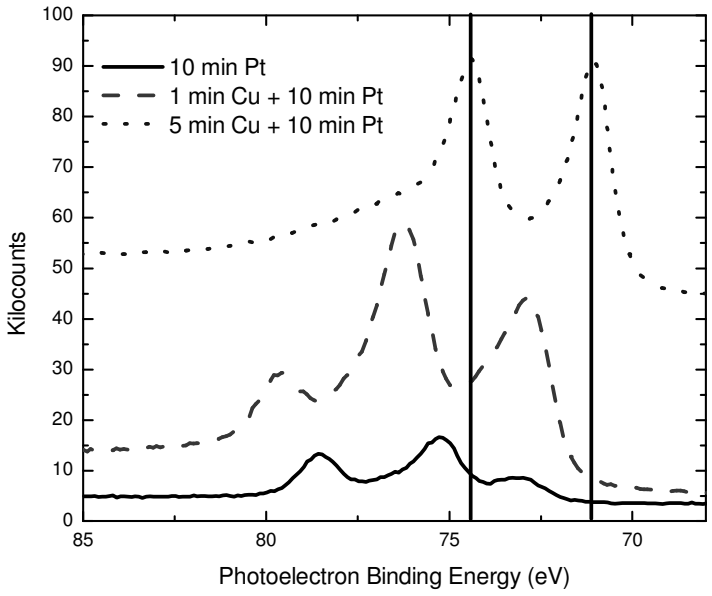

Figure 6.3: XPS Spectra of platinized TiO_2 nanotube electrodes. Lines indicate location of peaks for Pt reference foil.

It is apparent that the dipping of the TiO_2 nanotube electrode in H_2PtCl_6 solution resulted in the formation of intra-tube deposits of Pt species (Fig. 6.2A). This spontaneous growth likely occurs through the immobilization of $PtCl_6^{2-}$ at the exposed OH sites on the TiO_2 surface. This would explain the higher oxidation state for the spontaneously grown Pt species as evidenced by XPS analysis (Figure 6.3). This interpretation is further consistent with the EXAFS data for spontaneous growth, showing a lower first coordination shell distance of R=1.8Å compared to the 2.4Å coordination shell exhibited by the Pt deposits resulting from Cu replacement (Fig. 6.4). The presence of spontaneously grown Pt in the cationic form has many implications on its catalytic properties. For example, Hayden et al. showed very recently that the photocatalytic activity of the system CdS/TiO_2 is superior to the system CdS/TiO_2/Pt when used to photoelectrochemically disinfect E-coli.[6] On the other hand, Iwata et al. studied the charge carrier dynamics in TiO_2 and Pt/TiO_2 materials and found very fast electron decay kinetics in the Pt/TiO_2 system relative to the pure TiO_2 system.[21] They related this fast decay kinetics to the trapping of free electrons. However, in both cases, no explanation was given based on the electronic structure of Pt when attached to TiO_2. Our present results can clearly indicate the possibility of electron traps at the Pt cationic sites indicating that Pt cations can act as an electron sink. This finding is very important for the design of photoactive material systems.

When Cu precursor is used, the intra-tubular deposits are accompanied by some supra-tubular deposits, but in terms of Pt surface area, the intra-tubular deposits dominate. EDS shows us that even in the case of lower precursor content, 10 minutes are insufficient for Pt ions to replace all the intra-tube Cu. Increasing the amount of Cu

precursor deposition should result in topical Pt that is further away from the TiO_2 substrate and in diminishing Pt-TiO_2 metal-support interaction. The assertion is supported by the XPS data when comparing the Pt oxidation states between the samples. When surface Pt is relatively closer to the support (1 min. Cu deposit case) it remains cationic while the Pt which is further from the support (5 min. deposit case) is metallic. We suggest that in the former case the underlying TiO_2 continues to immobilize $PtCl_6^{2-}$ on the surface in much the same way as with the spontaneous Pt deposition scheme. In the latter case, the surface Pt is beyond the threshold Pt-TiO_2 metal-support interaction distance. At the same time the net atomic structure of Pt, as seen by EXAFS (Figure 6.4), for both cases where it is grown through Cu replacement retains the FCC-like structure characteristic of metallic Pt. This suggests that while the Pt deposits resulting from 1 minute Cu doses arrange themselves as Pt metal, their surface chemistry is still dominated by an oxidic character (as seen by XPS).

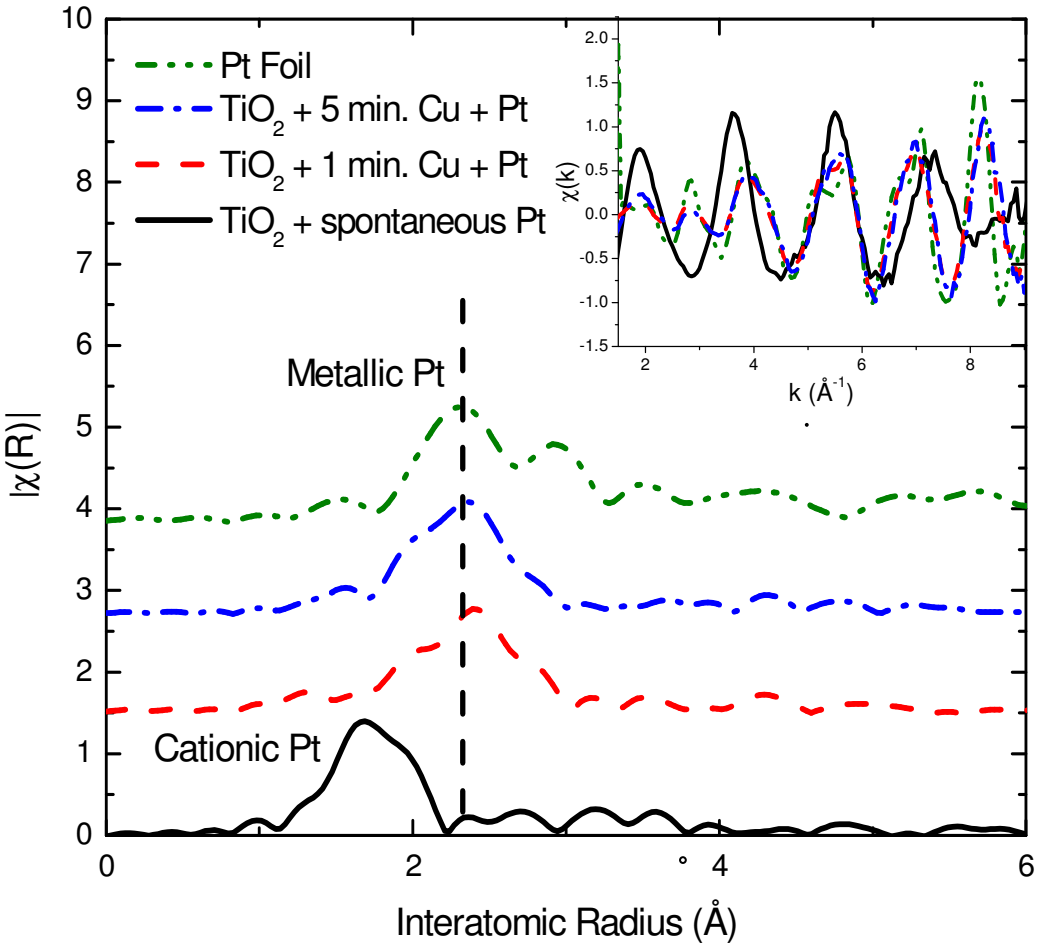

Figure 6.4: Fourier transform of Pt L3-edge EXAFS data of TiO_2 samples with and without varying Pt treatment methods. Inset shows k-space spectra before Fourier transform.

6.4 Catalytic Activity

To evaluate the electrocatalytic activity of the fabricated electrodes, cyclic voltammetric (CV) studies were carried out in 1M sulfuric acid with 1M methanol, see Fig. 6.5A. Note that the methanol electro-oxidation currents were seen during the forward sweep at 0.75V and during the reverse sweep at 0.52V for all samples treated with Pt, with higher currents recorded for the samples pre-modified with Cu layer. During the anodic scan, the current increases due to dehydrogenation of methanol followed by the oxidation of absorbed methanol residues, while in the cathodic scan, the re-oxidation of the residues is occurring. It is important to note that the cyclic voltammogram for the Pt-dipped TNT without any Cu modification is shown in 5x scale to aid readability. Figure 6.5B displays the peak currents after normalization to integrated Pt XPS peak area, which is proportional to the surface loading of Pt. The high electrocatalytic activity of Pt/TiO_2 hybrid electrodes can be mainly attributed to the remarkably active Pt sites on the TiO_2 nanotube matrix. As amorphous titania nanotubes have many OH groups on their surfaces [20], it is possible that these OH moieties help in the conversion of CO poisoning species into CO_2, leaving the active sites on Pt clean for further electrocatalytic reactions in a similar way to that which Ru is doing in the commercially used Pt-Ru/C catalysts. In addition, the strong metal-support interaction could be another reason for the observed enhanced electrocatalytic activity of methanol oxidation at Pt/TiO_2 hybrid electrodes.

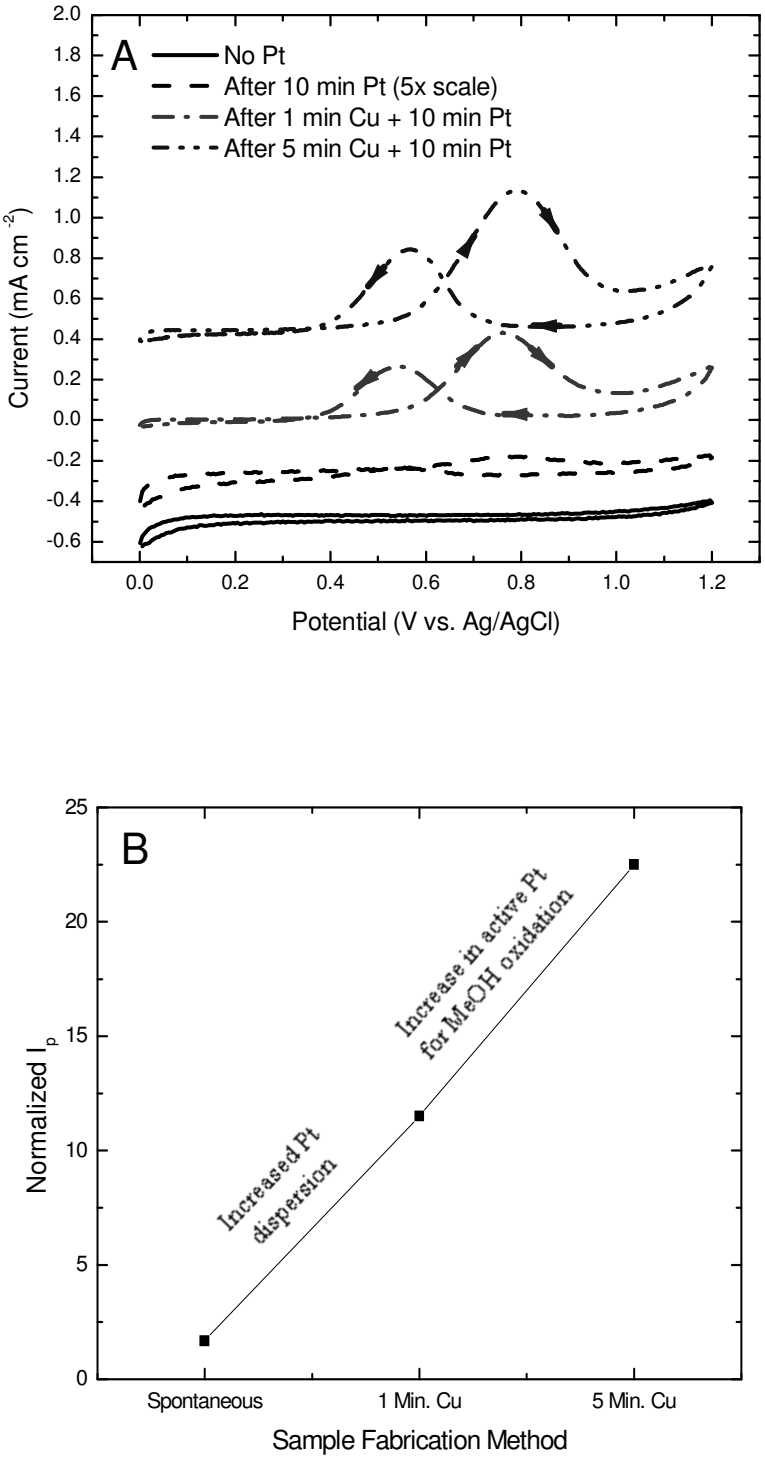

Figure 6.5: (A) Cyclic voltammograms of the electrodes in 1M H_2SO_4 + 1M Methanol. (B) Forward peak current (I_P) values normalized to Pt surface loading as measured by XPS.

By normalizing the methanol oxidation currents to the integrated XPS area for Pt, we get a measure of the reactivity per unit Pt present on the surface (Fig. 6.5B). This allows us to relate performance to the local environment and oxidation state of the as-grown deposits. While Cu replacement increases Pt dispersion, growth beyond a threshold film thickness ensures a predominance of metallic, rather than cationic, Pt on the surface. We see clearly that Pt grown beyond this threshold metal-support interaction distance retains metallic character and exhibits enhanced electrocatalytic activity towards methanol oxidation.

Additionally, the Pt-TNT electrodes were tested in 1M NaOH solution for photoelectrochemical water splitting applications. This test was performed using a Xe arc lamp and a filter to simulate the solar spectrum. The hypothesis when starting this experiment was that the cationic Pt sites would serve as electron traps and decrease the efficiency with which photoelectrons are made available for the water splitting reaction. This detrimental effect would be counter to what is expected for metallic Pt, which would ideally provide a catalytic reaction site for the water splitting reaction to occur (using the TNT-generated photoelectron). In experiment, we saw that the cationic-containing Pt samples performed significantly worse than the metallic-containing samples (Fig. 6.6). In fact, the samples with significant cationic Pt performed even worse than bare TNT itself, showing higher voltages and lower currents required for the water splitting reaction. As the Pt metal content was increased, the voltage required for the water splitting reaction to proceed decreased correspondingly. This suggests that the TiO_2-affected cationic Pt sites function as recombination sites for the photoinduced electron-hole pair and actually

decreases performance. As this cationic effect is minimized by employment of a Cu precursor, the performance is seen again to increase.

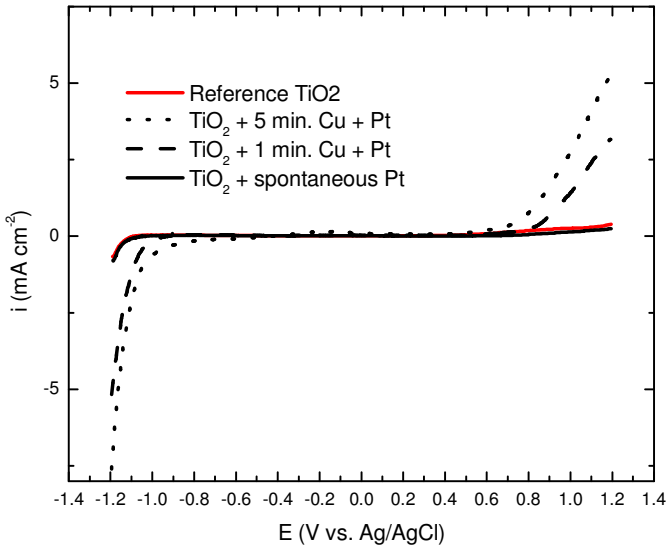

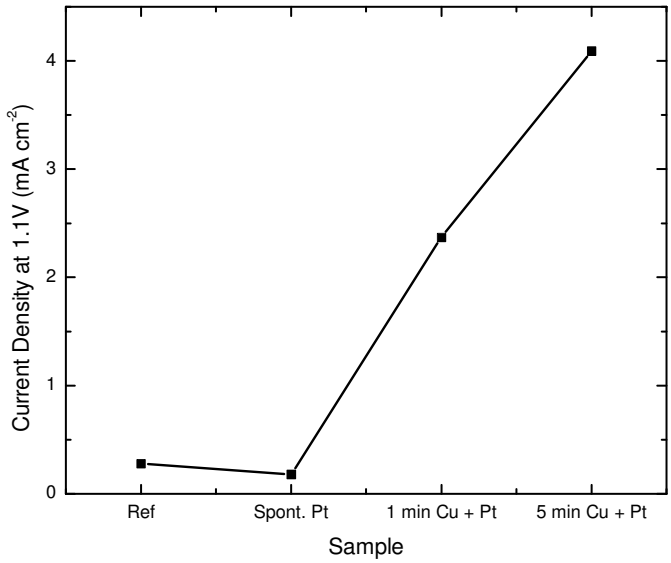

Fig. 6.6: (a) Sweep voltammetry of Pt-TiO_2 samples in 1M NaOH during exposure to Xe lamp with filter. (b) Oxidation current density for each sample at 1.1V.

6.5 Conclusions

In this section, the platinization of titanium-foil-supported, highly ordered, vertically oriented titania nanotube arrays (TNT) by spontaneous growth and galvanic replacement of a Cu precursor layer was presented. We have tracked, using SEM and quantitative image analysis techniques, the formation of increased intra-tubular metal deposition. Spontaneously grown Pt exhibits cationic local structure, limited dispersion and relatively low activity for methanol electro-oxidation and photocatalytic water splitting. With the pre-deposition of Cu, the dispersion of surface Pt is significantly increased. Increasing the metal-support distance, by increasing the thickness of the Cu pre-deposited layer, renders the surface Pt metallic rather than cationic, which further increases the activity of Pt for methanol electro-oxidation and water splitting.

6.6 Supplemental: Stereological Analysis of Morphology

It was possible to determine, with statistically relevant quantification methods, the location of Pt and Cu nuclei growing on the Pt-TNT and Pt-Cu-TNT architectures. Since the tubular structures inherent to a TNT substrate are all vertically oriented parallel to each other, and each tube is centered around a central void which runs the length of the tube, it was possible to focus on these voids as the primary feature for this analysis. The quantification technique utilizes point counting and intersection counting techniques and was used to quantify the void volume, the surface area of the void-tube interface, and the number density of voids. By tracking the changes in these values after various treatments of the TNT structure, it was possible to determine, for an average nanotube site, where the majority of the deposits (both Pt and Cu) were forming. This simple and powerful technique was applied to a series of SEM images. Since the tubes are all vertically oriented and can be assumed to exhibit consistent diameter as a function of individual tube height, fluctuations in the sample height could safely be neglected and the SEM images were treated as planar surfaces for the purposes of quantitative point and line counting.

For any TNT array, there is a certain amount of the surface plane that is occupied by void space, corresponding to the holes that make up the inner diameter of the tubular structures. Since the tubes are all parallel, it is possible to determine the volume fraction of voids as compared to the volume fraction of the actual TNT walls by measuring the area fraction in the surface plane as imaged by SEM. Furthermore, the area fraction can be approximated by measuring the fraction of a random set of points falling in the regime of interest. This type of extrapolation of point fraction measurements to volume fraction

values is commonly performed and is widely accepted[240]. This simple relation, written in terms of a two-phase α-β system, is given in Eq. 6.1:

$$V^{\alpha}/V_{tot} = A^{\alpha}/A_{tot} = P^{\alpha}/P_{tot} \quad \text{(Eq. 6.1)}$$

Where V^{α} denotes volume, A^{α} denotes area, and P^{α} denotes number of points of phase α in the imaging plane, while V_{tot}, A_{tot}, and P_{tot} denote the total volume, area, or number of test points in the sampling space. By tracking the decrease in this void area, we are essentially measuring the decrease in the inner diameter of the tubes themselves (which is correlated directly with thickening of the nanotube walls). This type of knowledge is extremely important for electrodeposition of metals onto tubular structures, as it allows us to determine if the deposition process is occurring preferentially at sites within the tubes or on top of the tubes. For example, if deposition proceeds exclusively at on-top tube sites, the observed wall thickness will not change appreciably (assuming no blocking of visible voids by sufficiently large on-top nuclei). On the other hand, if growth occurs exclusively inside the tubes, then the wall thickening rate will be significantly higher than if the growth was homogenous across the tube structure itself.

It is also possible to measure the surface area per unit volume of a specific interface. In this case, the interface in question is the tube/void boundary. The surface area of this boundary is equal to the surface area of the inner wall of the tubes. In other words, this parameter only measures the area internal to the tubes and excludes the on-top sites mentioned previously. This calculation is performed based on measurement of the number of intersections between a randomly placed test line and the phase boundary

corresponding to the interface of interest. The relationship between the measured intersection number and the calculated volumetric surface area is given in Eq 6.2, where S_v denotes the interfacial area per unit volume, and P_L denotes the number of measured intersections per unit test line length[241].

$$S_v = 2 \cdot P_L \quad \text{(Eq. 6.2)}$$

Finally, it was possible to measure the number density of voids per unit area of the image surface. This allows us to track the annihilation of internal tube voids through accumulation of electrodeposited material, or the creation of new perceived voids by the 'bridging' of an existing void by an electrodeposited particle. This figure is obtained simply by counting the number of voids in a series of randomly placed test areas, according to a specific set of counting rules[242].

The results of these imaging analysis tests are plotted in Figure 6.7(a-c). These data will help distinguish between two types of growth modes: on-top growth where deposits mask the underlying nanotubular voids, or internal growth where the deposit grows preferentially inside the tubes. It is clear from a cursory analysis of figure 6.7(a) that the total void volume decreases for both open-circuit and Cu-mediated Pt growth. This is to be expected and is congruent with both proposed growth modes. However, in figure 6.7(b), we see an increase in interfacial area for the spontaneous Cu deposit, and a decrease in interfacial area for the Cu-mediated deposit. This suggests that on-top growth (which would create new perceived interfacial area for bridging deposits) is occurring for the spontaneous growth step. Similarly, the Cu-mediated step leads to internal growth, based on the decrease in interfacial area, which corresponds to decreasing void radii.

This analysis is corroborated by the number density data plotted in figure 6.7(c), which exhibits a similar trend. Since there is no electrochemical reason to expect the spontaneous deposition step to create new voids, we conclude that the increased apparent number density is due to the presence of the previously suggested ‘bridging’ deposits which cause a single tube void to appear as two voids in the image. The void number density for the Cu-mediated case, which is greater than the initial case but less than the spontaneous case, also corroborates the interpretation of the interfacial area data, suggesting the presence of both internal and on-top deposition sites.

Thus we are able to conclude, based on statistically significant image processing techniques, that the morphological change induced by the Cu-mediated Pt deposition process is quantifiably different from the simple spontaneous growth mode. This allows us to correlate the changes in surface chemistry observed in XPS, and the increased performance for the methanol electro-oxidation reaction, with increased deposit dispersion and dominance of the internal growth mode on the tubular surface.

Figure 6.7: Results of quantitative image analysis as a function of sample preparation technique: (a) Volume fraction of voids in the TNT surface, (b) Void-Tube interfacial area per unit volume, and (c) Number density of voids in the TNT structure

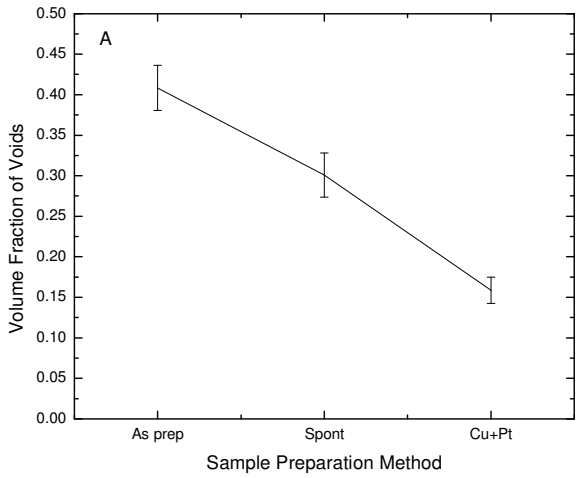

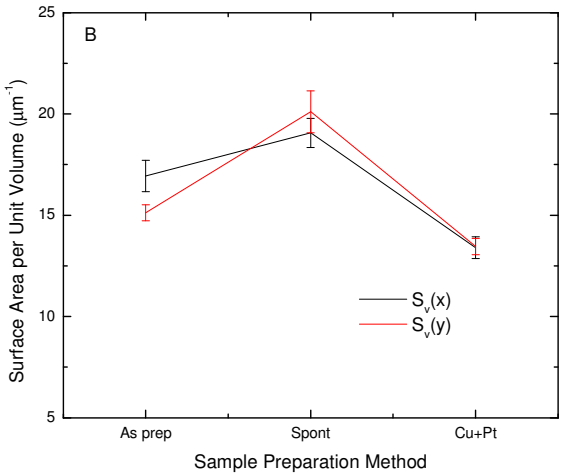

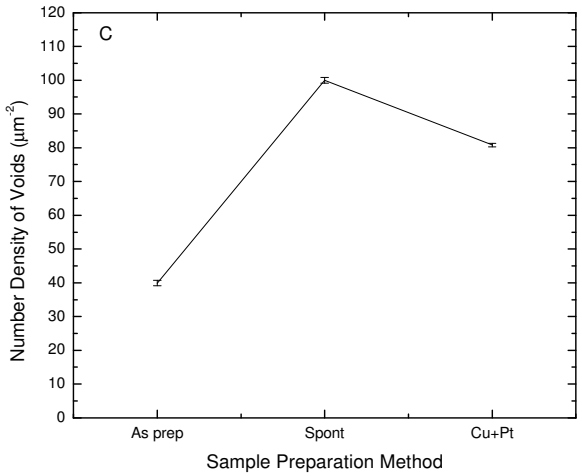

CHAPTER 7

CONCLUSIONS AND RECOMMENDATIONS

This study has addressed several structure-property relationships related to surface chemistry for both the Pt-Au and Pt-TiO_2 systems, including surface chemical identity, electronic structure, and local atomic structure. Changes in these properties have been shown to depend on fabrication method and nano-scale architecture of both nanotubular and nanofilm-overlayer geometries. A complementary suite of techniques, including X-ray photoelectron spectroscopy (XPS), X-ray absorption spectroscopy (XAS), and votammetric techniques have been shown to provide comprehensive information regarding coverage, electrochemical reactivity, valency, and structure of adsorbed surface species. This has led to the discovery of a novel behavior for CO electro-oxidation at the Pt-Au surface, which has been shown to result from increased OH^- affinity and enhanced substrate-adlayer electron transfer properties. Furthermore, the influence of a metal oxide such as TiO_2 on the oxidation of adlayer Pt deposits has been shown to play a significant role in the reactivity of Pt toward methanol electro-oxidation. Thus, this study allows for the identification of minimum thickness/size thresholds below which Pt deposits should not be fabricated on Au or TiO_2 supports in order to obtain ideal reactivities towards CO or methanol.

In addition to the creation of fundamental knowledge regarding electron transfer and atomic structure in these architectures, important discoveries have been made in the field of nanofilm fabrication by surface limited redox replacement (SLRR). This work has led to publication of the first-reported use of overpotentially grown sacrificial layers to

conduct SLRR, which will lead to further advances and the ability to use SLRR to grow a wider range of elements. Furthermore, flaws in the nominal reaction mechanism widely assumed to apply to traditional SLRR fabrication have been identified. These flaws include the assumption that the metal grown via SLRR is entirely zero-valent and have been exposed by detection of oxide species using cyclic voltammetry, XPS, and XAS. The use of this broad set of techniques has permitted not only the identification of the erroneous assumption that has been previously made, but also the proposal of a new reaction mechanism that accounts for these new experimental findings. Finally, this work identifies the range of sample geometries for which this new mechanism is applicable, and also the range of geometries for which the traditional mechanism is applicable.

This work also reports testing of the substrate-adlayer systems that will lead directly to improved catalyst performance. By conducting accelerated aging tests for the Pt-Au monolayer system using ethylene glycol and methanol electro-oxidation as probes, regimes of enhanced nanofilm corrosion have been successfully identified and correlated with specific chemical species and atomic structures on the catalyst surface. These aging tests have also shown that new reaction sites for the ethylene glycol reaction are created then annihilated during reaction cycling.

Many questions still remain to be answered in this field of bimetallic surface chemistry, however. This work has laid the groundwork for continuing studies using the same techniques of electrochemical fabrication followed by advanced X-ray analysis and reactivity testing. Several projects have been initiated during the course of this work that were not deemed complete enough for inclusion, specifically, the growth of nanoscale Pt and Au deposits on various other metal and metal-oxide substrates. These substrates

include Ni, Ag, MnO_2, and CeO_2. Additionally, the inverse monolayer-substrate system, Au on Pt, has been partially investigated and found to show interesting results with regard to partial film oxidation and electron transfer. The reader is also referred to Appendix I, in which a vacuum-based surface science study of the oxidation and reactivity toward epoxidation of the Ag-Ni monolayer-substrate system is presented.

Further innovations to the SLRR technique have also been initiated as a result of the work using Ni sacrificial layers shown here. Initial results using nonaqueous UPD of Li metal as a sacrificial layer to grow Cu adlayers have proven successful, but have not been pursued to completion due to limitations in synchrotron time. Thus it can be seen that this work, through the innovative use of electrochemical fabrication of high-precision monolayer samples, has added to the fundamental understanding of electron exchange at bimetallic surfaces as well as to the practical implementation of nanoscale Pt catalyst surfaces and the use of SLRR as a fabrication technique. Future studies that build on this work and complete the ongoing projects outlined in this section will lead to the study of a variety of metal-substrate pairings and the study of trends within these pairings.

APPENDIX A

ETHYLENE AND OXYGEN ON SILVER-NICKEL

A.1 Introduction

Catalysis science is persistently motivated by the search for low-cost multicomponent systems where the various components contribute in tandem or in concert towards important reactions. An ideal catalyst system would have only small but requisite amounts of the expensive components which would retain their value by remaining segregated to surface sites over multiple reaction cycles. Catalytically active transition metals in particular are prime candidates for this type of application. The Ag-Ni system, for example, where the two metals are virtually immiscible with one another,[243] is a model for such a system. With a low thermodynamic drive for intermixing, a small amount of silver decorating the surface of nickel should remain segregated to the surface with predictable catalytic properties.

Both Ni and Ag have separately been found to contribute to different parts of the overall conversion reaction from ethane to ethylene oxide (EO). EO and its derivatives are widely used in the plastic and other industries. A single Ni-Ag catalyst, with a small amount of Ag on the surface of Ni, has the potential to strongly impact these industries by catalyzing a one-step reaction from ethane to EO. The full conversion from ethane to EO involves an oxidative dehydrogenation of ethane to ethylene and the subsequent epoxidation reaction to convert the ethylene to ethylene oxide. Ag is currently the industrial catalyst for the latter reaction due to its high activity for ethylene oxidation[244-246]. Recently, Lei et al. have shown what appears to be the first example of epoxidation of

a higher alkene, in this case propylene, by using subnanometer sized Ag catalysts[247]. Ni-based catalysts, on the other hand, have been shown to be efficient for the dehydrogenation reaction in an oxidative environment[248-250]. In general, oxygen, important for the epoxidation reaction, adsorbs poorly on Ag at low temperatures in comparison to Ni, and so one would expect that ethylene epoxidation occurring at Ag sites might benefit from oxygen present on nearby or underlying Ni sites. Still, the effectiveness of a primarily Ni catalyst with only a nominal, submonolayer, amount of Ag on its surface for the overall epoxidation reaction has not been investigated systematically[251].

Considerable work has been previously reported for oxygen and ethylene adsorption on both Ag and Ni surfaces. The oxidation of Ni has been studied by temperature programmed desorption (TPD)[252], low energy electron diffraction (LEED),[253-255] X-ray photoelectron spectroscopy (XPS),[252, 254, 256-265] and other techniques. In general, Ag is a poor candidate for oxygen adsorption at low temperatures. However, Benndorf et. al. found that oxygen doses conducted at 500K+ could activate the Ag(111) surface for oxygen adsorption[256]. Additionally, the characterization of the various reconstructions of Ag-O surface oxides has been of significant interest[266-267]. Many studies have been conducted for ethylene on Ag, and some have attempted to modify Ag surfaces for the selective epoxidation of ethylene in preference to the full oxidation reaction[268-274]. In addition to single crystal studies, attempts to enhance the selectivity of Ag for epoxidation reactions have also been conducted. These studies attempted to oxidize the Ag surface, and succeeded in identifying two types of adsorbed oxygen species, corresponding to O^{1-} and O^{2-}. Neither of these species, in the absence of

the other, causes the selective epoxidation reaction. However, when both species are present, a selective epoxidation reaction similar to that shown in Eq. 1 proceeds[269-270]. It has also been found that modification of the Ag surface with alkali metals and Cl can enhance the activity of a Ag surface for ethylene epoxidation[273-274]. Additionally, it has been shown that the addition of Cu to Ag particles enhances selectivity by modification of the surface chemisorbed oxygen species[275].

Eq. 1 $3C_2H_4 + 3O_2 \rightarrow 2C_2H_4O + 2CO_2 + 2H_2$

In addition to the study of Ag surfaces, ethylene adsorbed and reacted on Ni surfaces has also been a subject of much study[276-282]. STM studies of ethylene decomposition on a clean Ni(111) surface indicate preferential C-C bond breakage on step edge sites at room temperature. This preference disappears for elevated temperatures. The addition of Ag to the Ni(111) surface has been shown to inhibit C-C bond breakage[278].

In this work we have made a systematic study of the role of Ni, of Ag and the cooperation of Ni with Ag in the ethylene oxidation reaction. The work was carried out on Ni(111) single crystals modified by high temperature oxidation and submonolayer Ag film growth and studied using temperature-programmed X-ray photoelectron spectroscopy (TP-XPS). In addition to TP-XPS, the dependence of the adsorbate behavior on substrate morphology was interpreted by quantitative analysis of low-energy electron microscopy (LEEM) and valence band photoemission electron microscopy (VPEEM) data. In this study, we report increases in ethylene oxidation activity and robustness arising from step-edge grown Ag on Ni(111), as well as a correlation of these properties with the presence of different oxygen species.

A.2 Experimental

The Ni(111) single crystal was prepared by cycles of Ar sputtering followed by annealing the sample to 1000K for 10-15 minutes. This protocol was sufficient to render clean and atomically flat Ni(111) surfaces free from impurities as verified by XPS and reported previously[265, 283]. After initial cleaning, sputtering was not repeated since heating to 1000K alone was sufficient to remove Ag, C, and O buildup during studies from the surface[284]. Ag layers of varying thicknesses were grown via vapor deposition on the surface of a freshly-cleaned Ni(111) single crystal using a Knudsen cell at a deposition rate of about 0.1 ML/min. This mode of Ag growth has been studied previously and been found to produce layer-by-layer growth up to 2 ML under the proper conditions[284].

LEEM and VPEEM data were collected on a commercial Elmitec LEEM III (low-energy electron microscope) equipped with a hemispherical energy analyzer for spectroscopic photoemission at the beamline U5UA of the National Synchrotron Light Source (NSLS), Brookhaven National Laboratory (BNL), Upton, NY (USA). Further description of the LEEM-PEEM system can be found in a previous work[285]. XPS spectra were collected at beamline U12A at the NSLS at BNL. The energy resolution of the XPS data is nominally 0.3eV. The photon energy was selected by way of a toroidal spherical grating monochromator (TSGM). The incident energies selected were element specific including C1s (400eV), O1s (600eV), and valence band (VB) (400eV). These energies were selected to optimize the photoelectron cross-section and surface sensitivity of the study. The reference valence band spectrum used to calibrate Ag coverage was collected at 40eV. XPS data were converted to binding energy by assigning zero binding energy (B.E.) relative to the Fermi edge using reference spectra. All XPS intensities were

normalized to the incident intensity of the photon source prior to quantitative analysis of the TP-XPS spectra. XPS peak fitting was performed with symmetric peakshapes (Gaussian).

A.3 Results and Discussion

Experiments performed, in order of presentation in the following results section, included Ag growth and calibration, low- and high-temperature oxidation of bare and Ag-modified Ni(111), and ethylene reaction on four permutations of Ag- and O-exposed Ni(111). For TP-XPS studies, samples were allowed to cool after heating to the indicated temperature before spectra were collected.

A.3.1 Ag Growth and Calibration:

Figure A.1 shows valence band spectra for the clean Ni(111), 0.3ML, and 0.7ML vapor deposits of Ag on Ni(111) as well as VPEEM reference data for one monolayer of Ag on Ni(111). The Ag $3d_{5/2}$ features at 6eV reflect the amount of silver grown on the surface, and increase with larger Ag deposits. The reference data correspond to exactly 1ML coverage as confirmed by LEEM imaging, and the 0.3ML and 0.7ML values are assigned based on quantitative comparison of peak sizes. Although spectra for clean Ni(111) and 0.3ML Ag+Ni(111) look similar, the difference in peak intensity at 3eV indicates Ag growth. This way of calibrating the coverage confirms results for the calibration of valence band spectra as previously reported by Varykhalov et al[286]. For oxidation studies, Ag was deposited at 600K. For ethylene studies, Ag was deposited at 400K then annealed at 800K. This was done to ensure that the Ag deposit had equilibrated to a stable morphology before dosing ethylene, in order to discriminate ethylene desorption events from Ag rearrangement events. Valence band spectra were employed to verify that comparable quantities of Ag were grown in both cases.

Additionally, the LEEM technique allowed the in-situ study of the sample surface with a high lateral resolution up to 10nm under ultra-high vacuum (UHV) conditions. This study

of the growth modes of vapor-deposited Ag on Ni(111) surfaces allowed us to identify the preferential adsorption of Ag at step-edge sites in the chosen temperature regime. Figure A.2 contains two LEEM images of Ag (light colored) growing on a stepped Ni(111) surface (dark colored) at 600K. Notice in Figure A.2A, for a coverage of 0.4 ML, the initial Ag growth at step edge sites (shown as lines across the substrate). In Figure A.2B, at an increased coverage of 0.65 ML, the Ag areas have covered significant terrace surface area. By this method we conclude that, for the samples used for photoelectron spectroscopy, our 0.3ML Ag deposit decorates primarily step-edge sites, leaving an overwhelming fraction of the Ni surface area exposed, while at 0.7ML the Ag covers both step-edge and terrace sites, which allows us to selectively probe the influence of these sites in the targeted chemical reactions. The electron energy used for the presented images is 14.0eV at 10 μm field of view.

A study outlining further details of the LEEM work performed, as well as analysis of silver growth modes at different temperatures, can be found in a recently published work[287]. Based on these LEEM images and corresponding valence band spectra, we conclude that our Ag deposits studied in XPS are all sub-monolayer coverage as calibrated previously, with smaller deposits decorating step edges and larger deposits covering both terrace sites and step edges.

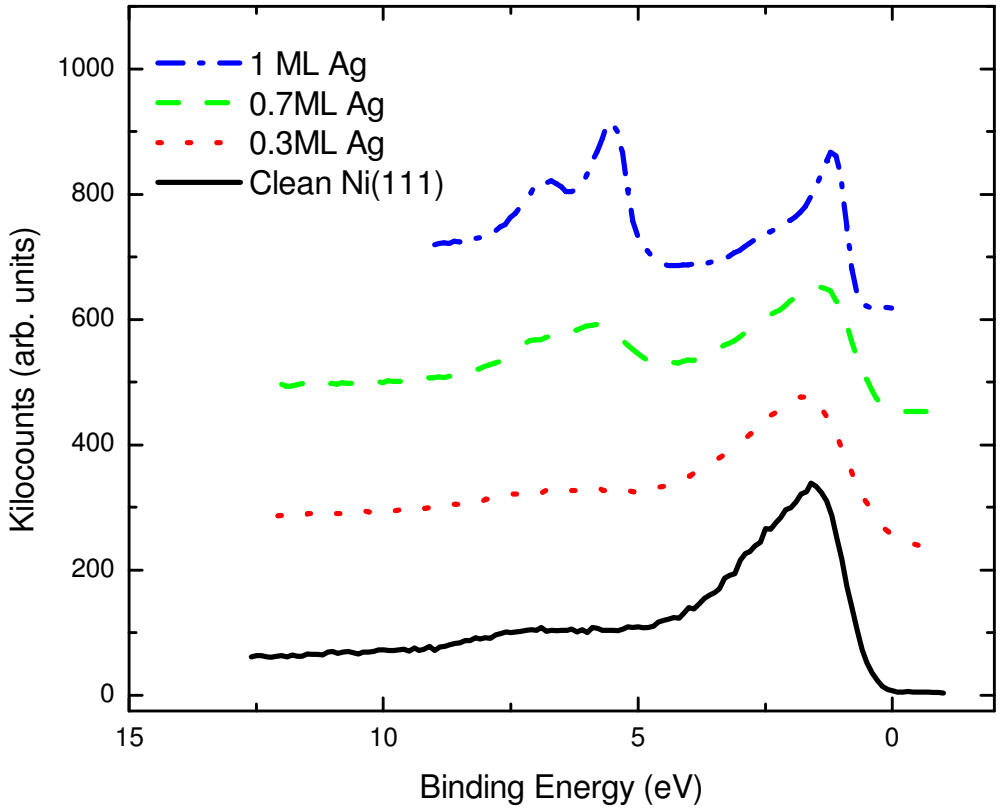

Fig. A.1: Valence band XPS spectra for the clean Ni(111) surface, (solid line) 0.3ML Ag, (dotted line), 0.7ML Ag, (dashed line) and reference VPEEM data for 1 ML Ag (dash-dot line), as verified by LEEM.

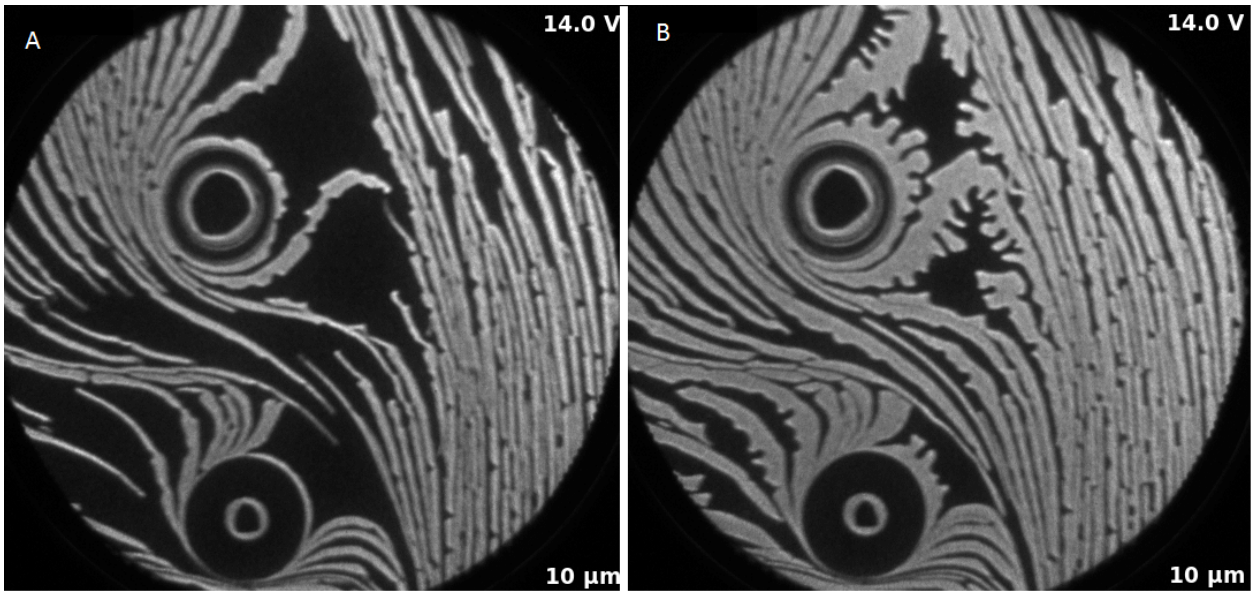

Fig. A.2: LEEM images collected for Ag (lightly colored) growing on Ni(111) (dark colored) from vapor-phase deposition. Images were taken at coverages of 0.4 ML (A) and 0.65 ML (B). Ag growth begins at step edges and then spreads to terraces. The electron energy used for the presented images is 14.0 eV at 10 µm field of view.

A.3.2. Study of Surface Oxidation

A.3.2.1. Oxidation of Ni(111):

The study of oxygen adsorption, reaction, and desorption on the Ni(111) and Ag-Ni(111) surfaces is key to understanding the results of, and the mechanism behind, the ethylene oxidation reaction on the same surface. First we examine and identify the types of surface oxygen formed with various amounts of surface Ag present, and then employ this knowledge of the substrate-oxygen reaction to assist our analysis of the ethylene-substrate-oxygen interactions, which will be presented in a following section.

Oxidation studies were conducted for three different substrate conditions: clean Ni(111), Ni(111) with 0.3 ML Ag (step edges and minimal Ag at terrace sites), and Ni(111) with 0.7ML Ag (step edges + large amount at terraces). In all cases oxygen was dosed at 10^{-6} Torr for 200s, resulting in a total dose of 200L. O_2 was dosed onto the fresh Ni(111) or Ag/Ni(111) surface at 100K followed by flash heating to various temperatures, after which XPS data were collected. This flash heating was conducted simply by heating to the indicated temperature and then immediately cooling prior to XPS measurement. Subsequently, the cleaned sample was held at 500K while exposed to oxygen, followed by flashing to discrete temperatures above 500K, after which XPS data were collected. The data are labeled according the temperatures they were flash heated to.

Figure A.3 shows the oxygen 1s XPS spectra for oxygen exposure at 100K on the 3 differently prepared samples. Three species of oxygen are apparent on the surface for these data. For clean Ni(111) (Fig. A.3A), the largest peak at 100K, at a binding energy of 532eV, shrinks upon initial heating. A small shoulder at 533.2eV is also present at 100K, but disappears with initial heating. At 250K, a pair of oxygen peaks at binding

energies 530.2eV and 532eV remains. As the sample is heated past 250K, the peak at 532eV disappears between 550K and 700K, while the 530.2eV peak persists in very small amounts even at 850K.

A.3.2.2 Oxidation of Ag/Ni(111):

For 0.3ML Ag coverage (Fig. A.3B) and 0.7ML coverage (Fig. A.3C) we observe similar behavior, with peaks present at the same binding energies and following the same trends as in Figure A.3A. As the Ag content is increased across these three figures, the overall magnitude of oxygen features changes. Samples with increased Ag coverage show a decrease in overall O1s intensity. This trend can be seen very clearly in Fig. A.3D, which presents the peak-fitted intensities of the two primary peaks (530.2eV and 532eV) for all three sample surfaces as a function of temperature.

In the case of the 500K oxidation, (Fig. A.4) a different behavior is observed. For clean Ni and 0.3ML coverage of Ag (Fig. A.4A-A.4B), primarily one type of oxygen (530.2eV) is observed, with a small shoulder near 532eV. The feature at 530.2eV decreases with increasing temperature as expected. No significant difference is observed between clean Ni (4A) and Ni with a 0.3ML Ag deposit (4B), with the exception of an overall increase in total oxygen adsorbed. We obtain total oxygen XPS area on the substrates, with Ni(111) normalized as 1, on both 0.3ML and 0.7ML Ag + Ni(111) of 1.19. These values were obtained by summing the total XPS area of both species of oxygen at 500K as plotted in Fig. A.4D. This suggests that chemisorbed oxygen at Ag step edge sites provides oxygen photoemission at similar binding energies as oxygen chemisorbed on the clean Ni surface, and that oxygen adsorbs more readily on step sites after Ag decoration.

For the 500K oxidation of 0.7ML Ag exposure on Ni(111), (Fig. A.4C) we see an increase in the magnitude of the feature at 532eV and an increase in total oxygen XPS area compared to bare Ni(111). This total value is approximately equal to that seen for 0.3MLAg. This feature then decreases from 550K to 700K. Assignment of chemical identities for the three oxygen species observed has been performed based on a review of previous literature and is summarized in Table A.1.

A.3.2.3 XPS Feature Identification and Analysis:

The feature at 530.2eV has been well-documented to represent O^{2-} species on both Ni[252, 257-262] and Ag [288-289] surfaces. The second species, observed at a binding energy of 532eV, has in the past been associated with O^{1-} species. Some studies have attributed this feature to OH^- groups in adsorbed water on the surface or, for oxidation in the presence of water, metal hydroxides[259, 288-289]. Other studies have found that species at this energy can be induced by oxidation of highly defective ion-bombarded surfaces. These studies have referred to this species as O^{1-} present in Ni_2O_3 "defect oxide" or oxygen-rich oxides of Ni[252, 257, 290]. Further studies have indicated that both OH^- groups and defect oxides contribute to this feature [260, 264]. In the absence of water, or at elevated temperatures, this species is likely to be an oxygen-rich or "defect" oxide of Ni or a similar species of chemisorbed oxygen at Ag-Ni sites.

A final species, consisting of a poorly resolved oxygen shoulder appears at 533.2eV for doses at 100K and has in the past been associated with adsorbed molecular oxygen[252, 258, 261]. As temperature is increased, this shoulder disappears. Additionally, with increasing temperature, the second peak (532eV) loses predominance in favor of the primary oxygen peak (530.2eV). This tendency matches those previously reported in

literature[245, 255-256]. In summary, based on the previous works outlined here and summarized in Table A.1, we conclude that the feature at 530.2eV is O^{2-}, the feature at 532eV is O^{1-}, and the poorly resolved feature at 533.2eV is molecularly adsorbed O_2. From this point on we will refer to the various oxygen species by these chemical assignments.

With the chemical species identified, we can outline the reaction pathways observed for varying amounts of Ag on the Ni(111) surface. For low-temperature oxygen exposures on all samples, physisorbed oxygen and O^{1-} species were initially the dominant species detected. Upon heating, these species decreased and O^{2-} became the primary species. Increased Ag coverage did not seem to have much effect on this trend other than to decrease the total amount of oxygen present on the surface. This suppressive effect seems to indicate that the low-temperature sticking coefficient for Ag is much lower than for Ni. The general behavior we observed for low-temperature oxidation of all substrate surfaces (Fig A.3) can be summarized by equations 2-5 as follows:

Eq. 2	$2O_2(g) \rightarrow O_2(ads) + O^{1-}(ads) + O^{2-}(ads)$	100K
Eq. 3	$2O_2(ads) \rightarrow 2O^{1-}(ads) + O_2(g)$	100K-250K
Eq. 4	$3O^{1-}(ads) \rightarrow O^{2-}(ads) + O_2(g)$	250K-400K
Eq. 5	$2O^{2-}(ads) \rightarrow O_2(g)$	>400K

In contrast to the 100K exposures, we observed significant changes with increasing Ag coverage for 500K oxidation. For Ni(111) and Ni(111)+0.3ML Ag (Figs. A.4A-A.4B) we observed the creation of primarily O^{2-} species, followed by their desorption. The general behavior we observed for high-temperature oxidation of these two surfaces can be summarized by equations 6 and 7 as follows:

Eq. 6	$O_2(g) \rightarrow 2O^{2-}(ads)$	500K
Eq. 7	$2O^{2-}(ads) \rightarrow O_2(g)$	>500K

After increasing the Ag coverage to 0.7ML, however, a second species of oxygen, corresponding to O^{1-}, was observed in significant quantities on the surface (Fig. A.4C). Furthermore, it is apparent based on LEEM data (Fig. A.2) that this new O^{1-} feature corresponds to the addition of Ag adsorbed at terrace sites grown during the 0.7ML deposition. This new species is certainly adsorbed at or beneath the Ag terrace sites, as the total oxygen area for 0.7ML coverage is comparable to that of 0.3ML coverage and higher than that of clean Ni(111). The idea that this shoulder arises from oxygen at the interface between Ni(111) and terrace Ag sites is reinforced by the shoulder's absence at higher temperatures on clean Ni(111) and the 0.3ML (primarily step-edge) dose of Ag on Ni(111). The total reaction pathway, written briefly to provide representative reactions, for 500K oxidation on Ni(111) + 0.7ML Ag can be summarized in equations 8-10 as follows:

Eq. 8	$O_2(g) \rightarrow O^{2-}(ads) + O^{1-}(ads)$	500K
Eq. 9	$3O^{1-}(ads) \rightarrow O^{2-}(ads) + O_2(g)$	550K-700K
Eq. 10	$2O^{2-} \rightarrow O_2(g)$	>700K

Based on the quantitative analysis of the two species of oxygen present, it is apparent that for 500K oxidation of the Ag/Ni(111) surface, significant amounts of O^{1-} do not form in the absence of terrace-grown Ag. This is in contrast with low-temperature oxygen doses (100K), which induce O^{1-} formation upon subsequent heating regardless of the presence or absence of Ag on the surface. This difference can be explained by a pathway in which multilayers of physisorbed oxygen at 100K can convert to O^{1-} at higher temperatures. Data congruent with these steps have been reported previously in literature[258]. For

oxidation at 500K, this accumulation of excess physisorbed oxygen never occurs, inhibiting the production of O^{1-} species. It is the addition of terrace-grown Ag, observed here only at 0.7ML Ag coverages, that induces these O^{1-} species to form under higher oxidation temperatures. In other words, oxygen chemisorption onto Ni(111) containing Ag primarily at step edge sites occurs as O^{2-}, while the presence of large amounts of terrace-grown Ag in addition to the step-grown Ag induces the formation of the O^{1-} species. The specific, concomitant, structural and morphological changes and the preferred sites for oxygen adsorption have been studied further using LEEM.

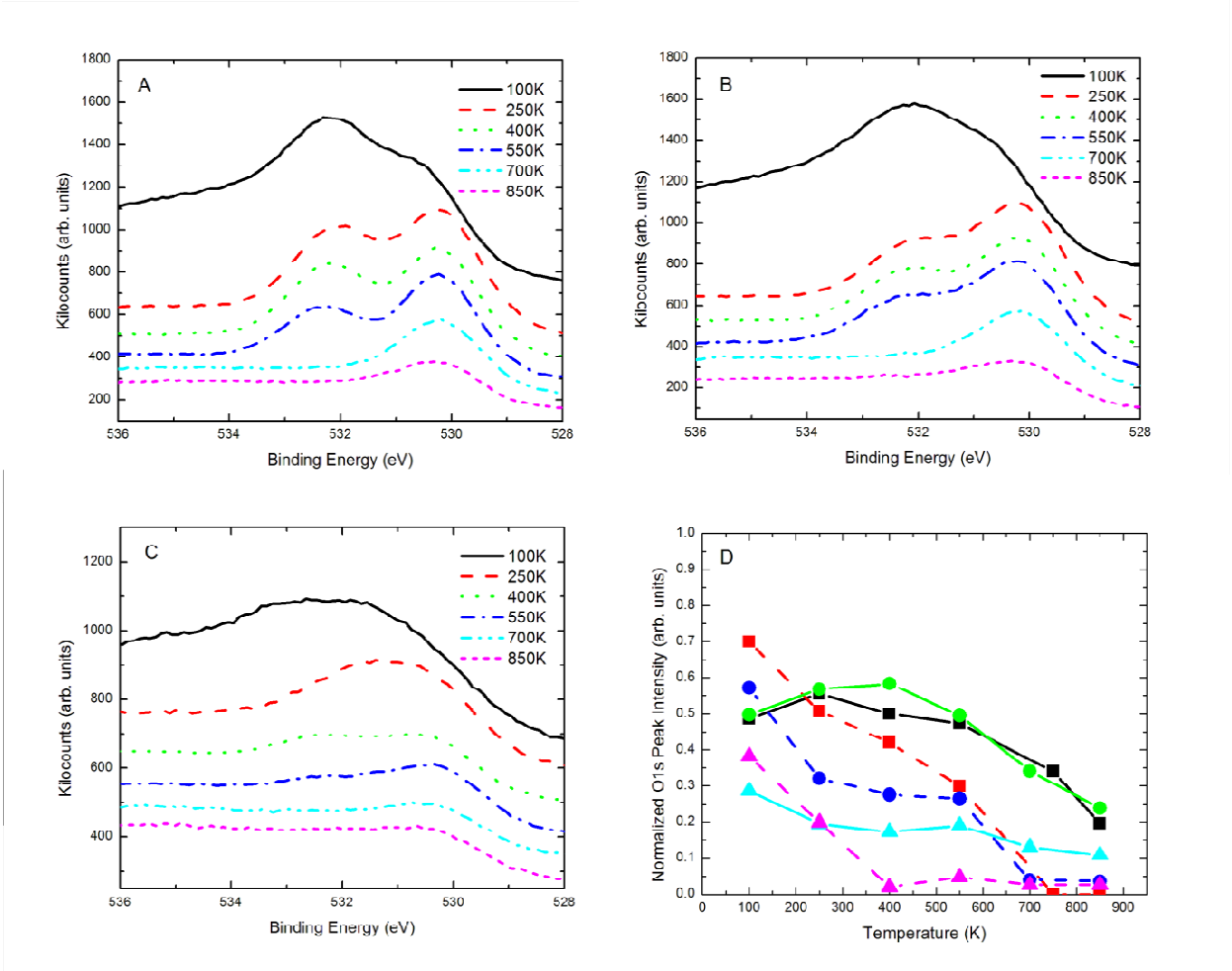

Fig. A.3: TP-XPS spectra of Oxygen dosed at 100K on (A) Ni(111), (B) Ni(111) + 0.3ML (step edge) Ag, and (C) Ni(111) + 0.7ML (step edge + terraces) Ag growth. Figure (D) shows fitted oxygen 1s peak areas for oxygen dosed at 100K on various surfaces. Solid lines are oxygen species at 530.2eV binding energy. Dashed lines are oxygen species at 532eV binding energy. Symbols used indicate which sample surface was studied: Clean Ni(111) (squares), Ni(111) + 0.3ML (step edge) Ag exposure (circles), and Ni(111) + 0.7ML (step edge + terrace) Ag exposure (triangles). Areas were normalized to the maximum O1s intensity observed across all studies.

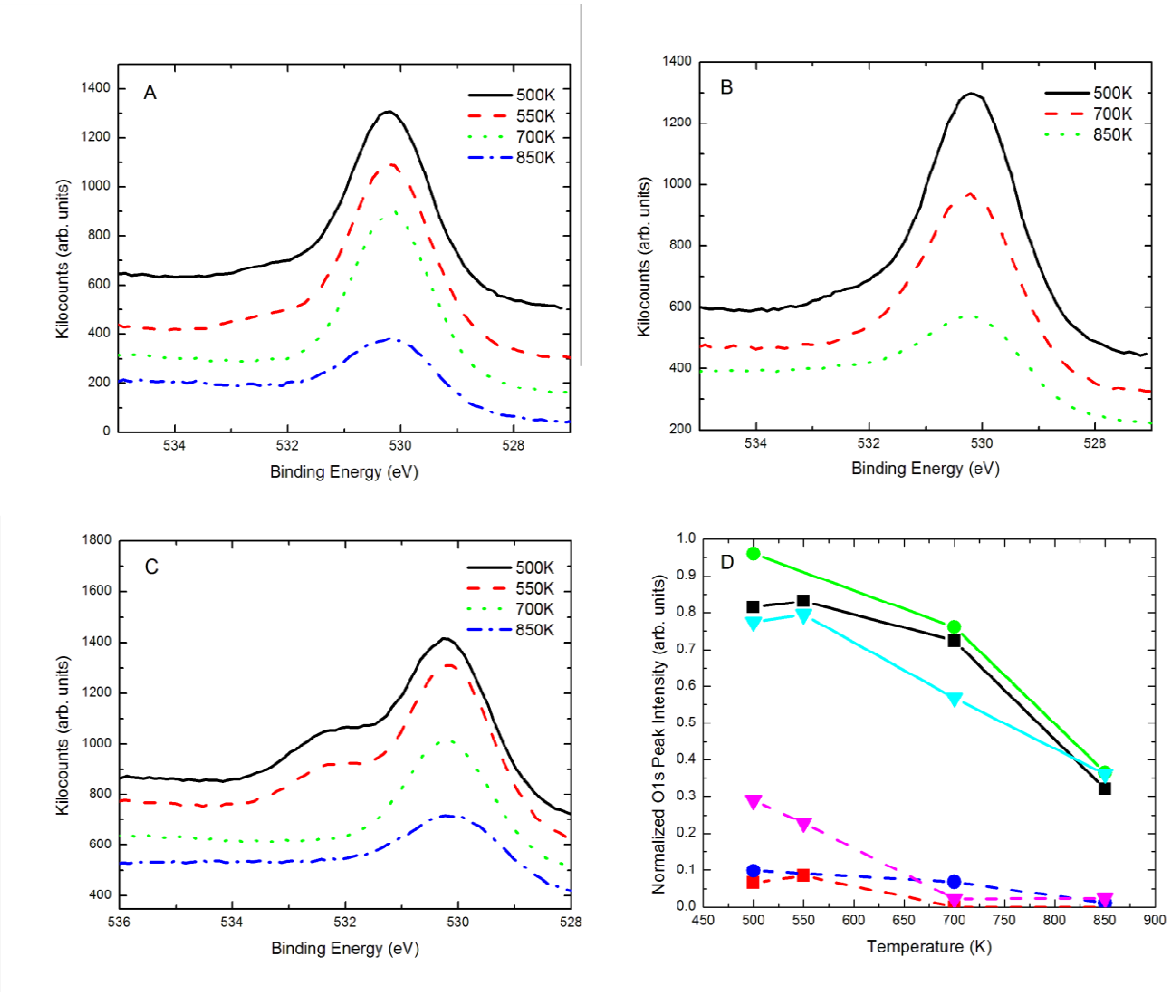

Fig. A.4: TP-XPS of oxygen dosed at 500K on (A) Ni(111), (B) Ni(111) + 0.3ML (step edge) Ag, and (C) Ni(111) + 0.7ML (step edge + terrace) Ag. Figure (D) shows fitted oxygen 1s peak areas for oxygen dosed at 500K on various surfaces. Solid lines are oxygen species at 530.2eV binding energy. Dashed lines are oxygen species at 532eV binding energy. Symbols used indicate which sample surface was studied: Clean Ni(111) (squares), Ni(111) + 0.3ML (step edge) Ag exposure (circles), and Ni(111) + 0.7ML (step edge + terrace) Ag exposure (triangles). Areas were normalized to the maximum O1s intensity observed across all studies.

Table A.1: Chemical states and reference binding energies for the 3 oxygen species considered in the present work.

Surface	**Binding Energy (eV)**	**Species Identity**	**Ref.**
Ni(polycrystalline)	529.5 531.4 533.2	NiO (O^{2-}) Chemisorbed O/Defect Oxide	[252]
Ni(100)	529.7 531.3	NiO (O^{2-}) Ni_2O_3 Defect Oxide	[257]
Ni(100) 80K	530 531.1 534.7	O^{2-} O^{1-} Molecular O_2 adsorbed	[258]
Ni(111) + H_2O	530.2 532.4	O^{2-} OH^-	[259]
NiO Crystal	529.7 531.5	NiO Ni_2O_3 (O^{1-})	[264]
Ag(111)	530.2	O^{2-}	[256]
Ag oxidized in H_2O	529.5 531.6	O^{2-} Surface OH^-	[288-289]

A.3.2.4 Oxidation Analysis by LEEM:

The application of intensity-voltage (I(V)) LEEM allows in-situ monitoring of the structural evolution of near-surface structure upon O_2 exposure and an identification of the evolving phases, as shown in the following. In the I(V) mode, LEEM images are recorded for a predefined set of kinetic energies of the incident electrons in a given range (e.g., up to 40 eV). From this stack of images, local changes in the reflected intensity *I* as a function of electron energy, i.e., accelerating voltage *V*, can be extracted with nanometer resolution. These so-called I(V) curves have already been shown to represent reliable fingerprints of oxygen-rich structures in transition metal oxidation and surface chemical reactions[266, 285]. While the author has also contributed to a full I(V)-LEEM investigation of the oxidation behavior of this system[287], the following discussion is restricted to the limiting cases of oxygen exposure on bare Ni(111) and Ag-covered Ni(111).

In Fig. A.5a, the result of Ni(111) oxidation is shown after saturation exposure to O_2 at about 450 K. In essence, the LEEM image shows a homogeneous, stepped surface, whose characteristic I(V) fingerprint, which has been extracted from the region indicated by a circle, is displayed in Fig. A.5c. The most prominent, revealing feature is the dominant peak at about 8eV, which is associated with the formation of NiO(111) domains[291]. In Fig. A.5b, the result of a 1200 L dose of O_2 on a Ni(111) surface covered by a mixture of 1 ML (bright) and 2 ML (dark) thick Ag islands is displayed. While the I(V) signature of the 2 ML region remains unchanged upon initial oxygen exposure within the error bars (see Ref. 53), the monolayer film assumes the I(V) curve depicted in Fig. A.5c. A comparison with the result for the oxidized Ni surface indicates that the

oxide-related peak has also strongly developed for the Ag-precovered surface. Furthermore, we note the existence of sharp, additional features at about 14 eV and 18 eV, which closely resemble the Ag-induced I(V) signature (Fig. A.5c) in the energy regime from about 13 eV to 21 eV as reproduced for a 2 ML Ag coverage on Ni(111) [46]. Since the I(V) curve for ultrathin NiO(111)/Ni(111) is rather featureless besides the sharp resonance at 8 eV while the I(V) signature for 2 ML Ag/Ni(111) is rather intense at kinetic energies between 13 eV and 21 eV, the most logical explanation is to interpret the experimental I(V) curve as an incoherent superposition of the individual I(V) fingerprints for ultrathin NiO(111) and a 2 ML Ag film on Ni(111). Hence, these results indicate the coexistence of 2 ML-thick Ag regions in close proximity to oxidized Ni(111) patches. Further support for this interpretation can be gained from earlier studies [46] where the Ag-related resonances were found to be of comparable sharpness for Ag layer thicknesses of 2 ML, but considerably smeared out for a single layer. Therefore, the shape of the resonances observed here points toward the onset of Ag agglomeration and partial dewetting, albeit at a length scale close to or even below the resolution limit of the microscope. As we do not observe any mass transport from the double layer regions, the formation of Ag double layers upon oxidation implies a nanoscale variation of the local Ag coverage, suggesting the formation of Ag-covered and Ag-free areas in previous Ag monolayer regions. Close inspection of the LEEM image recorded after O_2 exposure indeed reveals a slight contrast variation within the former 1 ML Ag regions, in agreement with this scenario. We note that this oxygen-induced dewetting process appears to be a general property of this system and is found to be even more pronounced for even higher temperatures, where we observe epitaxial growth of continuous 2 ML-

thick islands in these regions[291]. Since we do not find any evidence for the evolution of a new phase associated with the presence of O^{1-} species as detected by XPS, we conclude that the O^{1-} species induced by the terrace Ag is not sufficiently ordered to be detectable by I(V)-LEEM, which is not inherently chemically sensitive. This allows us to conclude that the O^{2-} species detected in XPS is formed as an ultrathin NiO(111) slab on-top of Ni(111), while the O^{1-} species is a disordered species, the location of which, based on the I(V)-LEEM results, could potentially be correlated with nanoscale Ag/NiO(111) domain boundaries and Ag-decorated surface steps.

In the following section we present data for the ethylene epoxidation reaction on these Ag-Ni(111) structures. By first understanding the morphology of these Ag deposits and their effect on the chemical state of the oxygen present, we relate phenomena observed during the ethylene reaction to the presence or absence of specific oxygen species.

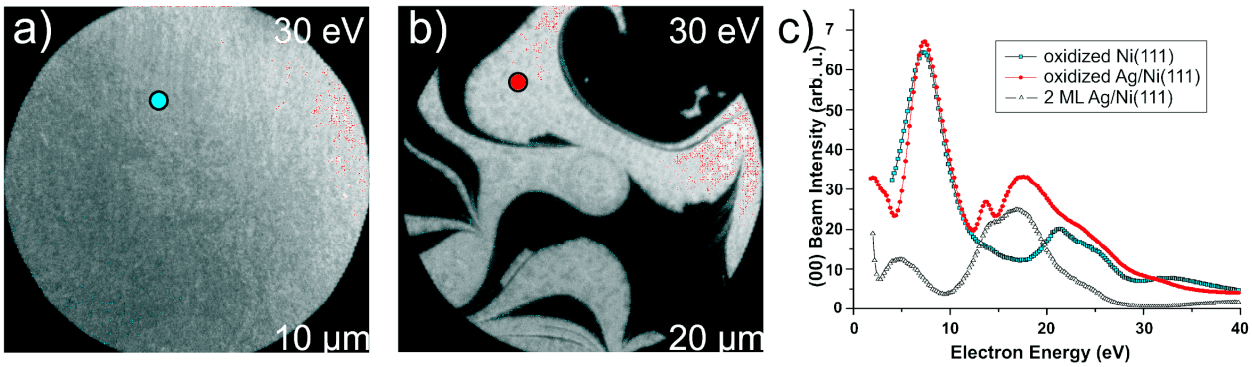

Fig. A.5: (a) LEEM image of a clean Ni(111) surface recorded after saturation exposure to O_2 at a substrate temperature of 450 K. (b) LEEM image of a Ni(111) surface pre-covered by a single Ag layer (bright) and a double Ag layer (dark) recorded after exposure to 1200 L of O_2. (c) Intensity-voltage curves extracted at positions indicated by circles in subfigures (a) and (b) from stacks of images. For convenience, a reference I(V) curve taken for a 2 ML Ag film on Ni(111) [287] has been added.

A.3.3. Reaction with Ethylene:

TP-XPS study of ethylene adsorption was performed for four permutations of Ag and O exposures on Ni(111) surfaces. For all experiments, ethylene was dosed at 10^{-8} Torr for 300s at 100K, yielding a total of 3 L. Previous studies for similar doses of ethylene reported coverages between 1 and 2 ML. [40] Figs. A.6 and A.7 present the C1s data for ethylene on these surfaces, including Ni(111), O-Ni(111), Ag-Ni(111) and O-Ag-Ni(111). Reference spectra were collected for commercially purchased ethylene oxide on Ni(111).

A.3.3.1 Ethylene on Ni(111)

In Figure A.6A, C1s XPS spectra of Ni(111) exposed to 3L ethylene at 100K are presented. A broad peak centered at 284eV appears initially. With annealing up to 250K the peak decreases in size and shifts to 283.5eV. This is evidence of ethylene (284eV) desorbing while leaving chemisorbed, partially dehydrogenated species on the surface (283.5eV). Further annealing causes the decrease of the 283.5eV peak gradually from 250-700K. By 700K almost all the C containing species have left the surface of Ni(111).

In Figure A.6B, TP-XPS spectra for Ni(111) pre-oxidized at 500K, then exposed to 3L ethylene at 100K are presented in the C1s region. Initially, as in Fig. A.6A, a peak corresponding to molecular ethylene is present at 284eV. This peak decreases in size and shifts to 283.5eV at 150K. The peak is gone by 250K. Additionally, a peak centered at 287.9eV appears at 150K. A reference spectrum of ethylene oxide (EO) on Ni(111) is also shown. This feature decreases steadily until 500K then disappears. The presence of O on the surface in Fig. A.6B has changed the interaction completely when compared to the case without O (Fig A.6A). The initial peak at 284eV decreases much more quickly in

the presence of O, and the new peak at 287.9eV, indicative of an oxygenated carbon containing species, is induced. The primary similarities between the two cases are the initial peak intensity at 100K, and the fact that essentially all C has left the surface at 700K for both the clean and oxidized surfaces. Figure A.6C depicts quantitatively the peak areas resulting from peak-fitting as described previously. It is readily apparent that the addition of oxygen to the surface causes a significant increase in the desorption of carbon-containing species, as well as the generation of a new species at a 287.9eV on the surface.

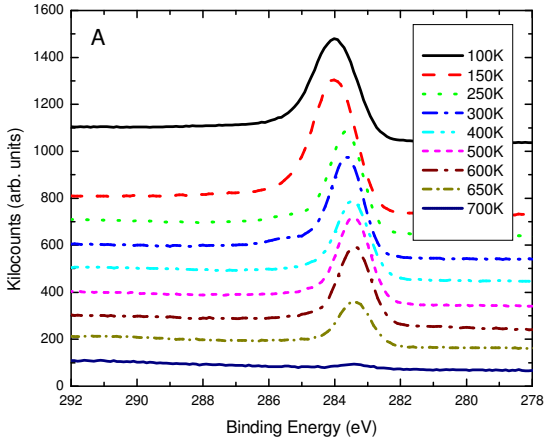

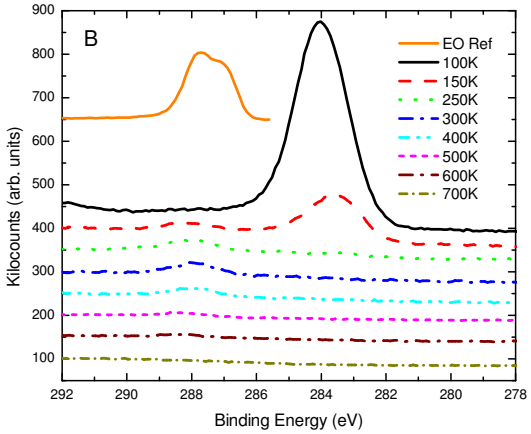

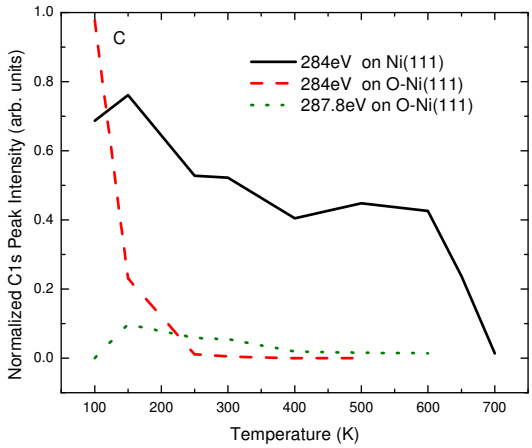

Fig. A.6: TP-XPS of ethylene on Ni(111) (A) and O-Ni(111) (B) including a reference spectrum of purchased ethylene oxide on Ni(111). Lower temperatures are plotted with more positive vertical shifts. Measurements were conducted at 100K after flashing to the temperature indicated in the plot. Figure (C) shows carbon 1s peak areas for ethylene dosed on clean and oxidized Ni(111). Molecular ethylene (284eV) on the non-oxidized surface (solid line), Molecular ethylene (284eV) on the oxidized surface (dashed line), and ethylene oxide (287.8) evolved on oxidized surfaces (dotted line).

A.3.3.2 Ethylene on Ag-Ni(111)

In Figure A.7A, TP-XPS spectra for 3L ethylene adsorbed at 100K on Ni(111) + 0.3ML Ag are presented in the C1s region. A primary peak at 284eV is present but decreases quickly while shifting to 283.8eV. No second species appears with continued heating. The 284eV feature is comparable to that for the oxidized Ni(111) surface without Ag present (Fig. A.6B). However, the initial intensity of the feature at 100K is approximately half of that for either Ni(111) surface without Ag. This indicates that Ag not only enhances desorption of ethylene at lower temperatures, but that the total amount initially adsorbed is decreased as well.

In Figure A.7B, TP-XPS spectra for 3L ethylene adsorbed at 100K on pre-oxidized (500K) Ni(111) + 0.3ML Ag are presented. A reference spectrum of ethylene oxide (EO) is also shown. As before, an initial peak appears at 284eV (physisorbed molecular ethylene) and decreases with increasing temperature while shifting to 283.7eV. It is worth noting that the total peak intensity at 100K is less here than in any of the previous figures. This indicates that the O-Ag-Ni(111) surface adsorbs molecular ethylene less readily than any of the other surfaces studied. Concurrently with this desorption of molecular ethylene, a new peak at 287.8eV appears. This feature remains relatively constant until 500K, after which it decreases and disappears. Figure A.7C depicts quantitatively the peak areas resulting from peak-fitting of the curves in Figure A.7A and A.7B. The addition of oxygen to the surface does not have as dramatic an effect on the desorption profile as in Figure A.6C, but still causes the generation of the second species observed at a new binding energy.

Finally, Figure A.8 depicts quantitatively the amount of oxygen-containing carbon species (287.8eV) produced for ethylene dosed and heated on Ag-Ni(111) compared to Ni(111). These data are the same data presented in Figs. A.6C and A.7C, but rather than normalizing to the maximum C1s value observed across all experiments, which gives an idea of the raw amount of species generated, they are normalized to the initial amount of ethylene adsorbed on the given surface. This gives a measurement of the amount of oxygen-containing species generated *per unit ethylene initially adsorbed*. It is evident from comparison that the Ag-containing surface is much more active for this reaction than the clean Ni(111) surface is. Additionally, the signal persists to higher temperatures for the Ag-containing surface.

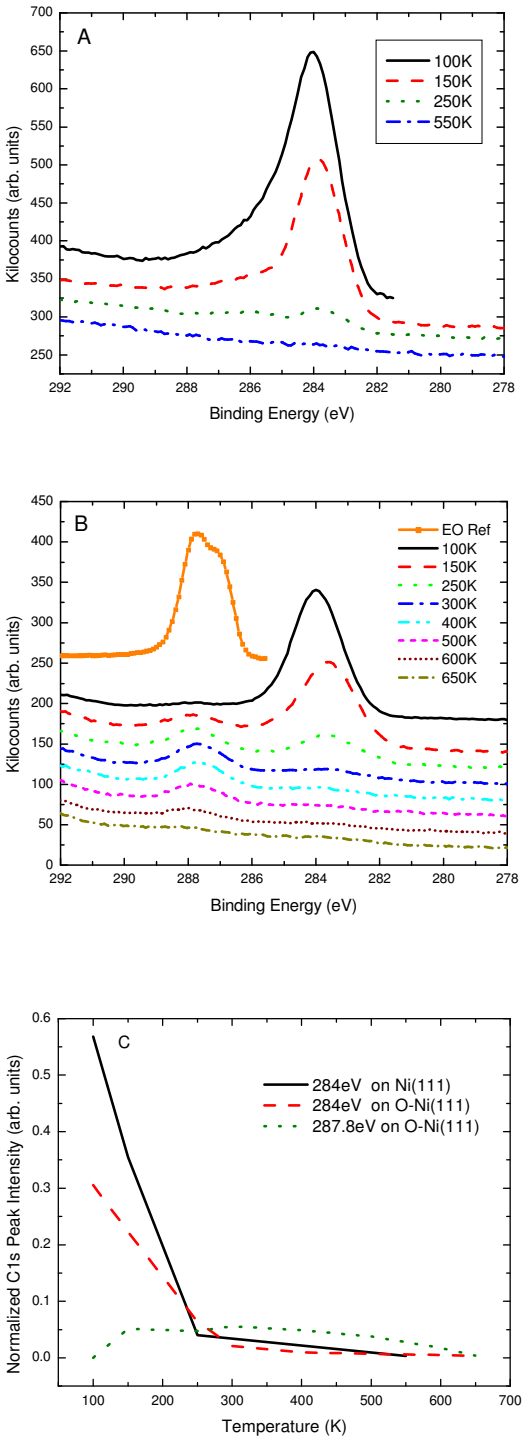

Fig. A.7: TP-XPS of ethylene on Ag-Ni(111) (A) and O-Ag-Ni(111) (B) including a reference spectrum of purchased ethylene oxide on Ni(111). Ag coverage was approximately 0.3ML. Lower temperatures are plotted with more positive vertical shifts.

Measurements were conducted at 100K after flashing to the temperature indicated in the plot. Figure (C) shows carbon 1s peak areas for ethylene dosed on Ag-Ni(111) with and without oxygen. Molecular ethylene (284eV) on the non-oxidized surface (solid line), Molecular ethylene (284eV) on the oxidized surface (dashed line), and ethylene oxide (287.8) evolved on oxidized surfaces (dotted line). Areas were normalized to the maximum C1s intensity observed on all samples studied. The reference ethylene oxide on Ni(111) spectra is shown in 1/3 scale.

A.3.3.3 Feature Identification and Analysis:

A series of previous work was referenced to assign chemical identities to the species observed. The feature at 284eV, which shifts with increasing temperature to lower binding energies, is assigned to be either physisorbed (molecularly) or chemisorbed (with progressive amounts of dehydrogenation) ethylene. This assignment is based on multiple references summarized in Table A.2. Similarly, the feature at 287.8eV can be assigned, based on comparison with previous studies, as ethylene oxide (C_2H_4O), which has been reported by different researchers at either 287.8eV or 287.3eV. Additionally, XPS data was collected for commercially purchased C_2H_4O (Fig. A.7B) on Ni(111), confirming the findings from literature.

As before, having identified the species detected in XPS, it is possible to propose reaction pathways on the various sample surfaces. Previous TPD studies of ethylene on Ni(111) have detected H_2 and C_2H_4 desorption products, and indicate that molecular ethylene begins to desorb from Ni(111) with initial heating above 150K, while dehydrogenation does not begin in significant quantities before heating above 300K[282, 292]. Reaction pathways proposed in these same studies indicate that, for temperatures above 300K, remaining carbonaceous species on the surface are most likely dehydrogenated ethylene chemisorbed to Ni, such as C_2H_2/Ni(111) and C_2H_3/Ni(111). As temperatures exceed 500K, C-C bond cleavage occurs in addition to dehydrogenation, and single-carbon adsorbed species such as CH appear. For ethylene dosed and heated on Ni(111) surfaces in the absence of oxygen, the proposed reaction pathway is outlined as follows in equations 11-13:

Eq. 11 $C_2H_4(g) \rightarrow C_2H_4(ads) \rightarrow C_2H_4(g)$ 100K-250K

Eq. 12 $4C_2H_4(ads) \rightarrow 2C_2H_2(ads) + 2C_2H_3(ads) + 3H_2(g)$ 250K-300K

Eq. 13 $2C_2H_2(ads) + 2C_2H_3(ads) \rightarrow C_2H_2(g)+C_2H_3(g) + 4CH(ads) + 0.5H_2(g)$ 300K-700K

The expected reaction pathway for desorption of oxygen-containing ethylene species from a O-Ni(111) surface is somewhat different. The likely gas-phase reaction products include hydrogen (resulting from dehydrogenation at elevated temperature), methoxy species (CH_3O), epoxides (C_2H_2O), and acetaldehyde. The proposed reaction mechanism is as follows in equations 14-17:

Eq. 14 $C_2H_4(g) \rightarrow C_2H_4$ (ads)

Eq. 15 C_2H_4 (ads)$\rightarrow C_2H_4(g)$ 100-250K

Eq. 16 $C_2H_4(ads) + O^{2-}(ads) \rightarrow C_2H_4O$ (ads) 250-300K

Eq. 17 $3C_2H_4O(ads) + O^{2-}(ads) \rightarrow CH_3CHO(g) + 2CH_3O(g) + C_2H_2O(g)$ 300K-700K

In the absence of oxygen, reaction pathways for Ag-modified Ni(111) are similar to those proposed for surfaces without Ag, with the primary difference being that the Ag-modified surface exhibits faster ethylene desorption at lower temperatures (150K-300K). In the presence of oxygen, however, the Ag-modified surface, in comparison to the non-modified surface, exhibits significantly less ethylene adsorption to begin with but has a similar desorption profile.

It is possible that the adsorbed oxygen present on the Ni surface behaved in a similar manner to the oxygen present in the Al_2O_3 support for the traditionally employed industrial Ag-Al_2O_3 catalyst. That is, rather than relying on competitive co-adsorption of a C_2H_4 and an oxygen at the same silver site, the presence of a more oxophilic metal (or metal oxide) support allows the Ag site to be dedicated to C_2H_4 adsorption with the necessary oxygen being provided either by stoichiometric oxygen (in the oxide) or by

adsorbed surface oxygen (on the oxophilic metal). This theory is supported by the decrease in oxygen adsorption observed in XPS after the addition of Ag to the Ni(111) surface, which indicates that oxygen adsorbed in our exact conditions is primarily restricted to the Ni sites.

Table A.2: Chemical states and reference binding energies for various carbonaceous species considered in the present work.

Chemical Species	**Substrate**	**Ref.**	**C 1s Binding Energy**
Ethylene Oxide (C_2H_4O)	Ni(110)	[280]	287.8
Ethylene Oxide (C_2H_4O)	Ni(110) @ 100K	[276]	287.3
Acetaldehyde (CH_3CHO)	Ni(110)	[276]	288.9
Methoxy (CH_3O)	Ni(110)	[276]	285.8
Decomposed Species (CH_x)	Ni(110)	[276]	283.4
Ethylene (C_2H_4)	Ni(100) @ 90K	[277]	283.8
Acetylide (CCH)	Ni(100) @ 265K	[277]	283.9
Acetylene (HC_2H)	Ni(100) @ 105K	[277]	283.1
Vinyl (-$CHCH_2$)	Ni(100)	[277]	283.5
Carbide	Ni(100)	[277]	282.9-283.1

This analysis also accounts for the deviation from previous results that indicate that a silver-based metallocycle is responsible for the selectivity determination of the silver surface. For larger silver deposits, this metallocycle is a common reaction step for the majority of ethylene oxidation and epoxidation reactions, and the specific details of the metallocycle will determine whether or not the desired epoxidation reaction or undesired combustion reactions proceed. Rather than considering the whole multitude of possible combustion reactions and products that could arise, it would be simpler to consider only two cases- one case which leads to the desired reaction and a second case which leads to combustion products. As it turns out, there is one intermediary product common to all of the combustion products and not seen in the epoxidation reaction. This product, acetaldehyde, is a possible side product of the reaction of ethylene and oxygen on the metallocycle site. The resulting acetaldehyde is then easily oxidized to CO or CO_2, which leaves the surface as a vapor-phase product

When assessing possible reaction pathways, it is important to consider the selectivity of the desired reaction product (C_2H_4O) compared with alternate byproducts, including combustion products such as CO. While this type of selectivity measurement is best performed by measuring the yield of various desorption products obtained, knowledge of the reaction pathways suggested in the literature allows us to make inferences based on the surface species observed in this work. A large body of previous work, including many such temperature programmed desorption (TPD) studies, has indicated that the production of a surface-confined acetaldehyde species is a common participant in the majority of reaction pathways leading to these undesired combustion species[272, 293]. In other words, residual acetaldehyde on the catalyst surface may be treated

as a marker for undesired reaction pathways. In conducting this type of analysis, it is important to remember that the ethylene reaction conducted was not conducted in the presence of vapor-phase oxygen, but rather in the presence of a limited amount of surface-confined oxygen. Thus it is reasonable to assume that, given the restricted oxygen supply, some of the intermediary acetaldehyde species would remain during XPS analysis, since acetaldehyde is known to adsorb on Ni(111) at room temperature or below. Based on XPS fingerprinting techniques, which indicate a significant difference (1.1eV) in binding energy between ethylene oxide and acetaldehyde, it is clear that acetaldehyde is not detected in the XPS data. This result seems to indicate that the decomposition of the adsorbed ethylene into combustion products via an acetaldehyde intermediary is not a dominant reaction.

It is important to note that the 0.3ML Ag grown for the ethylene oxidation experiment effectively blocks the step-edge sites, according to the VPEEM and LEEM investigations outlined earlier. Recalling the previous section, in which we analyzed the chemical identities of oxygen on Ni(111) and Ag-Ni(111) surfaces, we have seen that, for oxygen exposures at 500K, significant quantities of O^{1-} species form only in the presence of terrace-grown Ag. By this line of reasoning, it is evident that ethylene oxide has been formed in the near absence of O^{1-}, even though it has previously been shown that on a clean Ag(111) surface O^{1-} species are necessary for epoxidation[270]. It appears as though the presence of sub-monolayer Ag on Ni(111) step-edge sites enables the epoxidation reaction to proceed without the significant presence of O^{1-}. Additionally, we have shown that step-edge grown Ag increases the total amount of oxygen adsorbed, and we suggest that this increased oxygen affinity may be responsible for the increase in activity.

It is readily apparent from comparison of figures A.6C and A.7C that Ag suppresses the adsorption of ethylene in the absence of oxygen. On the other hand, Ag does not suppress the formation of ethylene oxide when oxygen is present on the surface. Rather, the ethylene oxide formed in the presence of Ag is actually more stable at higher temperatures, persisting on the surface to higher temperatures than ethylene oxide on clean Ni(111). This is an important result in that the window of reaction feasibility has been broadened by surface modification. We correlate this increase in oxide stability with previous results which indicate that Ag grown at step sites decreases the activity of Ni(111) for C-C bond breakage[278]. By inhibiting the C-C bond breakage, we have stabilized the oxidized ethylene against further reaction. Additionally, from examination of Fig. A.8, we see that the amount of ethylene oxide generated per unit ethylene adsorbed on a Ag-Ni(111) surface is much higher than on a bare Ni(111) surface, showing that the Ag-Ni interaction provides a significant activity increase.

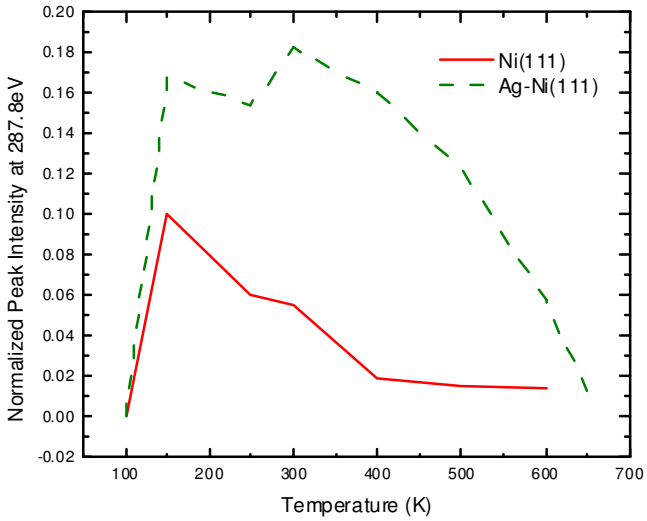

Fig. A.8: Carbon 1s peak intensity at 287.8eV (ethylene oxide species) normalized to initial ethylene peak area. This is a measure of ethylene oxide yield per unit molecular ethylene initially adsorbed.

A.4 Conclusions:

The results presented in this work indicate that the addition of submonolayer Ag to a Ni(111) surface increases the activity of the surface for ethylene epoxidation while simultaneously stabilizing the ethylene oxide produced from further reaction at elevated temperatures. We have shown that for 500K oxidation in UHV, terrace-grown Ag submonolayers promote an O^{1-} species on the Ni(111) surfaces, while step-edge deposits and clean Ni surfaces favor O^{2-} species. For deposits with a high degree of Ag grown at step-edge sites, we have correlated the absence of this O^{1-} species and increased total oxygen adsorption with the enhanced performance induced by Ag submonolayers on the Ni(111) surface, indicating that the Ag-Ni system does not require the presence of O^{1-} species for the epoxidation reaction, as has been shown to be the case for Ag(111) crystals.

Additionally, we have stabilized ethylene oxide at elevated temperatures by employing the ability of submonolayer Ag at step-edge sites to inhibit C-C bond breakage. Ethylene oxide species are more stable on Ni(111) surfaces at higher temperatures when step-edge sites are masked by vapor-deposited Ag. By combining Ag, which is an excellent catalyst for the epoxidation reaction, with a Ni substrate, which promotes both dehydrogenation and C-C bond breaking, in a site-specific growth mode, we have successfully paired two active metals in a manner that retains their desired attributes (epoxidation and dehydrogenation activities) while suppressing the C-C bond breakage that would otherwise be an undesired side-effect of the use of Ni as a support.

APPENDIX B

CHARTS AND TABLES

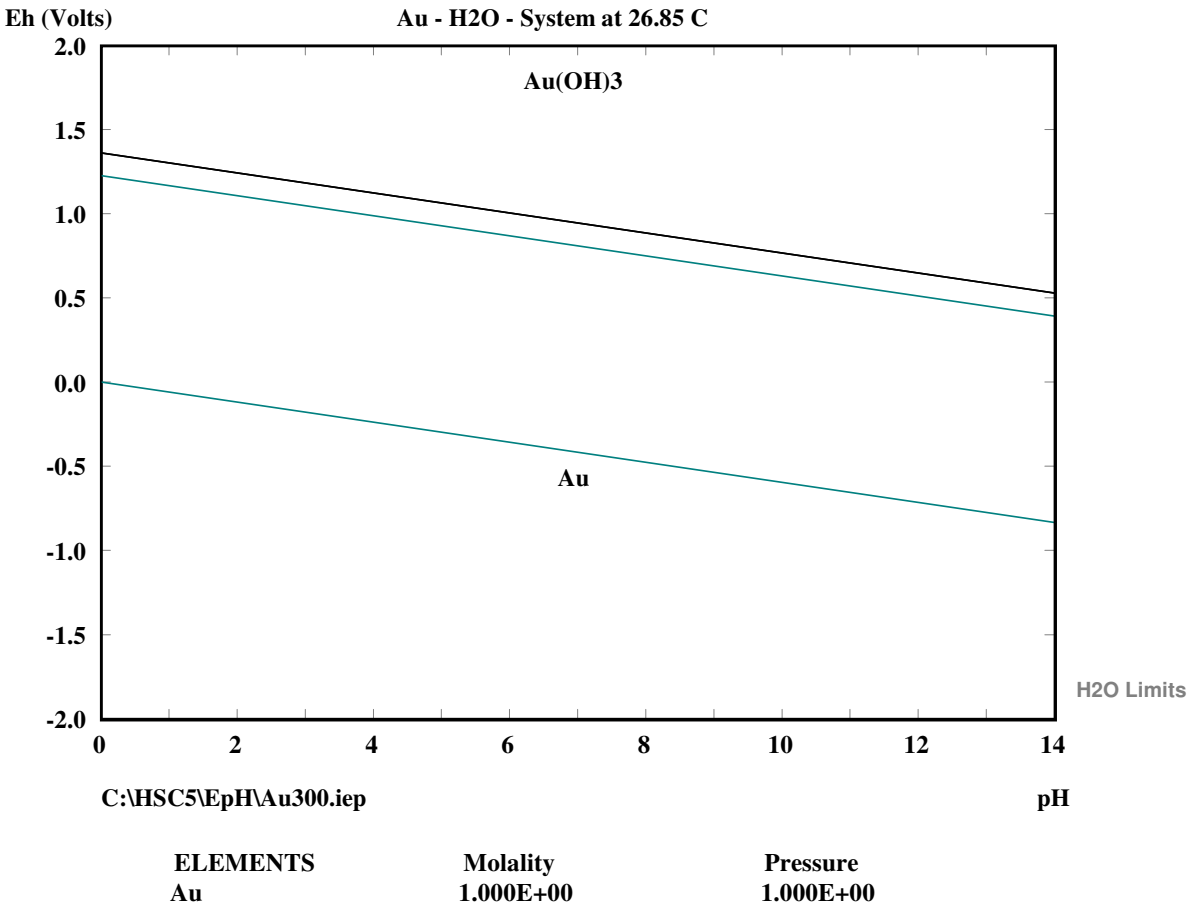

Figure B.1: Pourbaix potential-pH diagram for Au. Figure generated from HSC 5.1 using reference database[294].

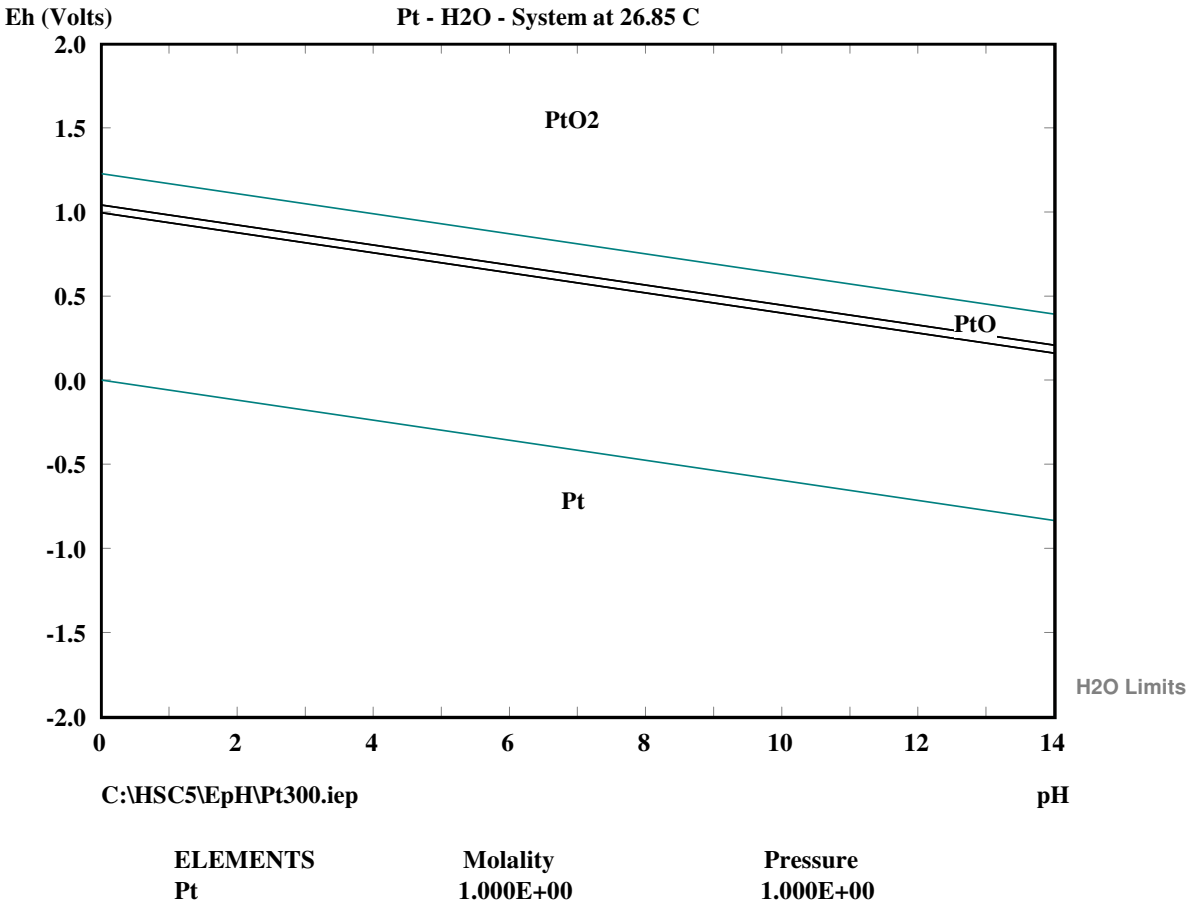

Figure B.2: Pourbaix potential-pH diagram for Pt. Figure generated from HSC 5.1 using reference database[294].

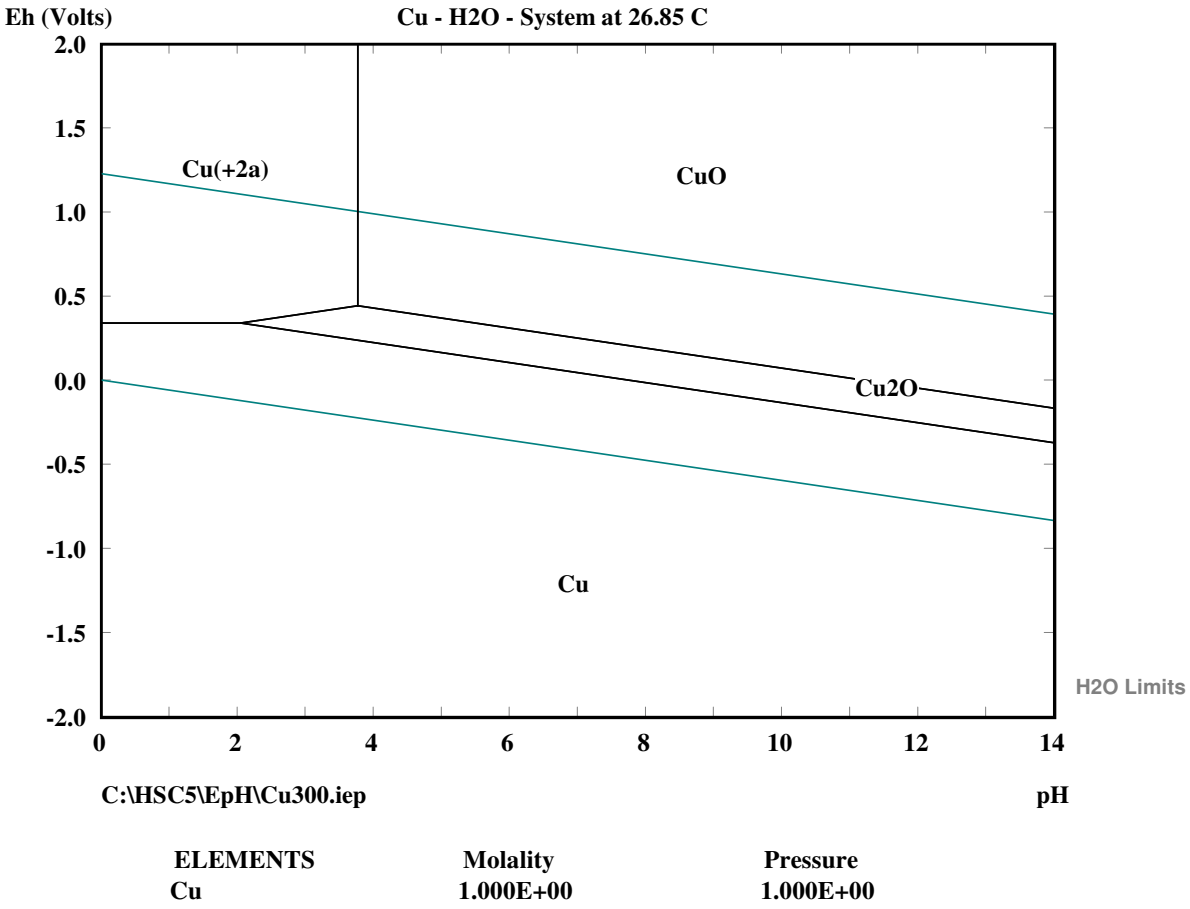

Figure B.3: Pourbaix potential-pH diagram for Cu. Figure generated from HSC 5.1 using reference database[294].

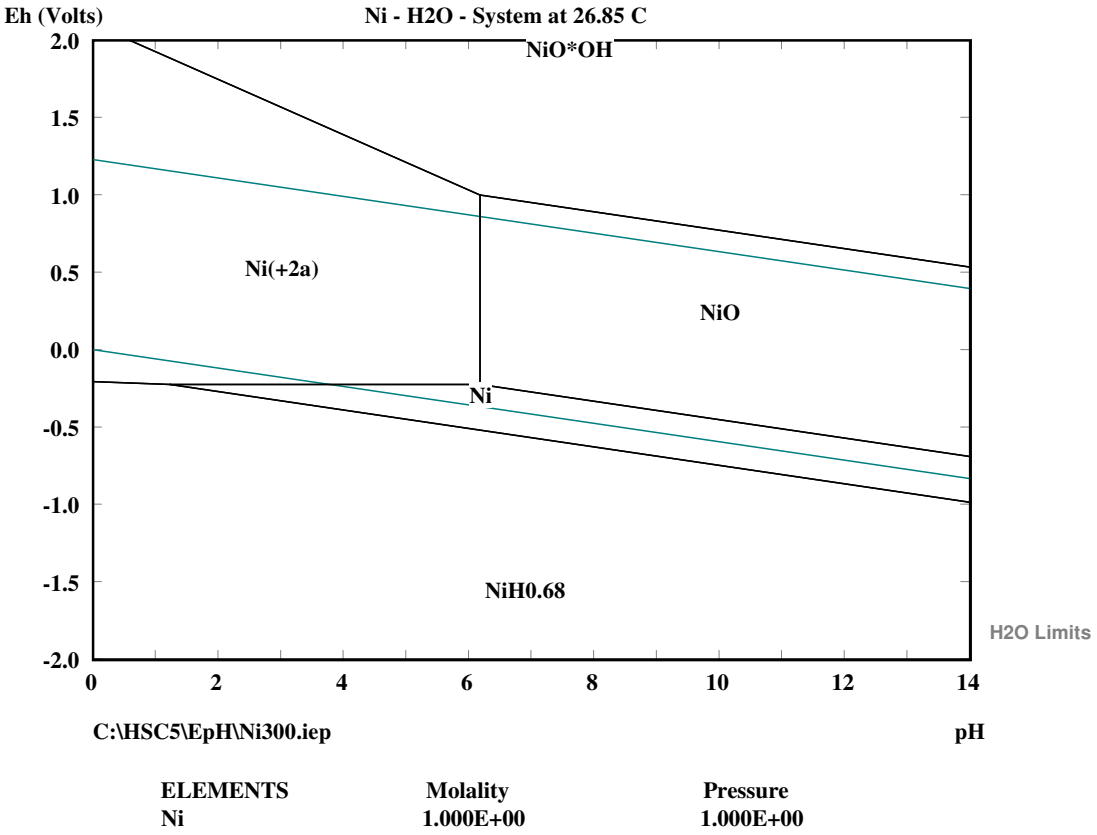

Figure B.4: Pourbaix potential-pH diagram for Ni. Figure generated from HSC 5.1 using reference database[294].

Table B.1: Selected standard potentials of interest for DMFCs and SLRR[96]

Reaction	Equilibrium Potential (V)
$Au^{+} + e^{-} \leftrightarrow Au$	1.692
$Pt^{2+} + 2e^{-} \leftrightarrow Pt$	1.18
$Pd^{2+} + 2e^{-} \leftrightarrow Pd$	0.951
$Ag^{+} + e^{-} \leftrightarrow Ag$	0.7996
$Rh^{3+} + 3e^{-} \leftrightarrow Rh$	0.758
$Ru^{2+} + 2e^{-} \leftrightarrow Ru$	0.455
$Cu^{2+} + 2e^{-} \leftrightarrow Cu$	0.3419
$Ru^{3+} + 3e^{-} \leftrightarrow Ru$	0.2487
$2H^{+} + 2e^{-} \leftrightarrow H_2$	0.00
$Pb^{2+} + 2e^{-} \leftrightarrow Pb$	-0.13
$Ni^{2+} + 2e^{-} \leftrightarrow Ni$	-0.257
$Co^{2+} + 2e^{-} \leftrightarrow Co$	-0.28
$Cr^{3+} + 3e^{-} \leftrightarrow Cr$	-0.7
$Zn^{2+} + 2e^{-} \leftrightarrow Zn$	-0.7618
$Cr^{2+} + 2e^{-} \leftrightarrow Cr$	-0.913
$Ti^{2+} + 2e^{-} \leftrightarrow Ti$	-1.6
$Al^{3+} + 3e^{-} \leftrightarrow Al$	-1.662
$Ce^{3+} + 3e^{-} \leftrightarrow Ce$	-2.336
$Li^{+} + e^{-} \leftrightarrow Li$	-3.04

REFERENCES

1. R. E. Rettew, J. W. Guthrie and F. M. Alamgir, *Journal of the Electrochemical Society*, 2009, **156**, D513-D516.
2. *Fundamental Science and Long-Term Impacts of the U.S. Department of Energy Basic Energy Science Catalysis Science Program*, The National Academies Press, 2009.
3. F. Alcaide, G. Álvarez, P. L. Cabot, O. Miguel and A. Querejeta, *International Journal of Hydrogen Energy*, 2010, **35**, 11634-11641.
4. M. Mougenot, A. Caillard, P. Brault, S. Baranton and C. Coutanceau, *International Journal of Hydrogen Energy*, **In Press, Corrected Proof**.
5. A. N. Gavrilov, O. A. Petrii, A. A. Mukovnin, N. V. Smirnova, T. V. Levchenko and G. A. Tsirlina, *Electrochim. Acta*, 2007, **52**, 2775-2784.
6. J. B. Goodenough, A. Hamnett, B. J. Kennedy, R. Manoharan and S. A. Weeks, *Journal of Electroanalytical Chemistry and Interfacial Electrochemistry*, 1988, **240**, 133-145.
7. S. Sen, F. Sen and G. Gokagac, *Physical Chemistry Chemical Physics*, 2011, **13**, 6784-6792.
8. N. Tsiouvaras, M. A. Peña, J. L. G. Fierro, E. Pastor and M. V. Martínez-Huerta, *Catal. Today*, 2010, **158**, 12-21.
9. M. S. Wong, P. J. J. Alvarez, Y. L. Fang, N. Akcin, M. O. Nutt, J. T. Miller and K. N. Heck, *J. Chem. Technol. Biotechnol.*, 2009, **84**, 158-166.
10. M. Garcia-Mota, J. Gomez-Diaz, G. Novell-Leruth, C. Vargas-Fuentes, L. Bellarosa, B. Bridier, J. Perez-Ramirez and N. Lopez, *Theor. Chem. Acc.*, 2011, **128**, 663-673.
11. D. R. Rolison, *Science*, 2003, **299**, 1698-1701.
12. J. Zhai, M. Huang and S. Dong, *Electroanalysis*, 2007, **19**, 506-509.
13. G. Centi and S. Perathoner, *Coordination Chemistry Reviews*, 2011, **255**, 1480-1498.
14. L. De Rogatis, M. Cargnello, V. Gombac, B. Lorenzut, T. Montini and P. Fornasiero, *Chemsuschem*, 2010, **3**, 24-42.
15. S. H. Elder, F. M. Cot, Y. Su, S. M. Heald, A. M. Tyryshkin, M. K. Bowman, Y. Gao, A. G. Joly, M. L. Balmer, A. C. Kolwaite, K. A. Magrini and D. M. Blake, *Journal of the American Chemical Society*, 2000, **122**, 5138-5146.
16. M. Kim and R. M. Laine, *Journal of the American Chemical Society*, 2009, **131**, 9220-9229.
17. A. Z. Moshfegh, *Journal of Physics D-Applied Physics*, 2009, **42**.
18. B. Podlovchenko, T. Gladysheva, A. Filatov and L. Yashina, *Russian Journal of Electrochemistry*, 2010, **46**, 1189-1197.
19. D. Rosario-Amorin, X. Wang, M. Gaboyard, R. Clerac, S. Nlate and K. Heuze, *Chemistry-a European Journal*, 2009, **15**, 12636-12643.
20. P. Strasser, *Reviews in Chemical Engineering*, 2009, **25**, 255-295.
21. C. J. Zhong, J. Luo, B. Fang, B. N. Wanjala, P. N. Njoki, R. Loukrakpam and J. Yin, *Nanotechnology*, 2010, **21**.

22. C. J. Zhong, J. Luo, P. N. Njoki, D. Mott, B. Wanjala, R. Loukrakpam, S. Lim, L. Wang, B. Fang and Z. C. Xu, *Energy & Environmental Science*, 2008, **1**, 454-466.
23. F. Klasovsky, P. Claus and D. Wolf, *Topics in Catalysis*, 2009, **52**, 412-423.
24. S. J. Cho, J. Lee, Y. S. Lee and D. P. Kim, *Catal. Lett.*, 2006, **109**, 181-187.
25. N. K. Allam and M. A. El-Sayed, *Journal of Physical Chemistry C*, 2010, **114**, 12024-12029.
26. N. K. Allam and C. A. Grimes, *Solar Energy Materials and Solar Cells*, 2008, **92**, 1468-1475.
27. J. Kaspar, P. Fornasiero and N. Hickey, *Catal. Today*, 2003, **77**, 419-449.
28. S. Royer and D. Duprez, *ChemCatChem*, 2011, **3**, 24-65.
29. F. H. M. Dekker, J. G. Nazloomian, A. Bliek, F. Kapteijn, J. A. Moulijn, D. R. Coulson, P. L. Mills and J. J. Lerou, *Applied Catalysis a-General*, 1997, **151**, 247-266.
30. Y. Matsumura, J. B. Moffat and K. Hashimoto, *Journal of the Chemical Society-Faraday Transactions*, 1994, **90**, 1177-1182.
31. A. A. Isse, G. Berzi, L. Falciola, M. Rossi, P. R. Mussini and A. Gennaro, *Journal of Applied Electrochemistry*, 2009, **39**, 2217-2225.
32. S. Rondinini, P. R. Mussini, P. Muttini and G. Sello, *Electrochim. Acta*, 2001, **46**, 3245-3258.
33. S. Rondinini and A. Vertova, *Electrochim. Acta*, 2004, **49**, 4035-4046.
34. S. B. Rondinini, P. R. Mussini, F. Crippa and G. Sello, *Electrochemistry Communications*, 2000, **2**, 491-496.
35. C. A. Paddon, F. L. Bhatti, T. J. Donohoe and R. G. Compton, *J. Phys. Org. Chem.*, 2007, **20**, 115-121.
36. A. A. Isse, S. Gottardello, C. Maccato and A. Gennaro, *Electrochemistry Communications*, 2006, **8**, 1707-1712.
37. Y. Z. Lu, Y. C. Wang and W. Chen, *Journal of Power Sources*, 2011, **196**, 3033-3038.
38. A. E. S. Sleightholme, J. R. Varcoe and A. R. Kucernak, *Electrochemistry Communications*, 2008, **10**, 151-155.
39. Q. Tang, L. Jiang, J. Qi, Q. Jiang, S. Wang and G. Sun, *Applied Catalysis B: Environmental*, 2011, **104**, 337-345.
40. Q. F. Yi, L. Li, W. Q. Yu, X. P. Liu, Z. H. Zhou and H. D. Nie, *Rare Metals*, 2010, **29**, 26-31.
41. Q. F. Yi, L. Li, W. Q. Yu, Z. H. Zhou and G. R. Xu, *Journal of Molecular Catalysis a-Chemical*, 2008, **295**, 34-38.
42. M. H. Atwan, D. O. Northwood and E. L. Gyenge, *International Journal of Hydrogen Energy*, 2007, **32**, 3116-3125.
43. L. D. Burke and W. A. O'Leary, *Journal of the Electrochemical Society*, 1988, **135**, 1965-1970.
44. M. AvramovIvic, V. Jovanovic, G. Vlajnic and J. Popic, *Journal of Electroanalytical Chemistry*, 1997, **423**, 119-124.
45. O. Perraud, F. Laibe and C. Valmalle, *Actualite Chimique*, 2011, 41-45.
46. J. J. Rauh, G. P. Lahm, T. F. Pahutski, G. V. Ullas and C. N. Filer, *Journal of Labelled Compounds & Radiopharmaceuticals*, 2010, **53**, 50-51.

47. P. G. Reddy, T. V. Pratap, G. D. K. Kumar, S. K. Mohanty and S. Baskaran, *European Journal of Organic Chemistry*, 2002, 3740-3743.
48. A. L. Cabrera, E. Moralesleal, J. Hasen and I. K. Schuller, *Catal. Lett.*, 1995, **30**, 11-23.
49. T. Honjo, K. Numazaki, H. H. Uchida, Y. Matsumura and Y. Nishi, *Journal of the Japan Institute of Metals*, 2004, **68**, 530-533.
50. X. Shan, J. H. Payer and J. S. Wainright, *Journal of Alloys and Compounds*, 2007, **430**, 262-268.
51. J. M. Skowronski, T. Rozmanowski, P. Krawczyk, Z. Rogulski and A. Czerwinski, *Journal of Nanoscience and Nanotechnology*, 2009, **9**, 3858-3865.
52. M. Yamauchi, H. Kobayashi and H. Kitagawa, *Chemphyschem*, 2009, **10**, 2566-2576.
53. T. S. Olson, B. Blizanac, B. Piela, J. R. Davey, P. Zelenay and P. Atanassov, *Fuel Cells*, 2009, **9**, 547-553.
54. D. M. Bernardi and M. W. Verbrugge, *Journal of the Electrochemical Society*, 1992, **139**, 2477-2491.
55. H. A. Gasteiger, S. S. Kocha, B. Sompalli and F. T. Wagner, *Applied Catalysis B-Environmental*, 2005, **56**, 9-35.
56. S. Mukerjee, S. Srinivasan, M. P. Soriaga and J. McBreen, *Journal of the Electrochemical Society*, 1995, **142**, 1409-1422.
57. U. A. Paulus, T. J. Schmidt, H. A. Gasteiger and R. J. Behm, *Journal of Electroanalytical Chemistry*, 2001, **495**, 134-145.
58. M. A. Barakat and M. H. H. Mahmoud, *Hydrometallurgy*, 2004, **72**, 179-184.
59. C. H. Kim, S. I. Woo and S. H. Jeon, *Industrial & Engineering Chemistry Research*, 2000, **39**, 1185-1192.
60. M. S. Kim, E. Y. Kim, J. Jeong, J. C. Lee and W. Kim, *Materials Transactions*, 2010, **51**, 1927-1933.
61. R. S. Marinho, J. C. Afonso and J. da Cunha, *Journal of Hazardous Materials*, 2010, **179**, 488-494.
62. K. Shams, M. R. Beiggy and A. G. Shirazi, *Applied Catalysis a-General*, 2004, **258**, 227-234.
63. K. Shams and F. Goodarzi, *Journal of Hazardous Materials*, 2006, **131**, 229-237.
64. M. Yamakawa, H. Ito and R. Noyori, *Journal of the American Chemical Society*, 2000, **122**, 1466-1478.
65. K. J. Haack, S. Hashiguchi, A. Fujii, T. Ikariya and R. Noyori, *Angew. Chem.-Int. Edit. Engl.*, 1997, **36**, 285-288.
66. L. Bartek, P. Kluson and L. Cerveny, *Collection of Czechoslovak Chemical Communications*, 2005, **70**, 1642-1652.
67. S. Takamizawa, N. Wakasa and T. Fuchikami, *Synlett*, 2001, 1623-1625.
68. D. Chatterjee, H. C. Bajaj, S. B. Halligudi and K. N. Bhatt, *Journal of Molecular Catalysis*, 1993, **84**, L1-L5.
69. B. J. Liaw, S. J. Chiang, S. W. Chen and Y. Z. Chen, *Applied Catalysis a-General*, 2008, **346**, 179-188.
70. R. V. Malyala, C. V. Rode, M. Arai, S. G. Hegde and R. V. Chaudhari, *Applied Catalysis a-General*, 2000, **193**, 71-86.

71. M. R. Hoffmann, S. T. Martin, W. Y. Choi and D. W. Bahnemann, *Chemical Reviews*, 1995, **95**, 69-96.
72. P. V. Kamat, *J. Phys. Chem. C*, 2007, **111**, 2834-2860.
73. A. L. Linsebigler, G. Q. Lu and J. T. Yates, *Chemical Reviews*, 1995, **95**, 735-758.
74. R. Asahi, T. Morikawa, T. Ohwaki, K. Aoki and Y. Taga, *Science*, 2001, **293**, 269-271.
75. N. Chandrasekharan and P. V. Kamat, *J. Phys. Chem. B*, 2000, **104**, 10851-10857.
76. W. D. Maier, S. J. Barnes, V. Gartz and G. Andrews, *Geology*, 2003, **31**, 885-888.
77. *Platinum 2011*, 2011.
78. J. Mizsei, L. Pirttiaho, M. Karppinen and V. Lantto, *Sensors and Actuators B-Chemical*, 2000, **65**, 195-198.
79. X. Liu, J. Chen, G. Liu, L. Zhang, H. Zhang and B. Yi, *Journal of Power Sources*, 2010, **195**, 4098-4103.
80. R. Bashyam and P. Zelenay, *Nature*, 2006, **443**, 63-66.
81. X. Liu, J. Chen, G. Liu, L. Zhang, H. M. Zhang and B. L. Yi, *Journal of Power Sources*, 2010, **195**, 4098-4103.
82. H.-Y. Chen and W. M. H. Sachtler, *Catal. Today*, 1998, **42**, 73-83.
83. R. Borup, J. Meyers, B. Pivovar, Y. S. Kim, R. Mukundan, N. Garland, D. Myers, M. Wilson, F. Garzon, D. Wood, P. Zelenay, K. More, K. Stroh, T. Zawodzinski, J. Boncella, J. E. McGrath, M. Inaba, K. Miyatake, M. Hori, K. Ota, Z. Ogumi, S. Miyata, A. Nishikata, Z. Siroma, Y. Uchimoto, K. Yasuda, K. I. Kimijima and N. Iwashita, *Chemical Reviews*, 2007, **107**, 3904-3951.
84. P. J. Ferreira, G. J. la O, Y. Shao-Horn, D. Morgan, R. Makharia, S. Kocha and H. A. Gasteiger, *Journal of the Electrochemical Society*, 2005, **152**, A2256-A2271.
85. M. Azaroual, B. Romand, P. Freyssinet and J.-R. Disnar, *Geochimica et Cosmochimica Acta*, 2001, **65**, 4453-4466.
86. A. Robertson, *Platinum Metals Review*, 1975, **19**, 64.
87. B. Lindstrom and L. J. Pettersson, *Cattech*, 2003, **7**, 130-138.
88. in *Studies in Surface Science and Catalysis*, eds. P. W. N. M. v. L. J. A. M. R.A. van Santen and B. A. Averill, Elsevier, 1999, vol. Volume 123, pp. 3-28.
89. J. N. Armor, *Catal. Today*, 2011, **163**, 3-9.
90. R. R. Adzic, J. Zhang, K. Sasaki, M. B. Vukmirovic, M. Shao, J. X. Wang, A. U. Nilekar, M. Mavrikakis, J. A. Valerio and F. Uribe, *Topics in Catalysis*, 2007, **46**, 249-262.
91. S. R. Brankovic, J. X. Wang and R. R. Adzic, *Surface Science*, 2001, **474**, L173-L179-L173-L179.
92. J. Y. Kim, Y. G. Kim and J. L. Stickney, *J. Electroanal. Chem.*, 2008, **621**, 205-213.
93. Y. G. Kim, J. Y. Kim, D. Vairavapandian and J. L. Stickney, *JOURNAL OF PHYSICAL CHEMISTRY B*, 2006, **110**, 17998-18006.
94. E. Leiva, *Electrochim. Acta*, 1996, **41**, 2185-2206.
95. T. L. Wade, B. H. Flowers, R. Vaidyanathan, K. Mathe, C. B. Maddox, U. Happek and J. L. Stickney, in *Nanophase and Nanocomposite Materials Iii*, eds. S. Komarneni, J. C. Parker and H. Hahn, Materials Research Society, Warrendale, 2000, vol. 581, pp. 145-150.

96. D. R. Lide, *CRC handbook of chemistry and physics*, CRC Press, 2003.
97. M. F. Mrozek, Y. Xie and M. J. Weaver, *Anal. Chem.*, 2001, **73**, 5953-5960.
98. D. Gokcen, S. E. Bae and S. R. Brankovic, *J. Electrochem. Soc.*, 2010, **157**, D582-D587.
99. Y. Ding, Y. J. Kim and J. Erlebacher, *Advanced Materials*, 2004, **16**, 1897-1900.
100. C. Xu, J. Su, X. Xu, P. Liu, H. Zhao, F. Tian and Y. Ding, *Journal of the American Chemical Society*, 2006, **129**, 42-43.
101. F. L. Jia, C. F. Yu, K. J. Deng and L. Z. Zhang, *J. Phys. Chem. C*, 2007, **111**, 8424-8431.
102. C. X. Xu, L. Wang, X. L. Mu and Y. Ding, *Langmuir*, 2010, **26**, 7437-7443.
103. C. X. Xu, R. Y. Wang, M. W. Chen, Y. Zhang and Y. Ding, *Physical Chemistry Chemical Physics*, 2010, **12**, 239-246.
104. K. Shin, K. A. Leach, J. T. Goldbach, D. H. Kim, J. Y. Jho, M. Tuominen, C. J. Hawker and T. P. Russell, *Nano Letters*, 2002, **2**, 933-936.
105. A. Wittstock, B. Neumann, A. Schaefer, K. Dumbuya, C. Kubel, M. M. Biener, V. Zielasek, H. P. Steinruck, J. M. Gottfried, J. Biener, A. Hamza and M. Baumer, *J. Phys. Chem. C*, 2009, **113**, 5593-5600.
106. H. Inoue, S. R. Brankovic, J. X. Wang and R. R. Adzic, *Electrochim. Acta*, 2002, **47**, 3777-3785.
107. S. R. Brankovic, J. X. Wang, Y. Zhu, R. Sabatini, J. McBreen and R. R. Adzic, *Journal of Electroanalytical Chemistry*, 2002, **524**, 231-241.
108. K. Sasaki, Y. Mo, J. X. Wang, M. Balasubramanian, F. Uribe, J. McBreen and R. R. Adzic, *Electrochim. Acta*, 2003, **48**, 3841-3849.
109. D. Wang, A. Villa, F. Porta, L. Prati and D. S. Su, *J. Phys. Chem. C*, 2008, **112**, 8617-8622.
110. J. K. Edwards and G. J. Hutchings, *Angew. Chem.-Int. Edit.*, 2008, **47**, 9192-9198.
111. P. Hernandez-Fernandez, S. Rojas, P. Ocon, A. de Frutos, J. M. Figueroa, P. Terreros, M. A. Pena and J. L. G. Fierro, *Journal of Power Sources*, 2008, **177**, 9-16.
112. X. L. Zhu, Y. P. Zhang and C. J. Liu, *Catal. Lett.*, 2007, **118**, 306-312.
113. J. R. Kitchin, oslash, J. K. rskov, M. A. Barteau and J. G. Chen, *Physical Review Letters*, 2004, **93**, 156801.
114. J. G. Chen, C. A. Menning and M. B. Zellner, *Surface Science Reports*, 2008, **63**, 201-254.
115. W. J. Zhou, Z. H. Zhou, S. Q. Song, W. Z. Li, G. Q. Sun, P. Tsiakaras and Q. Xin, *Applied Catalysis B-Environmental*, 2003, **46**, 273-285.
116. M. Chatterjee, A. Chatterjee, S. Ghosh and I. Basumallick, *Electrochim. Acta*, 2009, **54**, 7299-7304.
117. L. Demarconnay, S. Brimaud, C. Coutanceau and J. M. Léger, *Journal of Electroanalytical Chemistry*, 2007, **601**, 169-180.
118. A. Serov and C. Kwak, *Applied Catalysis B: Environmental*, **97**, 1-12.
119. Nicholso.Rs, *Analytical Chemistry*, 1965, **37**, 1351-&.
120. Nicholso.Rs, J. M. Wilson and M. L. Olmstead, *Analytical Chemistry*, 1966, **38**, 542-&.

121. A. J. Bard and L. R. Faulkner, *Electrochemical Methods Fundamentals and Applications*, Wiley, 2004.
122. V. S. Bagotzky and Vassilye.Yb, *Electrochim. Acta*, 1967, **12**, 1323-&.
123. C. Jin, Y. Song and Z. Chen, *Electrochimica Acta*, 2009, **54**, 4136-4140.
124. H. A. Gasteiger, N. Markovic, P. N. Ross and E. J. Cairns, *Journal of the Electrochemical Society*, 1994, **141**, 1795-1803.
125. A. Hamnett, *Catal. Today*, 1997, **38**, 445-457.
126. G. Blyholder, *J. Phys. Chem.*, 1964, **68**, 2772-&.
127. P. S. Bagus, C. J. Nelin and C. W. Bauschlicher, *J. Vac. Sci. Technol. A-Vac. Surf. Films*, 1984, **2**, 905-909.
128. P. S. Bagus and G. Pacchioni, *Surface Science*, 1992, **278**, 427-436.
129. N. Dimakis, M. Cowan, G. Hanson and E. S. Smotkin, *J. Phys. Chem. C*, 2009, **113**, 18730-18739.
130. F. Sette, St, ouml, J. hr, E. B. Kollin, D. J. Dwyer, J. L. Gland, J. L. Robbins and A. L. Johnson, *Physical Review Letters*, 1985, **54**, 935.
131. D. J. Burnett, A. T. Capitano, A. M. Gabelnick, A. L. Marsh, D. A. Fischer and J. L. Gland, *Surface Science*, 2004, **564**, 29-37.
132. H. Igarashi, T. Fujino, Y. M. Zhu, H. Uchida and M. Watanabe, *Physical Chemistry Chemical Physics*, 2001, **3**, 306-314.
133. J. C. Davies, J. Bonde, A. Logadottir, J. K. Norskov and I. Chorkendorff, *Fuel Cells*, 2005, **5**, 429-435.
134. B. Hammer, Y. Morikawa and J. K. Norskov, *Physical Review Letters*, 1996, **76**, 2141.
135. N. M. Markovic, B. N. Grgur, C. A. Lucas and P. N. Ross, *J. Phys. Chem. B*, 1999, **103**, 487-495.
136. J. M. Gottfried, K. J. Schmidt, S. L. M. Schroeder and K. Christmann, *Surface Science*, 2003, **536**, 206-224.
137. J. Y. Lin, P. Jones, J. Guckert and E. I. Solomon, *Journal of the American Chemical Society*, 1991, **113**, 8312-8326.
138. M. Schonnenbeck, D. Cappus, J. Klinkmann, H. J. Freund, L. G. M. Petterson and P. S. Bagus, *Surface Science*, 1996, **347**, 337-345.
139. R. M. Hammaker, S. A. Francis and R. P. Eischens, *Spectrochimica Acta*, 1965, **21**, 1295-1309.
140. M. T. M. Koper, A. P. J. Jansen, R. A. van Santen, J. J. Lukkien and P. A. J. Hilbers, *J. Chem. Phys.*, 1998, **109**, 6051-6062.
141. J. A. Pople, D. P. Santry and G. A. Segal, *J. Chem. Phys.*, 1965, **43**, S129-+.
142. C. C. J. Roothaan, *Reviews of Modern Physics*, 1951, **23**, 69-89.
143. L. Avalle, E. Santos, E. Leiva and V. A. Macagno, *Thin Solid Films*, 1992, **219**, 7-17.
144. X. Chen and S. S. Mao, *Chemical Reviews*, 2007, **107**, 2891-2959.
145. C. A. Grimes, Mor, G. K. , *TiO2 Nanotube Arrays: Synthesis, Properties, and Applications;*, Springer, Norwell, MA, 2009.
146. V. Iliev, D. Tomova, L. Bilyarska, A. Eliyas and L. Petrov, *Applied Catalysis B-Environmental*, 2006, **63**, 266-271.
147. J. A. Von Fraunhofer and C. Banks, *Potentiostat and its applications*, Daniel Davey, Hartford, Conn., 1972.

148. T. Hachiya, H. Honbo and K. Itaya, *Journal of Electroanalytical Chemistry*, 1991, **315**, 275-291.
149. E. Herrero, L. J. Buller and H. D. Abruña, *Chemical Reviews*, 2001, **101**, 1897-1930.
150. O. M. Magnussen, J. Hotlos, R. J. Nichols, D. M. Kolb and R. J. Behm, *Physical Review Letters*, 1990, **64**, 2929.
151. M. C. Santos and L. O. S. Bulhoes, *Electrochim. Acta*, 2003, **48**, 2607-2614.
152. Z. D. Wei, M. Atsushi, O. Tadayoshi and O. Masatoshi, *Acta Physico-Chimica Sinica*, 2002, **18**, 1120-1124.
153. Z. D. Wei, L. L. Li, Y. H. Luo, C. Yan, C. X. Sun, G. Z. Yin and P. K. Shen, *J. Phys. Chem. B*, 2006, **110**, 26055-26061.
154. Y. B. Mo, Y. Gofer, E. J. Hwang, Z. H. Wang and D. A. Scherson, *Journal of Electroanalytical Chemistry*, 1996, **409**, 87-93.
155. M. V. Ganduglia-Pirovano, K. Reuter and M. Scheffler, *Phys. Rev. B*, 2002, **65**.
156. F. P. Leisenberger, G. Koller, M. Sock, S. Surnev, M. G. Ramsey, F. P. Netzer, B. Klotzer and K. Hayek, *Surface Science*, 2000, **445**, 380-393.
157. V. Sudha and M. V. Sangaranarayanan, *J. Phys. Chem. B*, 2003, **107**, 3907-3913.
158. J. F. Watts, *An introduction to surface analysis by XPS and AES*, J. Wiley, Chichester, West Sussex, England ;, 2003.
159. *NIST X-ray Photoelectron Spectroscopy Database, Version 3.5 (National Institute of Standards and Technology, Gaithersburg, 2003); http://srdata.nist.gov/xps/.*
160. C. E. Bryson, *Surface Science*, 1987, **189**, 50-58.
161. L. Ley, S. P. Kowalczyk, F. R. McFeely and D. A. Shirley, *Phys. Rev. B*, 1974, **10**, 4881.
162. A. Rosengren and B. Johansson, *Phys. Rev. B*, 1980, **22**, 3706-3709.
163. D. C. Koningsberger and R. Prins, *X-ray absorption: Principles, applications, techniques of EXAFS, SEXAFS and XANES*, 1987.
164. T. Tanaka, K. K. Bando, N. Matsubayashi, M. Imamura and H. Shimada, *J. Electron Spectrosc. Relat. Phenom.*, 2001, **114**, 1077-1081.
165. D. E. Sayers, E. A. Stern and F. W. Lytle, *Physical Review Letters*, 1971, **27**, 1204-&.
166. P. J. Durham, J. B. Pendry and C. H. Hodges, *Computer Physics Communications*, 1982, **25**, 193-205.
167. M. G. Samant, J. Stohr, H. R. Brown, T. P. Russell, J. M. Sands and S. K. Kumar, *Macromolecules*, 1996, **29**, 8334-8342.
168. J. L. Solomon, R. J. Madix, W. Wurth and J. Stohr, *J. Phys. Chem.*, 1991, **95**, 3687-3691.
169. Y. S. Lee, C. N. Whang, Y. Jeon, B. S. Choi, T. J. Han, J. J. Woo and M. Croft, *Nucl. Instrum. Methods Phys. Res. Sect. B-Beam Interact. Mater. Atoms*, 1997, **129**, 387-391.
170. B. Ravel and M. Newville, *Journal of Synchrotron Radiation*, 2005, **12**, 537-541.
171. J. C. Woicik, B. Ravel, D. A. Fischer and W. J. Newburgh, *Journal of Synchrotron Radiation*, 2010, **17**, 409-413.
172. *Buehler SUM-MET - The Science Behind Materials Preparation*, Buehler Ltd., USA, 2004.

173. S. Motoo and N. Furuya, *Journal of Electroanalytical Chemistry*, 1985, **184**, 303-316.
174. M. Rodriguez-Lopez, A. Rodes, E. Herrero, P. Tunon, J. M. Feliu, A. Aldaz and A. Carrasquillo, *Langmuir*, 2009, **25**, 10337-10344.
175. T. J. Schmidt, V. Stamenkovic, M. Arenz, N. M. Markovic and P. N. Ross, *Electrochim. Acta*, 2002, **47**, 3765-3776.
176. L. A. Kibler, A. Cuesta, M. Kleinert and D. M. Kolb, *Journal of Electroanalytical Chemistry*, 2000, **484**, 73-82.
177. C. Thambidurai, Y. G. Kim and J. L. Stickney, *Electrochimica Acta*, 2008, **53**, 6157-6164.
178. N. V. Dimitrov, R. Vasiljevic, N., *Electrochemical and Solid-state Letters*, 2007, **10**, D79-D83-D79-D83.
179. R. V. Vasilic, LT. Dimitrov, N., *Electrochemical and Solid-state Letters*, 2005, **8**, C173-C176-C173-C176.
180. R. Vasilic, L. T. Viyannalage and N. Dimitrov, *Journal of the Electrochemical Society*, 2006, **153**, C648-C655-C648-C655.
181. L. T. Viyannalage, R. Vasilic and N. Dimitrov, *Journal of Physical Chemistry C*, 2007, **111**, 4036-4041.
182. S. Kumar and S. Z. Zou, *Langmuir*, 2007, **23**, 7365-7371.
183. S. Koh and P. Strasser, *Journal of the American Chemical Society*, 2007, **129**, 12624-+.
184. H. Nitani, T. Nakagawa, H. Daimon, Y. Kurobe, T. Ono, Y. Honda, A. Koizumi, S. Seino and T. A. Yamamoto, *Applied Catalysis a-General*, 2007, **326**, 194-201.
185. A. Sarkany, O. Geszti and G. Safran, *Applied Catalysis a-General*, 2008, **350**, 157-163.
186. W. J. Zhou and J. Y. Lee, *Electrochemistry Communications*, 2007, **9**, 1725-1729.
187. S. Morin, A. Lachenwitzer, F. A. Moller, O. M. Magnussen and R. J. Behm, *Journal of the Electrochemical Society*, 1999, **146**, 1013-1018.
188. S. R. Wang, J. He, J. L. Xie, Y. X. Zhu, Y. C. Xie and J. G. G. Chen, *Applied Surface Science*, 2008, **254**, 2102-2109.
189. M. Van Brussel, G. Kokkinidis, A. Hubin and C. Buess-Herman, *Electrochimica Acta*, 2003, **48**, 3909-3919.
190. P. P. Liu, X. B. Ge, R. Y. Wang, H. Y. Ma and Y. Ding, *Langmuir*, 2009, **25**, 561-567.
191. P. J. Cumpson and M. P. Seah, *Surface and Interface Analysis*, 1997, **25**, 430-446.
192. C. D. Wagner, L. E. Davis, M. V. Zeller, J. A. Taylor, R. H. Raymond and L. H. Gale, *Surface and Interface Analysis*, 1981, **3**, 211-225.
193. V. R. Stamenkovic, B. S. Mun, M. Arenz, K. J. J. Mayrhofer, C. A. Lucas, G. Wang, P. N. Ross and N. M. Markovic, *Nat Mater*, 2007, **6**, 241-247.
194. M. J. Janik, C. D. Taylor and M. Neurock, *Top. Catal.*, 2007, **46**, 306-319.
195. M. Ø. Pedersen, S. Helveg, A. Ruban, I. Stensgaard, E. Lægsgaard, J. K. Nørskov and F. Besenbacher, *Surface Science*, 1999, **426**, 395-409.
196. Y. D. Jin, Y. Shen and S. J. Dong, *Journal of Physical Chemistry B*, 2004, **108**, 8142-8147.
197. M. O. Pedersen, S. Helveg, A. Ruban, I. Stensgaard, E. Laegsgaard, J. K. Norskov and F. Besenbacher, *Surf. Sci.*, 1999, **426**, 395-409.

198. H. Möller and P. C. Pistorius, *Journal of Electroanalytical Chemistry*, 2004, **570**, 243-255.
199. J. H. Choi, K. W. Park, I. S. Park, K. Kim, J. S. Lee and Y. E. Sung, *JOURNAL OF THE ELECTROCHEMICAL SOCIETY*, 2006, **153**, A1812-A1817-A1812-A1817.
200. N. P. Lebedeva, G. N. Kryukova, S. V. Tsybulya, A. N. Salanov and E. R. Savinova, *Electrochimica Acta*, 1998, **44**, 1431-1440.
201. K. Matsuoka, Y. Iriyama, T. Abe, M. Matsuoka and Z. Ogumi, *Electrochimica Acta*, 2005, **51**, 1085-1090.
202. A. Bauer, K. Lee, C. J. Song, Y. S. Xie, J. J. Zhang and R. Hui, *Journal of Power Sources*, **195**, 3105-3110.
203. J. Zhang, K. Sasaki, E. Sutter and R. R. Adzic, *Science*, 2007, **315**, 220-222.
204. E. M. C. Alayon, J. Singh, M. Nachtegaal, M. Harfouche and J. A. van Bokhoven, *Journal of Catalysis*, 2009, **263**, 228-238.
205. J. Singh, M. Nachtegaal, E. M. C. Alayon, J. Stotzel and J. A. van Bokhoven, *ChemCatChem*, 2010, **2**, 653-657.
206. L. K. Ono, B. Yuan, H. Heinrich and B. R. Cuenya, *J. Phys. Chem. C*, 2010, **114**, 22119-22133.
207. T. Hachiya, H. Honbo and K. Itaya, *Journal of Electroanalytical Chemistry*, 1991, **315**, 275-291.
208. A. Kuzume, E. Herrero, J. M. Feliu, R. J. Nichols and D. J. Schiffrin, *Journal of Electroanalytical Chemistry*, 2004, **570**, 157-161.
209. R. Fu, H. Zeng, Y. LuSuk Yin, W. H. Chan and C. F. Ng, *Carbon*, 1995, **33**, 657-661.
210. H. Karhu, A. Kalantar, I. J. Väyrynen, T. Salmi and D. Y. Murzin, *Applied Catalysis A: General*, 2003, **247**, 283-294.
211. L. Guczi, *Catal. Today*, 2005, **101**, 53-64.
212. A. Borgna, T. F. Garetto, C. R. Apesteguía, F. Le Normand and B. Moraweck, *Journal of Catalysis*, 1999, **186**, 433-441.
213. S. E. Hoernstroem, L. Johansson, A. Flodstroem, R. Nyholm and J. Schmidt-May, *Surface Science*, 1985, **160**, 561-570.
214. E. Irissou, F. Laplante, S. Garbarino, M. Chaker and D. Guay, *The Journal of Physical Chemistry C*, **114**, 2192-2199.
215. L. D. Burke and D. T. Buckley, *Journal of Electroanalytical Chemistry*, 1994, **366**, 239-251.
216. M. Kaderavek and I. Paseka, *Electrochimica Acta*, 1989, **34**, 121-126.
217. M. Peuckert, F. P. Coenen and H. P. Bonzel, *Electrochimica Acta*, 1984, **29**, 1305-1314.
218. F. Tian, R. Jinnouchi and A. B. Anderson, *Journal of Physical Chemistry C*, 2009, **113**, 17484-17492.
219. A. U. Nilekar and M. Mavrikakis, *Surface Science*, 2008, **602**, L89-L94.
220. A. Rincon, M. C. Perez and C. Gutierrez, *Electrochim. Acta*, 2010, **55**, 3152-3156.
221. H. Tang, J. H. Chen, M. Y. Wang, L. H. Nie, Y. F. Kuang and S. Z. Yao, *Applied Catalysis A: General*, 2004, **275**, 43-48.

222. C. Zubrägel, C. Deuper, F. Schneider, M. Neumann, M. Grunze, A. Schertel and C. Wöll, *Chem. Phys. Lett.*, 1995, **238**, 308-312.
223. G. Selvarani, S. V. Selvaganesh, S. Krishnamurthy, G. V. M. Kiruthika, P. Sridhar, S. Pitchumani and A. K. Shukla, *The Journal of Physical Chemistry C*, 2009, **113**, 7461-7468.
224. X. Ge, R. Wang, P. Liu and Y. Ding, *Chem. Mater.*, 2007, **19**, 5827-5829.
225. Y. Xia, Y. Xiong, B. Lim and S. E. Skrabalak, *Angewandte Chemie International Edition*, 2009, **48**, 60-103.
226. R. E. Rettew, N. K. Allam and F. M. Alamgir, *ACS Applied Materials & Interfaces*, 2011, **3**, 147-151.
227. N. Sammes, ed., *Fuel Cell Technology*, Springer, 2006.
228. S. J. Tauster, S. C. Fung and R. L. Garten, *Journal of the American Chemical Society*, 1978, **100**, 170-175.
229. N. K. Allam, K. Shankar and C. A. Grimes, *Advanced Materials*, 2008, **20**, 3942.
230. S. C. Hayden, N. K. Allam and M. A. El-Sayed, *J. Amer. Chem. Soc.* , 2010
231. N. K. Allam and C. A. Grimes, *Langmuir*, 2009, **25**, 7234-7240.
232. N. K. Allam, F. Alamgir and M. A. El-Sayed, *ACS Nano*, 2010
233. N. K. Allam, X. J. Feng and C. A. Grimes, *Chemistry of Materials*, 2008, **20**, 6477-6481.
234. J. Shim, C. R. Lee, H. K. Lee, J. S. Lee and E. J. Cairns, *Journal of Power Sources*, 2001, **102**, 172-177.
235. V. B. Baez and D. Pletcher, *Journal of Electroanalytical Chemistry*, 1995, **382**, 59-64.
236. P. A. Mandelbaum, A. E. Regazzoni, M. A. Blesa and S. A. Bilmes, *Journal of Physical Chemistry B*, 1999, **103**, 5505-5511.
237. H. Iida and A. Igarashi, *Applied Catalysis a-General*, 2006, **298**, 152-160.
238. Y. L. Yu, Y. P. Hu, X. W. Liu, W. Q. Deng and X. Wang, *Electrochimica Acta*, 2009, **54**, 3092-3097.
239. A. Tegou, S. Armyanov, E. Valova, O. Steenhaut, A. Hubin, G. Kokkinidis and S. Sotiropoulos, *Journal of Electroanalytical Chemistry*, 2009, **634**, 104-110.
240. E. R. Weibel, G. S. Kistler and W. F. Scherle, *The Journal of Cell Biology*, 1966, **30**, 23-38.
241. A. J. Baddeley, H. J. G. Gundersen and L. M. Cruzorive, *J. Microsc.-Oxf.*, 1986, **142**, 259-276.
242. H. J. G. Gundersen, *J. Microsc.-Oxf.*, 1977, **111**, 219-223.
243. X. J. Liu, F. Gao, C. P. Wang and a. K. Ishida, *J. Electron. Mater.*, 2008, **37**.
244. R. Baratti, A. Gavriilidis, M. Morbidelli and A. Varma, *Chemical Engineering Science*, 1994, **49**, 1925-1936.
245. M. M. Bhasin, *Catal. Lett.*, 1999, **59**, 1-7.
246. X.-G. Zhou and W.-K. Yuan, *Chemical Engineering and Processing*, 2005, **44**, 1098-1107.
247. Y. Lei, F. Mehmood, S. Lee, J. Greeley, B. Lee, S. Seifert, R. E. Winans, J. W. Elam, R. J. Meyer, P. C. Redfern, D. Teschner, R. Schlögl, M. J. Pellin, L. A. Curtiss and S. Vajda, *Science*, 2010, **328**, 224-228.
248. E. Heracleous, K. W. A.F. Lee and A. A. Lemonidou, *J. Catal.*, 2005, **231**.
249. E. Heracleous and A. A. Lemonidou, *J. Catal.*, 2010, **270**, 67-75.

250. B. Solsona, F. Ivars, A. Dejoz, P. Concepción, M. I. Vázquez and J. M. L. Nieto, *Top. Catal.*, 2009, **52**
251. Y. Wu, B. F. Wu, Y. M. He and T. H. Wu, *Chem. Lett.*, 2009, **38**, 284-285.
252. C. R. Brundle and A. F. Carley, *Chem. Phys. Lett.*, 1975, **31**, 423-427.
253. I. L. Bolotin, A. Kutana and B. M. a. J. W. Rabalais, *Surface Science*, 2001, **472**, 205.
254. M. Caffio, B. Cortigiani, G. Rovida, A. Atrei, C. Giovanardi, A. d. Bona and S. Valeri, *Surface Science*, 2003, **531**, 368-374.
255. P. H. Holloway and J. B. Hudson, *Surface Science*, 1974, **43**, 141-149.
256. C. Benndorf, M. Franck and F. Thieme, *Surface Science*, 1983, **128**, 417-423.
257. T. Fleisch, N. Waked and W. N. Delgass, *Surface Science*, 1978, **78**, 141-158.
258. C. M. Kim, H. S. Jeong and E. H. Kim, *Surface Science Letters*, 2000, **459**, L457-L461.
259. M. Lorenz and M. Schulze, *Surface Science*, 2000, **454-456**, 234-239.
260. P. R. Norton, R. L. Tapping and J. W. Goodale, *Surface Science*, 1977, **65**, 13-36.
261. B. P. Payne, A. P. Grosvenor, M. C. Biesinger, B. A. Kobe and N. S. McIntyre, *Surface and Interface Analysis*, 2007, **39**, 582-592.
262. C. N. R. Rao, V. Vijayakrishnan, G. U. Kulkarni and M. K. Rajumon, *Applied Surface Science*, 1995, **84**, 284-289.
263. M. D. Rechtin and B. L. Averbach, *Journal of Physics and Chemistry of Solids*, 1975, **36**, 893-897.
264. M. W. Roberts and R. S. C. Smart, *Journal of the Chemical Society, Faraday Transactions I*, 1984, **80**, 2957-2968.
265. G. T. Tyuliev and K. L. Kostov, *Phys. Rev. B*, 1999, **60**, 2900.
266. M. Schmid, A. Reicho, A. Stierle, I. Costina, J. Klikovits, P. Kostelnik, O. Dubay, G. Kresse, J. Gustafson, E. Lundgren, J. N. Andersen, H. Dosch and P. Varga, *Physical Review Letters*, 2006, **96**.
267. J. Schnadt, A. Michaelides, J. Knudsen, R. T. Vang, K. Reuter, E. Laegsgaard, M. Scheffler and F. Besenbacher, *Physical Review Letters*, 2006, **96**.
268. M. A. Barteau, *Topics in Catalysis*, 2003, **22**, 3-8.
269. V. I. Bukhtiyarov, A. I. Boronin and V. I. Savchenko, *Journal of Catalysis*, 1994, **150**, 262-267.
270. V. I. Bukhtiyarov, I. P. Prosvirin and R. I. Kvon, *Surface Science Letters*, 1994, **320**, L47-L50.
271. C. T. Campbell and M. T. Paffett, *Surface Science*, 1984, **139**, 396-416.
272. S. Linic, J. Jankowiak and M. A. Barteau, *Journal of Catalysis*, 2004, **224**, 489-493.
273. R. M. Ormerod, K. L. Peat, W. J. Wytenburg and R. M. Lambert, *Surface Science*, 1992, **269**, 506-513.
274. E. A. Podgornov, I. P. Prosvirin and V. I. Bukhtiyarov, *Journal of Molecular Catalysis A*, 2000, **158**, 337-343.
275. S. Piccinin, S. Zafeiratos, C. Stampfl, T. W. Hansen, M. Havecker, D. Teschner, V. I. Bukhtiyarov, F. Girgsdies, A. Knop-Gericke, R. Schlogl and M. Scheffler, *Physical Review Letters*, 2010, **104**.
276. H. Hamadeh, O. Knauff, G. Pirug and H. P. Bonzel, *Surface Science*, 1994, **311**, 1-16.

277. R. Neubauer, C. M. Whelan, R. Denecke and H. P. Steinruck, *J. Chem. Phys.*, 2003, **119**, 1710-1718.
278. R. T. Vang, K. Honkala, S. Dahl, E. K. Vestergaard, J. Schnadt, E. Lægsgaard, B. S. Clausen, J. K. Nørskov and F. Besenbacher, *Surface Science*, 2006, **600**, 66-77.
279. M. Weinelt, W. Huber, P. Zebisch and H. P. Steinruck, *Surface Science*, 1992, **271**, 539-554.
280. M. Weinelt, P. Zebisch and H. P. Steinruck, *Surface Science*, 1993, **287/288**, 471-175.
281. F. Zaera and R. B. Hall, *Surface Science*, 1987, **180**, 1-18.
282. X. Y. Zhu, M. E. Castro, S. Akhter, J. M. White and J. E. Houston, *Surface Science*, 1988, **207**, 1-16.
283. S. Mroz and Z. Jankowski, *Surface Science*, 1995, **322**, 133-139.
284. S. Mroz, Z. Jankowski and M. Nowicki, *Surface Science*, 2000, **454-456**, 702-706.
285. E. V. J. I. Flege, G. Nintzel, L. H. Lewis, S Hulbert, and a. P. Sutter, *Nucl. Instr. and Meth. in Phys. Res. B*, 2007, **261**, 855.
286. A. Varykhalov, A. M. Shikin, W. Gudat, P. Moras, C. Grazioli, C. Carbone and O. Rader1, *Physical Review Letters*, 2005, **95**, 247601.
287. A. Meyer, J. I. Flege, R. E. Rettew, S. D. Senanayake, T. Schmidt, F. M. Alamgir and J. Falta, *Phys. Rev. B*, **82**.
288. E. R. Savinova, D. Zemlyanov and B. Pettinger, *Electrochim. Acta*, 2000, **46**, 175-183.
289. D. Y. Zemylanov, E. Savinova, A. Scheybal, K. Doblhofer and R. Schlogl, *Surface Science*, 1998, **418**, 441-456.
290. L. Salvati, L. E. Makovsky, J. M. Stencel, F. R. Brown and D. M. Hercules, *J. Phys. Chem.*, 1981, **85**, 3700-3707.
291. A. Meyer, J. I. Flege, S. D. Senanayake, B. Kaemena, R. E. Rettew, F. M. Alamgir and J. Falta, *LEEM/PEEM 7 Proceedings, IBM Journal of Research and Development,* , 2011.
292. X. Y. Zhu and J. M. White, *Surface Science*, 1989, **214**, 240-256.
293. S. Linic and M. A. Barteau, *Journal of the American Chemical Society*, 2003, **125**, 4034-4035.
294. M. Pourbaix, *Atlas of Electrochemical Equilibria in Aqueous Solutions*, National Association of Corrosion Engineers, 1974.